Systems-Oriented Analyses of Hepatic ^{13}C-Labeling and Metabolite Dynamics

Systemorientierte Analysen von Hepatischen ^{13}C-Markierungs- und Stoffwechseldynamiken

Von der Fakultät Energie-, Verfahrens- und Biotechnik der Universität Stuttgart
zur Erlangung der Würde eines Doktors der Ingenieurswissenschaften (Dr.-Ing.)
genehmigte Abhandlung

vorgelegt von
Klaus Maier
aus Stuttgart

Vorsitzender:	**Prof. Dr.-Ing. Ralf Takors**
Hauptberichter:	**Prof. Dr.-Ing. Dr. h.c. Matthias Reuss**
Mitberichter:	**Prof. Dipl. Ing. Dr. techn. Elmar Heinzle**
Tag der mündlichen Prüfung:	15. Dezember 2009

Institut für Bioverfahrenstechnik
Universität Stuttgart

2009

„Ich behaupte aber, dass in jeder besonderen Naturlehre
nur so viel eigentliche Wissenschaft angetroffen werden
könne, als darin Mathematik anzutreffen ist.“

Immanuel Kant

Table of contents

ACKNOWLEDGEMENTS ..... **I**

NOMENCLATURE ..... **II**

SUMMARY ..... **VII**

ZUSAMMENFASSUNG ..... **X**

LIST OF TABLES ..... **XX**

LIST OF FIGURES ..... **XXI**

1. INTRODUCTION **1**

1.1 Motivation and Scope 2

1.2 Contributions and Aims of the Study 5

2. EXPERIMENTAL SET-UP FOR NON-STATIONARY ^{13}C-LABELING EXPERIMENTS IN MAMMALIAN CELLS **8**

2.1 Introduction 10

2.2 Materials and Methods 12

2.2.1 Cell Culture 12

2.2.2 Transient ^{13}C-Labeling Experiment 12

2.2.3 Sampling and Extraction of Intracellular Metabolites 13

2.2.4 Extracellular Metabolite Data Analysis 13

2.3 Results and Discussion 13

2.3.1 Sampling and Extraction of Metabolites 13

2.3.2 Extracellular Metabolite Concentrations 14

2.3.3 Intracellular Metabolite Concentrations 16

2.3.4 Transient Mass Isotopomer Data 17

2.4 Conclusions 19

3. IDENTIFICATION OF METABOLIC FLUXES IN HEPATIC CENTRAL CARBON METABOLISM FROM TRANSIENT ^{13}C-LABELING DATA **20**

3.1 Introduction 22

3.2 Material and Methods 24

3.2.1 Extracellular Rates 24

3.3 Modeling 24

3.3.1 Large-Scale Stoichiometric Network Model 25

3.3.1.1 Network Consistency Checking 26

3.3.2 Isotopomer Network Model 27

3.3.2.1 Glycolysis 29

3.3.2.2 Pentose Phosphate Pathway 29

3.3.2.3 Tricarboxylic Acid Cycle 29

3.3.2.4 Anaplerosis 29

3.3.3 Isotopomer Balancing 30

3.3.4 Parameter Identification 31

3.3.5 Parameter Sensitivities 32

3.4 Results and Discussion 33

3.4.1 *In Vivo* and *In Silico* Labeling Dynamics 33

3.4.2 Intracellular Flux Distribution 34

3.4.3 Intracellular Metabolite Concentrations 39

3.5 Conclusions 41

4. QUANTIFICATION OF STATIN EFFECTS ON HEPATIC CHOLESTEROL SYNTHESIS BY TRANSIENT ^{13}C-FLUX ANALYSIS 43
4.1 Introduction 45
4.2 Materials and Methods 47
4.2.1 Cell Culture 47
4.2.2 Labeling Experiment 47
4.2.3 Metabolic Network Model 47
4.2.4 Simulation of Isotopomer Dynamics 49
4.2.5 Parameter Estimation 50
4.2.6 Confidence Limits 52
4.2.7 Flux Control 52
4.3 Results and Discussion 54
4.3.1 Labeling Dynamics 54
4.3.2 Flux Distribution 57
4.3.3 Metabolite Levels 61
4.3.4 Flux Control 62
4.4 Conclusions 65

5. DYNAMICS AND CONTROL OF THE CENTRAL CARBON METABOLISM IN HEPATOMA CELLS 67
5.1 Introduction 69
5.2 Material and Methods 72
5.2.1 Experimental Setup 72
5.2.2 Model Reconstruction 72
5.2.3 Model Simulation and Parameterization 76
5.2.4 Systems-Level Analyses 79
5.3 Results and Discussion 80
5.3.1 *In Vivo* and *In Silico* Metabolite Dynamics 81
5.3.2 Glycolysis Control 83
5.3.3 Control of the Pentose Phosphate Pathway 89
5.3.4 Control of the Tricarboxylic Acid Cycle 89
5.3.5 Control of Lactate Dehydrogenase, NADPH Consumption, and Oxidative Phosphorylation 93
5.3.6 Concentration Control over NADPH, NADH, ATP, and NAD 96
5.3.7 Partial Internal Response Coefficients 98
5.4 Conclusions 102

6. CONCLUSIONS AND OUTLOOK 104
6.1 Conclusions 105
6.2 Outlook 109

APPENDIX 115
A. Stoichiometry of the Large-Scale Network Model of Human Hepatic Metabolism 116
Reactions 116
Transporter 123
Compounds 126
B. Atom Mappings for Identifying Metabolic Fluxes in the Cholesterol Synthesis Pathway and Central Carbon Metabolism 132
C. Simulated and Measured Mass Fractions of Phosphoenolpyruvate, Malate, Fumarate, Alpha-Ketoglutarate, Citrate, and Cholesterol in Response to 0 and 50 nM Atorvastatin 134
D. Estimated Metabolic Fluxes and Reversibilities in Primary Rat Hepatocytes in Response to 0 and 50 nM Atorvastatin 136
E. Matrix of scaled elasticities 138
F. Experimentally Determined Initial Metabolite Concentrations 140
G. Matrix of Flux Control Coefficients 141
H. Matrix of Concentration Control Coefficients 143

REFERENCES 145

Acknowledgements

First and foremost, I want to thank Prof. Matthias Reuss for giving me the opportunity to work on this rewarding topic, for his ongoing interest in the project, for being a driving factor to the completion of this work, and for providing me with the necessary academic freedom. I am thankful to Prof. Elmar Heinzle for his interest in this thesis and for agreeing to referee it. I am grateful to Prof. Ralf Takors for providing me with the necessary resources to finish my work at the IBVT. I am immensely thankful to Klaus Mauch for managing the projects I was involved with during my doctorate work, for stimulating discussions, and for his professional advice.

Special thanks go to Ute Hofmann for developing and coordinating the majority of the chemical analyses that enabled the data-driven model-based analyses in the first place. I want to express my gratitude to Anja Niebel, Gaby Vacun, Lara Bogner, Sonja Seefried, and Monika Seiler for their excellent technical assistance. I am indebted to Prof. Jan Hengstler, Alexander Bauer, and Markus Schug for supplying me with isolated primary rat hepatocytes. I also want to acknowledge the contributions from the thesis works of Andreas Lehnart and Philipp Grimmer.

Many thanks to my co-workers Dirk Müller, Timo Hardiman, Martin Pfannmöller, Manuel Dietrich, Angel Sevilla Camins, Christoph Hold, Stefan Junne, and Corinna Kempter for the great time in the office and for uncounted bursts of laughter. Cordial thanks go out to numerous colleagues at the IBVT for the pleasant working atmosphere, for much advice on experimental and modeling issues, and for a memorable time, namely to Markus Samorski, Knut Behrendt, Jochen Schaub, Joachim Bucher, Prem Murugan, Wouter Berendsen, Christina Fritz, Michael Klann, Holger Perfahl, Tobias Vallon, Kerstin Falkner-Tränkle, Martin Siemann-Herzberg, Alexej Lapin, Peter Götz, Karin Lemuth, Oliver Vielhauer, Thomas Horn, Petra Schlack, Alexander Müller, Andreas Freund, Achim Hauck, Ulrich Peckmann, Christina Krämer, Jacek Puchalka, Beate Knoke, Gerhard Mayer, Naruemol Noisommit-Rizzi, Maksim Zakhartsev, Ilona Grimm, Salaheddine Laghrami, Mira Lenfers-Lücker, Martina Schweikert, and Andrea Seipel. Special thanks go to Renate Moser for being the soul of the institute. I also want to express my gratitude towards my colleagues from the Insilico Biotechnology AG for fruitful discussions and dependable programming assistance.

This work was funded through HepatoSys, a systems biology funding initiative of the German Federal Ministry of Education and Research.

Above all, I am deeply indebted to my family for their continuous support, most of all to Helga for her patience, for encouraging me, and for keeping me grounded.

Stuttgart, August 2009 Klaus Maier

Nomenclature

Symbols

c	Concentration
$\mathbf{c}$	Concentration vector
$\mathbf{c}^0$	Square diagonal steady state concentration matrix
C^C	Concentration control coefficient
$\mathbf{C}^C$	Matrix of concentration control coefficients
C^J	Flux control coefficient
$\mathbf{C}^J$	Matrix of flux control coefficients
$\overline{c}$	Average pool size, reference concentration
e	scaled elasticity
$\mathbf{E}$	Matrix of scaled elasticities
$\mathbf{FIM}$	Fisher information matrix
$\mathbf{H}$	Hessian matrix
$\mathbf{i}$	Vector of ones
$\mathbf{I}$	Isotopomer distribution vector, identity matrix
$\mathbf{IMM}$	Isotopomer mapping matrix
$\mathbf{J}$	Jacobian matrix
J	Steady state flux
$\mathbf{J}^0$	Steady state flux vector
$\mathbf{K}$	Kernel of the stoichiometric matrix
K_m	Halbsättigunskonzentration
$\mathbf{L}$	Link matrix
m	Mass isotopomer
$\mathbf{M}$	Mass isotopomer distribution vector
$\mathbf{N}$	Stoichiometric matrix
r	Reaction rate
$\mathbf{r}$	Reaction rate vector
r_{max}	Maximum reaction rate
R	Response coefficient
V_{cell}	Cell volume
$\otimes$	Element-by-element vector multiplication

Abbreviations

13PG	1,3-Diphosphoglycerate
2PG	2-Phosphoglycerate
3PG	3-Phosphoglycerate
6PG	6-Phosphogluconate
ACACCOA	Acetoacetyl-CoA
ACEACE	Acetoacetate
ACOA	Acetyl-CoA
ADP	Adenosine 5’-diphosphate
AKG	α-Ketoglutarate
ALA	Alanine
AMP	Adenosine 5’-monophosphate
ARG	Arginine
ASN	Asparagine
ASP	Aspartate
ATP	Adenosine 5’-triphosphate
BCAA	Branched chain amino acids
CHOL	Cholesterol
CHOL7	Cholesta-7.24-dien-3β-ol
CHOL8	Cholesta-8-en-3β-ol
CIT	Citrate
CMA	Covariance matrix adaption
CO2	Carbon dioxide
CYS	Cysteine
DAE	Differential algebraic equation
DEHYDCHOL	7-dehydrocholesterol
DEHYDDESMO	7-dehydrodesmosterol
DESMO	Desmosterol
DHAP	Dihydroxyacetone-phosphate
E4P	Erythrose-4-phosphate
EC	Energy charge
EMP	Embden-meyerhof-parnas pathway (glyoclysis)
EMU	Elementary metabolite unit
ES	Evolution strategy
F16P	Fructose-1,6-disphosphate

Abbreviations (continued)

F6P	Fructose-6-phosphate
FUM	Fumarate
G1P	Glucose-1-phosphate
G6P	Glucose-6-phosphate
GAP	Gylcerinealdehyde-3-phosphate
GC-MS	Gas chromatography-mass spectrometry
GDP	Guanosine 5'-diphosphate
GL6P	Glucono-1,5-lactone 6-phosphate
GLC	Glucose
GLN	Glutamine
GLU	Glutamate
GLY	Glycine
GTP	Guanosine 5'-triphosphate
HBUT	3-Hydroxybutyrate
HIS	Histidine
HMGCOA	3-Hydroxy-3-methylglutaryl-CoA
HMG-CoA reductase	3-Hydroxy-3-methylglutaryl-CoA reductase
HPLC	High performance liquid chromatography
IBVT	Institute of Biochemical Engineering (University of Stuttgart)
IKP	Dr. Margarete Fischer-Bosch Institute of Clinical Pharmacology (Stuttgart)
ILE	Isoleucine
INSILICO	Insilico Biotechnology AG (Stuttgart)
ISA	Isotopic spectral analysis
ISOCIT	Isocitrate
ISOVALMET	Isoleucine, valine, and methionine metabolism
LAC	Lactate
LATHO	Lathosterol
LC-MS	Liquid chromatography-mass spectrometry
LDL	Low-density lipoprotein
LEU	Leucine
Linlog	Linear-logarithmic
LSODA	Livermore solver of ordinary differential equations
LYS	Lysine
MAL	Malate

Abbreviations (continued)

MET	Methionine
MIDA	Mass isotopomder distribution analysis
NAD	Nicotinamide adenine dinucleotide (oxidized)
NADH	Nicotinamide adenine dinucleotide (reduced)
NADP	Nicotinamide adenine dinucleotide phosphate (oxidized)
NADPH	Nicotinamide adenine dinucleotide phosphate (reduced)
NXP	Nucleotides
OAC	Oxaloacetate
ODE	Ordinary differential equation
P5P	Pentose-5-phosphate
PCA	Perchloric acid
PEP	Phosphoenolpyruvate
PHE	Phenylalanine
PPP	Pentose phosphate pathway
PRO	Proline
PYR	Pyruvate
RIBO5P	Ribose-5-phosphate
RIBU5P	Ribulose-5-phosphate
ROS	Reactive oxygen species
S7P	Sedoheptulose-7-phosphate
SER	Serine
SUC	Succinate
SUCOA	Succinyl-CoA
TCA	Tricarboxylic acid cycle
THR	Threonine
TRP	Tryptophane
TYR	Tyrosine
VAL	Valine
VLDL	Very low-density lipoprotein
XYL5P	Xylulose 5-phosphate
ZYMO	Zymosterol

Indices

in	Intracellular
ex	Extracellular
for	Forward reaction
back	Backward reaction
net	Netto flux
cv	Cell volume

Greek letters

α	Factor that equals 1 if $\upsilon_{ij} > 0$, else 0
β	Reversibility factor
ε	Sensitivity
$\boldsymbol{\Theta}$	Parameter vector
ξ	weighting factor
σ	Standard deviation
$\boldsymbol{\Sigma}$	Covariance matrix
τ	Time constant
υ	Stoichiometric coefficient
ϕ	Fractional amount of the non-determined mass fraction
χ^2	Variance weighted sum of squared residuals
ψ	Permutations of reactant mass fractions

Summary

The hepatic metabolism is of particular pharmaceutical and medical relevance. In this thesis a data-driven model-based approach was undertaken to analyze the liver central metabolism at the systems-level. The work focused on the model-assisted interpretation of metabolome and fluxome data. Experimental observations of stationary and non-stationary ^{13}C-labeling and metabolite data enabled the identification of metabolic fluxes, metabolite dynamics, and patterns of metabolic control by means of transient ^{13}C-flux analysis, dynamic modeling, and metabolic control analysis. The major goals of this contribution were (i) to establish an experimental set-up and a computational framework for acquiring and analyzing transient ^{13}C-mass fraction data in mammalian cells and to use it to identify metabolic fluxes in HepG2 cells, (ii) to apply transient ^{13}C-flux analysis to quantify the effects of a therapeutic dose of the hypolipidemic drug atorvastatin on the cholesterol pathway and central metabolism in primary rat hepatocytes, and (iii) to provide systems-level analyses of the dynamics and control of the central carbon metabolism in hepatoma cells.

The experimental observation of the isotopic transient offers the temporal resolution needed to identify intracellular flux maps in mammalian cells from ^{13}C-labeling experiments. However, at the time of the onset of this thesis, transient ^{13}C-flux analysis had been only demonstrated with the prokaryote *Escherichia coli* (Nöh et al. 2007; Schaub 2007; Schaub et al. 2008). Therefore, to enable the estimation of metabolic fluxes from non-stationary ^{13}C-labeling data in slow- and non-growing mammalian cell batch and fed-batch cultures, reliable means were provided for simultaneous quenching of metabolism and extraction of intracellular intermediates. The chemical analyses were devised and coordinated by Ute Hofmann (Hofmann et al. 2008). The developed sampling procedures and chemical analyses were used to quantify metabolite levels and mass fractions in a dynamic labeling experiment with HepG2 cells using ^{13}C-labeled glucose as substrate. In glycolysis and the pentose-phosphate pathway (PPP), isotopic steady state was reached within 30 min, whereas in the tricarboxylic acid (TCA) cycle isotopic steady state was not attained within 120 min. The implemented experimental set-up was adequate to determine the labeling dynamics in the hepatic metabolite pools.

The experimental data observed from HepG2 cells were used to estimate the corresponding flux map. In order to identify the flux distribution, a computational framework was developed from previous work by Jochen Schaub (Schaub 2007). The framework estimates metabolite fluxes and concentrations from stationary and non-stationary labeling data and allows to automatically compile isotopomer models from user-defined spread-sheets containing the information about the atom transfer mechanisms. The flux estimation was based on a large-scale stoichiometric model, which

was used to estimate effluxes into the biomass, and an isotopomer model of glycolysis, the pentose-phosphate pathway, and the tricarboxylic acid cycle. The split ratio between glycolysis and the pentose-phosphate pathway was determined to 57 % and 43 %. It is worth noting that this was the first time metabolic fluxes were estimated in a mammalian system from a transient ^{13}C-labeling experiment. It is expected that non-stationary ^{13}C-flux analysis will gain importance in quantifying mammalian cell physiology at the systems-level.

The effects of a therapeutic concentration of the hypolipidemic drug atorvastatin on cholesterol biosynthesis and central metabolism were determined in primary rat hepatocytes using ^{13}C-labeled glutamine and transient ^{13}C-flux analysis. Isotopic steady state was observed within 4 h in the central metabolism but not in the cholesterol pathway, regardless of whether the hypolipidemic agent was administered or not. The estimation of the intracellular flux map was based on an isotopomer model comprising both positional isotopomer and mass isotopomer balance equations. The flux through the cholesterol pathway was found to drop from 0.27 to 0.08 mmol/(l_{cv} h) in response to the administration of the statin. Lathosterol is a precursor of cholesterol that can be used as a marker of cholesterol synthesis (Lindenthal et al. 2002). The concentration of the lathosterol pool decreased from 0.022 to 0.003 mmol/l_{cv} after administering atorvastatin, which is the reason why the time constant of this metabolite pool dropped from 6.2 to 4.6 min. Only minor differences were determined in the central carbon fluxes between cells treated with 50 nM atorvastatin and untreated cells. Moreover, further systems-level effects of the administered drug were deduced from the analysis of the metabolic control of the targeted 3-hydroxy-3-methylglutaryl-coenzyme A (HMG-CoA) reductase enzyme. The flux control coefficient of the HMG-CoA reductase over the cholesterol synthesis flux was determined to 0.46, i.e. cholesterol biosynthesis is not completely controlled by the HMG-CoA reductase. This means that other reaction steps may be also potent targets for lowering blood cholesterol levels.

A dynamic liver central carbon metabolism model was developed from metabolite time-series and applied to break down the control hierarchy in hepatoma cells. The dynamic metabolite data were collected from HepG2 cells in a stimulus response experiment in which the cells had been deprived of extracellular glucose. The metabolites in the central carbon metabolism showed substantial changes in intermediate levels, whereas the concentrations of the energy and reduction co-factors changed only moderately in response to the stimulus. The enzyme kinetics were described with the canonical linlog formalism, which had been reported previously to yield a good approximation quality, while only requiring the determination of comparatively few parameters (Heijnen 2005; Reuss et al. 2007; Visser and Heijnen 2003). The *in silico* metabolite time-series data were in accordance with the experimentally determined metabolite dynamics. To unravel the internal control structure of the hepatoma central carbon metabolism, concentration and flux control coefficients, partial flux control coefficients, and internal response coefficients were deduced. It should be noted that the control pat-

terns derived from analyzing the dynamic model quantified the mutual influences of individual enzymes and thus provided the so far most detailed investigation of the underlying control distribution in the hepatoma central metabolism. The control patterns found support the hypotheses that the glucose-6-phosphate dehydrogenase reaction and the Warburg effect (cancer cells have an increased glycolytic flux in the presence of an adequate oxygen supply) are promising targets for tumor treatment (Boren et al. 2002; Lopez-Lazaro 2008; Pelicano et al. 2006). The presented data-driven model-based analyses of the dynamics and control of the hepatoma central metabolism are important steps on the avenue towards the personalized prognosis of systems-level effects of drugs and nutrients.

Zusammenfassung

Eine lebende Zelle hängt nicht nur von ihren individuellen Komponenten ab, sondern auch von der Interaktion dieser Komponenten und dem Austausch von Signalen und Materie mit der Umgebung. Systemorientierte Ansätze werden deswegen zunehmend als besonders geeignet betrachtet, um die inhärente Komplexität von lebenden Systemen besser zu verstehen. Dabei sind modelbasierte Analysen von mehreren Ebenen der zellulären Organisation wertvolle Hilfsmittel, um ein Verständnis auf Systemebene zu erlangen. Neben der modellgestützten Interpretation von Genom, Transkriptom und Proteom Daten, gewinnen Metabolom und Fluxom basierte Untersuchungen zunehmend an Bedeutung. Die Identifizierung von metabolischen Flüssen, Stoffwechseldynamiken und der metabolischen Kontrollhierarchie sind wichtige Schritte auf dem Weg hin zu einem holistischen Verständnis und einer quantitativen Beschreibung von einem biologischen System. Dabei ist zu beachten, dass hierzu angemessene Methoden bereitzustellen sind, um stationäre und instationäre Markierungs- und Metabolitdaten zu erfassen, die nachfolgend durch hochentwickelte Werkzeuge aus den Bereichen der Systembiologie und des Metabolic Engineering analysiert werden können.

Die Leber erfüllt eine Vielzahl von lebenswichtigen Stoffwechselfunktionen im Körper, wie zum Beispiel die Detoxifizierung von Xenobiotika, die Aufrechterhaltung der Glucose-Homeostase sowie die Biosynthese von Cholesterol und Gallensalzen. Hepatozyten machen 70 % bis 80 % der cytoplasmatischen Masse der Leber aus und sind damit der häufigste Leberzelltyp (Ramadori et al. 2008). Aufgrund ihrer besonderen medizinischen und pharmazeutischen Relevanz wurden Hepatozyten vom Bundesministerium für Bildung und Forschung (BMBF) als Modellsystem für die erste nationale systembiologische Förderinitiative „HepatoSys“ gewählt. Durch dieses Forschungsprogramm sollte eine Basis zur nachhaltigen Stärkung dieser vielversprechenden Zukunftstechnologie in Deutschland geschaffen werden. In der ersten Förderphase (2004-2006) wurden zunächst drei regionale Forschungsnetzwerke sowie zwei überregionale Serviceplattformen installiert. Die Plattform Modellierung entwickelte Werkzeuge zur mathematischen Modellierung der hepatischen Physiologie. Die Plattform Zellbiologie war verantwortlich für die Versorgung der Forschungsnetzwerke mit einer ausreichenden Menge von primären Hepatozyten und hepatischen Zelllinien. Das Netzwerk Regeneration konzentrierte sich auf die Untersuchung von Signalkaskaden und die Expression bestimmter Gene im Kontext der Proliferation, Differenzierung und Apoptose. Das Netzwerk Endocytose untersuchte die Zusammenhänge zwischen Endocytose und Signaltransduktion. Das Hauptaugenmerk des Netzwerks Detoxifizierung lag auf der systemorientierten Analyse von Leberfunktion im Hinblick auf den Stoffwechsel von Arzneimitteln. Zu Beginn der zweiten Förderphase (2007-2009) wurde mit dem

Netzwerk Eisen ein weiteres Forschungsnetzwerk etabliert. Dieses Netzwerk forschte über die systemische Regulation des Eisenstoffwechsels in der Leber.

Die vorliegende Arbeit wurde im Rahmen eines Teilprojektes aus dem Netzwerk Detoxifizierung durchgeführt. Dabei ist hervorzuheben, dass der Abbau von Xenobiotika auf eine ausreichende Versorgung mit Precursorn und Cofaktoren aus dem zentralen Kohlenstoffmetabolismus angewiesen ist. Darüber hinaus ist der Zentralstoffwechsel der Wirkort von Statinen, wie zum Beispiel Atorvastatin und Pravastatin, die von dem Netzwerk Detoxifizierung in der zweiten Förderphase von „HepatoSys“ als Modelldrogen ausgewählt wurden. An der Bearbeitung dieses Teilprojekts waren beteiligt: Die Insilico Biotechnology AG (INSILICO; Klaus Mauch), das Dr. Margarete Fischer Bosch Institut für klinische Pharmakologie (IKP; Ute Hofmann, Sonja Seefried, Monika Seiler) sowie das Institut für Bioverfahrenstechnik an der Universität Stuttgart (IBVT; Matthias Reuss, Anja Niebel, Klaus Maier). Das IKP war verantwortlich für die Quantifizierung von Massenisotopomeren und Metaboliten aus stationären und dynamischen Proben. Das IBVT führte die Markierungs- und Stimulus-Response-Experimente durch, quantifizierte Nukleotide und realisierte die Datenanalyse. INSILICO stellte Software-Werkzeuge zur Analyse der Markierungs- und Metabolitdaten zur Verfügung und war mit dem Projektmanagement betraut. Dieses Zusammenspiel zwischen Experiment, Analytik und mathematischer Modellierung bildete das Fundament für die durchgeführten datengetriebenen modellbasierten Analysen.

In dieser Arbeit wurde ein datengetriebener modellbasierter Ansatz verfolgt, um den zentralen hepatischen Metabolismus auf Systemebene zu analysieren. Der Schwerpunkt lag dabei auf der modellgestützten Interpretation von Metabolom- und Fluxom-Daten. Die experimentelle Bestimmung von stationären und instationären Markierungs- und Metabolitdaten ermöglichte die Identifizierung von metabolischen Flüssen, Stoffwechseldynamiken und metabolischen Kontrollprinzipien auf Basis von transienter ^{13}C-Stoffflussanalyse, dynamischer Modellierung und metabolischer Kontrollanalyse. Die Hauptziele dieser Arbeite waren (i) die Etablierung eines experimentellen Set-ups und eines rechenbasierten Auswertungsrahmenwerks zur Erhebung und Analyse transienter Massenisotopomerdaten in Säugetierzellen und deren Einsatz zur Identifizierung metabolischer Flüsse in HepG2-Zellen, (ii) die Anwendung der instationären ^{13}C-Stoffflussanalyse zur Quantifizierung der Effekte einer therapeutischen Dosis des cholesterinsenkenden Medikaments Atorvastatin auf die Cholesterol-Synthese und den Zentralstoffwechsel in primären Rattenhepatozyten und (iii) die Untersuchung der Dynamik und Kontrolle des zentralen Kohlenstoffwechsels in Hepatoma-Zellen auf Systemebene.

Etablierung der instationären ^{13}C-Stoffflussanalyse in Säugetierzellen

Die Abschätzung der intrazellulären Flussverteilung ermöglicht eine quantitative Erfassung von metabolischen Regulationen und der zellulären Physiologie auf Systemebene. Aufgrund dieser Eigenschaft wurde die metabolische Flussanalyse zu einem der wertvollsten Werkzeuge im Bereich des Metabolic Engineering und der angewandten Systembiologie (Schaub 2007; Stephanopoulos et al. 1998). Die Kenntnis der intrazellulären Flussverteilung erwies sich als geeignet, um die Identifizierung von genetischen Targets zur Erhöhung von Produktivitäten und Ausbeuten von Produzentenstämmen zu unterstützen (Nielsen 2003; Wiechert and Nöh 2005). Daneben wird zunehmend das Potential der Flussanalyse erkannt, um die Gefahren und Nebenwirkungen von neuen Medikamenten zu analysieren sowie komplexe Stoffwechselkrankheiten quantitativ zu erfassen (Yarmush and Banta 2003; Yarmush and Berthiaume 1997). Dabei ist zu beachten, dass es auf Basis der ^{13}C-Stoffflussanalyse möglich ist, frei von Annahmen über Cofaktorbilanzen und Energieausbeuten, metabolische Flüsse in Reaktionszyklen und Parallelwegen zu schätzen (Wiechert 2001). Deswegen bieten markierungsbasierte Flussschätzungen zum gegenwärtigen Zeitpunkt die vertrauenswürdigste Form der Flussanalyse. Während eines Markierungsexperiments wird ein markiertes Substrat durch das intrazelluläre Reaktionsnetzwerk in metabolische Intermediate mit einem bestimmten Markierungsmuster umgewandelt. Dieses Markierungsmuster ist abhängig von der zugrundeliegenden Flussverteilung und kann durch Kernspinresonanzspektroskopie (Nuclear Magnetic Resonance, NMR) oder Massenspektrometrie (MS) detektiert werden. Die Flussverteilung kann durch lösen des inversen Problems bestimmt werden. Es ist hervorzuheben, dass die experimentelle Beobachtung der Markierungsdynamik die erforderliche zeitliche Auflösung bietet, um intrazelluläre Flussverteilungen auch in Säugetierzellen auf Grundlage von Markierungsexperimenten bestimmen zu können. Zu Beginn dieser Arbeit war die instationäre Flussanalyse bisher lediglich in dem Prokaryoten *Escherichia coli* exemplarisch demonstriert worden (Nöh et al. 2007; Schaub 2007; Schaub et al. 2008).

Um die tracer-basierte Schätzung metabolischer Flüsse nun auch in Batch und Fed-Batch Fermentationen von langsam und nicht wachsenden Säugetierzellen zu ermöglichen, wurden zunächst geeignete Techniken zum gleichzeitigen Quenching des Metabolismus und zur Extraktion intrazellulärer Metabolite etabliert. Dabei wurden mit einer kombinierten Anwendung von heißer Luft (150 °C für 5 s) und kochendem Wasser die besten Resultate im Hinblick auf den Energy Charge (0,88) und die Reproduzierbarkeit erzielt. Bei Einsatz von Perchlorsäure (PCA) wurde sogar ein Energy Charge von 0,93 bestimmt. Aufgrund der nachfolgenden LC-MS (Liquid Chromatography-Mass Spectrometry) Analytik, konnte diese Aufschlussmethode jedoch nicht zur Bestimmung der Massenisotopomere verwendet werden. Die erforderlichen Methoden zur chemischen Analytik wurden von Ute Hofmann implementiert und koordiniert (Hofmann et al. 2008). Die entwickelten Probenahmetechniken und

Analytikmethoden wurden dann verwendet, um Metabolitkonzentrationen und Massenfraktionen in HepG2-Zellen in einem dynamischen Markierungsexperiment mit ^{13}C-gelabelter Glucose zu bestimmen. Dabei wurde die Markierungsdynamik in der Glykolyse, im Pentosephosphatweg (PPP) und im Zitronensäurezyklus (TCA) erfasst. Bei allen Metaboliten wurden im Verlauf des Experiments eine Abnahme des unmarkierten Anteils und eine Zunahme von markierten Massenfraktionen beobachtet. In der Glykolyse und dem Pentosephosphatweg stellte sich innerhalb von 30 Minuten isotopische Stationarität ein, während im Zitronensäurezyklus auch nach 120 Minuten kein isotopisch stationärer Zustand erreicht wurde. Das entwickelte experimentelle Set-up war geeignet, um die Markierungsdynamiken in den hepatischen Metabolitpools zu erfassen.

Die in HepG2-Zellen erhobenen Daten wurden zur Identifizierung der dazugehörigen Flussverteilung verwendet. Zur Flussschätzung wurde ein rechenbasiertes Auswertungsrahmenwerk auf Grundlage einer früheren Arbeit von Jochen Schaub entwickelt (Schaub 2007). In diesem Rahmenwerk ist es möglich, metabolische Flüsse, Reversibilitäten und Konzentrationen aus stationären und instationären Markierungsdaten zu schätzen. Um den Parameterraum zu reduzieren, wurde ein großskaliges stöchiometrisches Modell entworfen und dazu verwendet, Abflüsse in die Biomasse zu schätzen. Zur Auswertung der Markierungsdaten wurde ein Isotopomerenmodell der Glykolyse, des Pentosephosphatwegs und des Zitronensäurezyklus eingesetzt. Dieses Modell umfasste 860 Bilanzgleichungen, weshalb die Formulierung des Gleichungssystems automatisiert wurde. Innerhalb des Rahmenwerks werden Isotopomerenmodelle auf Basis der in einer Textdatei beschriebenen Atomübergänge automatisch erzeugt. Dies ist auch unter dem Gesichtspunkt des Testens von Modellalternativen von besonderer Relevanz, da so verschiedene Modellvarianten zeitnah getestet werden können. Die Analyse der experimentellen Daten basierte auf der Verwendung eines effizienten Differentialgleichungslösers (LSODA), der dynamisch zwischen Integrationsmethoden für steife und nichtsteife Systeme umschaltet (Hindmarsh 1983), einer hochentwickelten globalen Optimierungsroutine (CMA-ES) (Hansen and Ostermeier 2001; Streichert and Ulmer 2005) und dem Konzept der freien Flüsse unter Verwendung der Insilico Discovery Software (Insilico Biotechnology AG, Stuttgart). Die simulierten Markierungsdynamiken stimmten mit den experimentellen Daten überein, d.h. das rechnergestützte Auswertungsrahmenwerk war geeignet, transiente Massenisotopomerdaten zu analysieren. Dies war die erste erfolgreiche Anwendung der instationären ^{13}C-Stoffflussanalyse im Kontext von Säugetierzellen.

Die Aussagekraft der tracer-basierten Flussschätzung wurde durch eine Sensitivitätsanalyse überprüft. Dadurch konnte gezeigt werden, dass das Verhältnis der Flüsse in die Glykolyse und in den Pentosephosphatweg durch die experimentell bestimmten ^{13}C-Markierungsdynamiken mit hoher Genauigkeit aufgeklärt werden konnte. Dies wurde auch in einer Nachfolgeuntersuchung bestätigt,

bei der die Konfidenzintervalle der geschätzten Flüsse durch Verwendung der Fisher Informationsmatrix approximiert wurden (Maier et al. 2007). Das Verhältnis zwischen dem Fluss in die Glykolyse und in den Pentosephosphatweg wurde zu 57 % und 43 % bestimmt. Im Gegensatz hierzu ergab eine stöchiometrische Stoffflussanalyse auf Basis des großskaligen Modells ein Verhältnis von 94 % (Glykolyse) und 6 % (Pentosephosphatweg). Da die ^{13}C-Stoffflussanalyse keine Annahmen über Cofaktorbilanzen und Energieausbeuten erfordert, wurde in dem großskaligen Modell folglich mindestens ein relevanter NADPH-konsumierender Prozess nicht berücksichtigt, wie zum Beispiel die Umsetzung von radikalen Sauerstoffspezies (Reactive Oxygen Species, ROS) durch Glutathion. Unter Berücksichtigung dieser Diskrepanz und des Vollkommenheitsgrads des großskaligen Modells, kann man die Hypothese formulieren, dass die ausreichende Berücksichtigung des Stoffwechsels von Cofaktoren im Kontext von Stoffwechselmodellen für Säugetierzellen sogar noch schwieriger sein könnte, als in Modellen für Hefen und Prokaryoten. Lee et al. betonten ebenfalls die gesteigerten Schwierigkeiten bei der Formulierung von stöchiometrischen Stoffwechselmodellen für Säugerzellen im Vergleich zu Bakterien und Hefen (Lee et al. 1999). Zusammengefasst ist festzuhalten, dass die Schätzung von metabolischen Flüssen auf Grundlage von instationären Markierungsdaten der am weitesten ausgereifte Ansatz zur Bestimmung intrazellulärer Flussverteilungen in Säugetierzellen ist. Es ist daher zu erwarten, dass die Bedeutung der instationären ^{13}C-Stoffflussanalyse für die systemorientierte Analyse der Physiologie von Säugetierzellen weiter zunehmen wird.

Die durch die Analyse der Markierungsdynamik erreichte höhere zeitliche Auflösung ermöglicht eine markierungsbasierte Schätzung von intrazellulären Flussverteilungen in industriell relevanten Batch und Fed-Batch Fermentation von tierischen Zellkulturen. Es ist folglich davon auszugehen, dass die instationäre ^{13}C-Stoffflussanalyse zukünftig eine wichtige Rolle bei Prozessentwicklungen sowie bei der Prozesskontrolle im Rahmen der Produktion von Biopharmazeutika mit Produktionsstämmen, wie zum Beispiel CHO (Chinese Hamster Ovary) Zellen, spielen wird.

Quantifizierung von Statin-Effekten auf die Cholesterol-Synthese und den Zentralstoffwechsel in primären Rattenhepatozyten

Die erfolgreiche Implementierung der instationären ^{13}C-Stoffflussanalyse ebnete den Weg zur Bestimmung von Flussverteilungen in primären Hepatozyten. Letztere sind durch noch kleinere Wachstumsraten als HepG2-Zellen gekennzeichnet und dedifferenzieren schnell. Um die Effekte einer therapeutischen Dosis des cholesterinsenkenden Medikaments Atorvastatin auf die Cholesterol-Synthese und den Zentralstoffwechsel zu quantifizieren, wurde ein dynamisches Markierungsexperiment mit Rattenhepatozyten durchgeführt. Da in vorhergehenden Experimenten festgestellt wurde, dass primäre Rattenhepatozyten Glucose ausschleusen, wurde ^{13}C-gelabeltes Glutamin als Tracer

eingesetzt. Unabhängig von der Anwendung des Medikaments stellte sich isotopische Stationarität im Zentralkohlenstoffwechsel innerhalb von 4 h ein, jedoch nicht im Cholesterolstoffwechsel. Die experimentelle Erfassung der Markierungsdynamik war also erforderlich, um die Flussverteilung im Cholesterolstoffwechsel zu ermitteln. Diese Arbeit war die erste, die experimentelle Messungen von stationären und instationären Markierungsdaten verwendete, um die Effekte von Statinen auf die Cholesterol-Synthese und den Zentralmetabolismus zu erfassen.

Die Schätzung der intrazellulären Flussverteilungen wurde auf Grundlage eines Isotopomerenmodells durchgeführt, das Bilanzgleichungen sowohl für Positionsisotopomere als auch Massenisotopomere beinhaltete. Durch die Modellierung des Cholesterolwegs mit Massenisotopomeren konnte die Zahl der erforderlichen Bilanzgleichungen drastisch reduziert werden. Beispielsweise konnte die Markierungsdynamik im Cholesterol-Pool durch 28 Massenisotopomeren anstatt mit 2^{27} Positionsisotopomeren beschrieben werden. Alternativ hätte man auch den von Antoniewicz et al. entwickelten EMU (Elementary Metabolite Unit) Ansatz anwenden können, um die Zahl der Bilanzgleichungen zu reduzieren (Antoniewicz et al. 2007a; Young et al. 2008). Durch die Ausnutzung von Erhaltungsrelationen und den Einsatz eines linear-impliziten Lösers für differential-algebraische Gleichungssysteme (LIMEX) (Deuflard et al. 1987) konnte sowohl die Geschwindigkeit als auch die numerische Stabilität der Berechnungen weiter verbessert werden.

Als Reaktion auf die Gabe des Medikaments fiel der Fluss durch den Cholesterolweg von 0,27 auf 0,08 mmol/(l_{cv} h), während die Konzentration des Lathosterol-Pools von 0,022 auf 0,003 mmol/l_{cv} fiel. Dadurch ergab sich eine Verringerung der zugehörigen Zeitkonstante dieses Metaboliten von 6,2 auf 4,6 Minuten. Lathosterol ist ein Precursor von Cholesterol, der sich als Marker für die Cholesterol-Biosynthese eignet (Lindenthal et al. 2002). Im zentralen Kohlenstoffwechsel wurden zwischen unbehandelten Zellen und Zellen, die in 50 nM Atorvastatin kultiviert worden waren, nur unwesentliche Unterschiede festgestellt. Die Abnahme des Flusses in die Cholesterolsynthese wurde durch eine erhöhte Ausschleusung von Ketonkörpern kompensiert. Dies war in Übereinstimmung mit vorherigen Studien bei denen Ratten mit den cholesterolsenkenden Mitteln Cholestyramine und Pravastatin behandelt wurden (Sato et al. 2002). Es ist zu betonen, dass derartige systemorientierte und quantitative Untersuchungen vielversprechende Ansätze bieten, zukünftige Risikobeurteilungen von Nebenwirkungen von neuen Arzneimitteln zu unterstützen. Vor kurzem verwendeten Niklas et al. metabolische Flussanalysen zur Erfassung der Wirkung von subtoxischen Konzentrationen von Medikamenten auf den Zentralstoffwechsel von HepG2-Zellen (Niklas et al. 2009).

Neben der Identifizierung der intrazellulären Flussverteilung ermöglicht die instationäre ^{13}C-Stoffflussanalyse die Abschätzung von nicht gemessenen stationären Poolgrößen. Diese Arbeit war die erste, die diese Charakteristik ausnutzte, um die instationäre ^{13}C-Stoffflussanalyse im Kontext

der metabolischen Kontrolltheorie sinnvoll einzubringen. So wurden weitere systemorientierte Auswirkungen des Medikaments durch die Betrachtung der metabolischen Kontrolle des durch die Droge inhibierten Enzyms 3-hydroxy-3-methylglutaryl-coenzyme A (HMG-CoA) Reduktase ermittelt. Der Flusskontrollkoeffizient der HMG-CoA Reduktase über den Cholesterol-Synthesefluss wurde zu 0,46 bestimmt, d.h. die Cholesterol-Biosynthese wird nicht ausschließlich durch die HMG-CoA Reduktase kontrolliert. Aufgrund des Summationstheorems für Flusskontrollkoeffizienten ergibt sich, dass evtl. auch andere Reaktionsschritte interessante Eingriffsmöglichkeiten zur Senkung der Blutcholesterolwerte bieten.

Die erfolgreiche Demonstration der instationären ^{13}C-Stoffflussanalyse mit primären Rattenhepatozyten war ein wichtiger Schritt auf dem Weg hin (i) zur Überwachung von Krankheitsfortschritten durch chemische Biopsie, (ii) zur quantitativen Erfassung der Effekte von Therapeutika auf den grundlegenden Metabolismus und (iii) zur auf metabolischen Kriterien beruhenden Entwicklung neuer Klassifikationsstrategien für Krankheitszustände (Lee et al. 1999).

Dynamik und Kontrolle des zentralen Kohlenstoffwechsels in Hepatoma-Zellen

Für eine detaillierte Betrachtung der Dynamik des hepatischen Zentralstoffwechsels sind experimentelle Beobachtungen und modellbasierte Analysen von intrazellulären Metabolit-Zeitreihen besonders geeignet. Die Identifizierung von Stoffwechseldynamiken auf Basis von mathematischen Modellen ermöglicht die Etablierung einer quantitativen Verknüpfung zwischen mikroskopischen und makroskopischen Phänomenen zu einem kohärenten Gesamtbild der zugrundeliegenden Prozesse (Bailey 1998). Dynamische Netzwerkmodelle sind hervorragende Werkzeuge, um das systemische Verständnis eines biochemischen Reaktionsnetzwerks zu verbessern und zu vertiefen. Die quantitative Erfassung der Beziehungen zwischen der Netzwerktopologie, den Reaktionskinetiken und den intrazellulären Stoffwechseldynamiken bietet eine geeignete Möglichkeit, die inhärente physiologische Komplexität lebender Systeme für den menschlichen Verstand besser begreiflich darzustellen. Darüber hinaus ermöglichen dynamische Modelle detaillierte Analysen der zugrundeliegenden hepatischen Kontrollhierarchie. Mit Ausnahme eines Modells für den Pentosephosphatweg (Sabate et al. 1995), war zu Beginn dieser Arbeit noch kein dynamisches Zentralstoffwechselmodell für Leberzellen in der Literatur beschrieben. Es sollte beachtet werden, dass die systemorientierte Interpretation von hepatischen Stoffwechseldynamiken ein erster Schritt ist hin zu genombasierten Risikoabschätzungen von Nährstoffen und Xenobiotika.

Um die Vorteile der dynamischen Modellierung zu nutzen, ist es zunächst erforderlich die zugrundeliegenden Enzymkinetiken entweder ausgehend von *in vitro* Messungen oder *in vivo* Zeitreihendaten zu identifizieren. Teussink et al. beobachteten jedoch signifikante Unterschiede zwischen Mo-

dellprädiktionen auf Basis von *in vitro* Kinetiken und *in vivo* Messungen (Teusink et al. 2000). Deswegen wird zunehmend der Einsatz von *in vivo* Metabolit-Zeitreihen aus Stimulus-Response-Experimenten befürwortet (Chassagnole et al. 2002; Nikerel et al. 2006; Rizzi et al. 1997; Theobald et al. 1997). Zur Beschreibung der intrazellulären Reaktionsraten können entweder mechanistische kinetische Ansätze und/oder approximative kinetische Formate eingesetzt werden. Die Details der zugrundeliegenden kinetischen Mechanismen sind jedoch oft noch nicht einmal für die gut untersuchten Stoffwechselwege des Zentralstoffwechsels bekannt. Deshalb werden mittlerweile verstärkt kanonische linear-logarithmische (linlog) Kinetiken als das Mittel der Wahl erkannt, um die intrazellulären Enzymkinetiken zu approximieren (Heijnen 2005; Reuss et al. 2007; Visser and Heijnen 2003; Westerhoff and van Dam 1987). Der linlog Formalismus ist durch ein gutes Approximationsvermögen bei einer gleichzeitig verhältnismäßig geringen Zahl zu identifizierender Parameter charakterisiert (Heijnen 2005; Nikerel et al. 2006). Kresnowati et al. verwendeten künstliche Metabolit-Zeitreihen, um die Parametrisierung eines auf linlog Kinetiken basierenden dynamischen Modells zu demonstrieren (Kresnowati et al. 2005). In einer explorativen Studie veranschaulichten Mauch et al., ausgehend von einem Stimulus-Reponse-Datensatz, die Eignung der linlog Kinetik und eines evolutionären Algorithmus für die Identifizierung eines dynamischen Ganzzellmodells für den Stoffwechsel in *Escherichia coli* (Mauch et al. 2004; Reuss et al. 2007). Magnus et al. verwendeten intrazelluläre Metabolitmessungen und linlog Kinetiken, um die Dynamik im Valin/Leucin Stoffwechsel in *Corynebacterium glutamicum* zu beschreiben (Magnus et al. 2006). Es ist hervorzuheben, dass die Identifizierung von dynamischen Modellen auf Grundlage von linlog Kinetiken und intrazellulären Metabolit-Zeitreihen zu Beginn dieser Arbeit an Fahrt gewann, aber noch nicht im Kontext von Säugetierzellen zum Einsatz gekommen war.

Die Analyse der metabolischen Kontrolle ermöglicht eine Quantifizierung des Einflusses von internen und externen Stimuli, wie zum Beispiel Nährstoffen und Medikamenten, auf metabolische Flüsse und Metabolitkonzentrationen (Heinrich and Rapoport 1974; Kacser and Burns 1973). Im Rahmen der metabolischen Kontrollanalyse beschreiben Elastizitäten den lokalen Effekt von Konzentrationsänderungen auf Reaktionsraten, während Kontrollkoeffizienten die globale Kontrolle über Flüsse und Intermediatkonzentrationen bemessen (Hofmeyr 2001; Visser and Heijnen 2002). Nach Cascante et al. ermöglicht eine solche quantitative Beschreibung die (i) Korrelation der Beiträge einzelner Gene und phänotypischer Charakteristika im Zusammenhang mit Stoffwechselerkrankungen sowie die (ii) Identifizierung von neuartigen Therapieansätzen in der Krebsbehandlung und von neuen Interventionsmöglichkeiten in der Medikamentenentwicklung (Cascante et al. 2002). Im Kontext des hepatischen Metabolismus wurde die Kontrollhierarchie bisher vor allem durch die Anwendung von Top-Down Methoden ermittelt (Ainscow and Brand 1999a; Ainscow and Brand 1999c; Soboll et al. 1998).

Dabei ist hervorzuheben, dass ein dynamisches Modell eine weitaus detailliertere Analyse der zugrundeliegenden Kontrollstrukturen ermöglicht, als die bisherigen Top-Down Ansätze.

In dieser Arbeit wurde ein auf linlog Kinetiken basierendes dynamisches Modell des zentralen Leberstoffwechsels entwickelt. Zur Parametrierung des Modells wurde ein Zwei-Schritt-Ansatz gewählt. In den Abschnitten 2 und 3 dieser Arbeit wurde in einem ersten Schritt die zugrundeliegende Flussverteilung durch eine instationäre ^{13}C-Stoffflussanalye aufgeklärt. Danach wurden stationäre Metabolitlevel und skalierte Elastizitäten, d.h. die kinetischen Parameter, aus stationären und instationären Metabolitdaten geschätzt. Die Metabolitdaten wurden in einem Stimulus-Response Experiment mit HepG2-Zellen erhoben, bei dem der Stoffwechsel durch Wegnahme der extrazellulären Glucose ausgelenkt worden war. Im zentralen Metabolismus wurden nach dem Einbringen des Störeinflusses deutliche Änderungen der Metabolitkonzentrationen beobachtet. Im Zitronensäurezyklus wurden für Zitrat, Isocitrat und *cis*-Aconitat gedämpfte Oszillationen ermittelt. Im Gegensatz hierzu wurden für die Konzentrationen der Energie-Cofaktoren und Reduktionsäquivalente nur moderate Änderungen festgestellt. Die *in silico* Zeitreihen stimmten gut mit den experimentell beobachteten Stoffwechseldynamiken überein.

Um die interne Kontrollstruktur des zentralen Kohlenstoffwechsels in Hepatoma-Zellen aufzuklären, wurden Konzentrations- und Flusskontrollkoeffizienten sowie partielle Flusskontrollkoeffizienten und partielle interne Responsekoeffizienten bestimmt. Dabei ist zu beachten, dass die auf Grundlage des dynamischen Modells ermittelten Kontrollprinzipien die gegenseitigen Wechselwirkungen auf Ebene der Enzyme beschreiben, wodurch die bislang detaillierteste Analyse der zugrundeliegenden Verteilung der Kontrolle im zentralen Metabolismus von Hepatoma-Zellen möglich wurde. Die Glucose-6-Phosphat Dehydrogenase übte eine starke negative Kontrolle über die Glykolyse aus. Darüber hinaus hatte dieses Enzym eine positive Kontrolle über den Pentosephosphatweg und die zelluläre NADPH Konzentration. Aufgrund dieser Ergebnisse und des zuvor ermittelten Verhältnisses der stationären Flüsse in die Glykolyse und in den Pentosephosphatwegs von 57 % zu 43 % lässt sich folgern, dass das Hepatoma-Wachstum durch NADPH limitiert ist. Es ist hervorzuheben, dass dieses Ergebnis die Hypothese unterstützt, wonach die Glucose-6-Phosphat Dehydrogenase Reaktion ein interessantes Target zur Tumorbekämpfung darstellt (Boren et al. 2002). Ein weiteres Ergebnis war, dass die Hepatoma-Zellen, im Gegensatz zu primären Zellen, keinen Pasteur-Effekt zeigten. Der Pasteur-Effekt bewirkte in primären Rattenhepatozyten eine negative Kontrolle der Atmung auf den glykolytischen Fluss (Ainscow and Brand 1999c). In HepG2-Zellen wurde dagegen eine positive Kontrolle der oxidativen Phosphorylierung über die Glykolyse festgestellt. Diese Kontrollstruktur erklärt sich durch den sogenannten Warburg-Effekt. Der Warburg-Effekt wird auch als aerobe Glykolyse bezeichnet und beschreibt die Besonderheit vieler Krebszellen, einen gesteigerten glycolytischen Fluss trotz ausrei-

chender Sauerstoffversorgung aufzuweisen. Interessanterweise wird dieser erhöhte glykolytische Fluss maligner Zellen ebenfalls zunehmend als vielversprechender Interventionspunkt zur Tumorbekämpfung wahrgenommen (Lopez-Lazaro 2008; Pelicano et al. 2006). Dies wird durch die vorliegenden Ergebnisse bekräftigt. Darüber hinaus wurden im Zitronensäurezyklus komplexe Kontrollhierarchien aufgeklärt. Eine Erhöhung der NAD und Pyruvat Konzentrationen erhöhten den Fluss in den Zitronensäurezyklus, während erhöhte Pyruvatlevel und ein erhöhtes NADPH/NADP-Verhältnis eine negative Kontrolle über die Reaktion des Malic Enzyme ausübten. Das ist der Grund, weshalb die Glucose-6-Phosphat Dehydrogenase und der ATP-Verbrauch eine positive Kontrolle über die ersten Reaktionen im Zitronensäurezyklus und eine negative Kontrolle über die letzten Reaktionen im Zitronensäurezyklus hatten. Die negative Kontrolle über das Malic Enzyme wurde auf die Reaktionen im hinteren Teil des Zitronensäurezyklus durch erhöhte Produktkonzentrationen übertragen. Diese Weiterleitung konnte durch die Analyse der entsprechenden partiellen Flusskontrollkoeffizienten aufgeklärt werden. Die vorgestellten datengetriebenen modellbasierten Analysen der Dynamik und Kontrolle des zentralen hepatischen Metabolismus sind ein wichtiger Beitrag auf dem Weg hin zur personalisierten Prognose der Effekte von Medikamenten und Nährstoffen auf Systemebene.

Das in dieser Arbeit entwickelte dynamische Zentralstoffwechselmodell könnte neue Möglichkeiten für eine systemorientierte Bewertung von Arzneimittelkandidaten zur Tumorbekämpfung eröffnen. Dabei sollte beachtet werden, dass die mit dem dynamischen Modell aufgeklärte interne Kontrollhierarchie die Hypothesen zur Beeinflussung der Glucose-6-Phosphat Dehydrogenase und des Warburg Effekts zur Tumorbehandlung unterstützten (Boren et al. 2002; Lopez-Lazaro 2008; Pelicano et al. 2006). Die Entwicklung neuer Medikamente und Kombinationstherapien könnte hierbei durch das dynamische Modell begleitet und angeleitet werden. Unter der Annahme, dass der Einfluss auf den Wirkort bzw. die Wirkorte abgeschätzt werden kann, können die metabolischen Konsequenzen aus der Gabe von Medikamenten oder Kombinationen von Medikamenten auf Systemebene vorhergesagt werden.

Auf dem Weg hin zur personalisierten Prognose der Wirkweise und Wirkdauer von Xenobiotika und Nährstoffen wird die modelbasierte Integration von Metabolom, Fluxom, Genom, Transkriptom und Proteom Daten eine wichtige Rolle spielen. Darüber hinaus ist zu erwarten, dass systemorientierte Analysen auf der Ebene von Zellen, Organen und des ganzen Körpers an Bedeutung zunehmen werden, um die direkten und pleiotropen Wirkungen von Medikamenten vollständig zu erfassen und neuartige Behandlungsstrategien zu entwickeln.

List of Tables

Table 1. Intracellular nucleotide concentrations in HepG2 cells (mean ± SD, n = 6). 14

Table 2. Metabolite uptake and secretion rates in nmol/(10^6cells·min). Negative values indicate net uptake. .. 15

Table 3. Intracellular metabolite concentrations in HepG2 cells. 17

Table 4. Mass isotopomer fractions (mean ± SD, n=3) in intracellular metabolites of HEPG2 cells. HepG2 cells were incubated with Williams medium E containing a mixture of 40 % naturally labeled glucose, 40 % U-^{13}C-labeled glucose and 20 % 1-^{13}C-labeled glucose. 18

Table 5. Atom mappings corresponding to the isotopomer model shown in Figure 4. Bidireactional reaction steps and irreversible reactions are indicated by "↔" and "→", respectively. 28

Table 6. Estimated metabolic fluxes in glycolysis, PPP, TCA and two anaplerotic reactions. Fluxes are normalized with respect to the glucose influx. 35

Table 7. Flux distribution sensitivity matrix. Only non-zero values are listed. 39

Table 8. Measured and estimated intracellular pool sizes. Concentrations are given in nmol/10^6cells. 40

Table 9. Experimentally determined extracellular rates (0 nM atorvastatin). Rates and corresponding standard deviations are given in mmol/(l_{cv}·h). 58

Table 10. Experimentally determined intracellular metabolite concentrations (mmol/(l_{cv}·h)). 62

Table 11. Reaction stoichiometry of the dynamic network model. The subscripts 'ex', 'in', and 'nb' denote extracellular, intracellular, and non-balanced metabolites, respectively. 73

Table 12. Activator and inhibitor influences. Regulatory influences and corresponding literature references. The modulator effects were included in the dynamic network model. In addition to these regulatory influences, the dynamic model did also account for substrate and product effects. 76

Table 13. Partial flux control coefficients over glucose-6-phosphate isomerase (r2). Partial flux control coefficients are only shown for metabolites influencing the glucose-6-phosphate isomerase reaction (r2), i.e. that have non-zero elasticities. The sum of the partial flux control coefficients over all intermediates equals the flux control coefficient. For the control of a reaction over its own flux, the flux control coefficient equals the sum of the partial flux control coefficients plus one. 86

Table 14. Partial flux control coefficients over fumarate hydratase (r34), succinate dehydrogenase (r40), and the malic enzyme (r43). Partial flux control coefficients are only shown for metabolites having non-zero elasticities. The sum of the partial flux control coefficients over all intermediates equals the flux control coefficient. For the control of a reaction over its own flux, the flux control coefficient equals the sum of the partial flux control coefficients plus one. 91

Table 15. Partial flux control coefficients over lactate dehydrogenase (r18) and oxidative phosphorylation (r41). Partial flux control coefficients are only shown for metabolites having non-zero elasticities. The sum of the partial flux control coefficients over all intermediates equals the flux control coefficient. For the control of a reaction over its own flux, the flux control coefficient equals the sum of the partial flux control coefficients plus one. 95

Table 16. Partial internal response coefficients. According to the connectivity theorem, the sum of the partial internal response coefficients for each intermediate is -1. Perturbations in moiety conserved sets cannot be opposed to reach the previous steady state, which is the reason why no partial response coefficients are listed for atp, adp, amp, nadp, nadph, nad, and nadh, respectively. 100

List of Figures

Figure 1. Experimental set-up for quantification of extra- and intracellular metabolite levels as well as determination of mass isotopomers. 13

Figure 2. Time courses of extracellular metabolite concentrations..... 16

Figure 3. Large-scale network model of the hepatic metabolism. The metabolic subnetwork (EMP, PPP, TCA), which was applied for ^{13}C flux analysis, is highlighted (cf. dotted line). Six reaction compartments are discriminated: cytosol (Cy), mitochondrion (Mi), peroxisome (Pe), nucleus (Nu), golgi apparatus (Go) and endoplasmic reticulum (ER). Abbreviations used for metabolic pathways: amino acid metabolism (AM), pentose phosphate pathway (PPP), Embden-Meyerhof-Parnas (EMP), tricarboxylic acid cycle (TCA), oxidative phosphorylation (OxP), ketone body synthesis (KBS), C_1 pool (C1), porphyrine synthesis (PoS), urea cycle (UC), pyrimidine synthesis (PyS), purine synthesis (PuS), RNA synthesis (RS), lipid synthesis (LS), cholesterol synthesis (CS), bile synthesis (BS), protein synthesis (PrS), fatty acid synthesis (FAS). 25

Figure 4. Metabolic subnetwork which was applied for ^{13}C flux analysis. Intermediates for which no measurement data was available, and non-balanced metabolites are shown inside ellipses and dashed boxes, respectively. Experimentally quantified metabolites are indicated in rectangles. Reversible and irreversible reactions are indicated by two-sided blue solid arrows and one-sided red dotted arrows. 27

Figure 5. Computational workflow for the evaluation of transient labeling experiments. Required user input and corresponding program output are shown inside rounded rectangles on the left- and right-hand sides. 31

Figure 6. Time courses of *in vivo* (symbols) and *in silico* (solid lines) labeling dynamics. 34

Figure 7. Sensitivities of the objective function value with respect to intracellular fluxes (r_i), estimated pool sizes (c_j), and reversibility factors (β_{ri}). Only values larger than 10^{-2} are listed. 36

Figure 8. Experimentally determined (red circles) and simulated (blue solid lines) mass fractions of 3-phosphoglycerate after administration of 0 nM (left) and 50 nM (right) atorvastatin. The error bars indicate standard deviations of the experimental data..... 54

Figure 9. Simulated (blue solid lines) and measured (red circles) transient mass isotopomer fractions of lathosterol (0 nM atorvastatin). The error bars indicate standard deviations of the experimental data. 55

Figure 10. Experimentally determined (white) and simulated (black) mass fractions of lathosterol after administration of 0 nM (top) and 50 nM (bottom) atorvastatin. The different time points are depicted from the left to the right: 4 h (left), 8 h (center), and 12 h (right) after addition of the tracer. The error bars indicate the standard deviations of the experimental data. 56

Figure 11. Experimentally determined (white) and simulated (black) mass fractions of citrate (0 nM atorvastatin), 12 h after adding the tracer. The error bars indicate standard deviations of the experimental data..... 57

Figure 12. Central carbon fluxes of primary rat hepatocytes cultured in atorvastatin-free (0 nM) medium. All fluxes are given in mmol/(lcv·h). CO2, standard errors and some links were omitted for reasons of clarity (cf Appendix D). The illustrated network comprises two reaction compartments: cytosol (C) and mitochondrion (M). The dotted line indicates the control volume of the ^{13}C sub-network..... 59

Figure 13. Metabolic fluxes in the cholesterol pathway. Shown are the fluxes corresponding to 0 nM (top) and 50 nM atorvastatin (bottom). All fluxes are given in mmol/(l_{cv}·h). The reactions are localized in the endoplasmic reticulum. Abbreviations used: zymo, zymosterol; chol7, cholesta-7.24-dien-3β-ol; dehyddesmo, 7-dehydrodesmosterol; desmo, desmosterol; chol8, cholesta-8-en-3β-ol; latho, lathosterol; dehydchol, 7-dehydrocholesterol; chol, cholesterol;..... 61

Figure 14. Reaction rates (cf. equation (17)) for 0 nM (solid line) and 50 nM (dashed line) atorvastatin. The highlighted reaction rates of 1.6 mM/h (black) and 0.5 mM/h (grey) denote the identified steady

state fluxes for 0 nM and 50 nM atorvastatin at the corresponding estimated HMG-CoA levels in the endoplasmic reticulum. 63

Figure 15. Flux control coefficients $C_{HR}^{J_i}$ with respect to the HMG-CoA reductase enzyme. 65

Figure 16. Metabolic network model. Extra- and intracellular metabolites are depicted with blue ellipses. Enzymatic reactions and transportation steps are indicated with red circles. Non-balanced compounds are shown within grey rounded rectangles. Directions of arrows reflect the direction of the steady state fluxes. The system boundary is indicated with a dashed line. Extra- and intracellular space are highlighted in white and grey. Some links were omitted for reasons of clarity (cf. Table 11 for the complete reaction stoichiometry) 74

Figure 17. Extracellular and intracellular metabolite dynamics. The subscripts 'in' and 'ex' denote intracellular and extracellular metabolites, respectively. The concentration values were normalized with respect to their reference values, i.e. the concentrations directly before the stimulus. The error bars indicate standard deviations of the experimental data. To perturb the central metabolism, the glucose-containing culture medium was exchanged with glucose-free medium. By consequence, the extracellular glucose level dropped, and this stimulated significant intracellular metabolite dynamics.. 82

Figure 18. Flux control coefficients. The colors in row i and column j indicate the control that enzyme j exerts over the flux i. Warm and cold colors denote positive and negative control, respectively. The indices i and j correspond to the reaction numbers shown in Table 11 and Figure 16. The glucose-6-phosphate dehydrogenase (r10) was found to have significant negative control over all glycolytic fluxes, whereas oxidative phosphorylation (r41) exerted positive control (Warburg effect). Furthermore, it is interesting to note that only a few fluxes were found to be significantly stimulated by an increase in the corresponding enzyme level. 84

Figure 19. Concentration control coefficients over glucose-6-phosphate (G6P), fructose-6-phosphate (F6P), and 6-phosphogluconate (6PG). The reaction indices correspond to the reaction numbers shown in Table 11 and Figure 16. 87

Figure 20. Concentration control coefficients over intracellular pyruvate. The reaction indices correspond to the reaction numbers shown in Table 11 and Figure 16. 92

Figure 21. Flux control coefficients over lactate dehydrogenase (r18), nadph consumption (r22), and oxidative phosphorylation (r41). The reaction indices correspond to the reaction numbers shown in Table 11 and Figure 16. 94

Figure 22. Concentration control coefficients over nadph, nadh, atp, and nad. The reaction indices correspond to the reaction numbers shown in Table 11 and Figure 16. 97

1

Introduction

Chapter outline

1.1 Motivation and Scope 2
1.2 Contributions and Aims of the Study 5

1.1 Motivation and Scope

A living cell does not only depend on its individual components but also on the interactions between these components and on the exchange of both signals and material with its environment. Therefore it is increasingly recognized that the inherent complexity of living matter is best tackled using quantitative systems-oriented approaches. To arrive at a systems-level understanding, model-based analyses of several levels of cellular organization are invaluable. Besides the model-assisted dissection of genome, transcriptome, and proteome data, metabolome and fluxome based investigations are gaining importance. The identification of metabolic fluxes, metabolite dynamics, and metabolic control patterns are important steps on the avenue towards a holistic understanding and quantitative description of a biological system. It is worth noting that for this purpose adequate means have to be provided for experimentally observing stationary and non-stationary ^{13}C-labeling and metabolite data that can be analyzed through the application of sophisticated systems biology and metabolic engineering techniques.

The liver plays a major role in metabolism and performs a plethora of vital functions in the body, a few of which are the detoxification of xenobiotics, the maintenance of glucose homeostasis, and the biosynthesis of cholesterol and bile acids; for a review see (Kuntz and Kuntz 2001). Parenchymal hepatocytes are the main liver cell type and make up 70 % to 80 % of the cytoplasmic mass of the liver (Ramadori et al. 2008). Due to its substantial pharmaceutical and medical relevance, the hepatocyte was selected as a model system by the Federal Ministry of Education and Research (BMBF) for the first German systems biology funding initiative “HepatoSys”. This research program aimed at establishing a national platform for systems biology in order to strengthen this promising next-generation technology in Germany. In the first project phase (2004-2006) three regional research networks and two national service platforms were installed. The task of the platform modeling was to develop tools for the mathematical modeling of the hepatic physiology. The platform cell biology was in charge of providing the networks with an adequate supply of primary hepatocytes and hepatic cell lines. The network regeneration investigated signal cascades and the expression of target genes to study the cellular processes responsible for proliferation, differentiation, and apoptosis. The network endocytosis endeavored to comprehend the complexity of the endocytic pathway and its relationship to signal transduction. The major emphasis of the network detoxification was the systems-oriented analysis of liver functions related to drug metabolism. In the second project phase (2007-2009), one further network was established, which was the network iron. This network focused on unraveling the systemic regulation of the liver iron metabolism.

This thesis was part of a sub-project in the network detoxification. It should be noted that the detoxification of xenobiotics depends on sufficient supply of precursors and co-metabolites from the central carbon metabolism. Furthermore, the central metabolism is the site of therapeutic action of

the hypolipidemic statins such as atorvastatin and pravastatin, which were chosen as model drugs by the network detoxification in the second funding period of “HepatoSys”. The sub-project partners involved were the Insilico Biotechnology AG (INSILICO; Klaus Mauch), the Dr. Margarete Fischer Bosch Institute of Clinical Pharmacology (IKP; Ute Hofmann, Sonja Seefried, Monika Seiler), and the Institute of Biochemical Engineering at the University of Stuttgart (IBVT; Matthias Reuss, Anja Niebel, Klaus Maier). Klaus Mauch was the principal investigator of the sub-project. The IKP was in charge of quantifying steady state and dynamic mass fraction and metabolite data. The IBVT executed the chemical labeling and stimulus response experiments, quantified nucleotide levels, and performed the data analysis. INSILICO provided software tools for analyzing the ^{13}C-labeling and metabolite data and was responsible for the management of the project. This structure of the sub-project facilitated a close cooperation between wet and dry lab experts. The interplay between experiment, chemical analyses, and mathematical modeling prepared the ground for the following data-driven model-based analyses of the hepatic metabolism.

Metabolic flux estimates provide a convenient basis for the quantitative assessment of metabolic regulations and cellular physiology at the systems-level. This is the reason why the determination of metabolic fluxes became one of the most fundamental tools in the maturing fields of metabolic engineering and applied systems biology (Schaub 2007; Stephanopoulos et al. 1998). Information on intracellular flux maps was demonstrated to be suitable for assisting the identification of genetic targets for improving both productivities and yields of producer strains (Nielsen 2003; Wiechert and Nöh 2005). Furthermore, since an intracellular flux distribution is a quantitative snapshot of the metabolic phenotype, flux analysis is increasingly recognized as a promising means for probing health and safety impacts of new drug candidates and for analyzing complex metabolic disorders in human diseases (Yarmush and Banta 2003; Yarmush and Berthiaume 1997). It is worth emphasizing that the determination of intracellular flux maps from isotopic tracer experiments enables the identification of metabolic fluxes in reaction cycles and parallel routes without any assumptions to be made on cofactor balances and energy yields (Wiechert 2001). Put differently, at present tracer-based flux analysis provides the most reliable flux estimates. In a chemical labeling experiment, the intracellular reaction network converts a labeled substrate into metabolic intermediates showing a particular labeling pattern that depends on the intracellular flux distribution. These labeling patterns can be elucidated by nuclear magnetic resonance (NMR) spectroscopy or mass spectrometry (MS) methods and the intracellular flux map is obtained through solving the inverse problem. At the time this thesis work was begun in the summer of 2005, the identification of metabolic fluxes from tracer data was still based almost exclusively on isotopic steady state measurements. To shorten the experimental duration of the labeling experiment, Wiechert and Nöh proposed considering the isotopic transient (Nöh et al. 2006b; Nöh and Wiechert 2006; Wiechert and Nöh 2005). Subsequently, non-stationary

^{13}C-flux analysis was realized for the first time in the prokaryote *Escherichia coli* (Nöh et al. 2007; Schaub 2007; Schaub et al. 2008), which was a major step towards the identification of metabolic fluxes in slow- and non-growing mammalian systems. To summarize, the experimental observation of non-stationary labeling data provides the temporal resolution needed for reasonably applying ^{13}C-flux analysis in the context of mammalian cell batch and fed-batch cultures.

To gain insight into the dynamics of the hepatic central metabolism, experimental observations and model-based analyses of intracellular metabolite time-series data are particularly suitable. The identification of metabolite dynamics using mathematical modeling provides a rigorous and quantitative linkage between microscopic and macroscopic phenomena, which is essential for organizing disparate information into a coherent whole (Bailey 1998). Dynamic network models are excellent means for improving our systemic understanding of biochemical reaction networks. The quantitative assessment of the relationships between the topology of the metabolic network, the reaction kinetics, and the intracellular metabolite dynamics provides an opportunity to make the physiological complexity better manageable and understandable for the human mind. Moreover, dynamic modeling enables detailed analyses of the internal hepatic control hierarchy. Importantly, until then, except from a core model of the pentose phosphate pathway (Sabate et al. 1995), no dynamic liver central metabolism model was described in the literature. Furthermore, it is worth emphasizing that the systems-level interpretation of the hepatic metabolite dynamics is a first move towards genome-based risk-assessments of nutrients and xenobiotics.

For the dynamic modeling of the hepatic metabolism, the corresponding enzyme kinetics have to be either identified from *in vitro* measurements or from *in vivo* metabolite dynamics. However, Teusink et al. observed significant differences between model predictions based on *in vitro* kinetics and *in vivo* measurements (Teusink et al. 2000), which led Chassagnole et al. and Nickerel et al. to advocate using *in vivo* metabolite time-series data obtained in stimulus response experiments for identifying intracellular enzyme kinetics (Chassagnole et al. 2002; Nikerel et al. 2006; Rizzi et al. 1997; Theobald et al. 1997). To describe the intracellular reaction rates, mechanistic rate equations and/or approximate kinetic formats can be used. The details of the kinetic mechanisms, though, are often not known even for well-studied pathways of the central carbon metabolism. Therefore, canonical linear-logarithmic (linlog) kinetics are increasingly recognized as adequate means for approximating the intracellular enzyme kinetics (Reuss et al. 2007; Visser and Heijnen 2003; Visser et al. 2004; Westerhoff and van Dam 1987). The linlog formalism was demonstrated to yield a good approximation quality while requiring comparatively few parameters to be determined (Heijnen 2005; Nikerel et al. 2006). Kresnowati et al. used artificial metabolite time-series to demonstrate the parameterization of a dynamic model based on linlog kinetics (Kresnowati et al. 2005). In an exploratory study Mauch et al. exemplified the feasibility of using linlog kinetics and an evolutionary algorithm for the identifica-

tion of a whole-cell dynamic *Escherichia coli* model from stimulus response metabolite data (Mauch et al. 2004; Reuss et al. 2007). Moreover, in the meantime, Magnus et al. used intracellular metabolite measurements and linlog kinetics to describe the dynamics in the valine/leucine synthesis pathway in *Corynebacterium glutamicum* (Magnus et al. 2006). It should be noted that at the beginning of this thesis the identification of dynamic models based on linlog kinetics from intracellular metabolite time-series data was gaining momentum but so far had not been applied in the context of mammalian systems.

Metabolic control analysis provides a mathematical framework that allows quantifying the systems-level effects of internal and external stimuli such as nutrients and drugs on the metabolic fluxes and intermediate levels (Heinrich and Rapoport 1974; Kacser and Burns 1973). Sensitivities determine the local effects of concentration changes on reaction rates, whereas control coefficients quantify the amount of global control exerted on fluxes and metabolite levels in the metabolic network (Hofmeyr 2001; Visser and Heijnen 2002). Cascante et al. illustrated that this quantitative description enables (i) correlating the contribution of individual genes and phenotypic characteristics in metabolic disease and (ii) identifying novel targets for cancer therapy and interventions in drug discovery (Cascante et al. 2002). In the context of the hepatic metabolism, the control hierarchy was mostly deduced from the direct analysis of steady state perturbation data by top-down methods (Ainscow and Brand 1999a; Ainscow and Brand 1999c; Soboll et al. 1998). It is worth noting that a dynamic network model enables a more detailed analysis of the underlying control principles than the previously used top-down approaches. Rather than describing the interaction of sub-systems, the control patterns derived from analysing a dynamic model quantify the mutual influences of individual reaction steps in the network. The envisaged systems-level analyses of the dynamics and control of the liver central metabolism are important steps towards the personalized prognosis of nutrient and drug effects.

1.2 Contributions and Aims of the Study

The main objective of this thesis is to provide quantitative systems-oriented analyses of the hepatic central metabolism based on metabolome and fluxome data. The work focuses on model-based interpretations of experimental observations of steady state and time-resolved transient ^{13}C-labeling and metabolite data. The experimental measurements are obtained in chemical labeling and stimulus response experiments with HepG2 cells and primary rat hepatocytes. Metabolic fluxes, metabolite dynamics, and metabolic control patterns are identified by means of transient ^{13}C-flux analysis, dynamic modeling, and metabolic control analysis. The thesis deals with three major contributions. In a first step, an experimental setup and a computational framework are developed for acquiring and analyzing non-stationary ^{13}C-labeling data from mammalian cells and are used to identify metabolic

fluxes in HepG2 cells. In a second step, transient ^{13}C-flux analysis is applied to quantify the effects of a therapeutic concentration of the hypolipidemic drug atorvastatin on cholesterol biosynthesis and the central carbon fluxes in primary rat hepatocytes. Thirdly, metabolite time-series data are collected in a stimulus response experiment with HepG2 cells and are used to develop the first dynamic liver central carbon metabolism model. The dynamic model is applied to unravel the internal control hierarchy of the hepatoma central metabolism. The different objectives are accounted for by self-contained chapters that portray the development and the application of the experimental and modeling methods as well as the interpretation of the obtained results.

The second chapter deals with the development of an experimental setup for observing metabolite and ^{13}C-labeling data in mammalian cells under isotopic non-stationary conditions. To enable the experimental observation of steady state intermediate levels and ^{13}C-labeling dynamics in hepatic cells grown adherently in six-well microtiter plates, adequate means are provided for the quenching of metabolism and the extraction of intracellular metabolites. A transient tracer experiment is carried out with HepG2 cells using ^{13}C-labeled glucose as substrate. Stationary intracellular intermediate concentrations and time-dependent mass isotopomer dynamics are quantified. Macroscopic rates are determined from extracellular metabolite measurements.

Chapter 3 addresses the first model-based identification of metabolic fluxes in mammalian cells from non-stationary ^{13}C labeling experiments. A computational framework is implemented to allow for an automated set-up of isotopomer models and the estimation of metabolic fluxes from stationary and non-stationary ^{13}C-labeling data. The framework draws on previous work by Jochen Schaub (Schaub 2007). A large-scale stoichiometric network model of the hepatic fed-state is reconstructed and used for estimating effluxes into the biomass. An isotopomer model is used to determine the metabolic fluxes in glycolysis, the pentose-phosphate pathway, and the tricarboxylic acid cycle in HepG2 cells.

The central focus of the fourth chapter is the quantification of cholesterol synthesis rates and the central metabolism fluxes in primary rat hepatocytes using non-stationary ^{13}C-flux analysis. A chemical labeling experiment is carried out using ^{13}C-labeled glutamine. The effects of a therapeutic concentration of the hypolipidemic agent atorvastatin on the cholesterol and central carbon fluxes are assessed. In order to estimate the intracellular flux distributions, an isotopomer model is build based on positional isotopomer and mass isotopomer balance equations. Moreover, systems-level effects of the administered drug are deduced from the analysis of metabolic control of the targeted 3-hydroxy-3-methylglutaryl-coenzyme A reductase enzyme.

The major aim of the fifth chapter is to provide systems-oriented investigations of the dynamics and control of the central carbon metabolism in hepatoma cells. Dynamic extra- and intracellular metabolite time-series data are collected from HepG2 cells in a stimulus response experiment. The

experimental data are applied to parameterize the first dynamic liver central carbon metabolism model. To quantitatively break down the internal control structure of the central carbon metabolism, concentration and flux control coefficients, partial flux control coefficients, and internal response coefficients are deduced.

The thesis concludes with an evaluative summary and an outlook on possible applications of the presented results and future research directions.

2

Experimental Set-up for Non-Stationary ^{13}C-Labeling Experiments in Mammalian Cells

Chapter Outline

2.1 Introduction 10
2.2 Materials and Methods 12
2.2.1 Cell Culture 12
2.2.2 Transient ^{13}C-Labeling Experiment 12
2.2.3 Sampling and Extraction of Intracellular Metabolites 13
2.2.4 Extracellular Metabolite Data Analysis 13
2.3 Results and Discussion 13
2.3.1 Sampling and Extraction of Metabolites 13
2.3.2 Extracellular Metabolite Concentrations 14
2.3.3 Intracellular Metabolite Concentrations 16
2.3.4 Transient Mass Isotopomer Data 17
2.4 Conclusions 19

Parts of this chapter are published as
Hofmann U, **Maier K**, Niebel A, Vacun G, Reuss M, Mauch K. 2008. Identification of Metabolic Fluxes in Hepatic Cells from Transient ^{13}C-Labeling Experiments: Part I. Experimental observations. Biotechnol Bioeng. 100(2): 344-54.

Abstract

An experimental set-up for acquiring metabolite and transient ^{13}C-labeling data in mammalian cells is presented. An efficient sampling procedure was established for hepatic cells cultured in 6-well plates as a monolayer attached to collagen, which allowed simultaneous quenching of metabolism and extraction of the intracellular intermediates of interest. Extracellular concentrations of glucose, amino acids, lactate, pyruvate, and urea were determined by GC-MS procedures and were used for estimation of metabolic uptake and excretion rates. Sensitive LC-MS and GC-MS methods were used to quantify the intracellular intermediates of tricarboxylic acid cycle, glycolysis, and pentose phosphate pathway and for the determination of isotopomer fractions of the respective metabolites. Mass isotopomer fractions were determined in a transient ^{13}C-labeling experiment using ^{13}C-labeled glucose as substrate. The absolute amounts of intracellular metabolites were obtained from a non-labeled experiment carried out in exactly the same way as the ^{13}C-labeling experiment, except that the media contained naturally labeled glucose only. Estimation of intracellular metabolic fluxes from the presented data is addressed in section 3 of this thesis. The implementation and validation of the GC-MS and LC-MS-MS methods used for quantification of metabolite levels and mass isotopomers was coordinated by Ute Hofmann. The HPLC-based determination of intracellular nucleotide levels was performed by Anja Niebel.

2.1 Introduction

Metabolic flux estimates provide a convenient basis for quantifying cell physiology in terms of involvement of metabolic pathways in overall cellular processes. Up to now, flux analysis has been routinely applied in metabolic engineering and applied systems biology for identifying potential targets for improving yields and productivities. Furthermore, flux identification is applicable to (i) the study of metabolic abnormalities in human diseases (Yarmush and Banta 2003), (ii) monitoring of *in vivo* function, (iii) adjustment of *in vitro* culture conditions in tissue engineering (Lee et al. 1999), (iv) functional analysis of genetic modifications (Hua et al. 2003), (v) rational medium formulation (Goel et al. 1993; Xie and Wang 1994), and (vi) screening (Fischer et al. 2004).

Currently, the most efficient approach for determining intracellular flux maps is based on isotopic tracer experiments, as the labeling information enables the identification of metabolic fluxes in reaction cycles and parallel routes. Whereas the kinetic isotope effect of ^{13}C labeled compounds in comparison to ^{12}C compounds is small and usually neglected, ^{13}C-flux estimation does not rely on assumptions for cofactor balances and energy yields (Schmidt et al. 1998; Wiechert 2001).

In the most commonly used method of tracer-based flux identification, the cells are grown until isotopic steady state in proteinogenic amino acids is reached (Sauer 2006). Subsequently, metabolic fluxes are estimated from labeling patterns in protein hydrolyzates. However, as metabolic steady state is a prerequisite for flux analysis, the applicability of this approach is restricted to continuous culture conditions, such as chemostat cultures or perfusion techniques. To circumvent this shortcoming, flux estimation from the isotopic transient in intracellular metabolite pools has been proposed (Wiechert and Nöh 2005). Flux identification from non-stationary labeling experiments, however, requires both exact quantification of intracellular metabolite concentrations and determination of relative isotopomer fractions of the respective intermediates. Additionally, extracellular metabolite concentrations can be used for the estimation of metabolite uptake and excretion rates. Thus, a broad spectrum of metabolites from different chemical classes of compounds such as amino acids, carboxylic acids, nucleotides as well as phosphorylated substances like sugar phosphates and phosphorylated carboxylic acids with varying physicochemical properties has to be determined.

Several experimental prerequisites have to be fulfilled to ensure reliable results. In this regard, appropriate procedures for sample preparation must be established, including (i) inactivation of metabolism, (ii) separation of extracellular metabolites, and (iii) efficient extraction of the required metabolites. Furthermore, analytical methods for quantification of these metabolites and determination of the isotopic distributions must also be established.

A large number of procedures have been described for the quenching of metabolism and the extraction of intracellular metabolites. These procedures, though, were mainly applied to microbial cells or plant tissue (for a review see (Villas-Boas et al. 2005)). Several aspects have to be taken into

account before these methods can reasonably be transferred to mammalian cell systems. First of all, hepatic cells are usually cultured as a monolayer attached to collagen in 6-well microtiter plates. Thus, sampling devices used for experiments in bioreactors are not applicable. Furthermore, since the methods used for stopping enzymatic reactions lead to partial disruption of the cell membrane, separation between extra- and intracellular metabolites requires removal of the cell culture medium prior to quenching and simultaneous extraction. Besides, due to limited sample sizes, a principal objective was to establish a single extraction method for all intermediates of interest. Moreover, in addition to the specific sampling needs of adherent mammalian cell cultures, it has been shown that the extraction method influences the metabolite profile (Maharjan and Ferenci 2003). Simultaneous extraction of virtually all intermediates from glycolysis, pentose phosphate pathway (PPP) and tricarboxylic acid cycle (TCA) in *Escherichia coli* using boiling water has been previously demonstrated (Bhattacharya et al. 1995).

For the determination of extracellular metabolites, quenching is not needed. As the cells grow adherently, it is sufficient to collect media samples. Extracellular metabolites such as glucose, amino acids, lactate, urea, and ketone bodies are routinely used as diagnostic parameters in clinical studies on metabolism. Several GC-MS methods exist for quantification of these metabolites after appropriate derivatization. Of course, these methods have to be adapted for the analysis of cell culture medium samples.

Quantification of metabolite concentrations in cell extracts can be performed with various analytical assays including enzymatic or chromatographic methods. The determination of isotopomer distributions, however, necessitates mass spectrometric methods. A combination of chromatographic and mass spectrometric methods is usually employed to achieve higher specificity, which is particularly advantageous for the analysis of isomers such as glucose-6-phosphate (G6P) and fructose-6-phosphate (F6P) that cannot be distinguished by mass spectrometry alone. Several LC-MS-MS methods for the determination of highly polar glycolytic intermediates are described in the literature (Buchholz et al. 2001; van Dam et al. 2002). These methods have also been applied to the determination of mass isotopomers (Nöh et al. 2007; van Winden et al. 2005). Mass isotopomer distributions of TCA intermediates have been determined in rat liver using GC-MS (Des Rosiers et al. 1995; Previs et al. 1996) and only recently a LC-MS-MS method for quantification of multiple intracellular metabolites including TCA intermediates in *Escherichia coli* has been described (Luo et al. 2007). So far, only a minority of the methods described refer to the analysis of hepatic cells. However, as analytical performance of the assays – especially in LC-MS – is strongly influenced by the sample matrix, the methods have to be adapted to ensure reliable and reproducible quantification.

This section describes the implementation and validation of the experimental set-up for flux identification in mammalian cell cultures from transient isotopomer data. The study addresses the quan-

tification of extracellular and intracellular metabolite concentrations as well as the determination of mass isotopomer fractions. Furthermore, estimates for extracellular rates are derived from measurements of extracellular metabolite levels. Implementation, validation, and evaluation of the analytical methods for quantifying metabolite levels and mass isotopomers are described in (Hofmann et al. 2008).

2.2 Materials and Methods

2.2.1 Cell Culture

HepG2 cells (ATCC® Number HB-8065™) were seeded at a density of 10^6 cells per well in standard six-well tissue culture plates and incubated at 37 °C in 5 % CO_2 atmosphere. The cells were cultured in William's medium E without glutamine (PAN Biotech GmbH, Aidenbach, Germany) supplemented with penicillin (100 U/ml), streptomycin (100 µg/ml), and Gibco™ Insulin-Transferrin-Selenium (100X) Supplement (Invitrogen, Karlsruhe, Germany). No fetal calf serum (FCS) was added to the medium. Oxygen supply and prevention of concentration gradients were ensured by continuous shaking at 20 rpm (Shaker DRS-12, ELMI, Riga, Latvia). Viability of the cells was investigated before starting the experiment by visual inspection.

2.2.2 Transient ^{13}C-Labeling Experiment

Initially, the overnight medium was replaced by 1 ml of fresh (unlabeled) culture medium. After two hours of equilibration, 1.5 ml of ^{13}C-labeled medium were added with the same molar composition as the normal culture medium, except that glucose was replaced by a mixture of U-^{13}C-labeled glucose and 1-^{13}C-labeled glucose (Campro Scientific, Veenendaal, Netherlands) at a molar ratio of 2:1. This resulted in a final mixture of 40 % naturally labeled glucose, 40 % U-^{13}C-labeled glucose and 20 % 1-^{13}C-labeled glucose. Samples for determination of mass isotopomers of intracellular metabolites were collected in triplicate after 2, 5, 10, 30, 60, 120, and 180 minutes. The corresponding experimental workflow is depicted in Figure 1.

Extracellular and intracellular intermediate levels were determined in parallel cultures that were treated identically, except that the medium added after two hours contained naturally labeled glucose only. Extracellular samples were taken after 0, 60, 120, and 180 minutes. 50 µl of the cell culture medium were diluted with 450 µl of water and frozen at -80 °C until further use. After 180 minutes the cells were worked up for determination of intracellular metabolite concentrations.

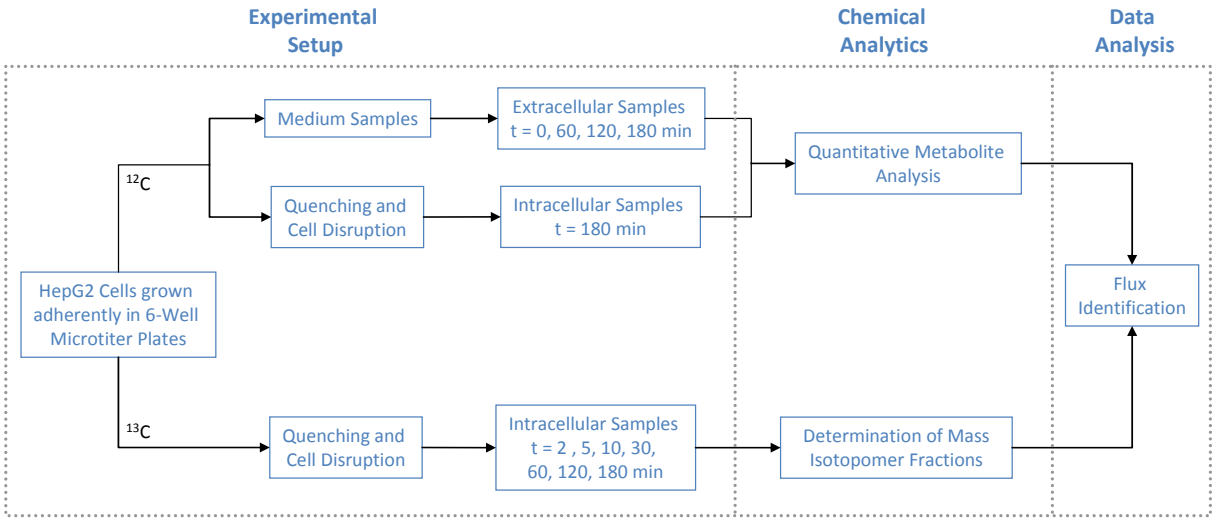

Figure 1. Experimental set-up for quantification of extra- and intracellular metabolite levels as well as determination of mass isotopomers.

2.2.3 Sampling and Extraction of Intracellular Metabolites

After removal of cell culture medium by suction within 5 s, simultaneous quenching and extraction of metabolites was performed by hot air (150 °C for 5 s) followed by the addition of 1.5 ml of boiling water. The entire contents of the well were transferred to a sample tube using a scraper and then homogenized by repeated pipetting. After centrifugation at 10,000 *g* for 10 min at 4 °C, the supernatant was frozen immediately at -80 °C until further use. The procedures for quantification of metabolite levels and mass isotopomers are elaborated on in (Hofmann et al. 2008).

2.2.4 Extracellular Metabolite Data Analysis

The software Table Curve 2D (Systat Software Inc.; Richmond, CA, USA) was used for fitting the extracellular time courses to a variety of differentiable functions by linear regression. Subsequently, the derivative with respect to time at t = 1.5 h was calculated for the estimation of extracellular rates.

2.3 Results and Discussion

2.3.1 Sampling and Extraction of Metabolites

Intracellular sampling was developed taking into account the constraints arising from the culture conditions, in which the HepG2 cells were cultured in 6-well microtiter plates as a monolayer attached to a collagen matrix. Furthermore, separation between extra- and intracellular metabolites necessitated the removal of cell culture medium prior to quenching of the metabolism and extraction of the cells. To minimize the sampling time, major focus was put on methods that can be used for simultaneous quenching and extraction of the cells.

In preliminary experiments different methods for extraction of intracellular metabolites were compared by applying GC-MS analysis for quantification of TCA intermediates and LC-MS-MS analysis for the quantification of sugar phosphates in the cell extracts. We found that perchloric acid extraction with subsequent neutralization of extracts was not compatible with the LC-MS-MS method employed, as it led to strong peak shifts and impaired peak shape. Furthermore, some metabolites like the ketone bodies are unstable under acidic conditions. Recovery of TCA intermediates showed high and reproducible yields when boiling polar solvents (water or ethanol) were used for extraction (data not shown). However, extraction of the polar sugar phosphates could only be achieved with boiling water. Virtually no extraction could be achieved with boiling ethanol although this procedure had been described for the extraction of G6P and F6P from yeast (Gonzalez et al. 1997).

The use of hot air (150 °C for 5 s) prior to treatment with boiling water resulted in improved quenching and increased reproducibility of the extraction procedure. In this regard, the effectiveness of quenching was assessed by determining the adenylate energy charge (EC), which is calculated by

$$EC = \frac{c_{ATP} + 1/2\, c_{ADP}}{c_{ATP} + c_{ADP} + c_{AMP}}. \quad (1)$$

The nucleotide levels determined by HPLC are shown in Table 1. The energy charge was determined at EC=0.88, which is in accordance with literature data for HepG2 cells (Hermes et al. 2005; Yang et al. 2004a). On the other hand, cell disruption by adding boiling water alone resulted in a temperature of about 60 °C and a corresponding EC of only 0.28 (data not shown), i.e. hot air treatment is necessary for effective quenching.

Table 1. Intracellular nucleotide concentrations in HepG2 cells (mean ± SD, n = 6).

Nucleotide	Concentration (nmol/10^6 cells)
ATP	21.08 ± 1.38
ADP	3.02 ± 0.43
AMP	1.62 ± 1.00
GTP	3.46 ± 0.78
GDP	0.41 ± 0.04

2.3.2 Extracellular Metabolite Concentrations

Examples of time courses of selected metabolites in cell culture medium from HepG2 cells are shown in Figure 2. Large quantities of lactate were released during the labeling experiment, which resulted in a high estimate of 31.6 nmol/(10^6cells·min) for the corresponding efflux. Similarly, overflow metabolism has been reported before for hybridoma cells (Doverskog et al. 1997). Lactate efflux and other extracellular rates that were deduced from the time courses of extracellular metabolite concentrations are summarized in Table 2. The glucose uptake rate was estimated at 16.3

nmol/(10^6cells·min), i.e. almost all glucose that was converted into pyruvate via glycolysis and the pentose-phosphate shunt was released as lactate. Alanine was taken up by the cells at a rate of 3.23 nmol/(10^6cells·min). Since alanine is easily converted into pyruvate by alanine transaminase (EC 2.6.1.2), alanine uptake also contributed to the lactate efflux. Glutamate was released with 0.53 nmol/(10^6cells·min) while glutamine uptake was negligible (0.01 nmol/(10^6cells·min)). In summary, the most relevant sources of carbon uptake were extracellular glucose and, to a lesser extent, alanine. Furthermore, significant amounts of the consumed carbon were released as lactate.

Table 2. Metabolite uptake and secretion rates in nmol/(10^6cells·min). Negative values indicate net uptake.

Metabolite	Uptake Rate
Glycolysis and Lactate Metabolism	
LAC	31.6 ± 1.9
GLC	-16.3 ± 0.004
Amino Acid and Urea Metabolism	
GLY	-0.21 ± 0.07
ALA	-3.23 ± 0.06
VAL	-0.16 ± 0.05
LEU	-0.32 ± 0.04
ILE	-0.19 ± 0.05
PHE	-0.10 ± 0.02
TYR	-0.06 ± 0.14
TRY	-0.04 ± 0.05
GLU	0.53 ± 0.06
ASP	-0.09 ± 0.12
PRO	0.07 ± 0.002
SER	0.08 ± 0.08
MET	-0.06 ± 0.05
GLN	-0.01 ± 0.001
HIS	-0.04 ± 0.004
ASN	-0.09 ± 0.05
LYS	-0.35 ± 0.11
ARG	-0.16 ± 0.14
THR	-0.11 ± 0.04
CYS	-0.05 ± 0.05
UREA	0.04 ± 0.03

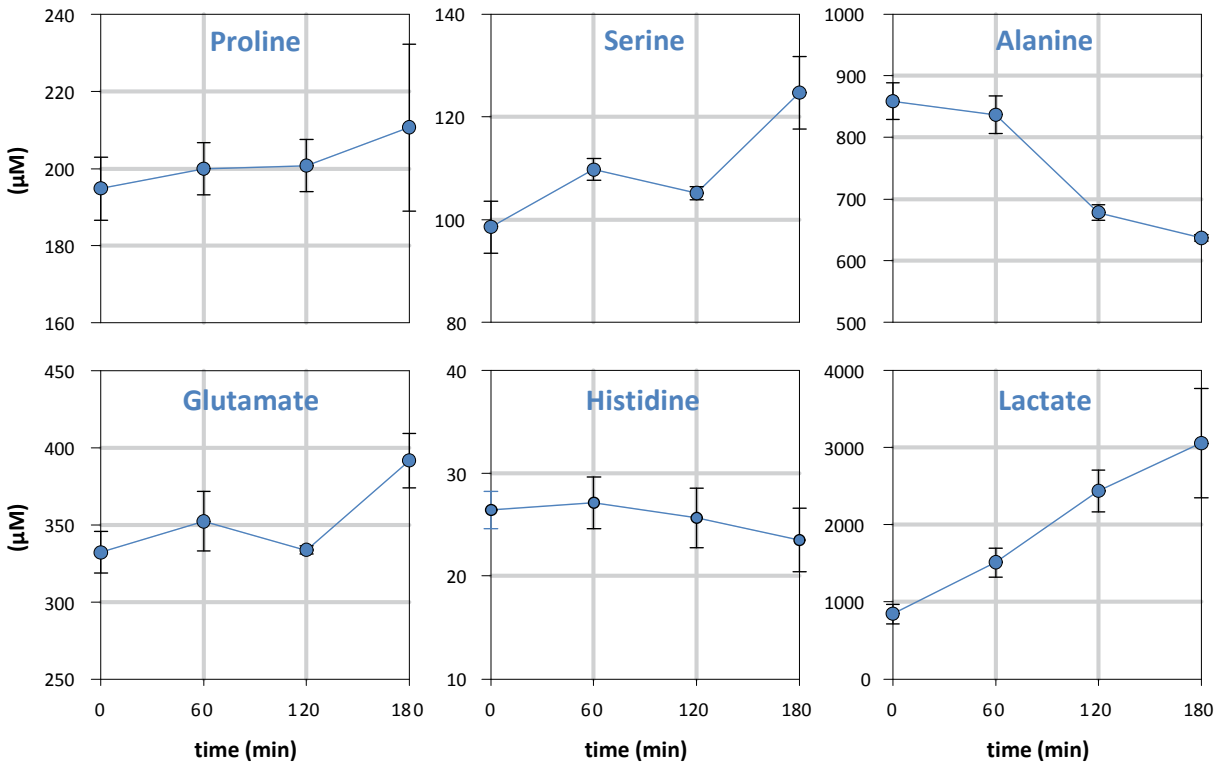

Figure 2. Time courses of extracellular metabolite concentrations.

2.3.3 Intracellular Metabolite Concentrations

Determination of the mass isotopomers and quantification of intracellular metabolite levels were performed in two independent experiments (for workflow see Figure 1). The absolute amounts of intracellular metabolites were obtained by applying the same experimental set-up as for the experiment with labeling, except that the medium contained naturally labeled glucose only. The advantage of this approach is that it is possible to use stable-isotope labeled analogues of the substances as internal standards for quantification, which leads to higher accuracy and improved reproducibility.

The analytical methods were successfully applied to the determination of absolute intracellular metabolite concentrations in HepG2 cells. The data are shown in Table 3, mean values, and RSD were calculated from three different wells worked-up separately prior to metabolite analysis. For the first time, it was possible to obtain quantitative data of the relevant intermediates of glycolysis, pentose phosphate pathway and TCA from HepG2 cells in a single experiment.

Table 3. Intracellular metabolite concentrations in HepG2 cells.

Metabolite	Concentration (pmol/10^6 cells)	RSD (%)
G6P	965	16
F6P	1070	14.4
G1P	115	19.4
3PG	738	5.3
PEP	333	4
PYR	17800	20
6PG	1050	3.5
RIBO5P	647	14.9
RIBU5P	314	25.5
MAL	1110	8.3
FUM	495	6.9
SUC	326	5.4
AKG	2020	9.6
CIT	2280	11.2
Acetoacetate	27	34.5
3-Hydroxybutyrate	28	30.4

2.3.4 Transient Mass Isotopomer Data

It was possible to reliably determine mass isotopomer fractions using GC-MS. Mass isotopomer fractions of intracellular metabolites in HepG2 cells obtained during the transient labeling experiment are summarized in Table 4. Mean values and standard deviations were calculated from measurements of three different wells. Reproducibility of the three wells was rather good demonstrating the suitability of the whole sampling procedure including cell extraction and subsequent analysis. Furthermore, the chosen time frame was appropriate for monitoring the labeling dynamics in glycolysis, PPP, and TCA in HepG2 cells. Thus, the transient isotopomer data is well suited for flux identification in this cell line. Replacement of the unlabeled intermediates by the ^{13}C-labeled analogues can be observed for all metabolites during the time course of the experiment.

As expected, the labeling dynamics were significantly faster in glycolysis and the PPP compared to the reactions in the TCA. While in glycolysis and pentose-phosphate shunt isotopic steady state was reached after roughly 30 minutes, the TCA intermediates showed differing labeling distributions even between 120 and 180 minutes.

Table 4. Mass isotopomer fractions (mean ± SD, n=3) in intracellular metabolites. HepG2 cells were incubated in a mixture of 40 % naturally labeled, 40 % U-^{13}C-labeled and 20 % 1-^{13}C-labeled glucose.

Time (min)	2	5	10	30	60	120	180
G6P							
M0	0.754 ± 0.033	0.664 ± 0.032	0.511 ± 0.07	0.402 ± 0.017	0.394 ± 0.008	0.4 ± 0.011	0.381 ± 0.022
m1	0.072 ± 0.022	0.095 ± 0.019	0.135 ± 0.021	0.14 ± 0.028	0.139 ± 0.006	0.172 ± 0.032	0.161 ± 0.017
m2	0.042 ± 0.022	0.049 ± 0.016	0.064 ± 0.012	0.037 ± 0.018	0.028 ± 0.016	0.019 ± 0.01	0.022 ± 0.021
m3	0.076 ± 0.01	0.089 ± 0.009	0.12 ± 0.013	0.064 ± 0.023	0.058 ± 0.011	0.065 ± 0.008	0.061 ± 0.026
m4	0.028 ± 0.014	0.021 ± 0.01	0.051 ± 0.024	0.038 ± 0.008	0.036 ± 0.012	0.029 ± 0.008	0.033 ± 0.009
m5	0.009 ± 0.01	0.021 ± 0.005	0.024 ± 0.018	0.077 ± 0.008	0.074 ± 0.016	0.071 ± 0.021	0.071 ± 0.008
m6	0.02 ± 0.026	0.062 ± 0.012	0.096 ± 0.032	0.242 ± 0.009	0.273 ± 0.03	0.244 ± 0.007	0.271 ± 0.019
F6P							
m0	0.796 ± 0.046	0.73 ± 0.017	0.611 ± 0.034	0.456 ± 0.014	0.427 ± 0.023	0.471 ± 0.148	0.34 ± 0.026
m1	0.087 ± 0.031	0.064 ± 0.02	0.097 ± 0.024	0.138 ± 0.02	0.131 ± 0.035	0.071 ± 0.045	0.117 ± 0.014
m2	0.012 ± 0.012	0.041 ± 0.021	0.061 ± 0.019	0.05 ± 0.01	0.033 ± 0.028	0.073 ± 0.014	0.053 ± 0.03
m3	0.039 ± 0.024	0.06 ± 0.009	0.104 ± 0.017	0.092 ± 0.024	0.171 ± 0.036	0.126 ± 0.031	0.14 ± 0.019
m4	0.027 ± 0.023	0.039 ± 0.012	0.038 ± 0.01	0.042 ± 0.023	0.055 ± 0.005	0.087 ± 0.051	0.086 ± 0.029
m5	0.011 ± 0.013	0.024 ± 0.008	0.036 ± 0.013	0.057 ± 0.012	0.046 ± 0.012	0.048 ± 0.03	0.052 ± 0.037
m6	0.028 ± 0.028	0.043 ± 0.011	0.053 ± 0.038	0.165 ± 0.011	0.137 ± 0.03	0.125 ± 0.074	0.212 ± 0.069
PG6							
m0	0.575 ± 0.052	0.471 ± 0.08	0.431 ± 0.106	0.339 ± 0.059	0.371 ± 0.02	0.383 ± 0.001	0.387 ± 0.004
m1	0.099 ± 0.006	0.127 ± 0.025	0.161 ± 0.082	0.165 ± 0.003	0.142 ± 0.018	0.15 ± 0.006	0.153 ± 0.01
m2	0.018 ± 0.014	0.014 ± 0.007	0.019 ± 0.015	0.019 ± 0.014	0.048 ± 0.015	0.022 ± 0.008	0.029 ± 0.013
m3	0.092 ± 0.032	0.084 ± 0.016	0.079 ± 0.039	0.066 ± 0.02	0.045 ± 0.021	0.064 ± 0.003	0.066 ± 0.009
m4	0.015 ± 0.009	0.032 ± 0.007	0.024 ± 0.015	0.027 ± 0.016	0.031 ± 0.012	0.041 ± 0.01	0.03 ± 0.008
m5	0.047 ± 0.01	0.055 ± 0.016	0.076 ± 0.054	0.093 ± 0.002	0.098 ± 0.01	0.101 ± 0.006	0.105 ± 0.005
m6	0.154 ± 0.039	0.218 ± 0.06	0.21 ± 0.149	0.291 ± 0.071	0.263 ± 0.045	0.239 ± 0.006	0.231 ± 0.002
3PG							
m0	0.839 ± 0.017	0.813 ± 0.026	0.688 ± 0.069	0.512 ± 0.008	0.507 ± 0.009	0.511 ± 0.007	0.509 ± 0.007
m1	0.027 ± 0.007	0.034 ± 0.01	0.055 ± 0.017	0.099 ± 0.01	0.101 ± 0.011	0.098 ± 0.002	0.097 ± 0.004
m2	0.015 ± 0.005	0.017 ± 0.005	0.031 ± 0.009	0.047 ± 0.008	0.05 ± 0.003	0.048 ± 0.006	0.051 ± 0.007
m3	0.119 ± 0.007	0.135 ± 0.012	0.226 ± 0.046	0.341 ± 0.005	0.342 ± 0.006	0.344 ± 0.003	0.343 ± 0.003
PEP							
m0	0.813 ± 0.009	0.781 ± 0.008	0.633 ± 0.079	0.494 ± 0.028	0.476 ± 0.021	0.518 ± 0.019	0.519 ± 0.023
m1	0.028 ± 0.006	0.045 ± 0.007	0.069 ± 0.015	0.106 ± 0.03	0.11 ± 0.024	0.095 ± 0.015	0.099 ± 0.013
m2	0.018 ± 0.003	0.017 ± 0.004	0.028 ± 0.014	0.042 ± 0.025	0.047 ± 0.02	0.051 ± 0.021	0.037 ± 0.007
m3	0.141 ± 0.009	0.157 ± 0.01	0.269 ± 0.056	0.358 ± 0.027	0.368 ± 0.026	0.336 ± 0.02	0.345 ± 0.006
CIT							
m0	0.943 ± 0.007	0.901 ± 0.004	0.867 ± 0.004	0.803 ± 0.011	0.726 ± 0.005	0.62 ± 0.027	0.554 ± 0.004
m1	0.012 ± 0.010	0.014 ± 0.005	0.019 ± 0.01	0.032 ± 0.009	0.059 ± 0.01	0.082 ± 0.011	0.099 ± 0.003
m2	0.032 ± 0.009	0.051 ± 0.006	0.069 ± 0.008	0.1 ± 0.005	0.144 ± 0.005	0.182 ± 0.017	0.208 ± 0.006
m3	0.011 ± 0.007	0.029 ± 0.004	0.039 ± 0.005	0.051 ± 0.003	0.051 ± 0.003	0.079 ± 0.009	0.091 ± 0.002
m4	0.002 ± 0.001	0.001 ± 0.002	0.001 ± 0.001	0.006 ± 0.002	0.012 ± 0.003	0.022 ± 0.003	0.028 ± 0.001
m5	0.001 ± 0.001	0.003 ± 0.001	0.005 ± 0.002	0.008 ± 0.002	0.009 ± 0.001	0.015 ± 0.001	0.02 ± 0.002
m6	n.d.	n.d.	n.d.	n.d.	n.d.	n.d.	n.d.
AKG							
m0	0.988 ± 0.007	0.986 ± 0.005	0.981 ± 0.008	0.922 ± 0.005	0.837 ± 0.012	0.736 ± 0.016	0.687 ± 0.022
m1	0.003 ± 0.005	0.004 ± 0.005	0.002 ± 0.003	0.015 ± 0.004	0.037 ± 0.003	0.073 ± 0.01	0.084 ± 0.007
m2	0.008 ± 0.005	0.008 ± 0.005	0.014 ± 0.005	0.052 ± 0.006	0.101 ± 0.007	0.144 ± 0.006	0.164 ± 0.013
m3	0.002 ± 0.001	0.002 ± 0.001	0.002 ± 0.001	0.009 ± 0.001	0.018 ± 0.001	0.03 ± 0.002	0.04 ± 0.003
m4	n.d.	n.d.	0 ± 0.001	n.d.	0.005 ± 0.003	0.013 ± 0.003	0.019 ± 0.001
m5	n.d.	n.d.	n.d.	0.002 ± 0	0.002 ± 0.001	0.004 ± 0.001	0.006 ± 0
FUM							
m0	0.976 ± 0.008	0.952 ± 0.011	0.932 ± 0.007	0.89 ± 0.006	0.861 ± 0.014	0.804 ± 0.015	0.767 ± 0.029
m1	0.001 ± 0.003	0.005 ± 0.004	0.005 ± 0.005	0.015 ± 0.005	0.024 ± 0.006	0.051 ± 0.006	0.056 ± 0.014
m2	0.011 ± 0.016	0.011 ± 0.01	0.012 ± 0.01	0.025 ± 0.006	0.06 ± 0.004	0.083 ± 0.005	0.100 ± 0.021
m3	0.011 ± 0.008	0.032 ± 0.004	0.051 ± 0.006	0.07 ± 0.004	0.055 ± 0.008	0.061 ± 0.013	0.075 ± 0.006
m4	n.d.	n.d.	n.d.	n.d.	0.000 ± 0.001	0.001 ± 0.001	0.002 ± 0.002
MAL							
m0	0.983 ± 0.003	0.966 ± 0.003	0.927 ± 0.007	0.864 ± 0.007	0.818 ± 0.004	0.743 ± 0.021	0.7 ± 0.008
m1	0.004 ± 0.002	0.008 ± 0.002	0.017 ± 0.003	0.032 ± 0.003	0.051 ± 0.001	0.079 ± 0.007	0.091 ± 0.004
m2	0.002 ± 0.001	0.002 ± 0.001	0.006 ± 0	0.03 ± 0.001	0.061 ± 0.001	0.087 ± 0.008	0.107 ± 0.005
m3	0.011 ± 0.001	0.025 ± 0.001	0.05 ± 0.005	0.075 ± 0.005	0.069 ± 0.003	0.087 ± 0.006	0.097 ± 0.002
m4	n.d.	n.d.	n.d.	n.d.	0.001 ± 0.001	0.004 ± 0.001	0.006 ± 0.001

n.d. not detected

2.4 Conclusions

Combined treatment of hot air and boiling water allows for a reliable quenching of metabolism and reproducible extraction of intracellular intermediates of glycolysis, PPP, and TCA (G6P, F6P, G1P, R5P, Ru5P, FBP, PEP, 3PG, 6PG, PYR, SUC, AKG, FUM. MAL, and CIT) in HepG2 cells. The GC-MS and LC-MS methods that were developed for quantification as well as for determination of isotopic distributions showed good accuracy and reproducibility and could be successfully applied for quantification of extracellular and intracellular metabolite concentrations. Metabolite uptake and excretion rates were derived from extracellular metabolite data. Additionally, isotopomer fractions of G6P, F6P, PEP, 3PG, 6PG, AKG, FUM, MAL, and CIT were reliably determined in a transient ^{13}C-labeling experiment using ^{13}C-labeled glucose as a substrate. Replacement of the unlabeled intermediates by the ^{13}C-labeled analogues was observed for all metabolites during the time course of the experiment (180 min). In this regard, the established experimental set-up was appropriate for the generation of transient isotopomer data for estimating intracellular flux distributions along with forward and backward fluxes and intermediate metabolite concentrations, as will be shown in section 3 of this thesis.

3

Identification of Metabolic Fluxes in Hepatic Central Carbon Metabolism from Transient ^{13}C-Labeling Data

Chapter Outline

3.1 Introduction 22
3.2 Material and Methods 24
3.2.1 Extracellular Rates 24
3.3 Modeling 24
3.3.1 Large-Scale Stoichiometric Network Model 25
3.3.1.1 Network Consistency Checking 26
3.3.2 Isotopomer Network Model 27
3.3.2.1 Glycolysis 29
3.3.2.2 Pentose Phosphate Pathway 29
3.3.2.3 Tricarboxylic Acid Cycle 29
3.3.2.4 Anaplerosis 29
3.3.3 Isotopomer Balancing 30
3.3.4 Parameter Identification 31
3.3.5 Parameter Sensitivities 32
3.4 Results and Discussion 33
3.4.1 *In Vivo* and *In Silico* Labeling Dynamics 33
3.4.2 Intracellular Flux Distribution 34
3.4.3 Intracellular Metabolite Concentrations 39
3.5 Conclusions 41

Parts of this chapter are published as
Maier K, Hofmann U, Reuss M, Mauch K. 2008. Identification of Metabolic Fluxes in Hepatic Cells from Transient ^{13}C-Labeling Experiments: Part II. Flux Estimation. Biotechnol Bioeng. 100(2): 355-70

Abstract

This section addresses the identification of metabolic fluxes and metabolite concentrations in mammalian cells from transient ^{13}C-labeling experiments. Whilst section 2 described experimental set-up and acquisition of required metabolite and ^{13}C-labeling data, this section focuses on setting up network models and the estimation of intracellular fluxes. Metabolic fluxes were determined in glycolysis, pentose phosphate pathway (PPP), and citric acid cycle (TCA) in a hepatoma cell line grown in aerobic batch cultures. In glycolytic and PPP metabolite pools isotopic stationarity was observed within 30 minutes, whereas in the TCA cycle the labeling redistribution did not reach isotopic steady state even within 120 minutes. *In silico* labeling dynamics were in accordance with *in vivo* ^{13}C-labeling data. Split ratio between glycolysis and PPP was 57%: 43%; intracellular glucose concentration was estimated at 101.6 nmol per 10^6 cells. In contrast to isotopic stationary ^{13}C-flux analysis, transient ^{13}C-flux analysis can also be applied to industrially relevant mammalian cell fed-batch and batch cultures.

3.1 Introduction

Quantitative determination of metabolic fluxes *in vivo* is a fundamental tool in metabolic engineering and applied systems biology. Information on intracellular flux distributions assists, for example, in identifying genetic targets for improving yields and productivities. In turn, flux analysis can be used in the evaluation of genetic manipulations as it enables a functional analysis of different mutant strains (Hua et al. 2003). Moreover, flux analysis is a basis for determining the level of engagement of several metabolic pathways in overall cellular processes (Stephanopoulos et al. 1998), flux - transcript profiling (Sonderegger et al. 2004), and estimating enzymatic capacities (Chassagnole et al. 2002). Accurate knowledge of intracellular flux distributions facilitates a quantitative description of cellular physiology. This knowledge can be exploited for a rational medium formulation as has been successfully demonstrated for both prokaryotic (Goel et al. 1993) and animal cell systems (Xie and Wang 1994). Since an intracellular flux distribution characterizes phenotypic behavior, it is also well suited for the analysis of metabolic abnormalities in human diseases (Yarmush and Banta 2003; Yarmush and Berthiaume 1997). Lee et al. highlighted the potential of metabolic flux analysis in the field of tissue engineering, where intracellular flux maps can be used for the optimization of *in vivo* function as well as the adjustment of *in vitro* culture conditions (Lee et al. 1999).

Several different mathematical approaches are applicable for the determination of intracellular flux distributions. All approaches for metabolic flux analysis rely on a steady state, i.e. all incoming fluxes into an intracellular metabolite pool equal the fluxes out of the pool. In stoichiometric flux analysis, fluxes are estimated on the basis of metabolite mass balances that are constrained by the reaction network stoichiometry and experimental observations of extracellular rates. If the systems degree of freedom is higher than the number of measured rates, linear programming can be used to obtain a unique solution for the intracellular fluxes subject to the optimization of a metabolic objective (e.g. maximal specific growth rate, etc.). This approach can be used to explore the capabilities and limitations of biochemical systems (Kauffman et al. 2003) given that an appropriate objective can be defined. Furthermore, ^{13}C-labeling data can be used to determine intracellular fluxes. The labeling information can be used for the elucidation of flux ratios in parallel routes and reaction cycles as well as exchange fluxes in reversible reactions. It permits flux estimation that is free from what are usually strong assumptions on cofactor balances and energy yields in stoichiometric flux analysis and linear programming (Schmidt et al. 1998; Wiechert 2001).

Until now, flux analysis has been predominantly applied for studying microbial physiology. However, mainly because of its technical feasibility and the need for a rational process design, flux analysis has also been increasingly applied to animal cells. In the last decade, metabolic flux distributions were identified in mammalian cell lines such as hybridoma (Bonarius et al. 1996; Bonarius et al. 2001; Bonarius et al. 1998; Zupke et al. 1995) and CHO (Altamirano et al. 2001; Nyberg et al. 1999) cells.

Balcarcel and Clark used flux analysis for screening mammalian cell cultures (Balcarcel and Clark 2003). Intracellular fluxes have been determined in heart (Malloy et al. 1988; Malloy et al. 1990), brain (Brand et al. 1992), and liver (Large et al. 1997; Lee et al. 1998; Lee et al. 1995; Yarmush et al. 1999) using ^{13}C-flux analysis. For quantifying metabolic fluxes in perfused livers, Lee et al. (Lee et al. 2000) reconstructed a hepatic network model. This model was subsequently used for quantifying the hepatic response to plasma exposure (Chan et al. 2003a) and for identifying improved culture conditions for sustained liver-specific functions in a bioartificial liver device (Chan et al. 2003b).

Mammalian cells lack a number of pathways that are abundant in microbial cells. Essential amino acids, for instance, have to be added to the medium as animal cells do not possess the necessary metabolic pathways for their synthesis, whereas for the most part microbes can be grown on a single carbon source. In stoichiometric modeling of microbes one can therefore omit many of the principal metabolic routes, such as amino acid degradation (Lee et al. 1999). On the other hand, hepatocytes for example, possess additional pathways (e.g. the urea cycle) that, in turn, are not present in prokaryotes and that augment the number of fluxes which cannot be calculated from uptake and excretion rates (Lee et al. 1999). Therefore, stoichiometric flux analysis alone is most often not suitable for observing metabolic fluxes in mammalian cells. In other words, it is necessary to either accept a narrowed view of metabolism, as only a subset of fluxes can be calculated (Klamt and Schuster 2002; Klamt et al. 2002), or to identify additional constraints that may result from further assumptions (Bonarius et al. 1997) or experimental data, most notably ^{13}C-labeling data (Wiechert 2001).

Traditionally, determinations of intracellular fluxes from ^{13}C-tracer experiments have relied on isotopic steady state, which necessitates continuous culture conditions. Industrially relevant fermentations and cultivations of mammalian cells, though, are rarely continuous, but fed-batch or even batch. Therefore, the conventional approach in ^{13}C-flux analysis, i.e. (i) growth of cells in continuous culture, (ii) waiting for one to four residence times, and (iii) analysis of the label distribution in proteinogenic amino acids that were obtained from protein hydrolyzates (Christensen and Nielsen 1999; Dauner and Sauer 2000), cannot be applied to cultured hepatocytes. To circumvent this limitation, Wiechert and Nöh suggested non-stationary ^{13}C-flux analysis (Wiechert and Nöh 2005), where the isotopic transient is taken into consideration. Since the length of an experiment can be reduced by orders of magnitude, non-stationary ^{13}C-flux analysis is particularly well suited, if not essential, for estimating intracellular flux distributions in systems like, for example, mammalian cell cultures where relatively long observation periods would put a risk to the assumption of a metabolic steady state and/or cellular stability. Moreover, the required amount of labeled and usually costly substrate is significantly lower in case of transient ^{13}C flux analysis compared to stationary tracer experiments. Furthermore, in contrast to stationary labeling experiments, non-stationary labeling experiments also allow for estimation of intracellular metabolite concentrations. Non-stationary ^{13}C flux analysis,

though, is experimentally and computationally more demanding. Recently, Nöh et al. demonstrated the successful implementation of non-stationary ^{13}C-flux analysis for *Escherichia coli* (Nöh et al. 2006a). Fluxes in the tricarboxylic acid cycle have been identified from transient ^{13}C-fractional enrichment data in perfused rat hearts (Chance et al. 1983) and in rat livers infused with alcohol (Jucker et al. 1998).

In order to perform non-stationary labeling experiments, intermediary mass isotopomers have to be quantified. This can be done with GC-MS and LC-MS techniques, as discussed in section 2 of this contribution, see also (Hofmann et al. 2008). Furthermore, the flux estimation process has to be adapted for the evaluation of transient labeling data (Nöh et al. 2006b). In this section the implementation of flux identification from isotopic transient labeling data in mammalian cell cultures is documented. Differences between microbial, lower eukaryotic and animal cells are addressed with emphasis on the time constants of the labeling dynamics. Moreover, the need to consider the isotopic transient for flux identification in mammalian cell cultures is illustrated.

3.2 Material and Methods

3.2.1 Extracellular Rates

For experimental determination of metabolite uptake and excretion rates, extracellular concentrations of all 20 amino acids, glucose, lactate, and urea were quantified as described in section 2. Extracellular rates for pyruvate (93.2 $\text{nmol}\cdot\text{h}^{-1}\cdot(10^6\text{cells})^{-1}$) and the two ketone bodies acetoacetate (2.3 $\text{nmol}\cdot\text{h}^{-1}\cdot(10^6\text{cells})^{-1}$) and 3-hydroxybutyrate (0.8 $\text{nmol}\cdot\text{h}^{-1}\cdot(10^6\text{cells})^{-1}$) were determined in another experiment under the same experimental conditions.

3.3 Modeling

A two-stage approach was applied for the identification of metabolic fluxes from transient labeling data. First, a comprehensive network model of the hepatic metabolism was reconstructed. This model was parameterized by the experimentally observed extracellular rates (Hofmann et al. 2008) in order to estimate the anabolic fluxes into the biomass during the labeling experiment. The latter were assumed to be unidirectional. Second, an isotopomer model was set up for the simulation of intracellular labeling dynamics. Metabolic fluxes, reversibility factors, and non-measured pool concentrations were then estimated by minimizing the deviation between experimental and simulated isotopomer data. Subsequently, the sensitivity of the objective function value with respect to the estimated parameters was analyzed.

3.3.1 Large-Scale Stoichiometric Network Model

A fully compartmentalized model of the human hepatic metabolism has been reconstructed based on the known stoichiometry of the underlying reaction network (Kanehisa and Goto 2000; Schomburg et al. 2002). The model accounts for 415 reactions (including 39 extracellular and 89 intracellular transportation steps) that convert 416 balanced compounds (cf. Figure 3). Its design was based on the description of the hepatic fed state, i.e. where glucose is metabolized. The stoichiometry of the model is provided in Appendix A.

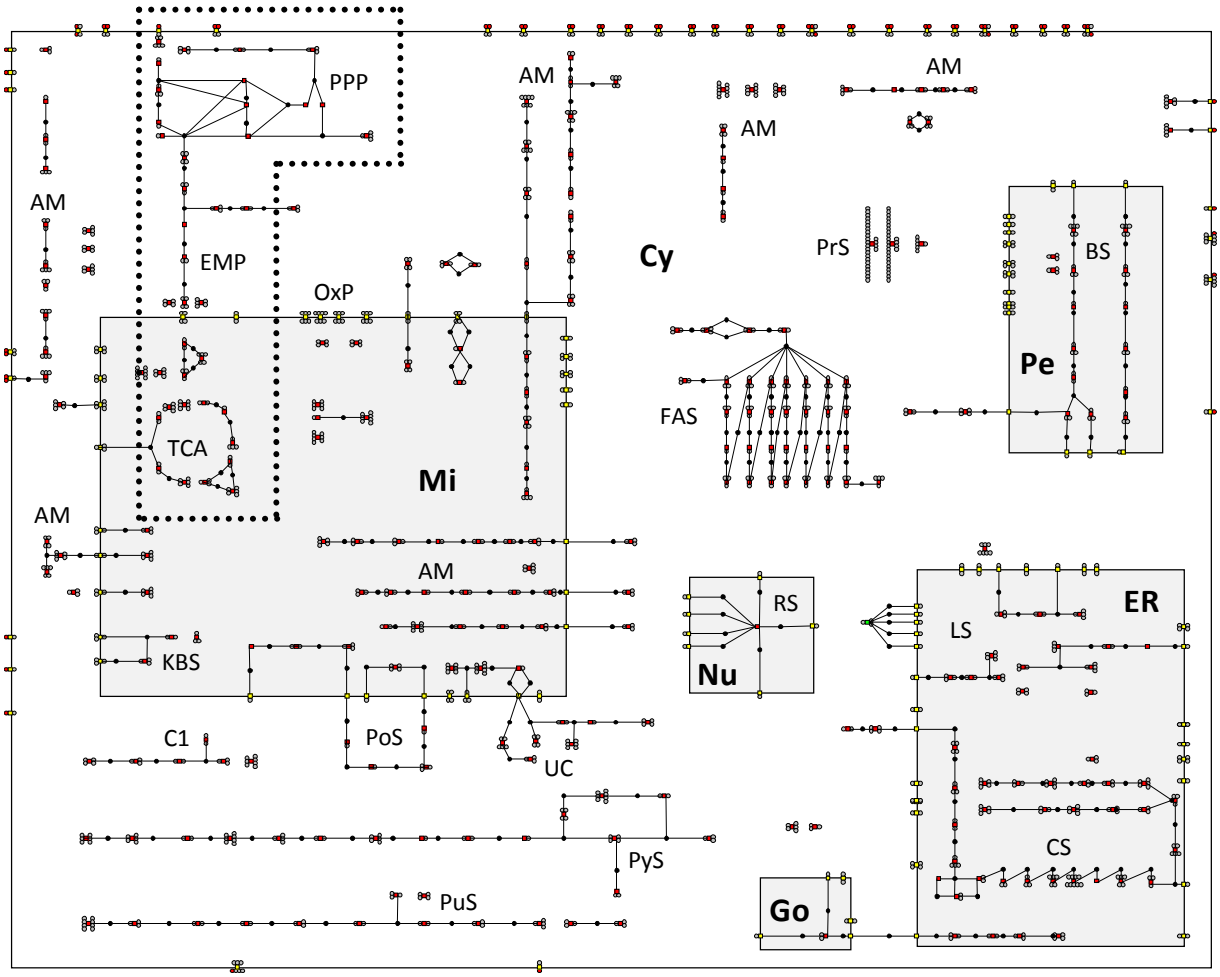

Figure 3. Large-scale network model of the hepatic metabolism. The metabolic subnetwork (EMP, PPP, TCA), which was applied for ^{13}C flux analysis, is highlighted (cf. dotted line). Six reaction compartments are discriminated: cytosol (Cy), mitochondrion (Mi), peroxisome (Pe), nucleus (Nu), golgi apparatus (Go) and endoplasmic reticulum (ER). Abbreviations used for metabolic pathways: amino acid metabolism (AM), pentose phosphate pathway (PPP), Embden-Meyerhof-Parnas (EMP), tricarboxylic acid cycle (TCA), oxidative phosphorylation (OxP), ketone body synthesis (KBS), C_1 pool (C1), porphyrine synthesis (PoS), urea cycle (UC), pyrimidine synthesis (PyS), purine synthesis (PuS), RNA synthesis (RS), lipid synthesis (LS), cholesterol synthesis (CS), bile synthesis (BS), protein synthesis (PrS), fatty acid synthesis (FAS).

The metabolic pathways included in the model are glycolysis, pentose-phosphate-pathway (PPP), tricarboxylic acid (TCA) and urea cycles, oxidative phosphorylation, glycogen storage, phospholipid- and sphingolipid synthesis, purine and pyrimidine pathways, the C_1-pool, haem biosynthesis, as well as amino acid and fatty acid metabolisms. Furthermore, liver-specific pathways, such as the synthesis of ketone bodies, were also implemented as ketogenesis is common in liver cells that oxidize fatty acids and/or unbranched amino acids, i.e. leucine, isoleucine, and valine (Emmison and Agius 1988). As hepatocytes are the major producer of both native cholesterol (85%) and primary bile acids, the corresponding metabolic routes were also integrated. The composition of ductular bile was estimated from literature data (Kuntz and Kuntz 2001).

Albumin is exclusively produced in the liver and constitutes the major plasma protein. It represents the predominant hepatic protein product and hence its secretion is the only protein secretion that was taken into account in the network. However, other liver-specific functions such as phase I and II detoxification of xenobiotics were not taken into consideration as fluxes through these reactions are negligible compared to fluxes in the central carbon metabolism (Chan et al. 2003a). The biomass composition of the liver cell was implemented according to the work of Harrison (Harrison 1953). Average RNA and protein compositions were adopted from the contribution of Echols et al. (Echols et al. 2002).

3.3.1.1 Network Consistency Checking

All reactions in the network model are both charge and elementally balanced, i.e. each reaction is consistent with respect to stoichiometry and redox state.

As the synthesis rate of albumin is frequently used as a criterion for the selection of hepatic cell lines (Knowles et al. 1980; Schippers et al. 1997), linear programming was performed subject to the maximization of the albumin secretion rate. The predicted value of 0.1 $nmol \cdot h^{-1} \cdot (10^6 cells)^{-1}$ was higher than experimentally determined values reported in the literature (Ballet et al. 1984; Chen et al. 2003; Kuntz and Kuntz 2001) which is reasonable as the synthesis of albumin is not the only metabolic objective of hepatic cells.

Network set-up, consistency proofs, statistical analysis, linear programming, and stoichiometric flux analysis, as well as SBML export were performed with the software Insilico Discovery (Insilico Biotechnology AG, Stuttgart, Germany). Due to both, the size of the network and the large condition number of the stoichiometric matrix, precise fractional arithmetic was applied in order to prevent numerical inaccuracies. Stoichiometric flux analysis was performed subject to data reconciliation by applying the method of weighted least squares (Wang and Stephanopoulos 1983). The simplex algorithm was applied for estimation of metabolic fluxes by linear programming (Press et al. 1992).

3.3.2 Isotopomer Network Model

The isotopomer model is a sub-model of the large-scale hepatic network. It comprises glycolysis, PPP, TCA, and two anaplerotic reactions. The model is shown in Figure 4 and the corresponding carbon atom transitions (Stryer 1995) are listed in Table 5. The network contains a total of 40 fluxes, from which 25 are assumed to operate bidirectionally. 15 free fluxes have to be determined in order to parameterize the isotopomer network model. When the isotopomer model was implemented, no intracellular reaction compartments were distinguished since, up to now, experimental quantification of compartmental metabolic concentration differences has not been feasible. Therefore, there is one single pool of intracellular intermediates and thus the estimated rates in the TCA cycle represent average values. However, neglecting the compartmentalization in the analysis of tracer experiments in hepatic cells is justified due to rapid equilibration of intermediates between the cytoplasm and the mitochondrial space via effective shuttle systems (Vogt et al. 1997; Yarmush et al. 1999).

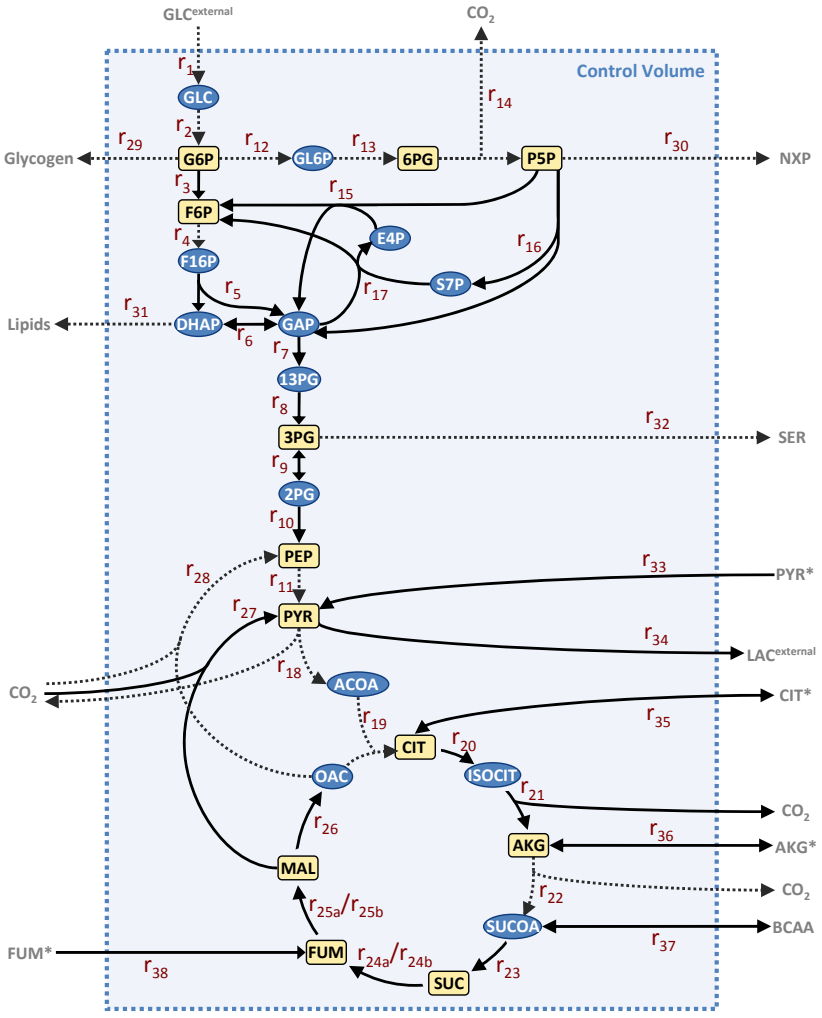

Figure 4. Metabolic subnetwork which was applied for ^{13}C flux analysis. Intermediates for which no measurement data was available, and non-balanced metabolites are shown inside ellipses and dashed boxes, respectively. Experimentally quantified metabolites are indicated in rectangles. Reversible and irreversible reactions are indicated by two-sided black arrows and one-sided dotted grey arrows.

Table 5. Atom mappings corresponding to the isotopomer model shown in Figure 4. Bidireactional reaction steps and irreversible reactions are indicated by "↔" and "→", respectively.

Reaction	Substrates	Reversibility	Products
Glycolysis			
r_1	$GLC^{external}$(1,2,3,4,5,6)	→	GLC(1,2,3,4,5,6)
r_2	GLC(1,2,3,4,5,6)	→	G6P(1,2,3,4,5,6)
r_3	G6P(1,2,3,4,5,6)	↔	F6P(1,2,3,4,5,6)
r_4	F6P(1,2,3,4,5,6)	→	F16P(1,2,3,4,5,6)
r_5	F16P(1,2,3,4,5,6)	↔	GAP(4,5,6) + DHAP(1,2,3)
r_6	DHAP(1,2,3)	↔	GAP(1,2,3)
r_7	GAP(1,2,3)	↔	13PG(1,2,3)
r_8	13PG(1,2,3)	↔	3PG(1,2,3)
r_9	3PG(1,2,3)	↔	2PG(1,2,3)
r_{10}	2PG(1,2,3)	↔	PEP(1,2,3)
r_{11}	PEP(1,2,3)	→	PYR(1,2,3)
PPP			
r_{12}	G6P(1,2,3,4,5,6)	→	GL6P(1,2,3,4,5,6)
r_{13}	GL6P(1,2,3,4,5,6)	→	6PG(1,2,3,4,5,6)
r_{14}	6PG(1,2,3,4,5,6)	→	P5P(2,3,4,5,6) + CO_2(1)
r_{15}	P5P(1,2,3,4,5) + E4P(6,7,8,9)	↔	GAP(3,4,5) + F6P(1,2,6,7,8,9)
r_{16}	P5P(1,2,3,4,5)(6,7,8,9,10)	↔	GAP(3,4,5) + S7P(1,2,6,7,8,9,10)
r_{17}	S7P(1,2,3,4,5,6,7) + GAP(8,9,10)	↔	E4P(4,5,6,7) + F6P(1,2,3,8,9,10)
TCA			
r_{18}	PYR(1,2,3)	→	CO_2(1) + ACOA(2,3)
r_{19}	ACOA(1,2) + OAC(3,4,5,6)	→	CIT(6,5,4,2,1,3)
r_{20}	CIT(1,2,3,4,5,6)	↔	ISOCIT(1,2,3,4,5,6)
r_{21}	ISOCIT(1,2,3,4,5,6)	↔	AKG(1,2,3,4,5) + CO_2(6)
r_{22}	AKG(1,2,3,4,5)	→	SUCOA(2,3,4,5) + CO_2(1)
r_{23}	SUCOA(1,2,3,4)	↔	SUC(1,2,3,4)
r_{24a}	SUC(1,2,3,4)	↔	FUM(1,2,3,4)
r_{24b}	SUC(1,2,3,4)	↔	FUM(4,3,2,1)
r_{25a}	FUM(1,2,3,4)	↔	MAL(1,2,3,4)
r_{25b}	FUM(1,2,3,4)	↔	MAL(4,3,2,1)
r_{26}	MAL(1,2,3,4)	↔	OAC(1,2,3,4)
Anaplerosis			
r_{27}	PYR(1,2,3) + CO_2(4)	↔	MAL(1,2,3,4)
r_{28}	OAC(1,2,3,4)	→	PEP(1,2,3) + CO_2(4)
Biomass			
r_{29}	G6P(1,2,3,4,5,6)	→	Glycogen(1,2,3,4,5,6)
r_{30}	P5P(1,2,3,4,5)	→	NXP(1,2,3,4,5)
r_{31}	DHAP(1,2,3)	→	Lipids(1,2,3)
r_{32}	3PG(1,2,3)	→	SER(1,2,3)
r_{33}	PYR*(1,2,3)	↔	PYR(1,2,3)
r_{34}	PYR(1,2,3)	↔	$LAC^{external}$(1,2,3)
r_{35}	CIT(1,2,3,4,5,6)	↔	CIT*(1,2,3,4,5,6)
r_{36}	AKG(1,2,3,4,5)	↔	AKG*(1,2,3,4,5)
r_{37}	BCAA(1,2,3,4)	↔	SUCOA(1,2,3,4)
r_{38}	FUM*(1,2,3,4)	↔	FUM(1,2,3,4)

3.3.2.1 Glycolysis

The hepatic glucose transporter (GLUT2) mediates facilitated bidirectional transfer of glucose across the plasma membrane. The ability to transport glucose in both directions, into and out of hepatocytes, is essential for the liver to be able to maintain glucose homeostasis. In consideration of this facilitated transport on the one hand and the high glucose level in the culture medium (2 $g \cdot l^{-1}$) on the other hand, the intracellular glucose pool was included in the model, in contrast to many similar studies using stationary ^{13}C-flux analysis. Furthermore, as the time constants of the labeling dynamics depend on the intracellular intermediate levels, all glycolytic metabolites were treated as separate pools, i.e. no pools were lumped. Consequently, whereas in stationary ^{13}C-flux analysis it is common to lump the triose-phosphates, dihydroxyaceton-phosphate (DHAP), and glyceraldehyd-3-phosphate (GAP) (Christensen et al. 2002; Schmidt et al. 1998; van Winden et al. 2005), DHAP and GAP were balanced individually in this study.

3.3.2.2 Pentose Phosphate Pathway

The pentose-phosphate pools could not be discriminated due to current experimental limitations. Therefore, the respective pools (xylose-5-phosphate, ribose-5-phosphate, and ribulose-5-phosphate) were lumped into the single pool p5p. This is a valid procedure as the pentose phosphate isomerase and epimerase reactions are quickly equilibrated (Nöh et al. 2006b; Wiechert and de Graaf 1996).

3.3.2.3 Tricarboxylic Acid Cycle

The TCA intermediates succinate (SUC) and fumarate (FUM) are symmetrical molecules, which in stationary ^{13}C-flux analysis is most commonly taken into account by implementing full label scrambling. However, particularly with regard to flux identification from isotopic transients, full label scrambling is reasonable only under the premise that no metabolite channeling occurs. In this context, orientation-conserved transfer of TCA cycle intermediates has been shown for *Saccharomyces cerevisiae* (Sumegi et al. 1990; Sumegi et al. 1993), as well as for human colon carcinoma (Malaisse et al. 1996) and heart cells (Sherry et al. 1994). Therefore, two distinct routes for both reactions, i.e. the conversion from succinate to fumarate (r24a and r24b) and the subsequent conversion of fumarate to malate (r25a and r25b), were implemented.

3.3.2.4 Anaplerosis

Malic enzyme and phosphoenolpyruvate carboxykinase reactions were included in order to replenish TCA cycle intermediates.

3.3.3 Isotopomer Balancing

Flux identification from tracer experiments is attributed to match unknown fluxes and reversibility factors to the measurement data. This requires a mathematical model that describes the relation between fluxes and the labeling state of the system over time. Hitherto several different mathematical approaches for characterizing the labeling state of a system have been proposed (Antoniewicz et al. 2007a; Schmidt et al. 1997; van Winden et al. 2002; Wiechert et al. 1999). The isotopomer approach was chosen for this study as it is intuitive and straightforward to implement.

For simulation and analysis of the chemical labeling experiment, the metabolic network model (cf. Figure 4) needs to be translated into the corresponding isotopomer balance equations (Schmidt et al. 1997). Thus, given metabolic steady state, the balance equation for the isotopomer distribution of metabolite i, which is produced in p reactions and consumed in q reactions, reads

$$c_i \frac{d\mathbf{l}_i}{dt} = \sum_{j=1}^{p} \left(\bigotimes_{k=1}^{o} \left[\sum_{m=1}^{\upsilon_{ij}} \mathbf{IMM}_{k\rightarrow m} \right] \mathbf{l}_k \right) r_j + \left(\sum_{j=1}^{q} \upsilon_{ij} r_j \right) \mathbf{l}_i \qquad (2)$$

where c_i denotes the intracellular concentration of metabolite i. $\mathbf{l}_i$ and $\mathbf{l}_k$ are isotopomer distribution vectors for metabolites i and k, respectively, and $\mathbf{IMM}_{k->m}$ is an isotopomer mapping matrix that describes the isotopomer transitions from substrate k to product m (Schmidt et al. 1997). There is exactly one **IMM** for each substrate product pair. υ_{ij} denotes the stoichiometric coefficient of metabolite i in reaction j, whose molar rate is r_j. The operator $\otimes$ denotes element-by-element vector-multiplication. Isotopomer distribution vectors contain molar fractions of the individual isotopomers of a metabolite, i.e. for each intermediate the total sum of all isotopomer fractions must equal one.

The computational workflow for the evaluation of the non-stationary ^{13}C-labeling experiment is shown in Figure 5. Firstly, a formulation of a metabolic network is supplemented by the description of the fate of each carbon atom in the system (cf. Table 5), from which the corresponding atom-mapping matrices are extracted (Zupke and Stephanopoulos 1994). The atom-mapping matrices, in turn, are used for assembling the isotopomer-mapping matrices according to Schmidt et al. (Schmidt et al. 1997). The latter are then used for compiling the isotopomer balances using equation (2). In this study the number of isotopomer balance equations was as high as 860, which is why the operational sequence had to be automated.

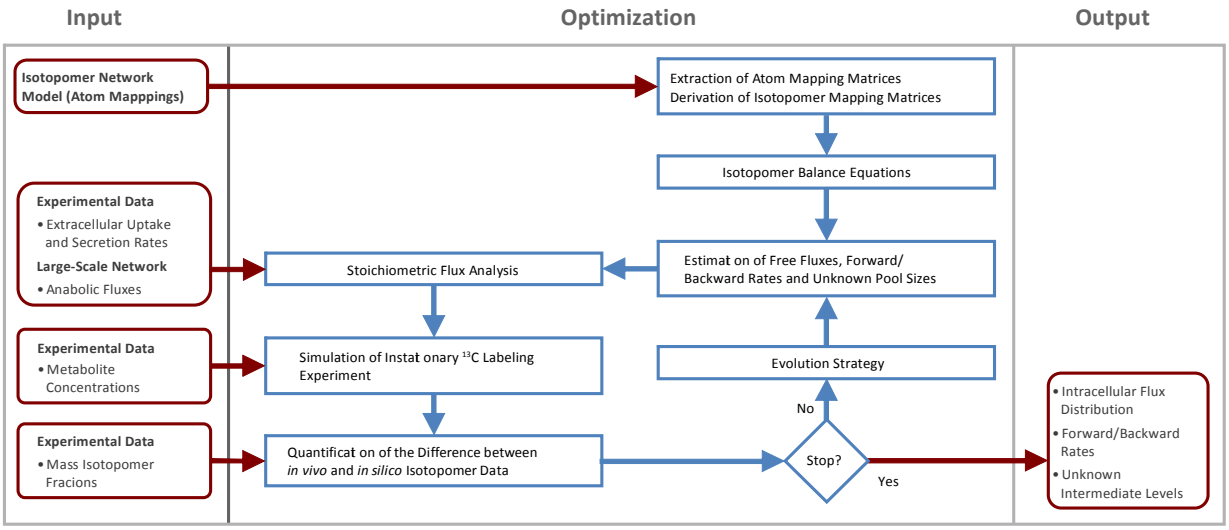

Figure 5. Computational workflow for the evaluation of transient labeling experiments. Required user input and corresponding program output are shown inside rounded rectangles on the left- and right-hand sides.

3.3.4 Parameter Identification

The actual parameter estimation procedure is launched with random initial values. Since glucose uptake and lactate excretion (r_1 and r_{34}) were determined experimentally, and four other fluxes are anabolic fluxes into the biomass (r_{29}, r_{30}, r_{31}, r_{32}), only a subset of nine free fluxes needs to be identified using the optimization routine. Subsequently, the nine flux estimates, the two experimentally determined extracellular rates and the four anabolic fluxes into the biomass are used to calculate the corresponding intracellular flux distribution by conventional stoichiometric flux analysis.

In bidirectional reaction steps forward and backward rates, $r_{i,\,for}$ and $r_{i,\,back}$, were deduced from the calculated net flux $r_{i,\,net}$ (≠0) and an estimate for the reversibility factor β_i as follows

$$\begin{aligned} r_{i,\,for} &= \beta_i r_{i,\,net} \\ r_{i,\,back} &= r_{i,\,for} - r_{i,\,net} \end{aligned} \tag{3}$$

Furthermore, the time constants of the labeling dynamics also depend on the intracellular metabolite levels. Consequently, metabolite concentrations that could not be determined experimentally were included as additional unknown parameters in the optimization procedure.

Large values for exchange fluxes can result in stiff systems which make it demanding to obtain numerically stable solutions (Nöh et al. 2006b; Wiechert et al. 2001; Yang et al. 2004b). On the other hand, the simulation step is the most time-consuming section in the flux identification procedure. To solve the equation system (2) efficiently, the Livermore Solver of Ordinary Differential Equations (LSODA) was used (Hindmarsh 1983), which is a solver that is capable of switching between Adams integration method and backward differentiation formula (BDF) automatically, depending on the stiffness of the problem.

The deviation between simulated and experimental data was quantified by the weighted sum of squared residuals

$$\chi^2(\boldsymbol{\Theta}) = \sum_{i=1}^{L} \left(\frac{m_{i,m} - m_{i,c}}{\sigma_i} \right)^2 \tag{4}$$

where $\chi^2(\boldsymbol{\Theta})$ denotes the value of the objective function corresponding to the values in the parameter vector $\boldsymbol{\Theta}$, L is the number of experimentally quantified mass isotopomers, $m_{i,m}$ and $m_{i,c}$ are measured and simulated values of mass-isotopomer i, respectively, and σ_i is the standard deviation of the i^{th} measured mass isotopomer.

After calculating the objective function, an evolutionary algorithm was used to generate a new parameter set, and the loop was repeated until the maximum number of function evaluations was reached. Altogether, more than $4 \cdot 10^5$ simulation runs were performed. In this study, an evolution strategy from the general optimization package JavaEvA (Streichert and Ulmer 2005) together with a self-adaptive mutation operator (covariance matrix adaption, CMA) (Hansen and Ostermeier 2001) was applied. The optimization runs were performed in parallel on a high- performance computing cluster (five nodes; Intel Xeon with 2.4 GHz). On average, a single simulation run took twelve seconds. The recently introduced EMU approach (Antoniewicz et al. 2007a) could be applied to further reduce the simulation times of larger reaction networks.

3.3.5 Parameter Sensitivities

The scaled sensitivity of the objective function value with respect to variations in the estimated free fluxes, reversibility factors, and unknown intermediate levels is given by

$$\varepsilon_i^{\chi^2(\boldsymbol{\Theta})} = \left| \frac{\partial \chi^2(\boldsymbol{\Theta})}{\partial \Theta_i} \frac{\Theta_i}{\chi^2(\boldsymbol{\Theta})} \right| \times 100\,\% \tag{5}$$

where $\boldsymbol{\Theta}$ and $\chi^2(\boldsymbol{\Theta})$ denote the best parameter set and the corresponding objective function value. The sensitivity values were calculated numerically using Ridders' method of polynomial extrapolation (Ridders 1982).

In isotopomer balancing the free fluxes $\mathbf{r_f}$ were chosen such that $\mathbf{N}_d$ had full rank. Thus, the sensitivities of the dependent fluxes $\mathbf{r_d}$ with respect to the estimated free fluxes can be calculated by

$$\frac{\partial \mathbf{r}_d}{\partial \mathbf{r}_f} = -\mathbf{N}_d^{-1}\mathbf{N}_f \tag{6}$$

$\mathbf{N}_d$ and $\mathbf{N}_f$ contain the entries of the stoichiometric matrix corresponding to dependent and free fluxes, respectively. The matrix $\partial \mathbf{r}_d / \partial \mathbf{r}_f$ denotes the sensitivities of the dependent fluxes to changes of $\mathbf{r}_f$, i.e. the entry i·j contains the sensitivity of flux $\mathbf{r}_{d,i}$ with respect to the j-th element in $\mathbf{r}_f$. Conse-

quently, examination of $\boldsymbol{\varepsilon}_{F(\Theta)}$ and $\partial \mathbf{r}_d / \partial \mathbf{r}_f$ provides a measure of the validity of the dependent flux estimates.

3.4 Results and Discussion

3.4.1 *In Vivo* and *In Silico* Labeling Dynamics

In vivo and *in silico* time courses of the intracellular labeling dynamics are both shown in Figure 6. After adding labeled substrate at time t=0 min, the mole fraction for m+0 (completely unlabeled) instantly falls, while the other mass isotopomers increase complementarily. The model predictions are consistent with the experimental data for almost all metabolites being studied. In case of fructose-6-phosphate, the predicted isotopomer dynamics are faster than the measured values and the steady state labeling distribution differs from the measurements. Furthermore, the simulated values of the mass isotopomers m+5 and m+6 of both metabolite pools glucose-6-phosphate and, to a lesser extent, 6-phosphogluconate are larger than the observed experimental data. One possible explanation for this discrepancy could be the activity of some metabolic pathway that was not included in the model. In the TCA cycle, the *in silico* data are in accordance with the observed slow label redistribution. The deviation in the first 10 minutes in the citrate-pool between simulated and measured labeling dynamics could be an indication that the *in vivo* concentration of citrate was larger than the observed value.

In the case of glycolytic metabolites (e.g. PEP), isotopic steady state was observed after 30 min. The rapid change in the label distribution of the glycolytic intermediates after addition of labeled substrate underlines the need for an effective quenching method (Hofmann et al. 2008). In the TCA cycle, the labeling is redistributed significantly slower than in glycolysis. The labeling distribution of α-ketoglutarate, for example, remained virtually constant in the first three to five minutes. Subsequently, the labeling was slowly redistributed. There was even a small change in the label distribution between the penultimate (120 min) and the final (180 min) measuring point. Thereby, the observed decelerated TCA labeling dynamics clearly emphasize the need for considering the isotopic transient for flux identification in mammalian cell cultures.

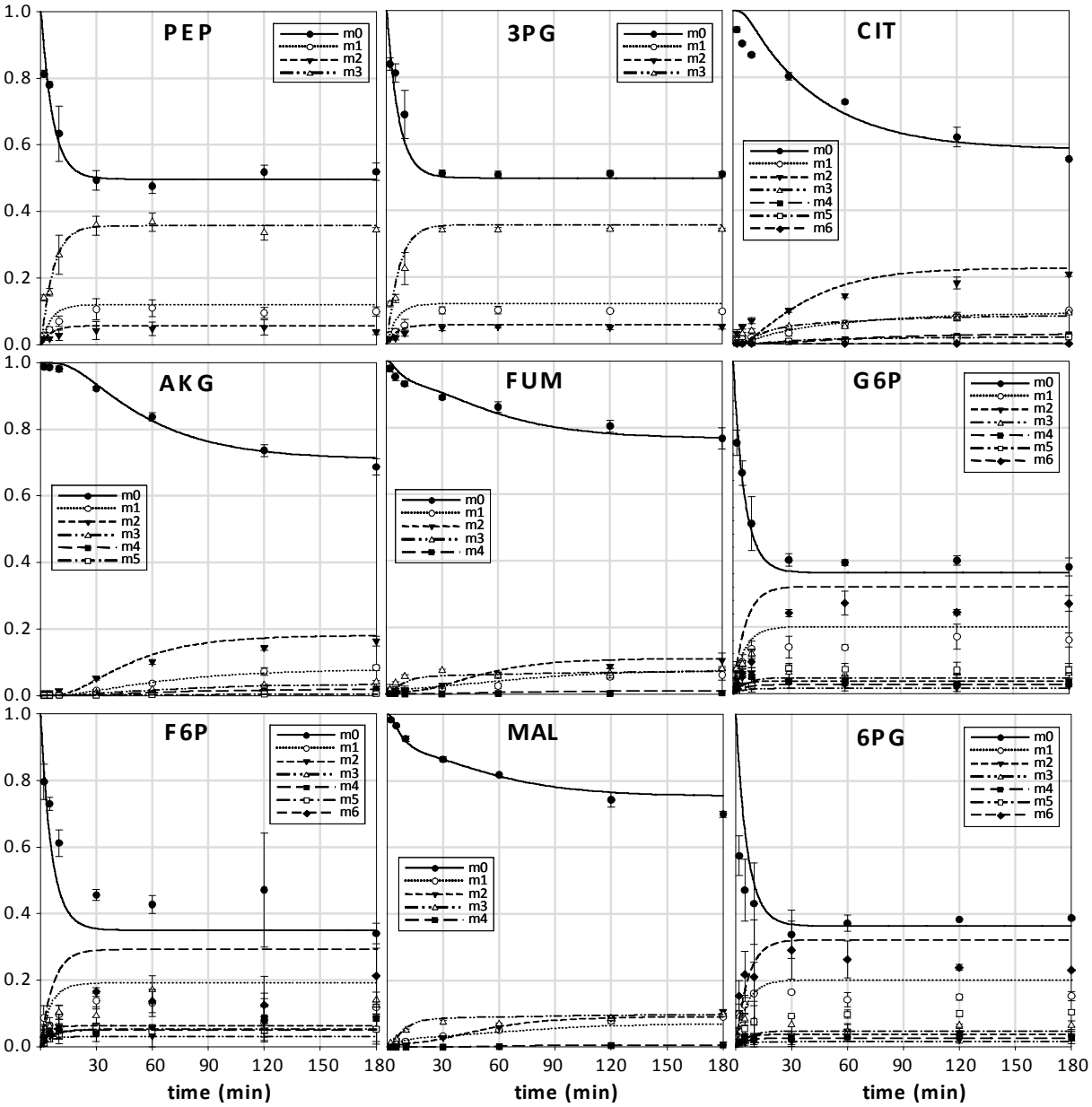

Figure 6. Time courses of *in vivo* (symbols) and *in silico* (solid lines) labeling dynamics.

3.4.2 Intracellular Flux Distribution

A summary of metabolic fluxes identified from transient isotopomer data and the corresponding flux estimates obtained by conventional stoichiometric flux analysis using the large-scale hepatic network model are given in Table 6. The corresponding parameter sensitivities of the isotopomer model are shown in Figure 7.

Table 6. Estimated metabolic fluxes in glycolysis, PPP, TCA and two anaplerotic reactions. Fluxes are normalized with respect to the glucose influx.

	Isotopomer Balancing			Stoichiometric Flux Analysis
Reaction	Forward	Backward	Net	Net
Glycolysis				
r_1			100	100
r_2			100	100
r_3	163.6	106.8	56.7	94.2
r_4			85.1	97.6
r_5	96	10.9	85.1	97.6
r_6	242.5	157.5	84.9	97.4
r_7	624.9	440.6	184.3	196.6
r_8	352	167.7	184.3	196.6
r_9	488	304.9	183.1	195.5
r_{10}	502.5	319.4	183.1	195.5
r_{11}			183.1	195.5
PPP				
r_{12}			43.1	5.6
r_{13}			43.1	5.6
r_{14}			43.1	5.6
r_{15}	15.1	0.9	14.2	1.7
r_{16}	14.2	0	14.2	1.7
r_{17}	14.2	0	14.2	1.7
TCA				
r_{18}			2.3	22
r_{19}			2.3	33.1
r_{20}	4.3	2	2.3	27.2
r_{21}	3.4	1.1	2.3	27.2
r_{22}			3.2	23.7
r_{23}	12	7.8	4.3	26.1
r_{24a}	4.3	0.6	3.8	26.1
r_{24b}	0.6	0.1	0.5	
r_{25a}	6.2	3.8	2.4	26.6
r_{25b}	5	3.1	1.9	
r_{26}	5.2	2.9	2.3	32.6
Anaplerosis				
r_{27}	3	5	-2	0
r_{28}			0	0
Biomass				
r_{29}			0.2	0.2
r_{30}			0.5	0.5
r_{31}			0.2	0.2
r_{32}			1.2	1.2
r_{33}	30	19.1	10.8	20.1
r_{34}	288	94.4	193.6	193.6
r_{35}	0	0	0	5.8
r_{36}	0.1	1	-0.9	3.4
r_{37}	1.1	0.1	1	2.4
r_{38}	0	0	0	0.5

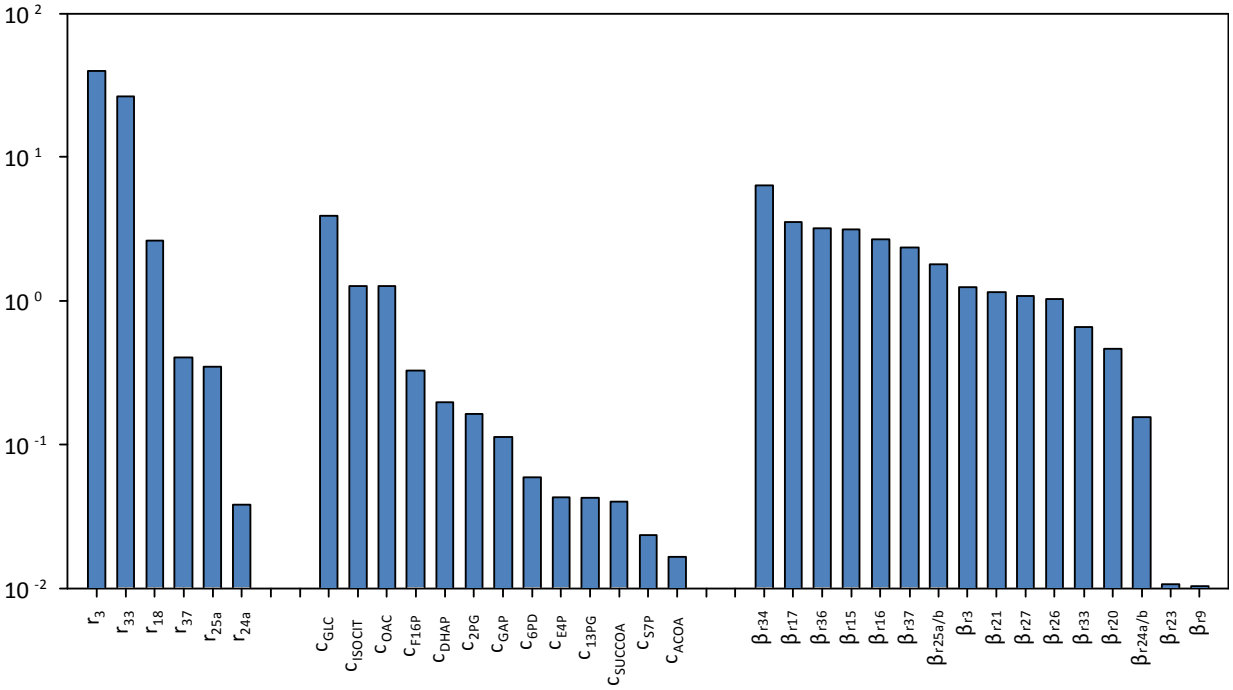

Figure 7. Sensitivities of the objective function value with respect to intracellular fluxes (r_i), estimated pool sizes (c_j), and reversibility factors (β_{ri}). Only values larger than 10^{-2} are listed.

In the case of stoichiometric flux analysis with the large-scale network model, the extracellular rates of albumin, haem, and bile were set to zero as the corresponding values are negligible (Axelson et al. 1991; Enosawa et al. 1996; Kuntz and Kuntz 2001). The χ^2-statistic (with one degree of redundancy), as described in detail by (Stephanopoulos et al. 1998; van der Heijden et al. 1994), resulted in a confidence level of 90.3% suggesting that the presumed biochemistry was statistically consistent with the experimentally observed substrate uptake and product excretion rates (Hofmann et al. 2008). The calculated fluxes were then used for estimation of the anabolic fluxes into the biomass in the isotopomer model (r_{29}=0.2, r_{30}=0.5, r_{31}=0.2, r_{32}=1.2). A sensitivity analysis was performed according to equation (4) in order to investigate the response of the objective function value subject to variations in these fluxes. The calculated scaled sensitivities to fluctuations in r_{29} (glycogen synthesis) and r_{31} (serine synthesis) were below 1 %. The sensitivities for r_{30} (nucleotide synthesis) and r_{32} (serine synthesis) were lower than 2 % and 3 %, respectively. However, the observed anabolic fluxes were rather small compared to the fluxes in glycolysis and the pentose-phosphate-pathway and thus moderate changes do not alter the calculated flux distribution significantly. Furthermore, the anabolic fluxes are effluxes and thus under-/overestimated flux values would result into apparent faster/slower label redistribution, which would be compensated by over-/underestimated pool sizes of subsequent metabolite pools. The sensitivity values corresponding to the latter were rather low (≤ 0.06 % for E4P, S7P and 6PD) to moderate (≤ 0.2 for 2PG and DHAP).

The isotopomer network model reveals a split ratio between glycolysis and the pentose-phosphate shunt of 57%:43%. This ratio differs significantly from the ratio of 94%:6% which was obtained by stoichiometric flux analysis using the large-scale network model. However, in contrast to isotopomer balancing, stoichiometric flux analysis relies on the correctness of the assumed NADP(H) and NAD(H) cofactor balances. Furthermore, in the case of isotopomer balancing, the split ratio could be established at a high level of precision as the flux estimate of the corresponding free flux r_3 (cf. Figure 4) showed the highest overall sensitivity. Thus, one (or several) relevant NADPH-consuming reactions were not included in the large-scale model, resulting in an underestimation of the cell's true NADPH demand. In this regard, the conversion of pyruvate to lactate via lactate-dehydrogenase (EC 1.1.1.27) in the large-scale hepatic network is assumed to work exclusively with NADH as cofactor. It was, however, shown that human lactate-dehydrogenase also acts with NADPH (Clausen 1969), although at a much lower rate. Considering the large quantities of lactate synthesized throughout the experiment, the quantity of NADPH consumed in this reaction could be seen as substantial. Additionally, hepatocytes are also known to show transhydrogenase activity. The corresponding enzyme, though, is located in mitochondria (Hoek and Rydstrom 1988) and was included in the large-scale model. Moreover, taking the high lactate production rate as indication of hypoxia, it is possible that the cells were under oxidative stress, to which a well recognized response is the generation of reactive oxygen species (ROS) (Chandel et al. 2000; Thannickal 2003). As protection against the damaging effects of ROS, cells are endued with several antioxidative acting enzymes such as catalase (EC 1.11.1.6), superoxide dismutase (EC 1.15.1.1) and in hepatocytes mainly glutathione peroxidase (EC 1.11.1.9) (Thannickal and Fanburg 2000). In the peroxidase reaction, H_2O_2 is detoxified by the transfer of two electrons from the reduced form of glutathione. The latter is subsequently re-reduced by the enzyme glutathione reductase (EC 1.8.1.7) at the expense of NADPH. It is clear that quantification of these two possible NADPH sinks would necessitate highly ambitious experimental set-ups, which emphasizes the advantage of isotopomer balancing for flux identification in mammalian cell cultures.

In isotopomer balancing, the reaction rates identified in the TCA cycle were much smaller compared to the glycolytic fluxes, which is in accordance with the experimentally observed extracellular rates of glucose (16.3 nmol/(10^6 cells·min)), alanine (3.2 nmol/(10^6 cells·min)) and lactate (31.6 nmol/(10^6 cells·min)). Furthermore, the small values of the estimated fluxes cannot be attributed to large extracellular pools buffering the label distribution but are a direct consequence of the slow labeling dynamics observed in the TCA (cf. Figure 6). In this regard, the lactate transportation step was assumed to operate reversibly and the corresponding sensitivity of the estimated reversibility factor was the highest of all reversibility sensitivities (cf. Figure 7). In addition, the observed gluta-

mine uptake rate was negligible and glutamate was even excreted during the experiment (Hofmann et al. 2008).

In case of stoichiometric flux analysis, the TCA flux estimates were larger compared to isotopomer balancing (cf. Table 6). However, the magnitudes of the TCA fluxes depend on the split ratio between glycolysis and the pentose-phosphate-shunt. The more carbon is released as carbon dioxide in the pentose-phosphate-shunt, the smaller the TCA fluxes will be. Consequently, the TCA fluxes obtained by conventional stoichiometric flux analysis are comparable to the values obtained from isotopomer balancing after adjusting the split ratio to the value identified by isotopomer balancing (data not shown).

According to the estimated flux values for the succinate dehydrogenase (r_{24a} and r_{24b}) and fumarate hydratase (r_{25a} and r_{25b}) reactions, the respective symmetric TCA intermediates are converted orientation-conserved in HepG2 cells. However, due to the low corresponding sensitivity values (0.04 for r_{24a} and 0.35 for r_{25a}) this conclusion is uncertain. Nonetheless, in the case of scrambling reactions the possibility of metabolite channeling and its potential consequences in terms of labeling dynamics should be addressed during the setup of isotopomer models.

Because of both, the maintenance of 5 % CO_2-atmosphere and continuous shaking throughout the experiment, no balance equations were set up for carbon dioxide in the isotopomer model. Therefore, only natural abundances of carbon are incorporated in carboxylation reactions (r_{28}) or in reversible decarboxylation reactions (r_{21}, r_{27}). In case of the isocitrate-dehydrogenase reaction (r_{21}) the reversibility factor was estimated at 3.1 and the corresponding sensitivity was 1.2 %. In the anaplerotic section the normalized flux rates for the free fluxes r_{27} and r_{28} were estimated at -2.0 and 0.0 and the corresponding sensitivity values were below 0.01 %.

Table 7 summarizes the sensitivities of the dependent fluxes with respect to the free fluxes identified from transient isotopomer data. The dependent fluxes in glycolysis and PPP are more sensitive to changes in r_3 than to changes in any other flux. On the other hand, r_3 gave the largest overall sensitivity of the objective function value (cf. Figure 7). The fluxes in the TCA cycle are particularly influenced by r_{18} and r_{33} and the objective function value was also sensitive to variations in these two free fluxes. Therefore, it can be concluded that the respective dependent fluxes in glycolysis, PPP, and TCA could be reasonably estimated with the method outlined.

Table 7. Flux distribution sensitivity matrix. Only non-zero values are listed.

	Free Fluxes								
Dependent Fluxes	r_3	r_{18}	r_{24a}	r_{25a}	r_{28}	r_{37}	r_{33}	r_{38}	r_{35}
r_2									
r_4	1/3								
r_5	1/3								
r_6	1/3								
r_7	1/3								
r_8	1/3								
r_9	1/3								
r_{10}	1/3								
r_{11}	1/3				1				
r_{12}	-1								
r_{13}	-1								
r_{14}	-1								
r_{15}	1/3								
r_{16}	1/3								
r_{17}	1/3								
r_{19}		1							
r_{20}		1							-1
r_{21}		1							-1
r_{22}	1/3	2				-1	-1	-1	
r_{23}	1/3	2					-1	-1	
r_{24b}	1/3	2	-1				-1	-1	
r_{25b}	1/3	2		-1			-1		
r_{26}		1			1				
r_{27}	1/3	-1			1		1		
r_{36}	1/3	-1				1	1	1	-1

3.4.3 Intracellular Metabolite Concentrations

Measured and estimated intracellular pool sizes are both listed in Table 8. The corresponding parameter sensitivities are shown in Figure 7. The predicted intracellular glucose level is two to three orders of magnitude higher than the other intermediary concentrations. As mentioned before, this is not surprising considering both the fairly high extracellular glucose concentration of 2 $g \cdot l^{-1}$ and the fact that glucose uptake (and release) is mediated by facilitated diffusion in liver cells (Thorens 1992). Besides, the observed sensitivity for this parameter was larger than those of all other estimated intermediate levels, which indicates that the estimated value is a good approximation of the actual intracellular concentration. Additionally, an even higher intracellular glucose level (167 nmol/10^6cells) has been reported for rat hepatocytes (Fulgencio et al. 2001). In this particular study, in which the authors analyzed the effect of metformin on fatty acid and glucose metabolism, the hepatocytes performed gluconeogenesis. The proposed method constitutes a new approach for the estimation of intracellular glucose levels. The remaining non-measured glycolytic pools were estimated in the range of between 0.34 and 1.56 nmol/10^6 cells, which is the same order of magnitude

as the experimentally determined glycolytic values, except for pyruvate (cf. Table 8). The pyruvate pool, however, is more prone to experimental inaccuracies than the other observed intermediate levels because of extracellular accumulation of this metabolite in combination with the fact that no washing step was performed during sampling in order to ensure instantaneous quenching of metabolism.

Table 8. Measured and estimated intracellular pool sizes. Concentrations are given in nmol/10^6cells.

Measured		Estimated	
G6P	1	GLC	101.6
F6P	1.1	F16P	1.3
3PG	0.7	GAP	0.9
PEP	0.3	DHAP	1.6
PYR	17.8	13PG	0.3
PG6	1	2PG	1.4
P5P	1	6PD	0.2
MAL	1.1	S7P	0.1
FUM	0.5	E4P	0.2
SUC	0.3	ACOA	6
AKG	2	OAC	1.8
CIT	2.3	ISOCIT	9.1
		SUCOA	4.5

Metabolite pools in the pentose-phosphate-shunt were predicted to be one order of magnitude smaller than the glycolytic intermediates. A similar ratio was found in rat liver cells for erythrose-4-phosphate (Sabate et al. 1995). In the same study, though, the sedoheptulose-7-phosphate concentration was found to be in the order of fructose-6-phosphate and fructose-1,6-bisphosphate. However, the small sensitivity values (cf. Figure 7) indicate that the corresponding values are rather uncertain.

Intracellular acetyl-CoA was estimated to be 6 nmol/10^6 cells. However, such a large intracellular concentration of acetyl-CoA is in conflict with the majority of experimental metabolite studies in mammalian cells where rather small intracellular concentrations were found for acetyl-CoA (Zhou et al. 2005). The corresponding sensitivity was small (0.02).

Intracellular isocitrate is predicted to be at higher concentration levels than all other TCA metabolites. This could be due to the fact that the assessed value includes not only the isocitrate pool, but also cis-aconitate. Additionally, the corresponding sensitivity (1.3) is the second largest of all concentration sensitivity values.

Differences between prokaryotic and eukaryotic labeling dynamics can be assessed by considering the respective time constants. The time constant τ that characterizes the labeling dynamics in the intermediary pools is determined by the ratio

$$\tau = \frac{\bar{c}}{v_{uptake}} \tag{7}$$

where $\bar{c}$ and v_{uptake} denote the average intermediary pool size and substrate uptake rate, respectively. As the glucose uptake rate was found to be significantly larger than all other influxes (Hofmann et al. 2008), it was the only uptake rate considered. Additionally, the respective time constant was estimated from a published dataset that was obtained in a similar study, in which *Escherichia coli* cells had been grown with saturated glucose uptake system in fed-batch culture (Nöh et al. 2006a). Furthermore, metabolite and flux data were taken from an experiment with *Saccharomyces cerevisiae*, in which the cells were grown in aerobe glucose-limited chemostat culture at $D = 0.1\ h^{-1}$ (Rizzi et al. 1997; Theobald et al. 1997). The time constants were determined to be 1.0 s in *Escherichia coli*, 3.6 s in *Saccharomyces cerevisiae* and 23.3 s in hepatoma cells. The substantial difference between prokaryotic and mammalian labeling dynamics is mirrored in the observed time courses of the glycolytic intermediates. In the case of HepG2 cells, isotopic steady state was reached in the phosphoenolpyruvate pool after approximately 30 minutes (cf. Figure 6). In contrast, Nöh et al. showed that the phosphoenolpyruvate mass isotopomers became isotopically stable in *Escherichia coli* in less than 20 seconds after the addition of labeled substrate (cf. Figure 2 in (Nöh et al. 2006a)). Therefore, ^{13}C-flux identification in mammalian cell cultures necessitates the consideration of the isotopic transient.

3.5 Conclusions

Metabolic fluxes were estimated from transient ^{13}C-labeling data in hepatic cells. Compared to stationary ^{13}C-flux analysis, experimental and computational efforts are larger. However, flux estimation in mammalian cells in batch culture systems was rendered feasible. Furthermore, the outlined method paves the way for flux analysis in primary hepatocytes, which are known to have even smaller growth rates and are prone to show dedifferentiation in the course of pharmacologically relevant experiments.

While quantification of extracellular glucose is routinely applied in clinical analytics (e.g. in blood samples), determination of the intracellular glucose pool is often challenging. Especially in cases where glucose itself is used as the (sole) carbon source in the cultivation of prokaryotic or lower eukaryotic cells, its intracellular quantification is difficult (de Koning and van Dam 1992 ; Teusink et al. 1998). In this regard, the outlined indirect method for the estimation of the intracellular glucose pool is a potential alternative. Theoretically, the procedure also enables the estimation of any other intracellular metabolite pool.

The fast glycolytic labeling dynamics emphasized the need for a reliable quenching method. In this regard, ineffective quenching of the metabolism could easily result in virtually accelerated label redistribution and thus in overestimated fluxes. By contrast, the slow label redistribution in the TCA cycle illustrated the need for considering the isotopic transient for flux identification in mammalian cell cultures. Even after 120 minutes the system was not at isotopic steady state.

As was demonstrated, the outlined method is well suited for the identification of the split ratio between glycolysis and the hexose monophosphate shunt. The results show that there must be at least one additional reaction consuming NADPH in significant amounts, which was not included in the large-scale hepatic network model. In this context, oxygen stress and the corresponding oxidization of glutathione were presented as potential NADPH sink. Furthermore, usage of NADPH as a cofactor by the human lactate-dehydrogenase enzyme has been reported in literature (Clausen 1969).

The question as to whether TCA intermediates are transferred orientation-conserved in HepG2 cells was addressed. However, due to the small corresponding sensitivities the results are ambiguous. Nonetheless, metabolite channeling constitutes a possible pitfall in flux identification from transient labeling data.

4

Quantification of Statin Effects on Hepatic Cholesterol Synthesis by Transient ^{13}C-Flux Analysis

Chapter Outline

4.1 Introduction 45
4.2 Materials and Methods 47
4.2.1 Cell Culture 47
4.2.2 Labeling Experiment 47
4.2.3 Metabolic Network Model 47
4.2.4 Simulation of Isotopomer Dynamics 49
4.2.5 Parameter Estimation 50
4.2.6 Confidence Limits 52
4.2.7 Flux Control 52
4.3 Results and Discussion 54
4.3.1 Labeling Dynamics 54
4.3.2 Flux Distribution 57
4.3.3 Metabolite Levels 61
4.3.4 Flux Control 62
4.4 Conclusions 65

Parts of this chapter are published as
Maier K, Hofmann U, Bauer A, Niebel A, Vacun G, Reuss M, Mauch K. 2009. Quantification of Statin Effects on Hepatic Cholesterol Synthesis by Transient ^{13}C-Flux Analysis. Metab Eng, vol. 11, pp. 292-309, Jul-Sep 2009

Abstract

The work presented in this section is the first to deal with the determination of cholesterol synthesis rates in primary rat hepatocytes using transient ^{13}C flux analysis. The effects of statins on cholesterol biosynthesis and central carbon fluxes were quantified at a therapeutic concentration of 50 nM atorvastatin using carbon-labeled glutamine. The flux through the cholesterol pathway decreased from 0.27 mmol/(l_{cv}·h) to 0.08 mmol/(l_{cv}·h) in response to the administration of the hypolipidemic drug. Isotopic steady state was reached within 4 h in the central carbon metabolism but not in the cholesterol pathway, regardless of whether atorvastatin was administered or not. Marked channeling was observed for the symmetrical tricarboxylic acid cycle intermediates, succinate and fumarate. Non-stationary ^{13}C-based flux identification delivers both intracellular fluxes and intermediate levels, which was for the first time utilized for investigating systems-level effects of the administered drug by quantifying the flux control of the 3-hydroxy-3-methylglutaryl-coenzyme A reductase. Alexander Bauer contributed the isolation of the primary rat hepatocytes. The quantification methods for determining metabolite levels and mass isotopomer fractions were developed and coordinated by Ute Hofmann.

4.1 Introduction

Metabolic flux estimates enable the quantitative assessment of cellular physiology and metabolic regulations. Isotopic tracer experiments are excellent means for determining intracellular flux distributions because they allow the identification of metabolic fluxes in parallel routes and reaction cycles without requiring any assumptions to be made on energy yields and cofactor balances (Schmidt et al. 1998; Wiechert 2001). In tracer experiments, the cellular machinery converts stable isotope-labeled substrates into metabolic intermediates with a distinct labeling pattern. These isotopic abundances, which are a function of the intracellular flux map, can then be detected by nuclear magnetic resonance (NMR) (Dauner et al. 2001) or by mass spectrometry (MS) (Hofmann et al. 2008). The flux distribution can be reconstructed from the labeling data by solving the inverse problem. So far, the most frequently employed tracer-based flux identification method is based on isotopic stationarity (Sauer 2006). The experimental observation of the isotopic transient, however, enables the identification of metabolic fluxes in slow- or even non-growing cellular systems, in which long observation times would potentially jeopardize the assumption of a metabolic steady state and/or cellular integrity (Maier et al. 2008a; Sauer and Zamboni 2008). In other words, the isotopic transient allows for a higher temporal resolution of flux distributions.

In vivo quantifications of cholesterol synthesis rates have traditionally been performed either by administering a labeled substrate and determining the rate of appearance of the labeled end product (Jeske and Dietschy 1980; Robins et al. 1985; Zilversmit et al. 1943) or by direct measurements obtained with the time-consuming fecal balance method (Connor et al. 1969). In terms of mass spectrometry data analysis, two similar approaches, i.e. mass isotopomer distribution analysis (MIDA) and isotopomer spectral analysis (ISA), enable the quantitative estimation of synthesis rates of biopolymers. These two methods apply a probability analysis for deriving (i) the fractional enrichment of the precursor and (ii) the fractional amount of the product that has been synthesized following the introduction of the tracer (Lindenthal et al. 2002). ISA (Clarenbach et al. 2005; Kelleher et al. 1994; Lindenthal et al. 2002) and MIDA (Bandsma et al. 1998; Di Buono et al. 2000; Neese et al. 1993) have been successfully employed for analyzing the synthesis rate of cholesterol. Antoniewicz et al. combined the central ideas of ISA with the recently developed elementary metabolite unit (EMU) approach (Antoniewicz et al. 2007a) to study metabolic fluxes in a isotopically non-stationary prokaryotic system (Antoniewicz et al. 2007b). Young et al. used non-stationary metabolic flux analysis based on the EMU theory to estimate flux distributions in brown adipocytes (Young et al. 2008). Yoo et al. combined conventional isotopic steady-state-based ^{13}C-flux analysis with ISA for quantifying the fluxes in the glutaminolysis and reductive carboxylation pathways in a brown adipocyte cell line (Yoo et al. 2008). Only recently, Jones et al. quantified hepatic gluconenogenesis and relative TCA cycle

fluxes in healthy controls and Type 1a glycogen storage disease patients using isotopically stationary ^{13}C-flux analysis (Jones et al. 2009).

Statins are competitive inhibitors of the 3-hydroxy-3-methylglutaryl-coenzyme A (HMG-CoA) reductase enzyme. The intracellular cholesterol level drops after the administration of such hypolipidemic drugs. This in turn stimulates low-density lipoprotein (LDL) receptors, which eventually leads to a beneficial increase in LDL clearance from the bloodstream and decreased blood cholesterol levels. Statins are very effective in reducing LDL levels and are therefore widely applied to treat hypercholesterolemia (Maron et al. 2000). Lindenthal et al. applied ISA to study the impact of the drugs simvastatin and pravastatin on the cholesterol metabolism in HepG2 cells and human liver slices (Lindenthal et al. 2002). Similarly, Clarenbach et al. used ISA to compare the effects of pravastatin and chenodeoxycholic acid in patients with cerebrotendinous xanthomatosis (Clarenbach et al. 2005). Kallien et al. applied GC-MS and MIDA to assess the long-term effects of pravastatin on biliary lipid secretion and cholesterogenesis in humans (Kallien et al. 1999).

Metabolic control analysis provides a mathematical framework for quantifying the responses of steady state fluxes to changing system parameters (Heinrich and Rapoport 1974; Kacser and Burns 1973). In this regard, the local effects of concentration changes on reaction rates, i.e. elasticity coefficients, can be estimated from experimental perturbation data using the double modulation method or a recently developed lin-log-based approach (Kacser and Burns 1979; Wu et al. 2004). The applicability of these approaches, however, depends on the availability of at least n steady state datasets when n elasticity coefficients are to be determined (Link and Weuster-Botz 2007). Wang and Hatzimanikatis developed a computational and statistical framework based on Monte Carlo sampling to address ambiguity in quantifying interactions between intracellular metabolism and extracellular process conditions (Wang and Hatzimanikatis 2006). Furthermore, systemic response coefficients can be determined after specifically decreasing an enzyme's activity in a metabolic pathway with an appropriate inhibitor (Fell 1992). In such cases, the application of transient ^{13}C flux identification is highly advantageous as it determines both the levels of intracellular metabolite concentrations and metabolic fluxes at steady state.

The present work describes the first transient ^{13}C flux analysis based determination of cholesterol synthesis rates in rat hepatocytes. In contrast to previous probability analysis based studies, non-stationary ^{13}C flux analysis is not restricted to the investigation of the cholesterol biosynthesis rate. That is why the effects of statins on cholesterol and central carbon fluxes could be quantified in one go at a therapeutic concentration of 50 nM atorvastatin using labeled glutamine as substrate. Furthermore, flux identification from transient tracer experiments delivers both steady state fluxes and intermediate levels. This information was utilized for the first time for further deducing systems-level effects of the drug from the control of the targeted enzyme, HMG-CoA reductase. The isolation of

primary rat hepatocytes (Alexander Bauer) and the quantification of metabolite levels and mass isotopomer fractions (Ute Hofmann) are described in (Maier et al. 2009).

4.2 Materials and Methods

4.2.1 Cell Culture

During the labeling experiment, the primary hepatocytes were incubated at 37 °C in 5 % CO_2 atmosphere. Alanyl-glutamine-free William's medium E (PAN Biotech GmbH, Aidenbach, Germany) was supplemented with glutamine (292 mg/l), penicillin (100 U/mL), streptomycin (100 mg/mL), and Gibco^{TM} Insulin-Transferrin-Selenium (100X) supplement (Invitrogen, Karlsruhe, Germany). No fetal calf serum was added to the medium. The 6-well plates were shaken at 20 rpm throughout the tracer experiment (Shaker DRS-12, ELMI, Riga, Latvia).

4.2.2 Labeling Experiment

Half of the cells was cultured overnight in atorvastatin-free medium and the other half was cultured overnight in 50 nM atorvastatin (Toronto Research Chemicals Inc., Canada). Initially, the overnight medium was replaced by fresh, label-free culture medium. After 4 h of equilibration, the medium was exchanged again so that the new medium contained 100 % U-^{13}C-labeled glutamine (Sigma-Aldrich Chemie GmbH, Germany). Samples were collected (in triplicate) 4 h, 8 h, and 12 h after the administration of the tracer and processed as previously described (Hofmann et al. 2008).

The extracellular metabolite concentrations, which were subsequently used to estimate the external rates, and the levels of intracellular intermediates were determined in atorvastatin-free cultures. These were treated identically, except that the medium added after 4 h contained naturally labeled glutamine. The intracellular samples were collected as specified above after pipetting off 1 ml of the cell culture medium for determining the extracellular metabolite levels. The cell number was determined by fixing the cells with a 3:1 methanol:acetic acid fixative solution (10 min at 37 °C and 4 °C). After fixation, the nuclei were stained for 15 min with Meyers Hämalaun (Sigma-Aldrich Chemie GmbH, Germany), rinsed with water (15 min) and air-dried. The stained nuclei were counted in digital images (10 per well) at 40-fold magnification (Multi Gauge, FUJIFILM Corporation, Japan).

4.2.3 Metabolic Network Model

A comprehensive network model of the hepatic metabolism was reconstructed previously (Maier et al. 2008a). An isotopomer model was set-up that is a sub-model of this large-scale network model. The isotopomer model comprises the lower part of gluconeogenesis, the TCA cycle, ketogenesis, anaplerosis, and cataplerosis as well as cholesterol synthesis. Three intracellular compartments, cytosol, mitochondria, and endoplasmic reticulum, are discriminated. The model accounts for 47 bal-

anced compounds that are converted in 73 reactions of which, in turn, 62 are specified as reversible. The corresponding carbon atom transitions (Berg et al. 2002) are listed in Appendix B. In implementing the model we accounted for the available experimental mass isotopomer data. In this regard, gluconeogenesis was modeled up to 3-phosphoglycerate. In the context of anaplerosis, which replenishes the TCA-cycle intermediates, the mitochondrial pyruvate carboxylase reaction was included in the model. In the cataplerotic section, which is active when C_4- and C_5-intermediates enter the TCA cycle during the catabolism of amino acids, the phosphoenolpyruvate carboxykinase and the citrate lyase reactions were taken into account (Owen et al. 2002). Since phosphoenolpyruvate carboxykinase and citrate lyase are key enzymes in glutaminolysis, both the cytosolic and mitochondrial malate dehydrogenase enzymes, were included in the model (Newsholme et al. 1985). The synthesis of fatty acids is considered by an efflux of cytosolic acetyl-CoA over the system boundary. Intercompartmental transportation steps were modeled as simple passive transporters and thus no dedicated shuttle or carrier-mediated transportation systems were included in the model. Exemplary, cytosolic and mitochondrial acetyl-CoA is directly exchanged without the indirection of the carnitine acyl transferase system. No distinction was made between cytosolic and mitochondrial 3-hydroxy-3-methylglutaryl-Coenzyme A synthase isoforms.

Full-label scrambling is often assumed for the rotational symmetric molecules fumarate and succinate (Antoniewicz et al. 2007b; Nöh et al. 2007) notwithstanding that the orientation-conserved transfer of labeled metabolites, which has been observed in colon carcinoma (Malaisse et al. 1996) and heart cells (Sherry et al. 1994), is recognized as a possible pitfall in tracer-based flux identification (van Winden et al. 2001). Consequently, the network model allows for both metabolite channeling and label scrambling. For experimental evidence reasons, the model also takes into account the transportation of TCA intermediates such as isocitrate, citrate, fumarate, malate, and alpha-ketoglutarate into the extracellular space.

Cholesterol synthesis was modeled with a condensed sequence of reactions because (i) the omitted reactions originate from a linear reaction sequence without further in- or effluxes and because (ii) the experimental mass isotopomer data were only available for lathosterol and cholesterol. Specifically, no C_{30}-molecule was integrated into the model, i.e. farnesyl diphosphate, which is a C_{15}-molecule, and a virtual C_{12}-farnesyl diphosphate intermediate condense to zymosterol. Two parallel routes are considered for the conversion of zymosterol into cholesterol, i.e. zymosterol is either converted via cholesta-7,24-dien-3β-ol, 7-dehydrodesmosterol, and desmosterol or via cholesta-8-en-3β-ol, lathosterol, and 7-dehydrocholesterol. Potential reactions between the metabolites in these parallel pathways (Lindenthal et al. 2002) were not included in the network model. The fluxes through these two branches could be discriminated due to measuring both lathosterol and cholesterol mass fractions. That is, the lathosterol measurements determine the flux through the cholesta-8-en-3β-ol,

lathosterol, and 7-dehydrocholesterol pools, and the cholesterol measurements constrain the flux through the cholesta-7,24-dien-3β-ol, 7-dehydrodesmosterol, and desmosterol pools.

4.2.4 Simulation of Isotopomer Dynamics

Central carbon metabolites reached isotopic steady state quickly, so one could apply conventional tracer-based flux analysis tools for quantifying the corresponding fluxes. The intermediates in the cholesterol pathway, though, necessitated the application of non-stationary ^{13}C-flux analysis as isotopic steady state was not reached within 12 h. Furthermore, transient ^{13}C-flux analysis constituted the basis for the subsequent systems-levels analyses. Therefore, intracellular labeling dynamics were simulated with positional and mass isotopomer balance equations. Under metabolic steady state conditions, the isotopomer balance equation for metabolite i reads:

$$\frac{d\left(c_i \mathbf{I}_i\right)}{dt} = \sum_{j=1}^{N} \left[\alpha \left(\bigotimes_{k=1}^{o} \left(\sum_{m=1}^{\upsilon_{ij}} \mathbf{IMM}_{k \to m} \right) \mathbf{I}_k \right) r_j + \left(1 - \alpha\right) \cdot \left(\upsilon_{ij} r_j \mathbf{I}_i \right) \right] \tag{8}$$

with

$$\alpha = \begin{cases} 1, & \text{if } \upsilon_{ij} > 0 \\ 0, & \text{else} \end{cases} \tag{9}$$

c_i, $\mathbf{I}_i$ and $\mathbf{I}_k$ denote the intracellular concentration of metabolite i and the isotopomer distribution vectors for metabolites i and k, respectively. Isotopomer distribution vectors contain molar ratios corresponding to the fractional amount of the individual positional isotopomers. $\mathbf{IMM}_{k->m}$ is an isotopomer mapping matrix, which describes the isotopomer transition from reactant k to product m (Schmidt et al. 1997). N is the overall number of reactions in the system and υ_{ij} equals the stoichiometric coefficient of metabolite i in reaction j, whose molar rate is r_j. The operator $\otimes$ denotes element-by-element vector multiplication.

In contrast to the ISA and MIDA approaches and similar to cumomer and EMU based analyses of tracer experiments, the application of the isotopomer approach allows for estimation of metabolic fluxes on the systems-level, i.e. flux estimates are not restricted to polymer synthesis rates. Unfortunately, the isotopomer approach becomes computationally intractable when the network metabolites are composed of too many C-atoms. Setting-up isotopomer balances for a molecule consisting of 27 carbon atoms such as cholesterol would necessitate the formulation of 2^{27} balance equations. As this is virtually impossible, mass isotopomer balance equations were set up for the metabolites of the cholesterol pathway instead, starting from farnesyl diphosphate. This is valid in the present case as (i) the measurement data consisted of mass isotopomer quantifications, (ii) the respective pathway is linear without any influx other than that from the farnesyl diphosphate synthetase reaction, and (iii) the involved reactions starting from zymosterol do not affect the carbon skeleton. However,

as the mapping from the positional to the mass isotopomer space is not bijective, the synthesis of farnesyl diphosphate had to be modeled as irreversible. Farnesyl diphosphate was integrated into the metabolic network and was modeled as (virtual) C_{12}- (farnesylA) and C_{15}-molecule (farnesylB) in order to reduce the number of terms in the balance equations for zymosterol. An "equivalent", direct conversion from isopentenyl diphosphate to zymosterol would have resulted in a significantly higher number of permutations of substrate molecule combinations in the respective zymosterol mass isotopomer balances. Likewise, the condensing of farnesylA and farnesylB had to be modeled as irreversible. Alternatively one could have applied the EMU approach for decreasing the number of required balance equations (Antoniewicz et al. 2007a; Young et al. 2008).

Similarly to equation (8), the mass isotopomer balance for a metabolite i is given by

$$\frac{d\left(c_i \mathbf{M}_i\right)}{dt} = \sum_{j=1}^{N}\left[\alpha\left(\psi_{ij} r_j\right) + \left(1-\alpha\right)\cdot\left(\upsilon_{ij} r_j \mathbf{M}_i\right)\right] \tag{10}$$

where $\mathbf{M}_i$ is a mass isotopomer distribution vector that contains molar ratios corresponding to the fractional amount of the individual mass isotopomers. The function ψ_{ij} sums up all permutations of reactant mass fractions such that the product molecule has the correct labeling state, i.e. in all but the zymosterol synthesis reaction, ψ_{ij} is equal to one substrate mass isotopomer having the same index number as the product mass isotopomer.

In order to increase both stability and performance of the numerical calculations, the system (950 positional and 253 mass isotopomer balance equations) was reformulated as a differential algebraic equation (DAE) system taking into account the isotopomer conservation relations, i.e. the sum of all mass or positional isotopomers of a particular metabolite had to equal one. The DAE-system was simulated with the linearly implicit differential algebraic solver LIMEX (Deuflard et al. 1987). On average, one simulation run took 1.7 seconds (Intel® Core2™ Quad CPU, 2.66 GHz, 4 GB RAM). The simulation did not slow down and no numerical inaccuracies were encountered even for large exchange fluxes.

4.2.5 Parameter Estimation

Metabolic fluxes, intracellular metabolite concentrations, and reversibility factors were identified by minimizing the differences between *in silico* model predictions and *in vivo* measurement data. That is, the variance-weighted sum of squared residuals between measured and simulated labeling data, $m_{i,j}^{d}$ and $m_{i,j}^{s}$, as well as the deviations between measured and estimated intracellular intermediate levels, c_k^m and c_k^e, and between experimentally determined and estimated extracellular fluxes, r_l^m and r_l^e, were minimized according to

$$\min_{\Theta} \quad \chi^2(\Theta) = \sum_{i=1}^{T} \xi^i_{^{13}C} \sum_{j=1}^{L} \left(\frac{m^d_{i,j} - m^s_{i,j}}{\sigma_{i,j}} \right)^2 + \sum_{k=1}^{C} \left(\frac{c^m_k - c^e_k}{\sigma_k} \right)^2 + \xi_f \sum_{l=1}^{F} \left(\frac{r^m_l - r^e_l}{\sigma_l} \right)^2 \tag{11}$$

The weighting factors $\xi^i_{^{13}C}$ and ξ_f were used for penalizing the discrepancies between measured and predicted mass fractions in the cholesterol pathway and between experimentally determined and estimated exchange fluxes, respectively.

The flux identification was launched by applying an evolution strategy together with a self-adaptive mutation operator (Hansen and Ostermeier 2001; Streichert and Ulmer 2005). In order to enable a thorough exploration of the search space, the optimization runs were restarted after 30,000 evaluations of equation (11) using the hitherto best parameters as starting values in the following iteration. Altogether, 10 optimization runs were performed for each statin data set with 10 restarts each. Subsequent to applying the evolution strategy, a sequential quadratic programming method from the MATLAB® optimization toolbox (The MathWorks, Inc., Natick, MA) was used as it delivers an estimate of the Hessian matrix that, in turn, was used for approximating the parameter confidence limits (cf. section 2.10 Confidence limits).

For parameterizing the dynamic simulation of the isotopomer system, 26 free fluxes had to be estimated by the optimization routine. The corresponding experimental data were available for 11 of these. The free fluxes estimates were used to calculate the dependent fluxes by stoichiometric flux analysis as outlined previously (Maier et al. 2008a). Likewise, a reversibility factor was estimated for each bidirectional reaction as the ratio between forward and net flux from which the corresponding forward and backward rates were deduced as described previously (Maier et al. 2008a).

In each iteration step, 47 intracellular intermediate concentrations were estimated of which 11 had been determined experimentally. The reference concentration $\bar{c}_m$ of a metabolite that is distributed over l intracellular reaction compartments was calculated according to

$$\bar{c}_m = \frac{1}{V_{cell}} \sum_{i=1}^{l} n_{m,i} \tag{12}$$

where $n_{m,i}$ equals the quantity of compound m in reaction compartment i. Likewise, the reference value for mass isotopomer $\bar{m}_{m,j}$ from metabolite m that is available in l compartments is given by

$$\bar{m}_{m,j} = \frac{\sum_{i=1}^{l} m_{m,j,i} \cdot n_{m,i}}{\sum_{i=1}^{l} n_{m,i}} \tag{13}$$

In the case of lathosterol and cholesterol, not all 28 mass isotopomers could be determined experimentally. Therefore, the optimization routine was applied in order to estimate the fractional

amounts ϕ_j of the non-determined mass fractions. Using the ϕ_j, the experimentally determined mass isotopomer values $m_{i,j}$ for these two metabolites were scaled by

$$m^*_{i,j} = \frac{m_{i,j}}{(1+\phi_j)} \tag{14}$$

Set-up of the metabolic network model and compilation of the isotopomer system were performed with the software Insilico Discovery (Insilico Biotechnology AG, Stuttgart, Germany).

4.2.6 Confidence Limits

Lack of information about the confidence limits makes it impossible to establish uncertainties associated with the estimated parameters. Therefore, the statistical significance of the identified fluxes was quantified by means of an approximation of the parameter covariance matrix $\mathbf{\Sigma}_p$ by

$$\mathbf{\Sigma}_p = \mathbf{H}^{-1} \tag{15}$$

where $\mathbf{H}^{-1}$ is the inverse of the Hessian, which is the second-order partial derivative of the objective function with respect to the parameter estimates. $\mathbf{H}$ was obtained from the sequential quadratic programming method, in which an estimate of the Hessian was updated at each iteration using the BFGS formula (Fletcher and Powell 1963). Please note that according to the Cramér-Rao inequality this approach can only deliver a lower bound of the parameter covariance matrix (Joshi et al. 2006). Furthermore, Young et al. pointed out that in case of non-stationary ^{13}C flux analyis, this method can be prone to numerical inaccuracies (Young et al. 2008).

The covariance matrix for all individual fluxes in the system $\mathbf{\Sigma}_v$ was obtained by

$$\mathbf{\Sigma}_v = \mathbf{K} \cdot \mathbf{\Sigma}_f \cdot \mathbf{K}^T \tag{16}$$

where $\mathbf{\Sigma}_f$ and $\mathbf{K}$ are the covariance matrix corresponding to the free fluxes and the kernel of the stoichiometric matrix, respectively (Antoniewicz et al. 2006).

4.2.7 Flux Control

Like other statins, atorvastatin also acts as a competitive inhibitor of the HMG-CoA reductase enzyme (Naoumova et al. 1997). It was therefore assumed that the inhibition of the HMG-CoA reductase enzyme obeys the following kinetic rate law:

$$r_{HR} = r_{max} \frac{c_s}{K_m\left(1+\frac{c_i}{K_i}\right)+c_s}. \tag{17}$$

Only the endoplasmic HMG-CoA pool was regarded as substrate c_s due to the predominant subcellular localization of the hepatic HMG-CoA reductase enzyme in this compartment (Keller et al. 1986; Mitropoulos et al. 1978). In the case of the atorvastatin-free reference experiment, equation (17) reduces to a simple Michaelis-Menten relation. In this context, given the identified flux through this enzyme at the steady state corresponding to 0 nM atorvastatin, r_{HR}^0, the maximum reaction rate r_{max} could be calculated by

$$r_{max} = \frac{r_{HR}^0 \left(K_m^0 + c_s^0 \right)}{c_s^0}. \tag{18}$$

Competitive inhibition is characterized by a constant maximum reaction rate r_{max}, whereas increasing inhibitor levels are accompanied by increasing apparent K_m values. Assuming a constant HMG-CoA reductase level, it was possible to calculate the apparent Michaelis constant corresponding to 50 nM of atorvastatin by

$$K_m^{50} = c_s^{50} \left(\frac{r_{max}}{r_{HR}^{50}} - 1 \right). \tag{19}$$

With respect to the apparent K_m value, the response coefficient $R_{K_m}^{J_i}$ of flux J_i can be approximated by

$$R_{K_m}^{J_i} = \frac{\partial J_i}{\partial K_m} \frac{K_m^0}{J_i^0} \approx \frac{\Delta J_i}{\Delta K_m} \frac{K_m^0}{J_i^0} = \frac{\left(J_i^0 - J_i^{50} \right)}{\left(K_m^0 - K_m^{50} \right)} \frac{K_m^0}{J_i^0} \tag{20}$$

Finally, by exploiting the partitioned response relation (Hofmeyr 2001), the corresponding flux control coefficient was calculated by

$$C_{HR}^{J_i} = \frac{R_{K_m}^{J_i}}{\varepsilon_{K_m}^{HR}} \tag{21}$$

where $\varepsilon_{K_m}^{HR}$ is the scaled elasticity coefficient of the HMG-CoA reductase enzyme, at the reference steady state with respect to the apparent K_m value, i.e.

$$\varepsilon_{K_m}^{HR} = \frac{\partial r_{HR}}{\partial K_m} \frac{K_m^0}{r_{HR}^0} = \frac{-\left(r_{max} c_s^0 \right)}{\left(K_m + c_s^0 \right)^2} \frac{K_m^0}{r_{HR}^0}. \tag{22}$$

4.3 Results and Discussion

4.3.1 Labeling Dynamics

Figure 8 shows time courses of the isotopic enrichment of 3-phosphoglycerate mass fractions after administration of 0 nM and 50 nM atorvastatin. Under both experimental setups, isotopic steady state was reached quickly after adding the tracer to the culture media. This was also reflected in all other central carbon intermediates (cf. Appendix C). After subjecting the cells to labeled glutamine at time t = 0 h, the m+0 mass fraction dropped rapidly. In the case of 0 nM atorvastatin, however, the m+0 mass fraction of 3-phosphoglycerate converged to 0.58, whereas in the case of 50 nM it converged to 0.48. Consequently, the other mass fractions were higher when the drug was administered. Nevertheless, for both physiological states, the simulated mass fractions were in accordance with the measured data.

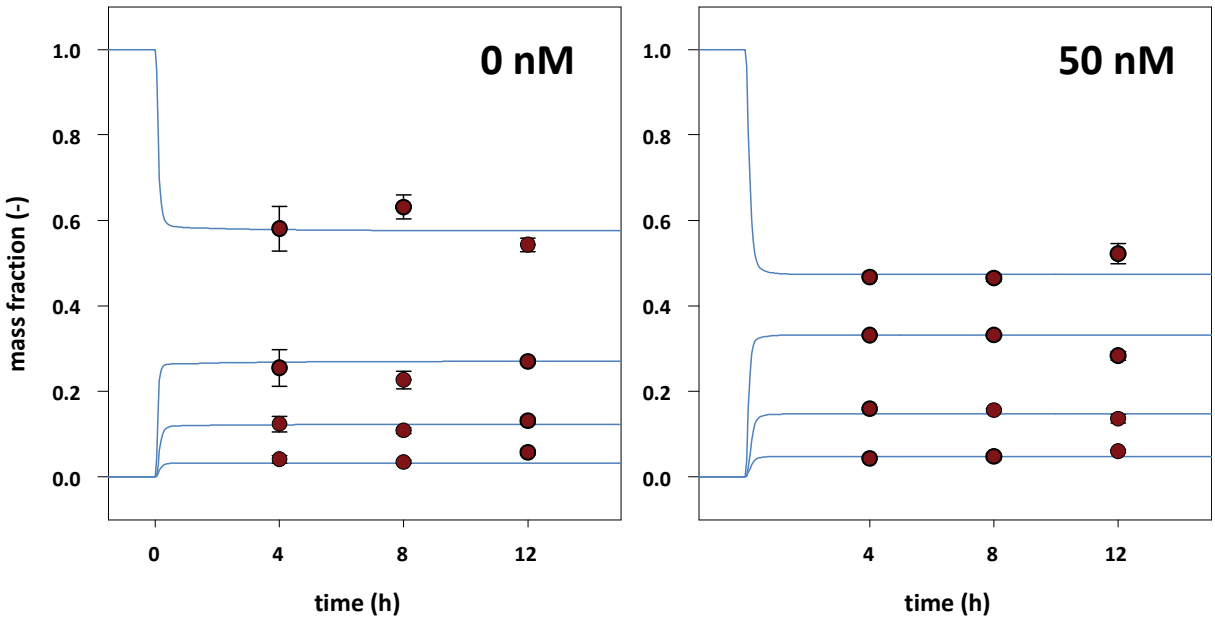

Figure 8. Experimentally determined (red circles) and simulated (blue solid lines) mass fractions of 3-phosphoglycerate after administration of 0 nM (left) and 50 nM (right) atorvastatin. The error bars indicate standard deviations of the experimental data.

Similarly, Lindenthal et al. applied mass spectrometry and ISA to investigate human cholesterol synthesis (Lindenthal et al. 2002). Constant precursor enrichment was observed within 4 h after infusing 1-^{13}C-acetate into the duodenum of human volunteers. In addition, Lindenthal et al. found that lipophilic simvastatin increased the acetate precursor enrichment in HepG2 cells and tended to do so in rat liver slices (Lindenthal et al. 2002). In contrast, administration of atorvastatin had no effect on the labeling distribution in the cytosolic and mitochondrial acetyl-CoA pools in primary rat hepato-

cytes. However, in the present study a physiological concentration of 50 nM atorvastatin was applied whereas Lindenthal et al. used 0.07 µM and 0.28 µM simvastatin.

In the case of cholesterol pathway intermediates, the situation was completely different with respect to isotopic stationarity. This is exemplified in Figure 9 for selected time profiles of lathosterol mass fractions that were observed in the atorvastatin-free experiment. The depicted mass fractions did not reach isotopic steady state even within 12 h. This shows that it is necessary to observe the isotopic transient in order to identify metabolic fluxes in the cholesterol pathway of mammalian cells. The exceptional labeling dynamics of the m+1 mass fraction in relation to the other mass fractions, i.e. the increase of m+1, seemed to be out of sync, was due to antecedent heterocondensation reactions (condensation of acetyl-CoA and acetoacetyl-CoA, r24; condensation of C_{15}-farnesyl diphosphate and a virtual C_{12}-farnesyl diphosphate, r33). If the turnover rate of one condensing partner is higher than that of the other, its pool reaches isotopic steady state faster. Condensing such two intermediates allows for qualitatively different time profiles of the mass fractions of a subsequent intermediate. Different dynamics of lathosterol mass isotopomers have been observed previously in dog and rat hepatocytes (Bederman et al. 2004a; Bederman et al. 2004b).

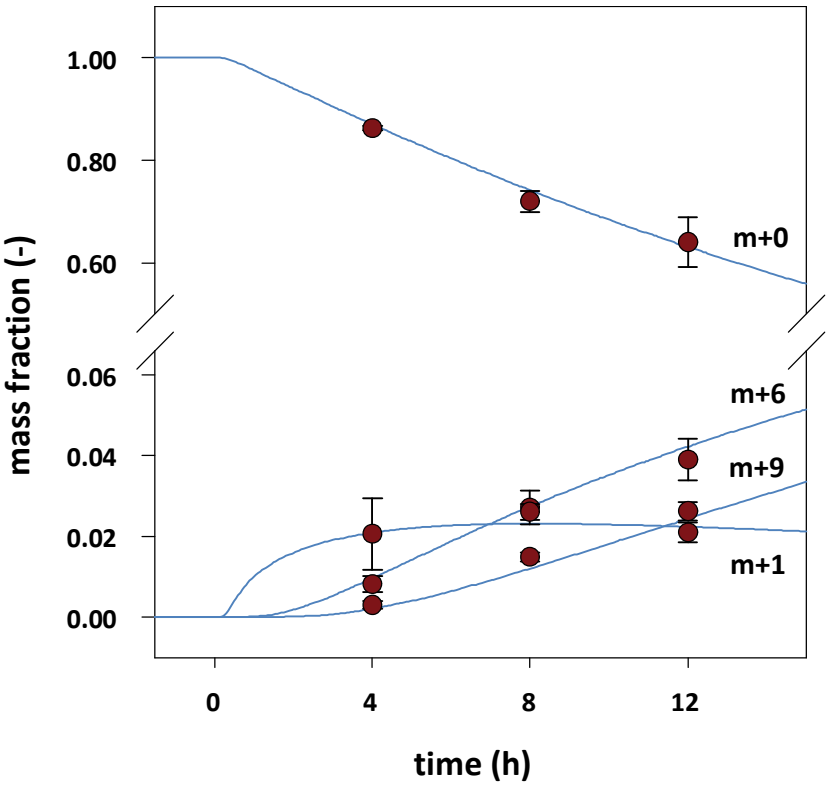

Figure 9. Simulated (blue solid lines) and measured (red circles) transient mass isotopomer fractions of lathosterol (0 nM atorvastatin). The error bars indicate standard deviations of the experimental data.

Figure 10 shows that the model predictions were consistent with the observed experimental data in the cholesterol pathway. Lathosterol was the intermediate used to exemplify this as it can be considered a marker for cholesterol synthesis (Kempen et al. 1988; Lindenthal et al. 2002). For the cells treated with 50 nM atorvastatin no substantial differences were observed between the mass isotopomer data after 8 h and 12 h. Thus, isotopic steady state was reached more quickly than in the atorvastatin-free experiment. 12 and 10 mass fractions could be experimentally resolved in the 0 and 50 nM atorvastatin time series data, respectively. The difference in the number of resolved mass fractions was due to the lower intracellular concentration in the atorvastatin-treated cells. The discrepancy in the m+2 mass fractions might result from the simplification of the condensation reactions in the applied isotopomer model, i.e. in the cell (i) dimethylallyl pyrophosphate is condensed with isopentenyl pyrophosphate to geranyl pyrophosphate, which is (ii) then condensed with yet another isopentenyl pyrophosphate molecule to farnesyl pyrophosphate. However, in the model, three 5-carbon molecules were directly condensed and the intermediary geranyl pyrophosphate was not taken into account.

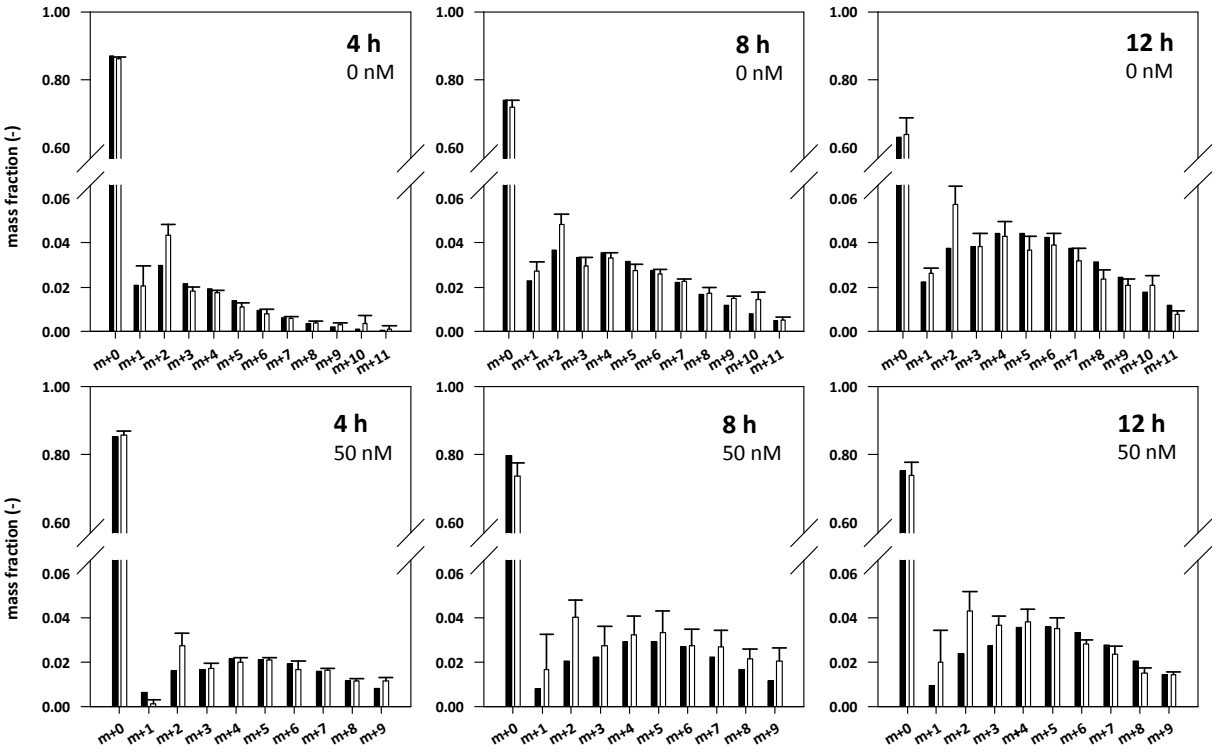

Figure 10. Experimentally determined (white) and simulated (black) mass fractions of lathosterol after administration of 0 nM (top) and 50 nM (bottom) atorvastatin. The different time points are depicted from the left to the right: 4 h (left), 8 h (center), and 12 h (right) after addition of the tracer. The error bars indicate the standard deviations of the experimental data.

In accordance with Des Rosiers et al. citrate was enriched in the m+5 mass fraction (cf. Figure 11), which is due to the reversal of the isocitrate dehydrogenase reaction (Des Rosiers et al. 1995). That is why, by setting up prospective isotopomer models, the common assumption about the irreversibility of this reaction in ^{13}C-based flux identification should be reassessed. The corresponding reversibilities, i.e. the ratios of the forward fluxes to the corresponding net fluxes (Maier et al. 2008a), were estimated as 69.3 and 81.6 for 0 nM and 50 nM atorvastatin, respectively. High exchange rates of the isoctriate dehydrogenase reaction have been reported previously for mammalian systems (Des Rosiers et al. 1995; Yoo et al. 2008). Similar or even higher reversibilities (up to 162.7) were estimated for r8 (aconitate hydratase), r30 (HMG-CoA reductase), r31 (mevalonate-5-pyrophosphate decarboxylase) and r49 (exchange of cytosolic and non-balanced carbon dioxide) (cf. Appendix D).

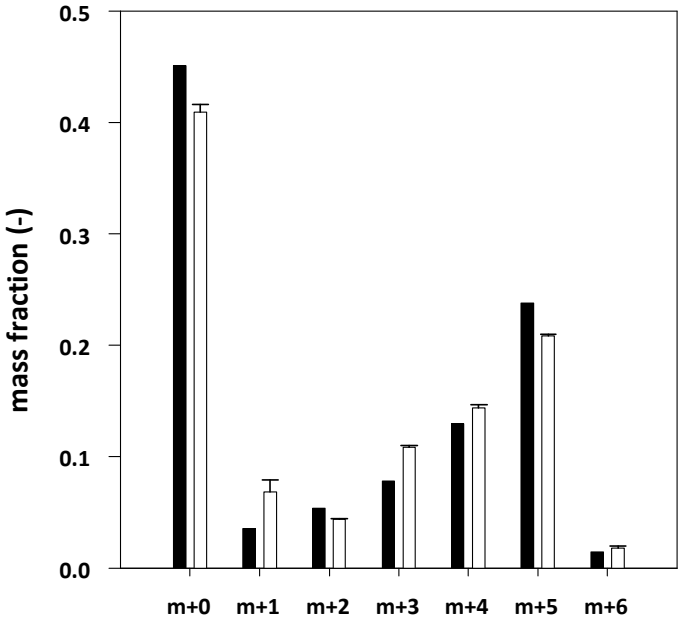

Figure 11. Experimentally determined (white) and simulated (black) mass fractions of citrate (0 nM atorvastatin), 12 h after adding the tracer. The error bars indicate standard deviations of the experimental data.

4.3.2 Flux Distribution

The experimentally determined extracellular rates are listed in Table 9. On average, each well contained $7.4 \cdot 10^5$ cells. An average cell volume of $5.9 \cdot 10^{-12}$ l was assumed in order to relate the estimated fluxes to the cellular volume (Wehner et al. 1995). The macroscopic rates (except for the ketone bodies, i.e. r21 and r22) that were determined in the atorvastatin-free reference experiment were used to constrain both the flux estimation from the 0 nM atorvastatin dataset and the flux estimation from the 50 nM atorvastatin dataset, respectively. This was feasible because on the one hand, the flux through the cholesterol pathway is smaller than the fluxes in the central carbon metabolism. On the other hand, side effects such as elevated liver enzyme levels (e.g. aminotrans-

ferases) are (i) rare, (ii) happen on a different timescale (weeks/months) and (iii) are often linked to high doses of atorvastatin (Chalasani 2005; Cohen et al. 2006). The rates r21 and r22, i.e. the exchange fluxes for acetoacetate and 3-hydroxybutyrate, were not adopted in the flux identification from the 50 nM atorvastatin dataset as the synthesis of ketone bodies is directly linked to the cholesterol pathway via the common intermediate HMG-CoA. In calculating the objective function (cf. equation (11)), discrepancies between estimated and experimentally determined extracellular rates were specifically penalized. Therefore, the model predictions were in very good accordance with the measured exchange rates. At 50 nM atorvastatin, the extracellular rates for the ketone bodies (r21 and r22) were higher than without atorvastatin. This is due to a decreased flux into the cholesterol pathway, which is accompanied by an increased ketone body synthesis rate. In contrast, Sato et al. showed that pravastatin led to reduced ketone body formation in diabetic rats due to an increased acetoacetyl-CoA synthetase activity (Sato et al. 2002). However, Sato et al. also found that control animals had much higher plasma ketone body levels following the administration of a hypocholesterolemic agent.

Table 9. Experimentally determined extracellular rates (0 nM atorvastatin). Rates and corresponding standard deviations are given in mmol/(l_{cv}·h).

Reaction	Rate
r21	3 ± 0.22
r22	4 ± 0.4
r43	42.7 ± 8.37
r44	12.4 ± 2.18
r45	3.7 ± 1.01
r46	1.2 ± 0.21
r47	12.1 ± 1.53
r50	0.13 ± 0.02
r51	0.02 ± 0.002
r52	0.5 ± 0.005
r53	0.05 ± 0.005

Figure 12 exemplifies the intracellular flux distribution in the central carbon metabolism in the absence of atorvastatin (0 nM). The differences in the central carbon net fluxes between the 0 nM and 50 nM atorvastatin datasets were mostly small (cf. Appendix D). According to the flux map, the labeling information needs to pass through several intracellular reactions and compartments before it enters the cholesterol pathway. The uniformly labeled glutamine was taken up by the cells and converted into glutamate. Glutamate was then transported into the mitochondria and converted into alpha-ketoglutarate. Subsequently, the labeling was transferred through the TCA cycle up to oxaloaceate, which was converted into (cytosolic) phosphoenolpyruvate and then into pyruvate. The labeling information was brought back into the mitochondria until it finally reached the HMG-CoA pool via acetyl-CoA and acetoacetyl-CoA. In a similar study, Yoo et al incubated brown adipocyte cells

in U-^{13}C-labeled glutamine and 5-^{13}C-labeled glutamine to quantify glutaminolysis and reductive carboxylation in the context of *de novo* fatty acid synthesis from glutamine (Yoo et al. 2008). They found that two thirds of the glutamine-derived alpha-ketoglutarate entering the TCA cycle were oxidized through succinate while the remainder traveled to citrate via reductive carboxylation, i.e. the net flux through the isocitrate dehydrogenase enzyme was inversed. In contrast, in rat hepatocytes the net flux through the isocitrate dehydrogenase was not inversed. Consistently, Young et al. and Yoo et al. reported pyruvate cycling with substantial fluxes through the reactions catalyzed by malic enzyme and pyruvate carboxylase in brown adipocytes (Yoo et al. 2008; Young et al. 2008). Jones et al. also observed hepatic pyruvate cycling through pyruvate carboxylase, phosphoenolpyruvate carboxykinase, and pyruvate kinase in a tracer study using U-^{13}C-glycerol in human volunteers (Jones et al. 2009). The primary rat hepatocytes analyzed in the present study did not exhibit pyruvate cycling, regardless of whether atorvastatin was administered or not. The flux through the pyruvate carboxylase was small compared to the fluxes through the pyruvate kinase and phosphoneolpyruvate carboxykinase. The phosphoenolpyruvate carboxykinase was found to be the most active cataplerotic enzyme.

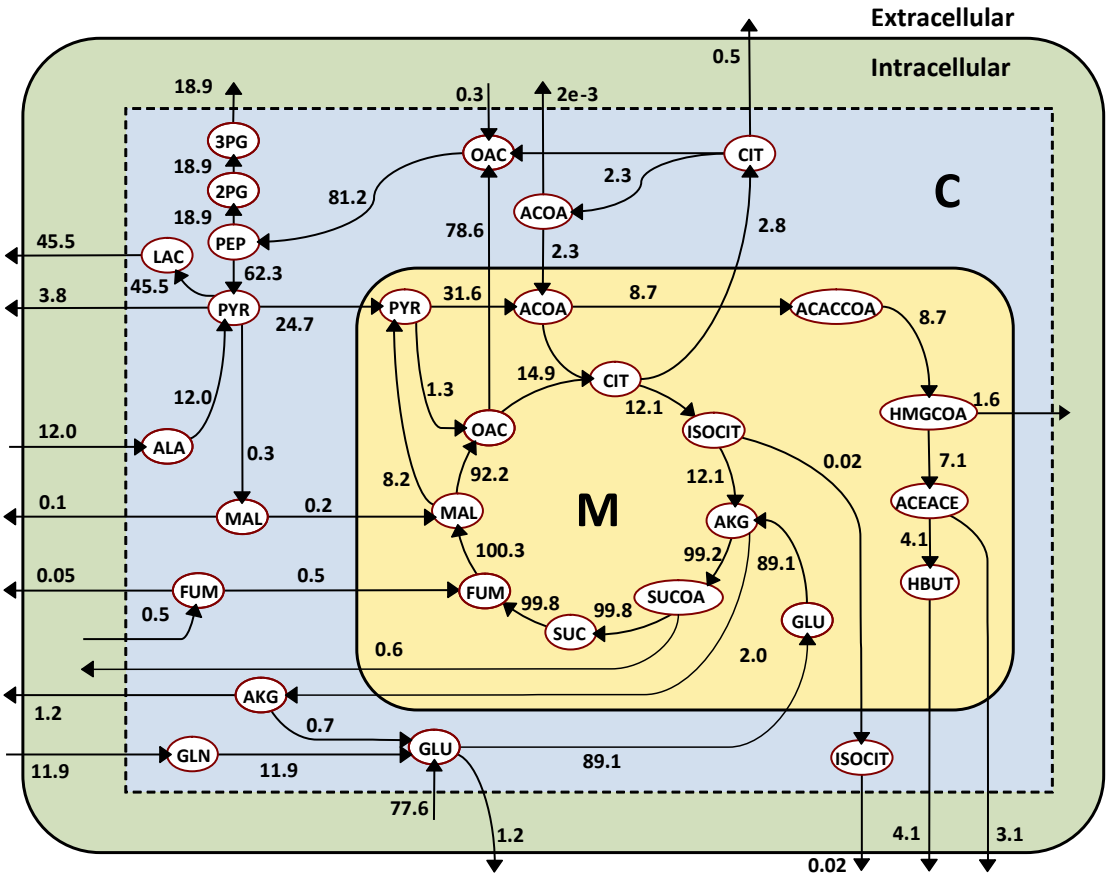

Figure 12. Central carbon fluxes of primary rat hepatocytes cultured in atorvastatin-free (0 nM) medium. All fluxes are given in mmol/(lcv·h). CO2, standard errors and some links were omitted for reasons of clarity (cf Appendix D). The illustrated network comprises two reaction compartments: cytosol (C) and mitochondrion (M). The dotted line indicates the control volume of the ^{13}C sub-network.

The primary rat hepatocytes performed gluconeogenesis. A gluconeogenic flux rate of 18.9 mmol/(l_{cv}·h) was estimated, which is in the same range as reported previously (Chan et al. 2003a). Extracellular glucose was monitored throughout the tracer experiment and remained constant at 2 g/l. However, neglecting any other efflux like nucleotide and lipid syntheses, the pentose-phosphate shunt, and glycogen storage, the estimated gluconeogenic flux would have resulted in a glucose secretion rate of 9.45 mmol/(l_{cv}·h). This would have increased the extracellular glucose level by less than 2 % in 12 h. In addition to this, the cells secreted large amounts of lactate (45.5 and 46.6 mmol/(l_{cv}·h)). Such overflow metabolism is a commonly observed phenomenon in cell culture systems (Doverskog et al. 1997). Furthermore, the model predicted a significant flux from outside the system into the cytosolic glutamate pool (77.6 mmol/(l_{cv}·h)). During the labeling experiment, however, even a small glutamate release rate of 1.2 mmol/(l_{cv}·h) was observed. This means that the glutamate influx stemmed exclusively from intracellular sources. Glutamate is a key intermediate in the central carbon metabolism that plays an important role in the degradation and/ or transamination of various amino acids. At the same, time the model predicts high exchange rates between (i) non-balanced uniformly-labeled glutamine outside the system boundary and cytosolic glutamine and between (ii) cytosolic glutamine and glutamate. That is why high labeling degrees can be observed for example for alpha-ketoglutarate (cf. Appendix D) despite the ratio of the absolute glutamate to glutamine influxes.

In both physiological states investigated, the symmetrical TCA intermediates succinate and fumarate were transferred orientation-conserved. In the case of 0 nM (50 nM) atorvastatin, 96.0 % (96.0 %) and 92.0 % (85.3 %) of the total flux were channeled through the succinate dehydrogenase and fumarate hydratase reactions, respectively. Channeling was previously observed in the TCA cycle in colon carcinoma (Malaisse et al. 1996) and heart cells (Sherry et al. 1994).

The flux distribution in the cholesterol pathway is detailed in Figure 13. The administration of the hypolipidemic drug resulted in a drop in the cholesterol synthesis rate from 0.27 mmol/(l_{cv}·h) to 0.08 mmol/(l_{cv}·h). In the absence of atorvastatin, roughly 78 % of the pathway flux was transferred through the cholesta-8-en-3β-ol, lathosterol, and 7-dehydrocholesterol pools. In contrast, when the drug was administered, only slightly more than half of the influx into the pathway was transferred via these three pools. The corresponding flux dropped from 0.21 mmol/(l_{cv}·h) to 0.045 mmol/(l_{cv}·h), whereas the flux through the cholesta-7,24-dien-3β-ol, 7-dehydrodesmosterol, and desmosterol pools decreased only from 0.056 mmol/(l_{cv}·h) to 0.035 mmol/(l_{cv}·h). This finding can be explained by a kinetic effect: At least one of the corresponding reactions converting zymosterol via cholesta-7,24-dien-3β-ol, 7-dehydrodesmosterol, and desmosterol to cholesterol (r37 - r39 and r41) is almost saturated, i.e. in the range of zeroth-order.

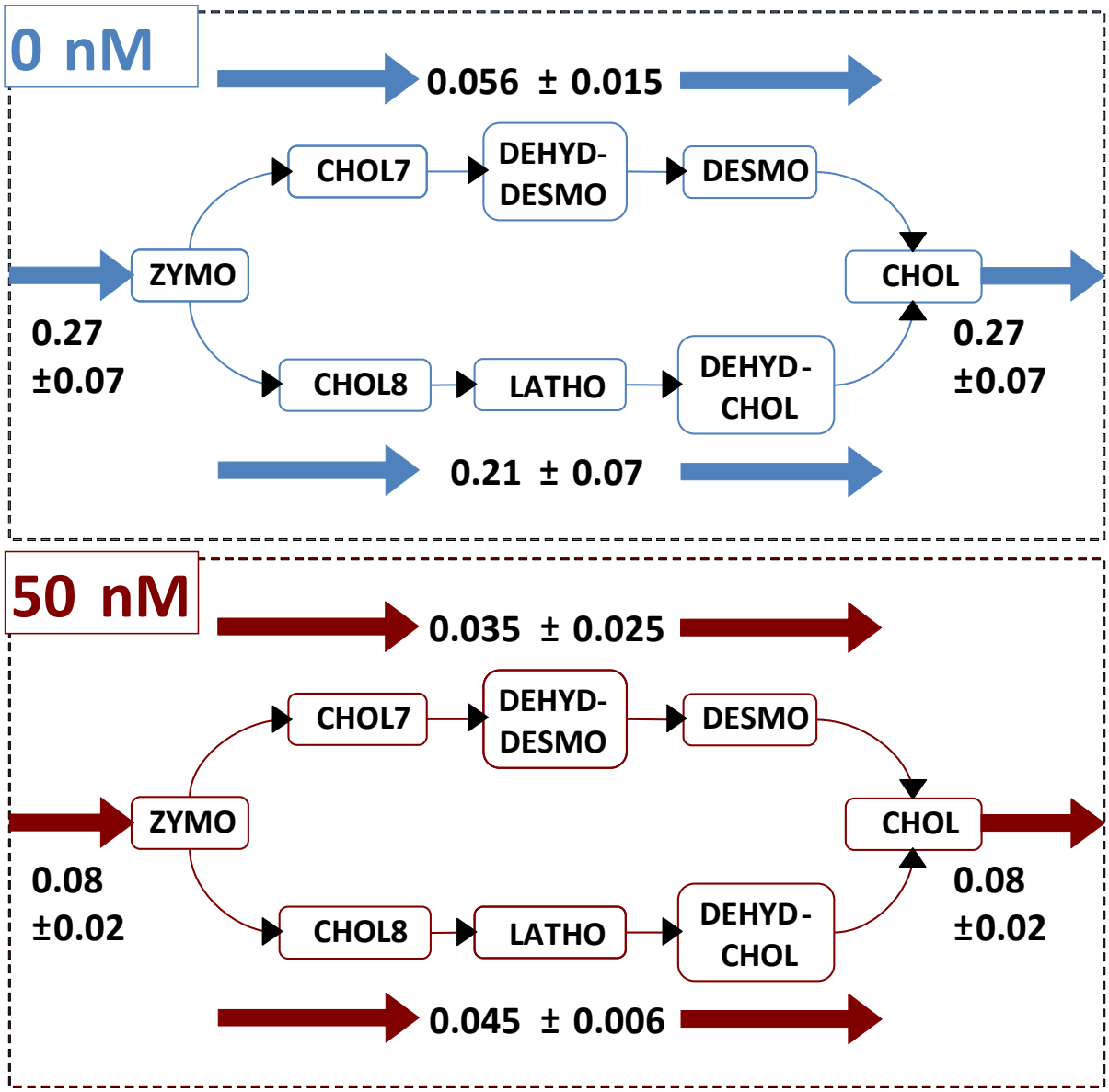

Figure 13. Metabolic fluxes in the cholesterol pathway. Shown are the fluxes corresponding to 0 nM (top) and 50 nM atorvastatin (bottom). All fluxes are given in mmol/(l_{cv}·h). The reactions are localized in the endoplasmic reticulum. Abbreviations used: ZYMO, zymosterol; CHOL7, cholesta-7.24-dien-3β-ol; DEHYDDESMO, 7-dehydrodesmosterol; DESMO, desmosterol; CHOL8, cholesta-8-en-3β-ol; LATHO, lathosterol; DEHYDCHOL, 7-dehydrocholesterol; CHOL, cholesterol;

4.3.3 Metabolite Levels

The experimentally observed intracellular intermediate levels are listed in Table 10. The only metabolites that were quantified in atorvastatin-treated cells were lathosterol (0.003 mmol/(l_{cv}·h)) and cholesterol (4.7 mmol/(l_{cv}·h)). While the cholesterol pool did not show a significant change, the lathosterol pool was reduced by roughly 87 %. This was reflected by the model predictions. In the case of cholesterol, one has to bear in mind that most of the cellular cholesterol is located in the plasma membrane (> 99 %) (Lange et al. 2004), which falsifies the experimental observations as the applied extraction method does not discriminate membrane-bound cholesterol from free cholesterol

but extracts membrane-bound cholesterol just as well. For this reason, lathosterol is the most suitable choice for analyzing the effects of the drug on cholesterol synthesis. The time constant for the lathosterol pool was calculated as the ratio between the (measured) pool size and the total influx into that pool (Zhao et al. 2008). As the concentration decrease was more pronounced than the decrease in the respective metabolic flux, the time constant dropped from 6.2 min to 4.6 min. That is why, notwithstanding the distinct differences in the predicted metabolic fluxes, the differences between the 0 nM and 50 nM atorvastatin datasets in the observed labeling dynamics in the lathosterol pool (cf. Figure 10) were moderate. However, as shown above, after administering the hypolipidemic drug, isotopic steady state was reached more quickly in the lathosterol pool. In contrast, Lindenthal et al. observed decreased fractional enrichment in HepG2 cells and rat liver slices after statin treatment (Lindenthal et al. 2002). Importantly, Lindenthal et al. started sampling directly after perturbing the cells with the hypolipidemic drug whereas in the present study the statin-treated primary rat hepatocytes were cultured overnight in 50 nM atorvastatin to ensure equilibration.

Table 10. Experimentally determined intracellular metabolite concentrations (mmol/(l_{cv}·h)).

Metabolite	Experimentally Determined 0 nM Atorvastatin
ISOCIT	0.01 ± 0.00003
CIT	1.49 ± 0.41
AKG	1.51 ± 0.58
FUM	0.25 ± 0.04
MAL	1.3 ± 0.31
PYR	0.93 ± 0.18
ACEACE	0.24 ± 0.07
HBUT	0.44 ± 0.1
CHOL	5.35 ± 0.59
DESMO	0.003 ± 0.001
LATHO	0.022 ± 0.006

The estimated fractional amounts ϕ_j of the non-determined mass fractions in the lathosterol and cholesterol pools (cf. equation (14)) were all lower than 1.9 % of the total mass. Furthermore, the corresponding sensitivities were very low, resulting in large standard errors of more than 1e+3 %, i.e. the simulation of the labeling dynamics seemed to be merely responding to these parameters.

4.3.4 Flux Control

With regard to metabolic control analysis, transient ^{13}C-based flux identification is more advantageous than the traditional isotopic steady-state-based metabolic flux estimation, as it delivers both steady state fluxes and metabolite levels. The estimated endoplasmic reticulum HMG-CoA levels amounted to 172.5 ± 40.8 µmol/l_{ER} and 116.0 ± 23.6 µmol/l_{ER} in the cases of 0 nM and 50 nM ator-

vastatin, respectively. Assuming an apparent K_m of 21.5 µM (Heller and Gould 1974), a maximal reaction rate of 1.79 mM/h was deduced. This means that the enzyme was operating at 89 % of its maximal rate (cf. Figure 14). After increasing the extracellular atorvastatin level to 50 nM, the apparent K_m increased to 317.8 µM, i.e. the operating point of the enzyme shifted from a nearly saturated to a non-saturated state. The observation that the non-inhibited HMG-CoA reductase enzyme was almost saturated illustrates why this enzyme is an adequate target for controlling endogenous cholesterol synthesis by (i) feedback control (Gibbons 2003) or (ii) hypolipidemic drugs such as e.g., statins. The scaled sensitivity of the HMG-CoA reductase reaction with respect to the Michaelis constant was determined as $\varepsilon_{K_m}^{HR}$ = -0.11.

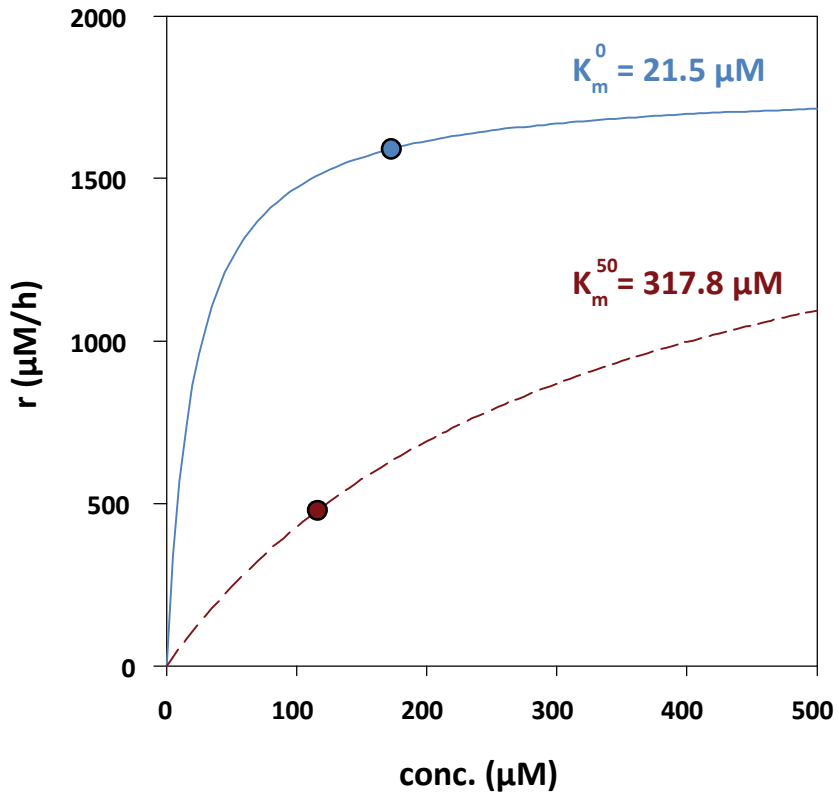

Figure 14. Reaction rates (cf. equation (17)) for 0 nM (solid line) and 50 nM (dashed line) atorvastatin. The highlighted reaction rates of 1.6 mM/h (black) and 0.5 mM/h (grey) denote the identified steady state fluxes for 0 nM and 50 nM atorvastatin at the corresponding estimated HMG-CoA levels in the endoplasmic reticulum.

In exploiting the partitioned response relation, the flux control coefficients with respect to the HMG-CoA reductase enzyme were calculated according to equation (21) (cf. Figure 15). As expected, the control of flux in the gluconeogenesis pathway (r1 - r5) and the TCA cycle (r6 - r14) barely depended on the HMG-CoA reductase enzyme. The reactions in the ketone bodies synthesis pathway (r19 - r24) showed moderate to negligible dependences on HMG-CoA reductase enzyme activity.

Larger flux control coefficients were observed in the anaplerotic/cataplerotic section. The applied metabolic network model, however, took into account both cytosolic (r27) and mitochondrial (r28) malic enzymes (Crow et al. 1982; Wiseman et al. 1991). This redundancy might possibly result in partial non-identifiability, which would explain the large flux control coefficients that were predicted for the cytosolic (r27) and mitochondrial (r28) isoforms. In addition, large (r30 - r36, r40 and r42) and moderate (r37 - r39 and r41) control coefficients were observed within the cholesterol pathway. The moderate flux control coefficients resulted from the aforementioned kinetic effect. This means that (at least) one of the corresponding enzymes seemed to be saturated. Enzyme saturation may also explain why the control exerted by the HMG-CoA reductase enzyme is smaller in this part of the cholesterol pathway. Nonetheless, the observation that (i) the majority of the flux entering the cholesterol pathway in the non-inhibited state was channeled through the cholesta-8-en-3β-ol, lathosterol, and 7-dehydrocholesterol pools (cf. Figure 13), and that (ii) the HMG-CoA reductase operated near to saturation render this enzyme a perfect target for regulating endogenous cholesterol synthesis. This is exploited *in vivo* by controlling the flux through the HMG-CoA reductase enzyme by phosphorylation and dephosphorylation (Clarke and Hardie 1990), regulated degradation (McGee et al. 1996), and regulated transcription (Espenshade 2006). In the context of inter-compartmental exchange fluxes, large control coefficients were observed for r54 (acetyl-CoA; cytosol $\rightleftharpoons$ non-balanced) and r61 (alpha-ketoglutarate; cytosol $\rightleftharpoons$ mitochondrion). In case of r54, the corresponding flux estimates were affected by high degrees of uncertainty, i.e. standard errors that were greater than 30 % of the predicted flux value. The increase in r61, though, was compensated for by an equivalent decrease in the r64 reaction (glutamate; cytosol $\rightleftharpoons$ mitochondrion). The large flux control coefficient estimates for the r62 (fumarate; cytosol $\rightleftharpoons$ mitochondrion) and r63 (malate; cytosol $\rightleftharpoons$ mitochondrion) reactions are probably explained by the fact that the urea cycle was not taken into account in the metabolic network model.

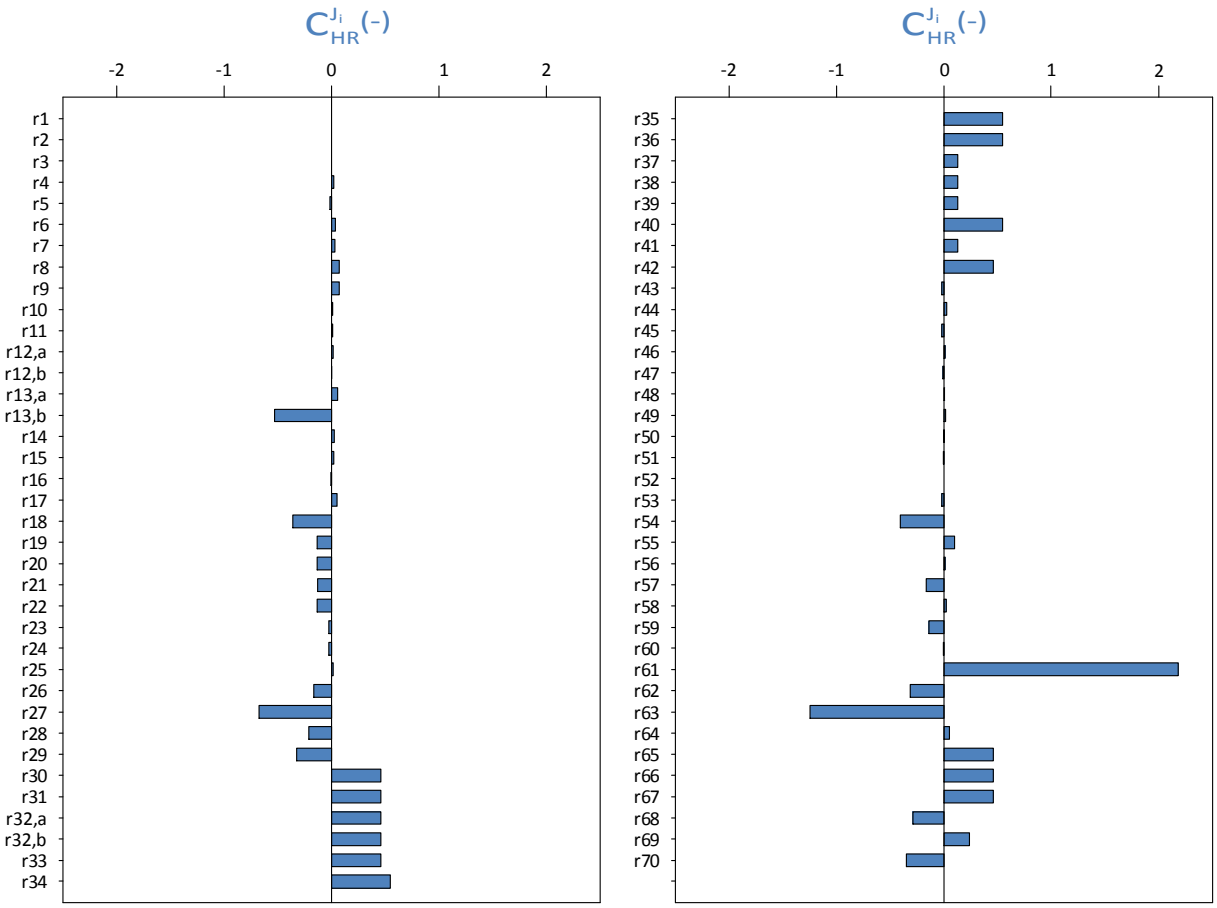

Figure 15. Flux control coefficients $C^{J_i}_{HR}$ with respect to the HMG-CoA reductase enzyme.

4.4 Conclusions

Metabolic fluxes were identified in two physiological states in (i) the cholesterol pathway and (ii) the central carbon metabolism in primary rat hepatocytes. Flux estimation was based on a compartmented isotopomer model that comprised both positional and mass isotopomer mass balances.

In the central carbon metabolism, the isotopic enrichment became steady even before the first sampling point after 4 h. In contrast, in the atorvastatin-free labeling experiment no isotopic steady state was observed within 12 h in the cholesterol pathway. Therefore, taking into account the isotopic transient proved to be a necessary condition for flux identification in this pathway – at least in mammalian cell systems.

Citrate was specifically enriched in the m+5 mass fraction. In order to reproduce this isotopic enrichment *in silico*, it was mandatory to allow for a reversible mitochondrial isocitrate dehydrogenase reaction. Furthermore, the model enabled the prediction of the marked channeling of TCA intermediates. Label scrambling of the symmetrical TCA intermediates succinate and fumarate played only a minor part in primary rat hepatocytes.

Only minor differences were observed in the central carbon fluxes between cells treated with or without 50 nM atorvastatin. However, major differences were observed in the cholesterol pathway

where the flux decreased from 0.27 mmol/(l_{cv}·h) to 0.08 mmol/(l_{cv}·h) in response to the administration of the hypolipidemic drug. The flux through the cholesta-8-en-3β-ol, lathosterol, and 7-dehydrocholesterol pools was found to be more affected than the flux through the cholesta-7,24-dien-3β-ol, 7-dehydrodesmosterol, and desmosterol pools. This finding was attributed to a kinetic effect. The isotopomer approach applied in this study allowed for a more detailed investigation of statin effects on the cholesterol pathway than previous ISA and MIDA based analyses.

In the non-inhibited state, the HMG-CoA reductase enzyme operated in the zeroth order regime. The addition of the competitive inhibitor atorvastatin led to an increase in the enzyme's apparent K_m value from 21.5 µM to 317.8 µM. Furthermore, in exploiting the partitioned response relation, flux control coefficients were determined with respect to infinitesimal changes in the HMG-CoA reductase concentration, which enabled the quantification of the control of the HMG-CoA reductase over the cholesterol pathway and the central carbon metabolism. In summary, the characteristics that render this enzyme an effective target for controlling endogenous cholesterol synthesis are (i) the saturation of the HMG-CoA reductase enzyme and (ii) the distinct level of control the enzyme exerts over the flux through the cholesterol pathway. Transient ^{13}C-based flux identification turned out to be a particularly suitable approach for such analyses as it delivers both intracellular fluxes and intermediate concentrations. According to the summation theorem of flux control coefficients, the sum over all flux control coefficients is equal to unity for each reaction (Hofmeyr 2001). The flux control coefficient of the HMG-CoA reductase over the reaction catalyzing the cholesterol efflux was 0.46. This means that the HMG-CoA reductase does not completely control cholesterol synthesis. Other enzymes might be potent targets for lowering cholesterol synthesis with hypolipidemic drugs as well.

5

Dynamics and Control of the Central Carbon Metabolism in Hepatoma Cells

Chapter Outline

5.1 Introduction 69
5.2 Material and Methods 72
5.2.1 Experimental Setup 72
5.2.2 Model Reconstruction 72
5.2.3 Model Simulation and Parameterization 76
5.2.4 Systems-Level Analyses 79
5.3 Results and Discussion 80
5.3.1 *In Vivo* and *In Silico* Metabolite Dynamics 81
5.3.2 Glycolysis Control 83
5.3.3 Control of the Pentose Phosphate Pathway 89
5.3.4 Control of the Tricarboxylic Acid Cycle 89
5.3.5 Control of Lactate Dehydrogenase, NADPH Consumption, and Oxidative Phosphorylation 93
5.3.6 Concentration Control over NADPH, NADH, ATP, and NAD 96
5.3.7 Partial Internal Response Coefficients 98
5.4 Conclusions 102

Parts of this chapter are submitted to BMC Systems Biology

Abstract

The liver plays a major role in metabolism and performs a number of vital functions in the body. Therefore, the determination of hepatic metabolite dynamics and the analysis of the control of the respective biochemical pathways are of great pharmacological and medical importance. Extra- and intracellular time-series data from stimulus-response experiments are gaining in importance in the identification of *in vivo* metabolite dynamics while dynamic network models are excellent tools for analyzing complex metabolic control patterns. This is the first study that has been undertaken on the data-driven identification of a dynamic liver central carbon metabolism model and its application in the analysis of the distribution of metabolic control in hepatoma cells.

Dynamic metabolite data were collected from HepG2 cells after they had been deprived of extracellular glucose. The concentration of 25 extra- and intracellular intermediates was quantified using HPLC, LC-MS-MS, and GC-MS. The *in silico* metabolite dynamics were in accordance with the experimental data. The central carbon metabolism of hepatomas was further analyzed with a particular focus on the control of metabolite concentrations and metabolic fluxes. It was observed that the enzyme glucose-6-phosphate dehydrogenase exerted substantial negative control over the glycolytic flux, whereas oxidative phosphorylation had a significant positive control. The control over the rate of NADPH consumption was found to be shared between the NADPH-demand itself (0.65) and the NADPH supply (0.38).

Based on time-series data, a dynamic central carbon metabolism model was developed for the investigation of new and complex metabolic control patterns in hepatoma cells. The systems-oriented identification of metabolite dynamics is a first step towards the genome-based assessment of potential risks posed by nutrients and drugs.

The chemical analyses were coordinated by Ute Hofmann and are described in the paper submitted to BMC Systems Biology.

5.1 Introduction

Dynamic network models of the hepatic metabolism enable quantitative systems-level analyses of (i) detailed metabolic control patterns, (ii) metabolic implications in liver cancer, and (iii) metabolic processes such as detoxification. Moreover, systems-oriented analyses of the dynamics and control of the central carbon metabolism in the liver are an important step on the avenue towards the personalized prognosis of drug actions and/or long-term effects. This will eventually lead to a reduction in potential side effects and healthcare costs as well as enabling quick, rational decisions to be made in the course of expensive drug discovery processes. However, due to the limitations of wet and dry lab procedures (Hold and Panke 2009; Jamshidi and Palsson 2008), model-based analyses of the liver metabolism have so far mainly focused on the identification of metabolic fluxes (Chan et al. 2003b; Hofmann et al. 2008; Lee et al. 2003; Maier et al. 2008a; Yarmush et al. 1999) and the coarse-grained quantification of the control of metabolic sub-networks (Ainscow and Brand 1999c; Groen et al. 1982; Melendezhevia et al. 1992; Torres et al. 1986). It is worth noting that the analysis of metabolic control patterns using dynamic network models enables a more detailed interpretation of the hepatic control distribution than could be achieved with top-down approaches. In the context of oxidative phosphorylation and the dynamic interplay of catabolism and anabolism, the cofactors NAD(H), NADP(H), ATP/ADP/AMP need to be taken into account by mass balances when analyzing the systems-level effect of the energy metabolism. However, for identifying network models time-series of cofactor concentrations have until now mainly been used in external approximation functions (Dräger et al. 2009; Magnus et al. 2006; Rizzi et al. 1997) rather than for predicting the effect of cofactor concentrations on metabolic fluxes and intermediate concentrations.

Several metabolic functions and processes are constantly and concurrently maintained in the liver, which is a complex organ performing a plethora of vital functions (Kuntz and Kuntz 2001). These functions include the biosynthesis of cholesterol and bile acids, the bilirubin-, porphyrin-, and carbohydrate metabolisms as well as the detoxification of xenobiotics. The detoxification metabolism, i.e. the phase I and phase II degradation of exo- and endogenous substances, is directly linked with the central carbon metabolism, as it relies on the adequate supply of precursors such as NADPH and UDP-glucuronide. Moreover, glucose homeostasis is another liver-specific task of major pharmaceutical and medical importance, and should not be analyzed without taking into account the central carbon metabolism (Berg et al. 2002). Liver cells have an important role in the metabolism of lipids. In the fed state, fatty acids are actively synthesized, esterified, and secreted into the bloodstream along with very-low-density lipoproteins (VLDL). During starvation fatty acids are degraded and ketone bodies are released (Berg et al. 2002). The human hepatoma-derived cell line HepG2 has retained several characteristic liver-specific metabolic functions, and is therefore regarded as an excellent means for examining the liver metabolism (Guo et al. 2006; Javitt 1990; Knowles et al. 1980).

Furthermore, HepG2 cells were derived from a hepatoblastoma carcinoma, and therefore facilitate the investigation of the effects of tumors on the hepatic metabolism.

When building a dynamic model, the enzyme kinetics can be either deduced from non-physiological *in vitro* measurements or from intracellular metabolite time-series data. Teusink et al. reconstructed a dynamic model of yeast glycolysis based on *in vitro* kinetics; the authors observed substantial differences between model-predicted and experimentally determined *in vivo* metabolite levels (Teusink et al. 2000). Therefore, Chassagnole et al. and Nikerel et al. advocate the use of *in vivo* metabolite time-series data for the identification of intracellular enzyme kinetics (Chassagnole et al. 2002; Nikerel et al. 2006). This creates the need for sophisticated procedures for (i) the quenching of the metabolism, (ii) the extraction of intracellular metabolites, and (iii) the absolute quantification of intermediate concentrations (Villas-Boas et al. 2005). Hofmann et al. succeeded in providing such procedures for quantifying central carbon metabolites in HepG2 cells (Hofmann et al. 2008). Luo et al. used liquid-chromatography mass spectrometry to quantify the intracellular metabolites in glycolysis, the pentose-phosphate pathway, and the tricarboxylic cycle in *Escherichia coli* (Luo et al. 2007). Schaub and Reuss investigated the *in vivo* dynamics of glycolytic intermediates in *Escherichia Coli* and showed the importance of growth rate-dependent metabolome analysis (Schaub and Reuss 2008). So far, transient metabolite data have mainly been used for deducing the kinetic parameters in dynamic models of metabolic pathways in prokaryotes and yeast. Rizzi et al. reconstructed a dynamic model of glycolysis and the tricarboxylic acid cycle in *Saccharomyces cerevisiae* (Rizzi et al. 1997). Enzyme kinetics were modeled with mechanistic rate equations and the kinetic parameters were identified in stimulus response experiments (Theobald et al. 1997). Chassagnole et al. used mechanistic rate equations and metabolite time-series data to build a dynamic model of the central carbon metabolism in *Escherichia coli* (Chassagnole et al. 2002). Kresnowati et al. exemplified the parameterization of a dynamic model based on linlog kinetics from artificial metabolite time-series data (Kresnowati et al. 2005). Magnus et al. applied linlog kinetics and intracellular intermediate measurements to model metabolite dynamics in the valine/leucine synthesis pathway in *Corynebacterium glutamicum* (Magnus et al. 2006).

The analysis of metabolic control provides a mathematical framework for quantifying the responses of fluxes and intermediate concentrations to changes in internal and external parameters such as nutrient and drug concentrations at the systems level (Heinrich and Rapoport 1974; Hofmeyr 2001; Kacser and Burns 1973; Visser and Heijnen 2002). Control coefficients determine the amount of control exerted on a flux or concentration at any step in a particular pathway. The control of the central carbon metabolism in the liver has been studied in cells isolated from fed rats using top-down methods (Ainscow and Brand 1999c). The reactions of the cell were grouped into nine blocks that were linked to each other by five intermediates. The control pattern observed quantified how the

sub-systems interacted with one another. Elasticities were determined experimentally using the multiple modulation approach. Subsequently, Ainscow and Brand used the elasticities and control coefficients to evaluate the mutual importance of internal regulatory pathways (Ainscow and Brand 1999a). In order to quantify the effect of a distinct block on the steady state flux through another block, the flux control coefficients were divided into partial flux control coefficients. Internal response coefficients were determined in order to assess the blocks that are most important in counteracting an increase in intermediate. The authors also investigated the effects of hormonal stimuli on rat hepatocytes by comparing the fractional changes in the fluxes and intermediate levels using the previously determined kinetics (Ainscow and Brand 1999b). Soboll et al. applied top-down methods to analyze the control distribution in oxidative phosphorylation, gluconeogenesis, ureagenesis, and ATP turnover in isolated perfused rat liver (Soboll et al. 1998). The authors observed different control patterns for the active and inactive states. By titration with a specific phosphorylase inhibitor (CP-91149), Aiston et al. found that the phosphorylase enzyme had substantial control over glycogen synthesis in rat hepatocytes (Aiston et al. 2001). The authors concluded that the phosphorylase enzyme is a promising target for controlling hyperglycaemia in type-2 diabetes, both in the absorptive and post-absorptive states. Groen et al. applied the double modulation method to determine the elasticities and flux control coefficients of the enzymes involved in the gluconeogenetic pathway in rat hepatocytes (Groen et al. 1986). The largest flux control coefficient was found for pyruvate carboxylase, regardless of whether glucagon was administered or not. In order to determine flux control coefficients as a function of the extracellular glucose level in rat hepatocytes, Meléndez-Hevia et al. set up a model that comprised the first three glycolytic enzymes (Melendezhevia et al. 1992). At physiological glucose concentrations, glucokinase exerted the greatest control over the glycolytic flux. These results were similar to experimental observations performed with rat liver homogenates. Sabate et al. reconstructed from literature data a dynamic model of the pentose-phosphate pathway in fasted rat hepatocytes (Sabate et al. 1995). A sensitivity analysis revealed that the metabolic fluxes were mainly regulated by the glucose-6-phosphate dehydrogenase and transketolase enzymes.

The objective of this study is to provide systems-level analyses of the dynamics and control of the central carbon metabolism in hepatoma cells. Transient extra- and intracellular intermediate concentrations were experimentally observed in HepG2 cells in a stimulus response experiment. The experimental data were then used to parameterize a dynamic network model of the hepatic central carbon metabolism. The reaction kinetics were approximated using canonical linlog kinetics. This approach yields a good approximation quality while only requiring the determination of comparatively few parameters (Hadlich et al. 2008; Heijnen 2005; Nikerel et al. 2006). Systems-level effects were deduced from the analysis of metabolic control. In contrast to previous analyses, the control patterns quantified the mutual influences of individual enzymes rather than describing how the sub-

systems interacted with each other. In other words, using a dynamic network model allows for a more detailed investigation of the underlying control principles. Internal regulatory pathways were further quantified by breaking up flux control coefficients into partial flux control coefficients. Internal response coefficients were investigated to assess system responses to changes in intermediates.

5.2 Material and Methods

5.2.1 Experimental Setup

HepG2 cells (ATCC® Number HB-8065™) were incubated at 37 °C in 6-well-plates in 5 % CO2 atmosphere. The cells were cultured in alanyl-glutamine-free William's medium E (PAN Biotech GmbH, Aidenbach, Germany) that was supplemented with penicillin (100 U/mL), streptomycin (100 mg/mL), and GibcoTM Insulin-Transferrin-Selenium (100X) supplement (Invitrogen, Karlsruhe, Germany). No fetal calf serum was added to the medium. The 6-well plates were shaken at 20 rpm throughout the experiment (Shaker DRS-12, ELMI, Riga, Latvia). The number of cells was determined with a Neubauer counting chamber. The intracellular flux map corresponding to this experimental setup was determined previously (Hofmann et al. 2008; Maier et al. 2008a). The main flux was found to be the conversion of glucose to lactate. Thus, for designing an efficient stimulus response experiment, the glucose flux was considered as the most promising candidate for perturbing the central metabolism of the hepatoma cells. However, the cells were grown in a batch culture, and extracellular glucose was provided in excess. Therefore, it was concluded that an extracellular glucose pulse would not yield essential changes, whereas glucose deprivation was expected to trigger a substantial metabolic response.

Before depriving the cells of extracellular glucose, they were treated as previously described (Hofmann et al. 2008): The overnight medium was replaced with fresh culture medium, which was then exchanged with glucose-free medium after 2 h of equilibration. Extra- and intracellular samples were collected in triplicate directly before and after the stimulus, as well as 1, 2, 5, 10, 30, 60, 120, and 180 min after glucose deprivation. The sampling approach and the processing of the samples were done as previously described (Hofmann et al. 2008).

5.2.2 Model Reconstruction

A metabolic network model was reconstructed for the identification of hepatic metabolite dynamics. The model was based on a previously published isotopomer model used for the estimation of intracellular fluxes from transient ^{13}C-labeling data (Maier et al. 2008a). The model accounts for 45 balanced compounds that are converted into each other by 49 reactions, including 5 transportation steps. The corresponding metabolic scheme is shown in Figure 16 and the complete reaction stoichiometry is listed in Table 11.

Table 11. Reaction stoichiometry of the dynamic network model. The subscripts 'ex', 'in', and 'nb' denote extracellular, intracellular, and non-balanced metabolites, respectively.

Reaction number	Enzyme name	Stoichiometry	
		Substrates	Products
r1	glucokinase	$GLC_{in} + ATP_{in}$	$G6P_{in} + ADP_{in} + H_{nb}$
r2	glucose-6-phosphate isomerase	$G6P_{in}$	$F6P_{in}$
r3	phosphofructokinase	$F6P_{in} + ATP_{in}$	$F16P_{in} + ADP_{in} + H_{nb}$
r4	fructose-bisphosphate aldolase	$F16P_{in}$	$DHAP_{in} + GAP_{in}$
r5	triose-phosphate isomerase	$DHAP_{in}$	GAP_{in}
r6	glyceraldehyde-3-phosphate dehydrogenase	$GAP_{in} + P_{nb} + NAD_{in}$	$13PG_{in} + NADH_{in} + H_{nb}$
r7	phosphoglycerate kinase	$13PG_{in} + ADP_{in} + H_{nb}$	$G3P_{in} + ATP_{in}$
r8	phosphoglycerate mutase	$G3P_{in}$	$G2P_{in}$
r9	pyruvate kinase	$PEP_{in} + ADP_{in} + H_{nb}$	$PYR_{in} + ATP_{in}$
r10	glucose-6-phosphate dehydrogenase	$G6P_{in} + NADP_{in}$	$GL6P_{in} + NADPH_{in} + H_{nb}$
r11	6-phosphogluconolactonase	$GL6P_{in} + H2O_{nb}$	$6PG_{in} + H_{nb}$
r12	phosphogluconate dehydrogenase	$6PG_{in} + NADP_{in}$	$RIBU5P_{in} + CO2_{nb} + NADPH_{in}$
r13	ribose-5-phosphate isomerase	$RIBU5P_{in}$	$RIBO5P_{in}$
r14	ribulose-phosphate 3-epimerase	$RIBU5P_{in}$	$XYL5P_{in}$
r15	transketolase	$RIBO5P_{in} + XYL5P_{in}$	$GAP_{in} + S7P_{in}$
r16	transketolase	$XYL5P_{in} + E4P_{in}$	$GAP_{in} + F6P_{in}$
r17	phosphopyruvate hydratase	$G2P_{in}$	$PEP_{in} + H2O_{nb} + H_{nb}$
r18	lactate dehydrogenase	$PYR_{in} + NADH_{in} + H_{nb}$	$LAC_{in} + NAD_{in}$
r19	adenosinetriphosphatase	$ATP_{in} + H2O_{nb}$	$ADP_{in} + P_{nb} + H_{nb}$
r20	alanine transaminase	$ALA_{in} + AKG_{in}$	$PYR_{in} + GLU_{in}$
r21	phosphoglucomutase	$G6P_{in}$	$G1P_{in}$
r22	nadph consumption	$NADPH_{in} + A_{nb}$	$NADP_{in} + AH_{nb}$
r23	glycogen synthesis	$UTP_{nb} + G1P_{in}$	$UDP_{nb} + Glycogen_{nb} + H_{nb}+PP_{nb}$
r24	transaldolase	$S7P_{in} + GAP_{in}$	$F6P_{in} + E4P_{in}$
r25	adenylate kinase	$ATP_{in} + AMP_{in}$	$2 \cdot ADP_{in}$
r26	glycerol synthesis	$DHAP_{in}$	$GLYCEROL_{nb}$
r27	nucleotide synthesis	$RIBO5P_{in} + ATP_{in}$	$NXP_{nb} + AMP_{in} + H_{nb}$
r28	serine synthesis	$G3P_{in} + NAD_{in} + GLU_{in} + H2O_{nb}$	$SER_{in} + P_{nb} + NADH_{in} + 2 \cdot H_{nb} + AKG_{in}$
r29	citrate synthase	$OAC_{in} + ACOA_{in} + H2O_{nb}$	$CIT_{in} + COA_{in} + H_{nb}$
r30	aconitate hydratase	CIT_{in}	$CISAC_{in} + H2O_{nb}$
r31	aconitate hydratase	$CISAC_{in} + H2O_{nb}$	$ISOCIT_{in}$
r32	isocitrate dehydrogenase	$ISOCIT_{in} + NAD_{in}$	$AKG_{in} + CO2_{nb} + NADH_{in}$
r33	succinate-CoA ligase	$SUCOA_{in} + P_{nb} + ADP_{in}$	$SUC_{in} + COA_{nb} + ATP_{in}$
r34	fumarate hydratase	$FUM_{in} + H2O_{nb}$	MAL_{in}
r35	malate dehydrogenase	$MAL_{in} + NAD_{in}$	$OAC_{in} + NADH_{in} + H_{nb}$
r36	pyruvate dehydrogenase complex	$PYR_{in} + NAD_{in} + COA_{nb}$	$CO2_{nb} + NADH_{in} + ACOA_{in}$
r37	alpha-ketoglutarate dehydrogenase complex	$AKG_{in} + NAD_{in} + COA_{nb}$	$SUCOA_{in} + CO2_{nb} + NADH_{in}$
r38	pyruvate synthesis	PYR_{nb}	PYR_{in}
r39	valine leucine isoleucine metabolism	$ISOVALMET_{nb}$	$SUCOA_{in}$
r40	succinate dehydrogenase	$SUC_{in} + 0.6 \cdot NAD_{in} + 0.2 \cdot O2_{nb}$	$FUM_{in} + 0.6 \cdot NADH_{in} + 0.6 \cdot H_{nb} + 0.4 \cdot H2O_{in}$

Table 11 (continued)

Reaction number	Reaction name	Stoichiometry	
		Substrates	Products
r41	oxidative phosphorylation	$NADH_{in}$ + 0.5·$O2_{nb}$ + 3.5·H_{nb} + 2.5·ADP_{in} + 2.5·P_{nb}	NAD_{in} + 3.5·$H2O_{nb}$ + 2.5·ATP_{in}
r42	alpha-ketoglutarate synthesis	AKG_{nb}	AKG_{in}
r43	malic enzyme	MAL_{in} + $NADP_{in}$	PYR_{in} + $CO2_{nb}$ + $NADPH_{in}$
r44	glutamate dehydrogenase	GLU_{in} + $H2O_{nb}$ + NAD_{in}	AKG_{in} + $NH4_{nb}$ + $NADH_{in}$ + H_{nb}
r45	lactate transport	LAC_{in}	LAC_{ex}
r46	pyruvate transport	PYR_{in}	PYR_{ex}
r47	glucose transport	GLC_{in}	GLC_{ex}
r48	alanine transport	ALA_{ex}	ALA_{in}
r49	serine transport	SER_{in}	SER_{in}

The Phosphoenolpyruvate carboxykinase enzyme was found to be inactive in the reference state (Maier et al. 2008a), and, thus, it was not included in the dynamic network model.

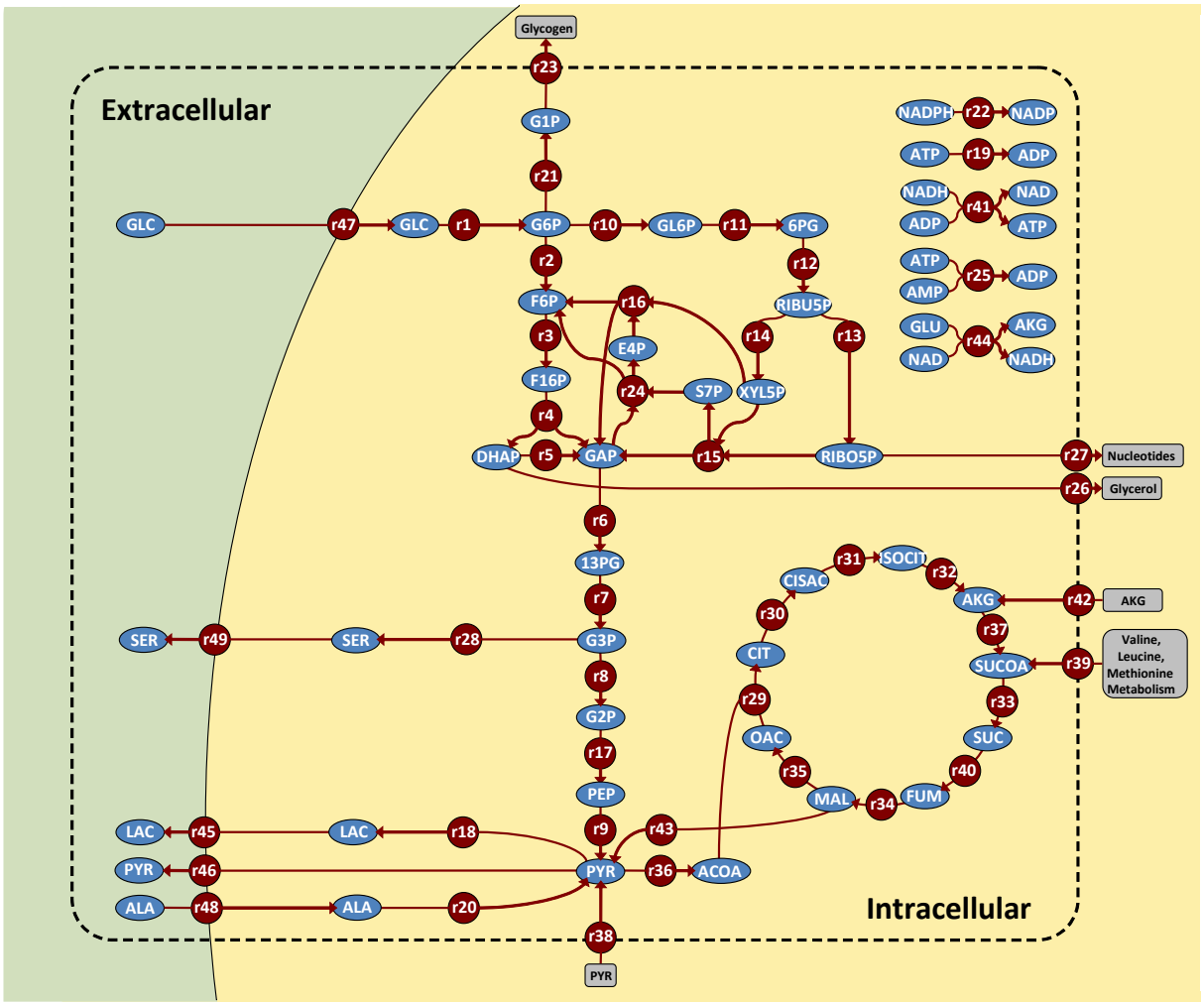

Figure 16. Metabolic network model. Extra- and intracellular metabolites are depicted with blue ellipses. Enzymatic reactions and transportation steps are indicated with red circles. Non-balanced compounds are shown within grey rounded rectangles. Directions of arrows reflect the direction of the steady state fluxes. The system boundary is indicated with a dashed line. Extra- and intracellular space are highlighted in green and yellow. Some links were omitted for reasons of clarity (cf. Table 11 for the complete reaction stoichiometry)

The metabolic pathways under consideration contain 3 conserved moieties ($c_{amp}+c_{adp}+c_{atp}$=const; $c_{nadp}+c_{nadph}$=const; $c_{nad}+c_{nadh}$=const). The model comprises glycolysis (EMP), the pentose-phosphate pathway (PPP), and the tricarboxylic acid (TCA) cycle. In the cataplerotic section, the malic enzyme, which decarboxylates malate to pyruvate, is taken into account. Reduced NADH is regenerated in the lactate dehydrogenase and oxidative phosphorylation reactions. P/O ratios of 2.5 and 1.5 were assumed for NADH and succinate, respectively (Hinkle 2005). Based on experimental evidence (Maier et al. 2008a), the metabolic state was assumed to be that of fed hepatic cells. Accordingly, no gluconeogenetic reactions were included. Exchange fluxes with the system boundary took into account glucose and alanine uptake, glycogen storage, the metabolism of glutamate, valine, leucine, and methionine, glycerol and nucleotide synthesis, as well as serine, lactate, and pyruvate excretion. In addition, reactions that represented ATP and NADPH consumption relating to the basal metabolism were included. 31 regulatory effects (21 inhibitions and 10 activations) were found in a literature search (Schomburg et al. 2002) and included (cf. Table 12). The network model discriminated 5 extracellular (glucose, lactate, serine, pyruvate, alanine) and 40 intracellular metabolites. The sampling and quenching routine used in this work did not allow discriminating between compartmental concentration differences and, thus, compartmentalization was not accounted for in the dynamic network model. However, it should be noted that the simulated metabolite dynamics in the TCA cycle represent average values integrating cytosolic and mitochondrial network dynamics. The metabolic pathways neither contained dead-end metabolites nor strictly detailed balanced sub-networks (Schuster and Schuster 1991). Furthermore, all reactions were consistent with respect to mass conservation and redox state. The stability of the dynamic model was investigated by calculating the eigenvalues of its Jacobian matrix (cf. sub-section 5.2.4 Systems-level Analyses). All real parts of the eigenvalues were found to be negative, which means that the system was asymptotically stable. It was important to demonstrate the asymptotic stability of the dynamic model with regard to the envisaged control analysis because in earlier studies it was seen that large-scale dynamic network models tended to be prone to instability (Magnus 2008).

Table 12. Activator and inhibitor influences. Regulatory influences and corresponding literature references. The modulator effects were included in the dynamic network model. In addition to these regulatory influences, the dynamic model did also account for substrate and product effects.

Enzyme Identifier	EC-Number	Activators	Inhibitors
glucokinase	2.7.1.2		F6P (Veiga-da-Cunha and Van Schaftingen 2002)
glucose-6-phosphate isomerase	5.3.1.9		6PG (Tsuboi et al. 1971)
6-phosphofructokinase	2.7.1.11	AMP (Berg et al. 2002)	CIT (Bloxham and Lardy 1973)
fructose-bisphosphate aldolase	4.1.2.13		ADP, ATP, E4P, F6P, G1P, G6P, RIBO5P (Bais et al. 1985)
triose-phosphate isomerase	5.3.1.1		ATP (Gracy 1975)
glyceraldehyde-3-phosphate dehydrogenase	1.2.1.12		ADP, ATP (Gregus and Nemeti 2005)
phosphoglycerate kinase	2.7.2.3		AMP (Scopes 1973)
pyruvate kinase	2.7.1.40	G6P, F6P, G1P (Staal et al. 1975), F16P (Dombrauckas et al. 2005)	ALA (Kahn and Marie 1982)
glucose-6-phosphate dehydrogenase	1.1.1.49		ATP (Cho and Joshi 1990)
phosphoglucomutase	5.4.2.2		F16P (Fazi et al. 1990)
UTP-glucose-1-phosphate uridylyltransferase	2.7.7.9		AMP (Stryer 1995)
alpha-ketoglutarate dehydrogenase	1.2.4.2	ADP (Gibson et al. 2000)	ATP (Gibson et al. 2000)
valine, isoleucine, methionine metabolism	-	NAD, AKG (Ogata et al. 1999)	GLU, NADH (Kanehisa and Goto 2000)
isocitrate dehydrogenase	1.1.1.41	ADP (Soundar et al. 2003)	
pyruvate dehydrogenase	1.2.4.1	AMP (Lazo and Sols 1980)	

5.2.3 Model Simulation and Parameterization

The following set of metabolite mass balances was set up to describe the time-dependent behavior of the metabolic system presented above:

$$\frac{d}{dt}\left(\frac{\mathbf{c}}{\mathbf{c}^0}\right) = \left(\mathbf{c}^0\right)^{-1} \cdot \mathbf{N} \cdot \mathbf{r} \,. \tag{23}$$

N denotes the stoichiometric matrix and **r** the rate vector. $\left(\mathbf{c}^0\right)$ is a square diagonal matrix with steady state concentrations on its main diagonal; $\left(\frac{\mathbf{c}}{\mathbf{c}^0}\right)$ denotes the normalized metabolite concentration vector.

The ordinary differential equations (ODEs) were reformulated as differential algebraic equations (DAEs) to improve both the performance and stability of the numerical integrations, i.e. the conservation relations were solved algebraically. The DAE system was simulated with the linearly implicit differential algebraic solver LIMEX (Deuflard et al. 1987). On average, one simulation run took 0.2 seconds (Intel® Core2™ Quad CPU, 2.66 GHz, 4 GB RAM).

Canonical linear-logarithmic (linlog) kinetics were applied for approximating the reaction rates in equation (23) (Visser and Heijnen 2003; Visser et al. 2004; Westerhoff and van Dam 1987). The linlog formalism has been used for modeling *in vivo* kinetics and metabolic redesign (Visser and Heijnen 2003). Linlog kinetics were shown to have a good approximation quality and to need only relatively few parameters to be identified (Hadlich et al. 2008; Heijnen 2005; Nikerel et al. 2006). In linlog kinetics, all rate equations share a standardized mathematical format in which influences of metabolite and effector levels on reaction rates are taken into consideration by adding up logarithmic concentration terms. The standardized format is advantageous if not all kinetic mechanisms are known in detail, which is often the case even for well-studied pathways of the central carbon metabolism (Bulik et al. 2009; Hold and Panke 2009). The matrix notation of the linlog rate equation is given by (Visser and Heijnen 2003)

$$\mathbf{r} = \mathbf{J}^0 \cdot \left(\frac{\mathbf{e}}{\mathbf{e}^0} \right) \cdot \left(\mathbf{i} + \mathbf{E}_c^0 \cdot \ln\left(\frac{\mathbf{c}}{\mathbf{c}^0} \right) \right) \tag{24}$$

in which $\mathbf{J}^0$ is the reference steady state flux distribution, $\left(\frac{\mathbf{e}}{\mathbf{e}^0} \right)$ is a diagonal matrix containing relative enzyme levels, and **i** is a vector of ones. $\mathbf{E}_c^0$ is a matrix whose entries are scaled elasticity coefficients ε_{ij} that describe the local effect of an infinitesimal change in concentration j on the rate of reaction i, i.e.

$$\varepsilon_{ij} = \left(\frac{\partial r_i}{\partial c_j} \right)^0 \cdot \frac{c_j^0}{r_i^0}. \tag{25}$$

Assuming constant enzyme levels, equation (24) can be reduced to

$$\mathbf{r} = \mathbf{J}^0 \cdot \left(\mathbf{E}_c^0 \cdot \ln\left(\frac{\mathbf{c}}{\mathbf{c}^0} \right) \right). \tag{26}$$

Parameterizing the kinetic model requires the specification of a reference steady state, i.e. $\mathbf{J}^0$ and $\mathbf{c}^0$, and the corresponding kinetic parameters, i.e. $\mathbf{E}_c^0$. Therefore, a two-step approach was applied. In a previous study $\mathbf{J}^0$ was estimated from transient ^{13}C-labeling data (Hofmann et al. 2008; Maier et al. 2008a). In the present study, $\mathbf{c}^0$ and $\mathbf{E}_c^0$ are determined from stationary and non-stationary me-

tabolite measurements. Each rate equation was assumed to be dependent on its substrate and product levels. In some instances additional effectors were taken into account; for details see Table 12. Altogether, 174 scaled elasticities had to be estimated. The matrix of scaled elasticity values is listed in Appendix E. Furthermore, 42 reference steady state intermediate levels had to be identified (42 balanced compounds + 3 conserved moieties). The corresponding experimental data were available for 30 of these. This means that 216 unknown parameters had to be specified in order to run a simulation.

At the outset of a simulation run, all intracellular metabolite levels $\frac{\mathbf{c}_{in}}{\mathbf{c}^0}(t=0)$ were set to 1.0. The initial values for the extracellular metabolites were determined by

$$\frac{\mathbf{c}_{ex}}{\mathbf{c}^0}(t=0) = \frac{\mathbf{c}_{ex}^{+}}{\mathbf{c}^0} \tag{27}$$

where $\mathbf{c}_{ex}^{+}$ denotes the extracellular metabolite levels immediately after the perturbation. The unknown elasticity coefficients and reference concentrations were identified by minimizing the differences between *in silico* model simulations and *in vivo* measurement data: The variance-weighted sum of squared residuals χ^2 between experimentally observed and simulated metabolite data, $\mathbf{c}^m$ and $\mathbf{c}^s$, was minimized according to

$$\min_{\mathbf{E}_c^0, \mathbf{c}^0} \chi^2\left(\mathbf{E}_c^0, \mathbf{c}^0\right) = \left(\mathbf{c}^s - \mathbf{c}^m\right)^T \cdot \boldsymbol{\Sigma}_m^{-1} \cdot \left(\mathbf{c}^s - \mathbf{c}^m\right) \tag{28}$$

in which $\boldsymbol{\Sigma}_m$ is a diagonal matrix containing the measurement variances. An evolution strategy was applied for parameter fine-tuning that included a self adapting mutation operator (Hansen and Ostermeier 2001; Streichert and Ulmer 2005). To enable a thorough exploration of the search space, the optimization runs were restarted after 100,000 evaluations of equation (28) using the best parameters currently available as starting values in the following iteration. Altogether, more than six million simulation runs were performed.

No confidence limits were calculated for the estimated parameters. For parameter estimation, however, a multi-start optimization approach was taken and the distribution of control was consistently determined from the parameters estimated and, thus, was considered to be reliable. It is worth noting that in an exploratory study, Nikerel et al. investigated the identification of kinetic parameters in a dynamic model based on linlog kinetics, and found that the underlying control structures were inherently robust against non-identifiable elasticities (Nikerel et al. 2006). Moreover, due to the substantial nonlinearities of the dynamic network model, methods based on linearization, like e.g. the inversion of the Fisher information matrix (FIM), are inadequate, whereas Monte-Carlo-

based approaches would be most suitable to determine the confidence ellipsoids. However, Monte-Carlo methods are computationally too demanding for the outlined model complexity.

5.2.4 Systems-Level Analyses

In this study, the local stability of the biochemical system was investigated by analyzing the eigenvalues of its Jacobian matrix $\mathbf{J}$ given by

$$\mathbf{J} = \mathbf{N}_R \cdot \mathbf{E}_c^0 \cdot \mathbf{L} \tag{29}$$

where $\mathbf{N}_R$ and $\mathbf{L}$ are the reduced stoichiometric matrix and link matrix, respectively (Hofmeyr 2001). A steady state is asymptotically stable if all real parts of the eigenvalues of the Jacobian matrix $\mathbf{J}$ are negative.

A metabolic control analysis was carried out to assess systemic steady state properties. In this context, the concentration control coefficient $C_{ij}^{c^0}$ determines the relative effect of changing enzyme level j on steady state concentration i, i.e.

$$C_{ij}^{c^0} = \left(\frac{\partial c_i}{\partial e_j} \right)^0 \cdot \frac{e_j^0}{c_i^0}. \tag{30}$$

Similarly, a flux control coefficient $C_{ij}^{J^0}$ describes the relative effect changing enzyme level j has on steady state flux i, i.e.

$$C_{ij}^{J^0} = \left(\frac{\partial J_i}{\partial e_j} \right)^0 \cdot \frac{e_j^0}{J_i^0}. \tag{31}$$

By applying the summation and connectivity theorems, the concentration and flux control coefficients can be calculated from the estimated elasticities and steady state concentrations (Visser and Heijnen 2003)

$$\mathbf{C}^{c^0} = -\mathbf{L} \cdot \left[\mathbf{N}_R \cdot \mathbf{E}_c^0 \cdot \mathbf{L} \right]^{-1} \cdot \mathbf{N}_R \tag{32}$$

and

$$\mathbf{C}^{J^0} = \mathbf{I} + \mathbf{E}_c^0 \cdot \mathbf{C}^{c^0}. \tag{33}$$

The control that one enzyme exerts over another is mediated by changes in the levels of intermediates. Enzymatic reaction rates respond to changes in substrate, product, and effector levels. The concept of a partial flux control coefficient allows the quantification of the fractions of the flux change in relation to changes occurring in individual intermediates (Ainscow and Brand 1999a; Holzhütter et al. 1985; Sauro 1990). Partial flux control coefficients can be obtained by partitioning flux

control coefficients. In accordance with equation (33), the flux control coefficient $C_{ij}^{J^0}$, which quantifies the change in steady state flux i with respect to changes in enzyme j, is given by

$$C_{ij}^{J^0} = \sum_{x=1}^{\text{all metabolites}} \varepsilon_{ix} \cdot C_{xj}^{c^0} + \begin{cases} 0 & \text{if } i \neq j \\ 1 & \text{if } i = j \end{cases}. \tag{34}$$

The individual summands $\varepsilon_{ix} \cdot C_{xj}^{c^0}$ are termed partial flux control coefficients. They partition the flux control coefficient through the changes in each intermediate, i.e. $\varepsilon_{ix} \cdot C_{xj}^{c^0}$ quantifies what fraction of the change in the flux through enzyme i can be attributed to the change in metabolite x. Initially, partial flux control coefficients were divided by the total flux control coefficient and referred to as conditional elasticities (Holzhütter et al. 1985) and partitioned regulatory coefficients (Sauro 1990). However, Ainscow and Brand pointed out that the normalization precludes easy comparison between partitioned terms of different flux control coefficients (Ainscow and Brand 1999a). Therefore, partial flux control coefficients were not scaled in the present study.

A stable system that operates at steady state will counteract changes in intermediate levels and eventually return to its original steady state (Ainscow and Brand 1999a). Elevated intermediate concentrations may be counteracted by a decrease in production and/or elevated consumption of these intermediates. By quantifying these effects, the partial internal response coefficients R_{ii}^{j} allow the assessment of their importance in restoring the steady state (Ainscow and Brand 1999a; Kahn and Westerhoff 1993), i.e.

$$R_{ii}^{j} = \varepsilon_{ji} \cdot C_{ij}^{c^0}. \tag{35}$$

According to the connectivity theorem the sum of the partial internal response coefficients for each intermediate is -1. For a given enzyme j and metabolite i, the internal response coefficient R_{ii}^{j} is identical to the partial flux control coefficient of the enzyme over itself (Ainscow and Brand 1999a). Graphically oriented network set-up, automated generation of the DAE system, and the quantification of metabolic control were performed with the Insilico Discovery software (Insilico Biotechnology AG, Stuttgart, Germany).

5.3 Results and Discussion

In the present study, a stimulus response experiment was performed with HepG2 cells. After growing HepG2 cells on a glucose-containing medium, they were incubated with fresh medium for two hours and then exposed to a medium lacking glucose. Metabolite time-series data were determined and used to parameterize a dynamic network model of the central carbon metabolism. The model takes into account 49 reactions (including 5 transportation steps) that convert 45 balanced compounds (40

intracellular and 5 extracellular metabolites). The metabolic network is depicted in Figure 16 and the reaction stoichiometry is listed in Table 11 (see also the model reconstruction in subsection 5.2.2).

The following paragraphs will focus on the concordance of the model simulations with the experimental data and on the application of the model for quantifying and interpreting the distribution of metabolic control.

5.3.1 *In Vivo* and *In Silico* Metabolite Dynamics

A total of 25 metabolite time courses were experimentally determined, of which 5 corresponded to extracellular metabolites and 20 to intracellular metabolites. The experimental data and the corresponding model simulations are summarized in Figure 17. In vivo and in silico data were normalized with respect to the estimated reference values. It is worth noting that the perturbation triggered significant changes in the metabolite levels, and these changes provided important information about the underlying network dynamics.

After exchanging the glucose-containing culture medium with the glucose-free medium, the extracellular glucose level dropped drastically. The remaining extracellular glucose was consumed by the cells within a period of 120 min. The extracellular pyruvate and lactate levels also dropped considerably because of the medium exchange, but started to accumulate again. At the end of the experiment, i.e. after 180 min the pyruvate values were even slightly higher than the estimated initial level. Lactate did not reach 50 % of its initial value, which was the result of a decreasing lactate secretion rate. The initial efflux rate was twenty times higher for lactate than for pyruvate. This means that, in absolute terms, still more lactate than pyruvate was produced during the experiment. Extracellular alanine was consumed throughout the experiment, while extracellular serine accumulated. It is worth noting that besides the lack of glucose, the system was also perturbed as a result of the changes occurring in the extracellular pyruvate, lactate, alanine, and serine levels.

In accordance with the extracellular glucose levels, the intracellular glucose pool also decreased steeply. HepG2 cells have high GLUT2 transporter activities (Wu et al. 2009). The GLUT2 transporter, which has a large K_m value, facilitates the diffusion of glucose into or out of the cells (Thorens 1996). It can therefore be assumed that the steep decrease in the intracellular glucose pool was the result of the diffusion of intracellular glucose into the extracellular space. Consistently, the model simulations showed that the flux of glucose uptake was inversed immediately after the stimulus occurred. The intracellular glucose concentration further decreased and eventually converged to zero. All other glycolytic metabolite levels except for phosphoenolpyruvate and pyruvate decreased sharply immediately after the stimulus and continued to gradually decrease thereafter.

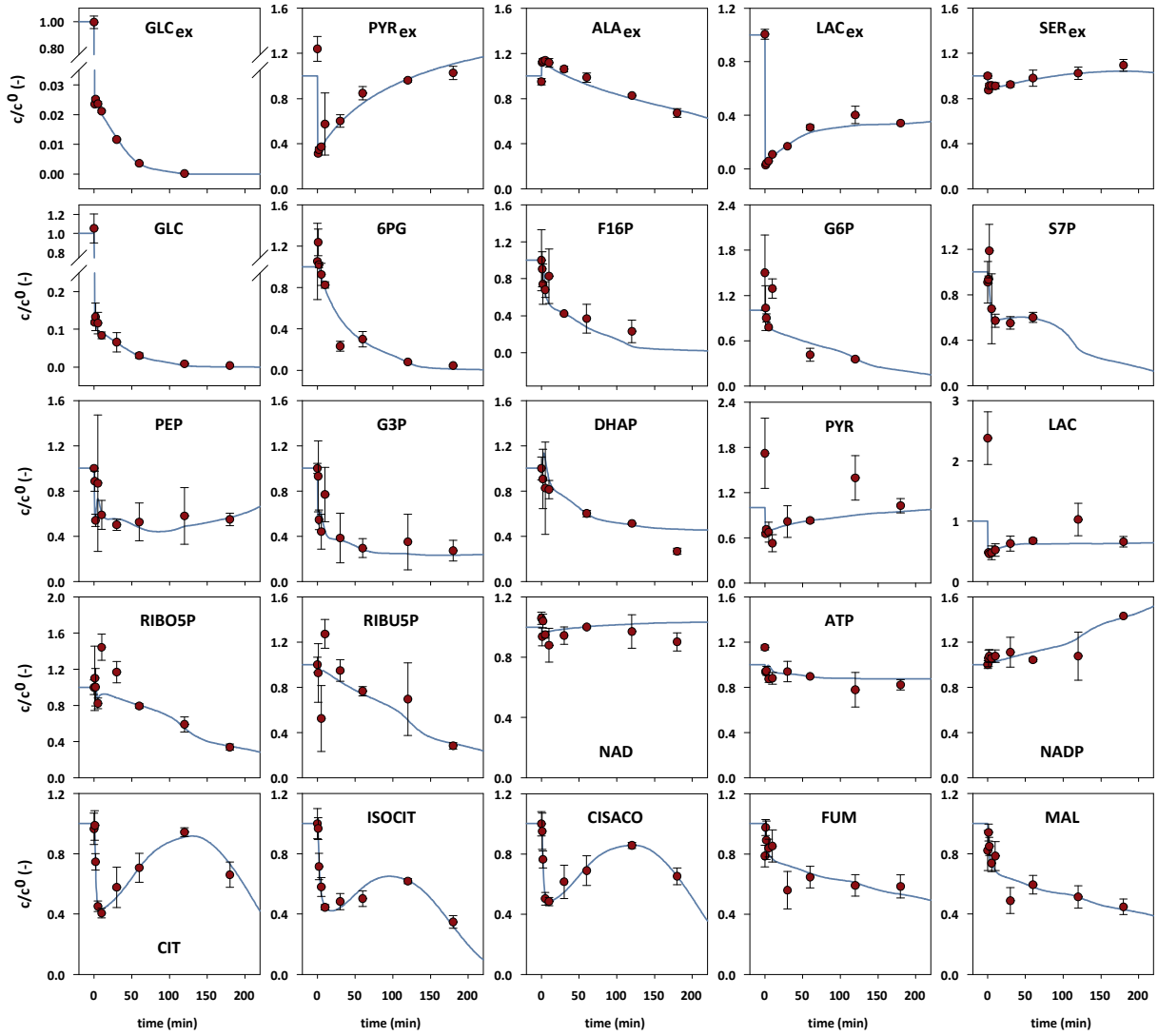

Figure 17. Extracellular and intracellular metabolite dynamics. The subscripts 'in' and 'ex' denote intracellular and extracellular metabolites, respectively. The concentration values were normalized with respect to their reference values, i.e. the concentrations directly before the stimulus. The error bars indicate standard deviations of the experimental data. To perturb the central metabolism, the glucose-containing culture medium was exchanged with glucose-free medium. By consequence, the extracellular glucose level dropped, and this stimulated significant intracellular metabolite dynamics.

In the first 10 min of the experiment, the model simulations showed decreasing ribose-5-phosphate and ribulose-5-phosphate levels, followed by an increase, and then another decrease. Some discrepancy between the initial experimental data points and the simulations was observed for both metabolites, which could be an indication of a damped oscillation with rather high amplitude.

The first TCA cycle intermediate pools, i.e. citrate, cis-aconitate, and isocitrate, exhibited oscillatory dynamics. This was also found in the model simulations. It is interesting to note that three pairs of conjugate-complex eigenvalues were observed for the Jacobian matrix, which suggests that the system is capable of damped oscillations. The model simulations showed a non-oscillating decrease of fumarate and malate. There was some discrepancy between the simulated time courses for fu-

marate and malate and the experimentally observed concentrations after 30 min. However, the corresponding standard deviations were large.

The time courses of the experimentally determined cofactors NAD, ATP, and NADP only deviated slightly from their initial values. This means that despite the substantial changes in the metabolite levels in the central carbon metabolism, the homeostatic regulatory machinery of the hepatoma cells only allowed for small changes among the highly linked cofactors: ATP decreased slightly but remained at above 80 % of its steady state concentration, the NAD level increased only marginally, NADP increased a little more, reaching 143 % of its initial value. In contrast to these observations, distinct cofactor dynamics have been observed in similar stimulus response experiments in prokaryotes and yeast (Chassagnole et al. 2002; Magnus et al. 2006; Theobald et al. 1997).

The experimentally determined reference intermediate levels are provided as supplementary data (cf. Appendix F).

5.3.2 Glycolysis Control

Metabolic control patterns are only valid for the physiological condition and cell type used in a particular experiment. For example, Soboll et al. reported significant differences in the control patterns between metabolically inactive and active states in isolated perfused rat liver (Soboll et al. 1998). In the present study, the reference state of the HepG2 cells was characterized by a sufficient supply of substrates, including glucose. Therefore, the hepatoma cells underwent glycolysis rather than gluconeogenesis (Maier et al. 2008a).

The matrix of flux control coefficients is shown in Figure 18 and is also included in the supplementary data section (cf. Appendix G). The glucose-6-phosphate dehydrogenase enzyme (r10) exerted a substantial negative control over the glycolytic fluxes (r1-r9, r17). The ribose-5-phosphate isomerase (r13) and one transketolase (r15: ribose 5-phosphate + xylulose 5-phosphate = glyceraldehyde 3-phosphate + sedoheptulose 7-phosphate) reaction also had a negative control over the glycolytic flux. In contrast, the phosphogluconate dehydrogenase (r12), the ribulose-phosphate 3-epimerase (r14), and the second transketolase reaction (r16: xylulose 5-phosphate + erythrose 4-phosphate = glyceraldehyde 3-phosphate + fructose-6-phosphate) had a positive control over glycolysis. In each case, the effect on the glucose-6-phosphate isomerase (r2) was far greater than on any other glycolytic flux. The flux through this enzyme depends on the concentration of substrate (glucose-6-phosphate), product (fructose-6-phosphate), and inhibitor (6-phosphogluconate). In other words, in order to increase the flux through this enzyme, a perturbation must either lead to an increase in the substrate concentration, or to a decrease in its product and/or inhibitor levels. The corresponding concentration control coefficients were determined in order to find out the effect that was the most significant (cf. Figure 19; cf. Appendix H). It is interesting to note that the glucose-6-phosphate dehy-

drogenase (r10) exerted positive and negative control over the glucose-6-phosphate and fructose-6-phosphate levels. However, the enzyme also had positive control over 6-phosphogluconate.

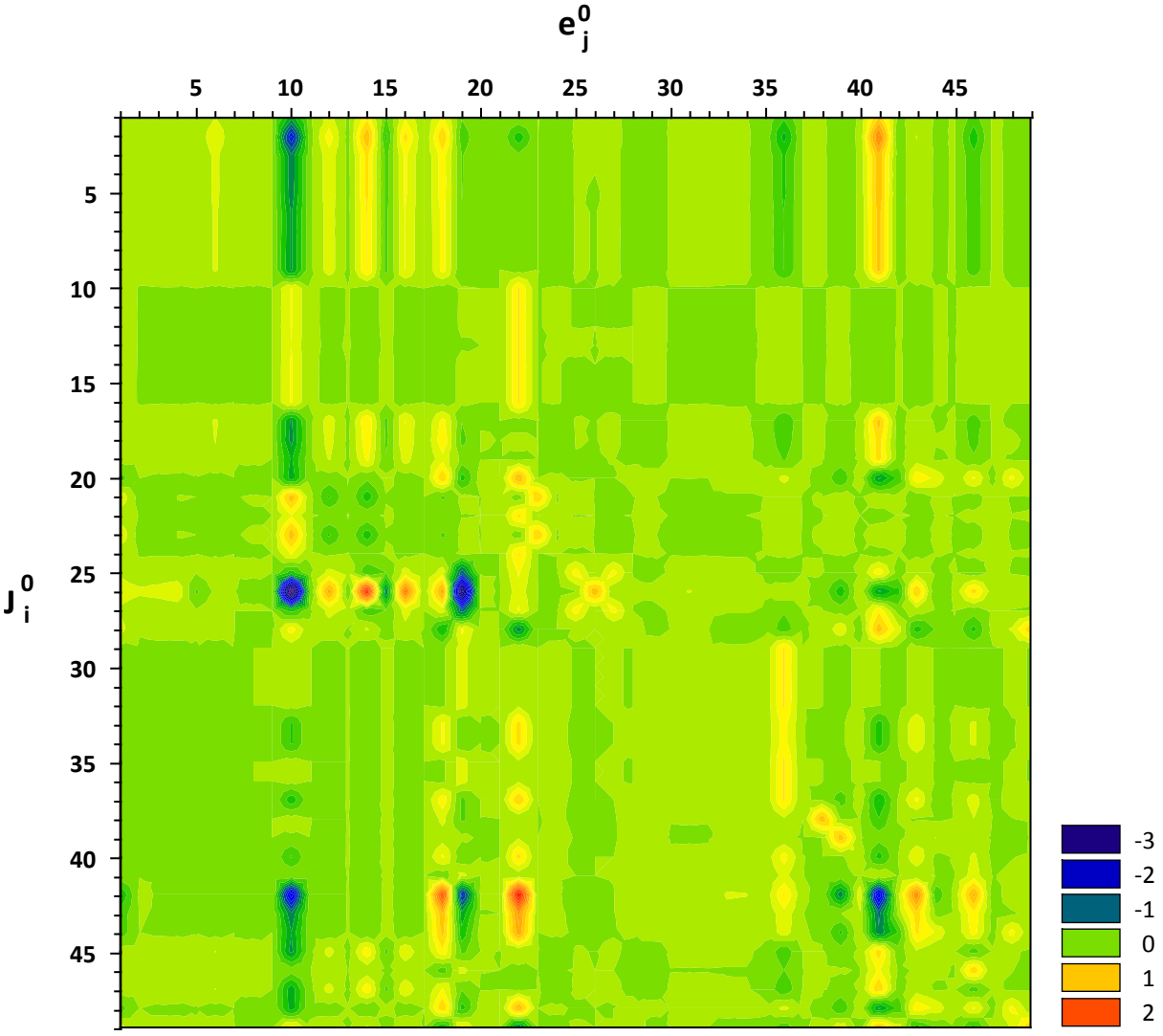

Figure 18. Flux control coefficients. The colors in row i and column j indicate the control that enzyme j exerts over the flux i. Warm and cold colors denote positive and negative control, respectively. The indices i and j correspond to the reaction numbers shown in Table 11 and Figure 16. The glucose-6-phosphate dehydrogenase (r10) was found to have significant negative control over all glycolytic fluxes, whereas oxidative phosphorylation (r41) exerted positive control (Warburg effect). Furthermore, it is interesting to note that only a few fluxes were found to be significantly stimulated by an increase in the corresponding enzyme level.

Concentration control coefficients provide a quantitative measure of the effects glucose-6-phosphate dehydrogenase had on the relevant substrate, product, and inhibitor levels. Partial flux control coefficients combine this information with the corresponding elasticity value to quantify the fractions to which individual changes in the concentrations of intermediates contribute to the total flux control coefficient. Table 13 shows the partial flux control coefficients over the glucose-6-

phosphate isomerase (r2). The partial flux control coefficients confirmed that 6-phosphogluconate was the key mediator of the negative control exerted by glucose-6-phosphate dehydrogenase. Strong inhibitory effects of 6-phosphogluconate on the glucose-6-phosphate isomerase rate have been reported for various tissues and organisms (Gaitonde et al. 1989; Parr 1956; Tsuboi et al. 1971). The phosphogluconate dehydrogenase (r12) and the ribulose-phosphate 3-epimerase (r14) exerted a negative control over glucose-6-phosphate and 6-phosphogluconate as well as a positive control over fructose-6-phosphate (cf. Figure 19). For both enzymes, the partial flux control coefficients over the flux through the glucose-6-phosphate isomerase (r2), corresponding to the inhibitory 6-phosphogluconate, were found to outweigh the substrate and product effects. In contrast, the second transketolase reaction (r16: xylulose 5-phosphate + erythrose 4-phosphate = glyceraldehyde 3-phosphate + fructose-6-phosphate), which also had positive control over the glucose-6-phosphate isomerase flux, exerted a negative control over all relevant intermediate levels. In this case, though, the impact of 6-phosphogluconate on the flux control was found to play only a minor role. Previous top-down approaches used to quantify the distribution of metabolic control in hepatocytes did not take into account the influences of the pentose-phosphate pathway on the glycolytic flux (Ainscow and Brand 1999a; Ainscow and Brand 1999c; Soboll and Brown 2000; Soboll et al. 1998). Boren et al. recognized the glucose-6-phosphate dehydrogenase (r10) as an interesting target in tumor therapy (Boren et al. 2002). They found a flux control coefficient of 0.41 on tumor growth for the glucose-6-phosphate dehydrogenase in mice bearing Ehrlich ascites tumor cells. In addition, cancer cells have a large number of mitochondrial DNA mutations, which possibly results in a dysfunction of the mitochondrial respiratory chain (Chen et al. 2007). Carew et al. found a correlation between mitochondrial mutations and an increased generation of reactive oxygen species (ROS) in human leukemia cells (Carew et al. 2003). These findings suggest that tumor cells have an elevated demand for reduced NADPH due to the increased scavenging of ROS via glutathione (Berg et al. 2002). From the results of the present study, it can further be concluded that the negative control coefficients of glucose-6-phosphate dehydrogenase over the glycolytic fluxes indicate that hepatoma growth is more limited by NADPH than by ATP supply. Moreover, the steady state split ratio between glycolysis and the pentose-phosphate pathway of 57 % to 43 % (Maier et al. 2008a) provides further evidence for the cells' requirements for reduction equivalents.

Table 13. Partial flux control coefficients over glucose-6-phosphate isomerase (r2). Partial flux control coefficients are only shown for metabolites influencing the glucose-6-phosphate isomerase (r2), i.e. that have non-zero elasticities. The sum of the partial flux control coefficients over all intermediates equals the flux control coefficient. For the control of an enzyme over its own flux, the flux control coefficient equals the sum of the partial flux control coefficients plus one.

	Partial flux control coefficient through			Flux control coefficient
Enzyme	$G6P_{in}$	$F6P_{in}$	$6PG_{in}$	
r1	5.64	-2.31	-3.18	0.15
r2	-0.61	-0.52	0.24	0.11
r3	-0.34	0.33	0.14	0.13
r4	-0.44	0.42	0.18	0.16
r5	-0.06	0.06	0.02	0.02
r6	-1.11	0.74	0.76	0.38
r7	-0.02	0.01	0.01	0.01
r8	-0.06	0.03	0.04	0.02
r9	0	0	0	0
r10	6.68	4.09	-12.4	-1.63
r11	0.3	0.19	-0.56	-0.07
r12	-3.12	-2.86	6.49	0.5
r13	0.19	-0.21	-0.05	-0.07
r14	-5.06	-2.9	8.98	1.02
r15	1.16	-1.2	-0.4	-0.44
r16	-1.91	1.62	0.97	0.69
r17	0	0	0	0
r18	-2.24	1.85	1.2	0.81
r19	-1.42	-0.03	1.12	-0.33
r20	0.02	-0.01	-0.02	-0.01
r21	0	0	0	0
r22	0.78	1.37	-2.69	-0.54
r23	-0.02	0.01	0.01	0
r24	0.1	-0.1	-0.03	-0.04
r25	-0.04	-0.01	0.06	0.01
r26	-0.01	0	0	0
r27	-0.05	0	0.06	0.01
r28	0.04	-0.02	-0.03	-0.01
r29	0.62	-0.39	-0.42	-0.2
r30	-0.08	0.09	0.02	0.03
r31	-0.14	0.17	0.03	0.06
r32	-0.08	0.1	0.02	0.04
r33	-0.02	0.06	-0.02	0.02
r34	-0.02	0.05	-0.02	0.02
r35	0.18	-0.11	-0.12	-0.06
r36	2.15	-1.36	-1.46	-0.67
r37	-0.01	0.01	0	0
r38	-0.1	0.05	0.08	0.03
r39	0.17	-0.32	0.05	-0.09
r40	-0.03	0.09	-0.03	0.03
r41	-4.38	2.55	3.32	1.48

Table 13 (continued)

Enzyme	Partial flux control coefficient through $G6P_{in}$	Partial flux control coefficient through $F6P_{in}$	Partial flux control coefficient through $6PG_{in}$	Flux control coefficient
r42	0.37	-0.42	-0.1	-0.15
r43	-0.45	0.57	0.09	0.21
r44	0.09	-0.13	0	-0.04
r45	-0.05	0.04	0.03	0.02
r46	1.82	-0.94	-1.4	-0.53
r47	1.24	-0.51	-0.7	0.03
r48	0.12	-0.05	-0.11	-0.03
r49	0.18	-0.1	-0.14	-0.06

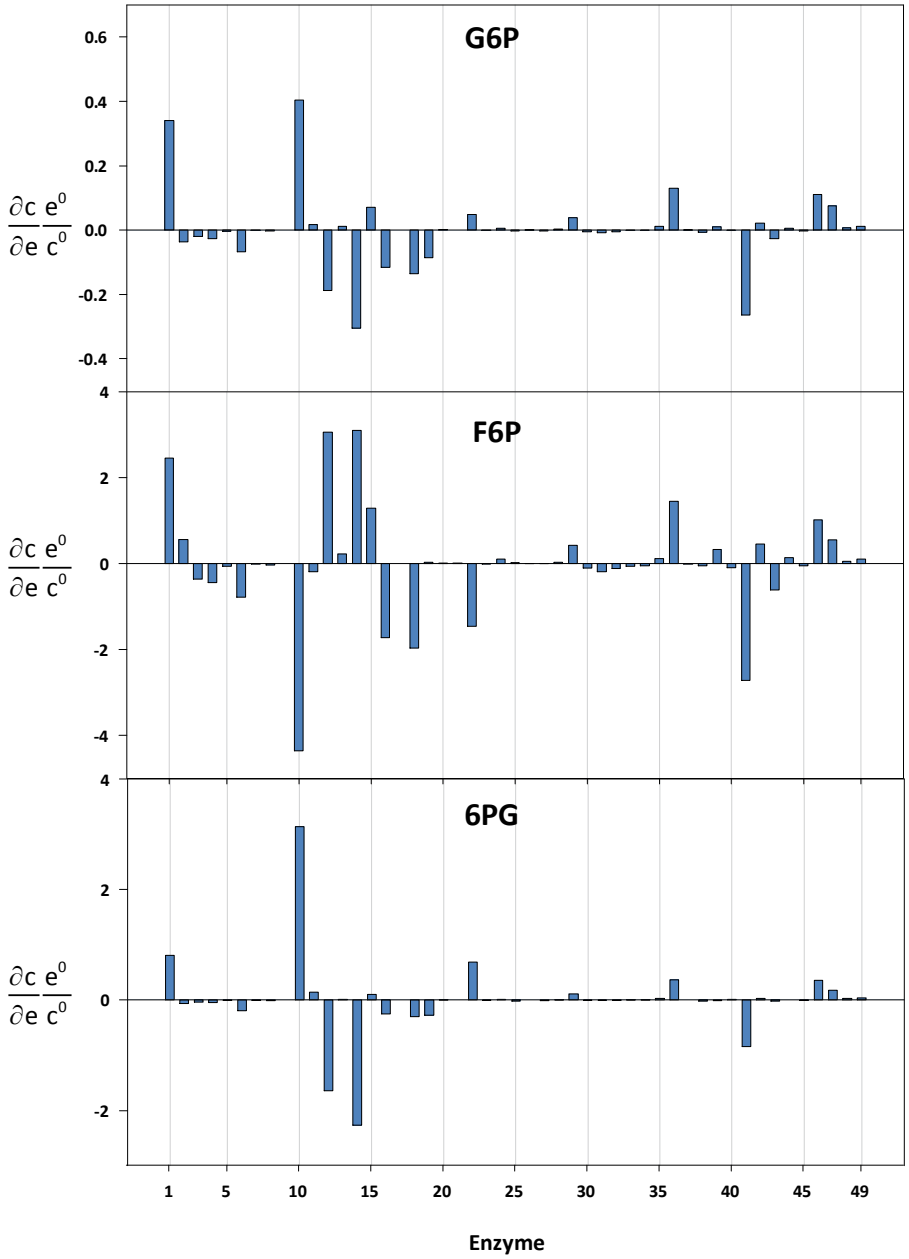

Figure 19. Concentration control coefficients over glucose-6-phosphate (G6P), fructose-6-phosphate (F6P), and 6-phosphogluconate (6PG). The enzyme indices correspond to the reaction numbers shown in Table 11 and Figure 16.

In accordance with the negative control over the glycolytic fluxes, glucose-6-Phosphate dehydrogenase (r10) was found to have substantial negative control over the formation of glycerol (r26).

Lactate dehydrogenase (r18) had a substantial positive control over the glycolytic fluxes. Ainscow and Brand reported positive control of lactate production on glycolysis in primary hepatocytes isolated from fed rats (Ainscow and Brand 1999c). The control coefficient (0.12) was smaller than the values of the individual glycolysis enzymes determined in this study (0.43 – 0.8). However, hepatoma cells, like most tumor cells, produce large amounts of lactate under aerobic conditions. Consequently, the lactate dehydrogenase enzyme is likely to be closer to saturation in tumor cells than in primary cells. An enzyme with a low elasticity coefficient, i.e. an enzyme operating close to saturation, hardly responds to changes in the levels of its substrate and/or product molecules. Therefore, saturated enzymes exhibit a larger flux control compared to unsaturated enzymes (Moreno-Sanchez et al. 2008).

The pyruvate dehydrogenase complex (r36) and the pyruvate secretion step (r38) had a negative control over the glycolytic flux. For pyruvate oxidation, Ainscow and Brand also observed a negative control over glycolysis in rat hepatocytes (Ainscow and Brand 1999c). Increasing the flux through the pyruvate dehydrogenase complex led to an increased flux through the TCA cycle, which, in turn, increased the intracellular NADH/NAD ratio. Besides, the pyruvate dehydrogenase complex exerted negative control over the lactate dehydrogenase enzyme (-0.35), which leads to an even higher NADH/NAD ratio. Pyruvate secretion had negative control over both the lactate dehydrogenase (-0.29) and the pyruvate dehydrogenase complex (-0.03). Consequently, the negative control over glycolysis exerted by the pyruvate dehydrogenase complex was found to be more substantial than the negative control of the pyruvate transportation step. Ainscow and Brand observed a negative control for oxidative phosphorylation over the glycolytic flux in primary rat hepatocytes (flux control coefficient of -0.26) (Ainscow and Brand 1999c). This was attributed to the Pasteur effect, where the increased activity of oxidative phosphorylation slows down glycolysis. In an analysis of the partial flux control coefficients of the glycolysis block, Ainscow and Brand found for isolated rat hepatocytes that the Pasteur effect was mostly due to an increase in ATP, which was opposed by a decreasing NADH/NAD ratio (Ainscow and Brand 1999a). However, in the case of HepG2 cells, oxidative phosphorylation (r41) had a substantial positive control of glycolysis, with control coefficients ranging from 0.82 to 1.48. This suggests that the respiration rate has a limiting effect on the growth of hepatomas. This has also been proposed for prokaryotic systems (Andersen and von Meyenburg 1980; Ingledew and Poole 1984). Furthermore, Lo et al. reported only low respiration for rapidly growing, poorly differentiated hepatic tumors, an effect which was ascribed to the loss of mitochondria during dedifferentiation (Lo et al. 1968). The aforementioned increased mitochondrial DNA mutation rate can also lead to a dysfunction of the mitochondrial respiratory chain (Chen et al. 2007). Warburg was

the first to describe what is today known as the Warburg effect or aerobic glycolysis: In contrast to normal liver tissue, liver cancer cells have an increased glycolytic flux in the presence of oxygen (Warburg et al. 1924). The Warburg effect is often observed in tumor tissue. In fact, the elevated glycolytic flux of malignant cells is increasingly recognized as a promising target for the treatment of cancer (Lopez-Lazaro 2008; Pelicano et al. 2006).

5.3.3 Control of the Pentose Phosphate Pathway

The control of the pentose-phosphate pathway (r10-r16, r24) depends to a great extent on the demand for reduction equivalents (r22) and the glucose-6-phosphate dehydrogenase (r10). This means that flux control coefficients of 0.63 and 0.41 of the individual fluxes in the pentose-phosphate shunt were observed for NADPH consumption (r22) and the glucose-6-phosphate dehydrogenase (r10), respectively. Kather et al. also reported that the glucose-6-phosphate dehydrogenase and the NADPH/NADP ratio control the pentose-phosphate pathway of isolated fat-cells (Kather et al. 1972). Sabate et al. described a kinetic pentose-phosphate pathway model for fasted rat livers (Sabate et al. 1995), which, however, does not take into consideration NADPH consumption. The authors concluded that the pentose-phosphate pathway fluxes were mainly regulated by the glucose-6-phosphate dehydrogenase and transketolase reactions.

The predominant control of the pentose-phosphate pathway by the glucose-6-phosphate dehydrogenase (r10) and the demand for reduction equivalents (r22) is also interesting with respect to the discussion of modular structures in metabolic networks. Using dynamic modeling and experimental observations of in vivo metabolite dynamics, Vaseghi et al. concluded that in Saccharomyces cerevisiae the pentose-phosphate pathway acts as a functional unit that is controlled by the demand for biosynthesis and is modulated by the energy state of the cell (Vaseghi et al. 1999). In accordance with the yeast enzyme, the flux through the human glucose-6-phosphate dehydrogenase is also modulated by the cellular ATP level (Cho and Joshi 1990). In this work, the elasticity value of the glucose-6-phosphate dehydrogenase with respect to ATP was determined to -0.7. Together with the observed control principles, this suggests a similar dynamic regulation scheme in hepatoma cells.

5.3.4 Control of the Tricarboxylic Acid Cycle

Ainscow and Brand applied top-down methods to elucidate metabolic control patterns in isolated rat hepatocytes. They included only one common reaction block for pyruvate transport, TCA cycle, and five-sixths of the respiratory chain (Ainscow and Brand 1999a; Ainscow and Brand 1999c). Thus, the approach used in the present study allows a more detailed investigation of the control patterns of the TCA cycle. The glucose-6-phosphate dehydrogenase (r10) exerted little positive and substantial negative control over the first (r29-r32) and last (r33, r34, r40, r43) fluxes in the TCA cycle, respectively. Partial flux control coefficients were calculated in order to find out where these different ef-

fects stem from. The results are listed in Table 14. As can be seen, the negative control over the malic enzyme (r43) was due to an increased NADPH level (-1.13) and a decreased NADP (-0.63) level. These effects were partially compensated by lower intracellular pyruvate (0.32) and increased malate (0.45) levels. The increase in the malate concentration, in turn, is the key mediator of the negative control over the fumarate hydratase (r34). A decreased flux through this enzyme was accompanied by elevated fumarate levels, which resulted in a substantial negative flux control coefficient for the flux through the succinate dehydrogenase (r40). Likewise, the flux through the succinate-CoA ligase enzyme (r33) was negatively controlled by its product succinate. To summarize, the positive and negative control over the NADPH and NADP levels of the glucose-6-phosphate dehydrogenase (r10) enzyme led to a negative control of the malic enzyme (r43). The negative control of the adjacent TCA cycle fluxes was mediated by elevated product levels. Consequently, the consumption of reduction equivalents (r22) was expected to lead to a complementary control pattern, and this was indeed the case. Similarly, lactate dehydrogenase (r18) exerted a positive control over the final fluxes of the TCA cycle. However, in contrast to glucose-6-phosphate dehydrogenase (r10) and the consumption of reduction equivalents (r22), lactate dehydrogenase had a minor effect on the cellular NADPH/NADP ratio. However, as expected, lactate dehydrogenase exerted a substantial negative control over the intracellular pyruvate concentration. Figure 20 depicts the concentration control coefficients for intracellular pyruvate. The negative control of lactate dehydrogenase (r22) over the intracellular pyruvate level results in a strong positive control over the malic enzyme flux (1.17; cf. Table 14). The positive control was mediated through the downstream fluxes in the TCA cycle by decreasing the product levels. The ATP-consuming reaction (r19) had a positive control over the first fluxes in the TCA cycle (citrate synthase, r29; aconitate hydratase, r30, r31; isocitrate dehydrogenase, r32) as well as over the flux through the pyruvate dehydrogenase (r36). The flux control coefficient for the pyruvate dehydrogenase flux of 0.29 (cf. Appendix G) was mainly due to increased NAD (0.2) and pyruvate (0.14) levels and, to a lesser extent, a lower NADH level (0.08). These effects were opposed by an increased acetyl-CoA level (-0.13). The elevated intracellular pyruvate level mediated a negative control over the malic enzyme (-1.1). As for pyruvate dehydrogenase, the negative control of the malic enzyme was accompanied by an increased malate level, which led to a negative control of the flux through the fumarate hydratase enzyme. A substantial positive control of the complete TCA cycle was observed for the pyruvate dehydrogenase complex (r36). Using a top-down approach, Ainscow and Brand observed in rat hepatocytes that the pyruvate oxidation block had a positive control over itself (Ainscow and Brand 1999c). Oxidative phosphorylation (r41) had the highest positive control over the intracellular steady state pyruvate level (cf. Figure 20). Therefore, the control pattern of the pyruvate oxidation block on the TCA cycle was similar to the one corresponding to the ATP consumption (r19) reaction.

Reaction r42 describes the exchange of alpha-ketoglutarate with the biomass. In the dynamic network model, the rate of r42 depends only on the level of its product alpha-ketoglutarate. The corresponding elasticity coefficient was determined to -0.5. This means that changes in the level of alpha-ketoglutarate are directly mirrored in changes in the flux through the r42 reaction, and, thus, r42 was found to be strongly influenced by several enzymes.

Table 14. Partial flux control coefficients over fumarate hydratase (r34), succinate dehydrogenase (r40), and the malic enzyme (r43). Partial flux control coefficients are only shown for metabolites having non-zero elasticities. The sum of the partial flux control coefficients over all intermediates equals the flux control coefficient. For the control of an enzyme over its own flux, the flux control coefficient equals the sum of the partial flux control coefficients plus one.

	r34		r40				r43			
Enzyme	MAL_{in}	FUM_{in}	NAD_{in}	SUC_{in}	FUM_{in}	$NADH_{in}$	PYR_{in}	$NADP_{in}$	MAL_{in}	$NADPH_{in}$
r1	-0.598	0.414	0	0.126	-0.247	-0.063	-0.06	-0.127	0.085	-0.227
r2	0.089	-0.091	0	-0.002	0.055	-0.055	-0.025	0.017	-0.013	0.030
r3	0.061	-0.075	0	0.006	0.045	-0.064	-0.032	0.011	-0.009	0.019
r4	0.077	-0.094	0	0.008	0.056	-0.081	-0.04	0.014	-0.011	0.024
r5	0.011	-0.013	0	0.001	0.008	-0.011	-0.005	0.002	-0.002	0.003
r6	0.178	-0.22	-0.001	0.018	0.132	-0.191	-0.093	0.031	-0.025	0.056
r7	0.003	-0.003	0	0	0.002	-0.003	-0.001	0	0	0.001
r8	-0.026	0.02	0	0.004	-0.012	0.002	-0.021	0.002	0.004	0.003
r9	0	0	0	0	0	0	0	0	0	0
r10	-3.145	2.72	0.003	0.349	-1.624	0.847	0.315	-0.631	0.449	-1.131
r11	-0.143	0.123	0	0.016	-0.074	0.038	0.014	-0.029	0.02	-0.051
r12	0.196	-0.261	-0.001	0.03	0.156	-0.25	-0.125	0.033	-0.028	0.060
r13	-0.034	0.043	0	-0.004	-0.026	0.038	0.019	-0.006	0.005	-0.011
r14	0.422	-0.549	-0.002	0.058	0.328	-0.51	-0.253	0.073	-0.06	0.131
r15	-0.209	0.257	0.001	-0.02	-0.153	0.221	0.109	-0.037	0.03	-0.066
r16	0.322	-0.398	-0.001	0.032	0.238	-0.344	-0.17	0.057	-0.046	0.102
r17	-0.001	0.001	0	0	0	0	-0.001	0	0	0
r18	2.173	-1.728	-0.001	-0.342	1.031	-0.243	1.168	0.052	-0.31	0.093
r19	-2.522	2.34	0.004	0.208	-1.397	1.004	-1.099	0.004	0.36	0.007
r20	0.004	-0.005	0	0	0.003	-0.004	-0.002	0	-0.001	-0.001
r21	-0.001	0.001	0	0	-0.001	0.001	0	0	0	0
r22	2.787	-2.107	0	-0.482	1.258	-0.096	0.069	0.579	-0.398	1.037
r23	0	0	0	0	0	0	-0.001	0	0	0.001
r24	-0.018	0.022	0	-0.002	-0.013	0.019	0.009	-0.003	0.003	-0.006
r25	-0.012	0.01	0	0.001	-0.006	0.003	-0.007	0.001	0.002	0.001
r26	-0.002	0.002	0	0	-0.001	0.001	-0.001	0	0	0
r27	0.007	-0.006	0	0	0.004	-0.003	-0.002	0.001	-0.001	0.002
r28	0.023	-0.019	0	-0.003	0.011	-0.003	0.018	-0.001	-0.003	-0.002
r29	0.584	-0.44	0	-0.094	0.263	-0.024	0.23	-0.018	-0.083	-0.032
r30	0.077	-0.069	0	-0.006	0.041	-0.027	0.009	0.003	-0.011	0.005
r31	0.141	-0.127	0	-0.011	0.076	-0.05	0.016	0.005	-0.02	0.009
r32	0.084	-0.075	0	-0.007	0.045	-0.03	0.009	0.003	-0.012	0.005
r33	-0.755	0.823	0	0.592	-0.492	-0.033	0.014	0	0.108	-0.001
r34	-0.703	-0.234	0	-0.046	0.139	-0.03	0.013	0	0.1	-0.001

Table 14 (continued)

	r34		r40				r43			
Enzyme	MAL_{in}	FUM_{in}	NAD_{in}	SUC_{in}	FUM_{in}	$NADH_{in}$	PYR_{in}	$NADP_{in}$	MAL_{in}	$NADPH_{in}$
r35	0.168	-0.126	0	-0.027	0.075	-0.007	0.066	-0.005	-0.024	-0.009
r36	2.012	-1.515	0	-0.323	0.904	-0.084	0.793	-0.061	-0.287	-0.109
r37	-0.002	0.004	0	0.008	-0.002	-0.004	0.001	0	0	0
r38	-0.07	0.057	0	0.009	-0.034	0.012	-0.049	0.003	0.01	0.005
r39	-0.36	0.334	0	0.039	-0.199	0.133	-0.034	-0.007	0.051	-0.013
r40	-1.177	1.284	0	-0.076	-0.766	-0.051	0.022	-0.001	0.168	-0.001
r41	-2.273	1.782	0.001	0.316	-1.064	0.255	-1.765	0.133	0.324	0.239
r42	-0.235	0.231	0	0.021	-0.138	0.112	0.053	-0.013	0.034	-0.023
r43	1.774	-1.405	-0.001	-0.27	0.839	-0.199	-0.03	0.006	-0.253	0.011
r44	-0.239	0.201	0	0.032	-0.12	0.049	-0.1	-0.002	0.034	-0.004
r45	0.053	-0.042	0	-0.008	0.025	-0.006	0.028	0.001	-0.007	0.002
r46	1.285	-1.044	-0.001	-0.167	0.623	-0.214	0.888	-0.052	-0.183	-0.094
r47	-0.132	0.091	0	0.028	-0.055	-0.014	-0.013	-0.028	0.019	-0.050
r48	0.022	-0.027	0	0.001	0.016	-0.023	-0.013	-0.003	-0.003	-0.005
r49	0.107	-0.086	0	-0.014	0.051	-0.015	0.08	-0.005	-0.015	-0.010

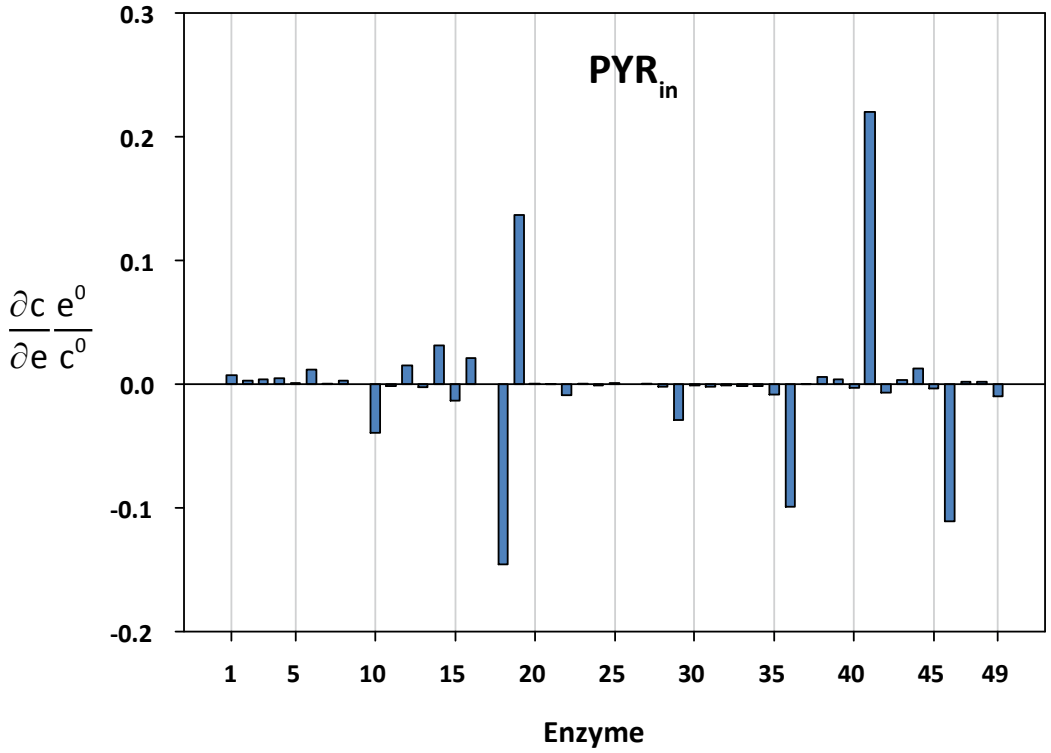

Figure 20. Concentration control coefficients over intracellular pyruvate. The enzyme indices correspond to the reaction numbers shown in Table 11 and Figure 16.

5.3.5 Control of Lactate Dehydrogenase, NADPH Consumption, and Oxidative Phosphorylation

Figure 21 depicts the flux control coefficients for lactate dehydrogenase (r18), NADPH consumption (r22), and oxidative phosphorylation (r41). The glycolytic enzymes had positive control over lactate production. However, the effect was less significant compared to primary hepatocytes that were isolated from fed rats (Ainscow and Brand 1999c). The pentose-phosphate pathway exerted a significant control over the glycolytic flux and thus had substantial control over the flux through lactate dehydrogenase (r18). The corresponding partial flux control coefficients are listed in Table 15. Most of the control of the pentose phosphate pathway was mediated by its influence on the NADH level. Changes in NAD and pyruvate concentrations also contributed to the total flux control coefficient, albeit to a lesser extent. Similarly to the control pattern observed in rat hepatocytes (Ainscow and Brand 1999c), the pyruvate dehydrogenase complex (r36) exerted a negative control over the lactate dehydrogenase flux. The same authors also emphasized the importance of the pyruvate level with regard to the lactate production rate (Ainscow and Brand 1999a). Ainscow and Brand found that lactate dehydrogenase (r18) had little control over its own flux, as increased activity was strongly counteracted by low pyruvate levels. The effect exerted by decreasing pyruvate levels could also be observed in hepatoma cells, but was less pronounced. Therefore, the lactate dehydrogenase had more control over its own flux. Furthermore, in contrast to the situation observed in primary hepatocytes, the oxidative phosphorylation (r41) in hepatoma cells had substantial positive control over the lactate production rate. This was mainly due to its increasing effect on the pyruvate level (0.95). NADPH consumption (r22) was mainly controlled by itself (0.65). However, it is important to note that it is not only the demand of NADPH alone that affects the NADPH consumption flux, but also the supply of NADPH (0.38). This means that an increase in NADPH production yields an increase in NADPH consumption, i.e. a stimulation of biosynthetic reactions. Put differently, the dependence of NADPH demand on NADPH supply provides further evidence for the hypothesis that tumor growth is limited by NADPH production. Numerous papers have dealt with the control of oxidative phosphorylation in isolated rat liver cells (Ainscow and Brand 1999c; Brown et al. 1990; Soboll et al. 1998). The results found for hepatoma cells agree with those previously found: Inhibition of oxygen consumption resulting from an increased flux through glycolysis (Crabtree effect) was low (Ainscow and Brand 1999c), the consumption of ATP (r19) and the pyruvate dehydrogenase complex (r36) positively controlled oxidative phosphorylation (Ainscow and Brand 1999c; Brown et al. 1990) and oxidative phosphorylation had a strong control over its own flux (Ainscow and Brand 1999c; Soboll et al. 1998).

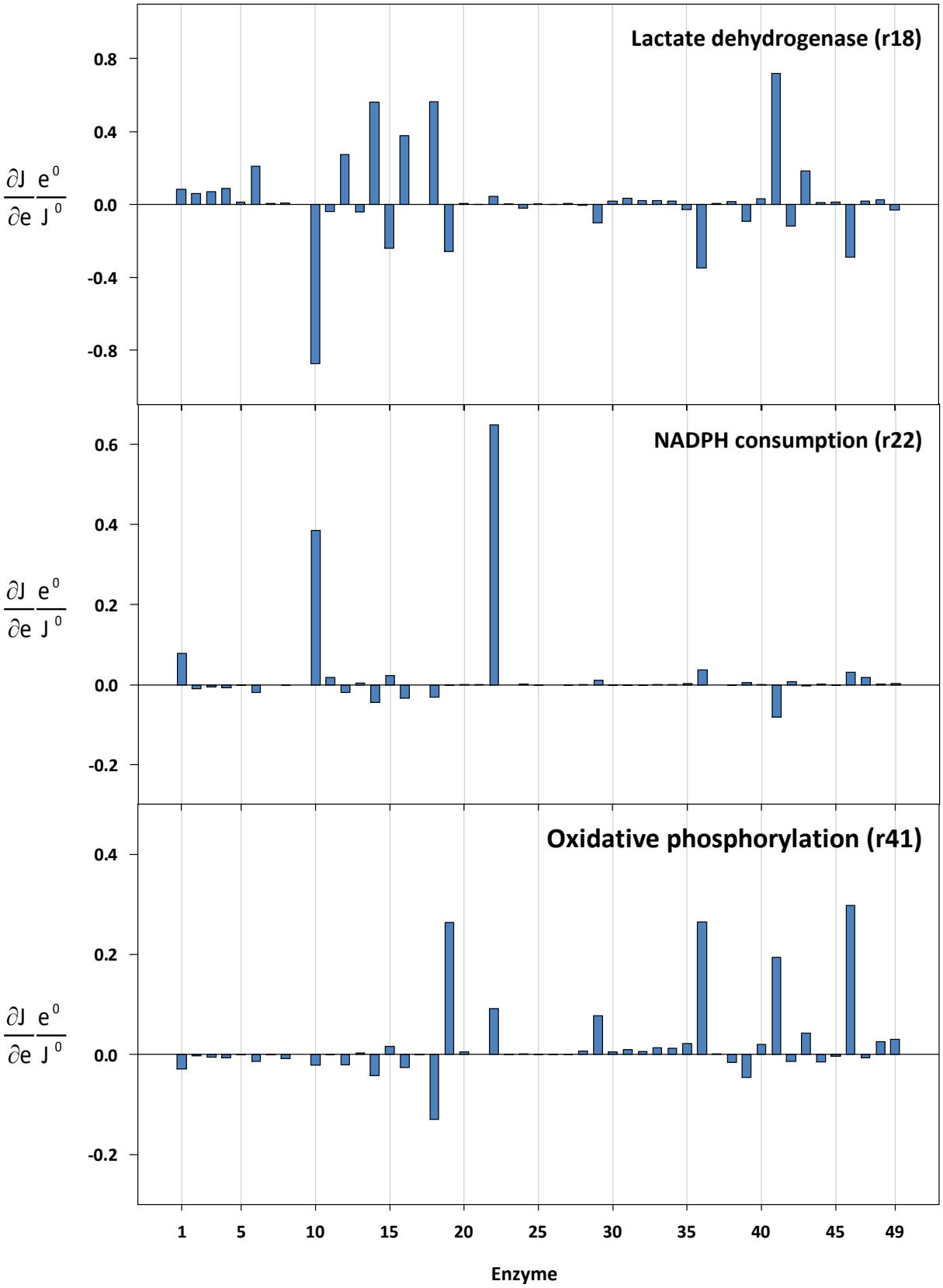

Figure 21. Flux control coefficients over lactate dehydrogenase (r18), NADPH consumption (r22), and oxidative phosphorylation (r41). The enzyme indices correspond to the reaction numbers shown in Table 11 and Figure 16.

Table 15. Partial flux control coefficients over lactate dehydrogenase (r18) and oxidative phosphorylation (r41). Partial flux control coefficients are only shown for metabolites having non-zero elasticities. The sum of the partial flux control coefficients over all intermediates equals the flux control coefficient. For the control of an enzyme over its own flux, the flux control coefficient equals the sum of the partial flux control coefficients plus one.

	Lactate dehydrogenase (r18)					Oxidative phosphorylation (r41)				
	Partial flux control coefficient through				Flux control coefficient	Partial flux control coefficient through				Flux control coefficient
Enzyme	NAD_{in}	PYR_{in}	LAC_{in}	$NADH_{in}$		ATP_{in}	NAD_{in}	ADP_{in}	$NADH_{in}$	
r1	0.011	0.032	-0.002	0.043	0.084	-0.012	0.001	-0.06	0.042	-0.029
r2	0.009	0.014	-0.001	0.038	0.059	-0.007	0.001	-0.034	0.037	-0.003
r3	0.011	0.017	-0.002	0.044	0.071	-0.008	0.002	-0.041	0.044	-0.003
r4	0.014	0.022	-0.002	0.056	0.089	-0.011	0.002	-0.052	0.055	-0.006
r5	0.002	0.003	0	0.008	0.012	-0.001	0	-0.007	0.008	0
r6	0.032	0.05	-0.005	0.132	0.209	-0.025	0.005	-0.124	0.129	-0.015
r7	0	0.001	0	0.002	0.003	0	0	-0.002	0.002	0
r8	0	0.012	0	-0.002	0.009	-0.001	0	-0.005	-0.002	-0.008
r9	0	0	0	0	0	0	0	0	0	0
r10	-0.142	-0.17	0.021	-0.584	-0.875	0.096	-0.02	0.476	-0.573	-0.021
r11	-0.006	-0.008	0.001	-0.027	-0.04	0.004	-0.001	0.022	-0.026	-0.001
r12	0.042	0.067	-0.007	0.173	0.275	-0.033	0.006	-0.163	0.169	-0.021
r13	-0.006	-0.01	0.001	-0.026	-0.041	0.005	-0.001	0.024	-0.026	0.002
r14	0.086	0.137	-0.014	0.352	0.561	-0.068	0.012	-0.331	0.345	-0.042
r15	-0.037	-0.059	0.006	-0.152	-0.242	0.029	-0.005	0.142	-0.149	0.017
r16	0.058	0.092	-0.009	0.237	0.377	-0.045	0.008	-0.222	0.233	-0.026
r17	0	0	0	0	0	0	0	0	0	0
r18	0.041	-0.632	-0.014	0.168	0.564	-0.05	0.006	-0.25	0.165	-0.129
r19	-0.168	0.594	0.006	-0.693	-0.261	0.162	-0.024	0.805	-0.679	0.264
r20	0.001	0.001	0	0.003	0.005	0	0	0.001	0.003	0.004
r21	0	0	0	-0.001	-0.001	0	0	0.001	-0.001	0
r22	0.016	-0.037	-0.001	0.066	0.044	0.005	0.002	0.02	0.065	0.092
r23	0	0.001	0	0	0.001	0	0	0	0	0
r24	-0.003	-0.005	0	-0.013	-0.02	0.002	0	0.012	-0.013	0.001
r25	0	0.004	0	-0.002	0.002	0	0	0.002	-0.002	0
r26	0	0	0	-0.001	-0.001	0	0	0.001	-0.001	0
r27	0.001	0.001	0	0.002	0.004	0	0	-0.002	0.002	0
r28	0.001	-0.009	0	0.002	-0.006	0.001	0	0.004	0.002	0.007
r29	0.004	-0.125	0.002	0.017	-0.101	0.01	0.001	0.05	0.017	0.078
r30	0.005	-0.005	0	0.019	0.018	-0.002	0.001	-0.012	0.019	0.006
r31	0.008	-0.008	-0.001	0.035	0.034	-0.004	0.001	-0.022	0.034	0.009
r32	0.005	-0.005	0	0.021	0.02	-0.003	0.001	-0.013	0.02	0.005
r33	0.005	-0.008	0	0.022	0.02	-0.002	0.001	-0.008	0.022	0.013
r34	0.005	-0.007	0	0.021	0.018	-0.002	0.001	-0.008	0.02	0.011
r35	0.001	-0.036	0.001	0.005	-0.029	0.003	0	0.014	0.005	0.022
r36	0.014	-0.429	0.008	0.058	-0.348	0.035	0.002	0.171	0.057	0.265
r37	0.001	-0.001	0	0.003	0.003	0	0	-0.001	0.003	0.002
r38	-0.002	0.026	0	-0.008	0.016	-0.001	0	-0.007	-0.008	-0.016
r39	-0.022	0.018	0.002	-0.092	-0.094	0.008	-0.003	0.039	-0.09	-0.046
r40	0.009	-0.012	-0.001	0.035	0.031	-0.003	0.001	-0.013	0.034	0.019

Table 15 (continued)

	Lactate dehydrogenase (r18)					Oxidative phosphorylation (r41)				
	Partial flux control coefficient through				Flux control	Partial flux control coefficient through				Flux control
Enzyme	NAD_{in}	PYR_{in}	LAC_{in}	$NADH_{in}$	coefficient	ATP_{in}	NAD_{in}	ADP_{in}	$NADH_{in}$	coefficient
r41	-0.043	0.954	-0.017	-0.176	0.718	-0.105	-0.006	-0.523	-0.172	0.194
r42	-0.019	-0.028	0.003	-0.078	-0.122	0.011	-0.003	0.054	-0.076	-0.014
r43	0.033	0.016	-0.004	0.137	0.183	-0.016	0.005	-0.081	0.135	0.043
r44	-0.008	0.054	0	-0.034	0.012	0.003	-0.001	0.016	-0.033	-0.015
r45	0.001	-0.015	0.024	0.004	0.014	-0.001	0	-0.006	0.004	-0.003
r46	0.036	-0.48	0.007	0.148	-0.289	0.025	0.005	0.122	0.145	0.297
r47	0.002	0.007	0	0.01	0.019	-0.003	0	-0.013	0.009	-0.007
r48	0.004	0.007	-0.001	0.016	0.026	0.002	0.001	0.008	0.015	0.026
r49	0.003	-0.043	0.001	0.01	-0.03	0.003	0	0.016	0.01	0.029

5.3.6 Concentration Control over NADPH, NADH, ATP, and NAD

The steady state NADPH level was found to be very sensitive to two enzymes – the glucose-6-phosphate dehydrogenase (r10) and the consumption of reduction equivalents (r22) (concentration control coefficients for NADPH, NADH, ATP, and NAD are shown in Figure 22). In both cases, the absolute values were above 1, i.e. 1.58 for r10 and and -1.45 for r22. This means that the NADPH level was equally controlled by supply and demand. In addition, NADPH responded moderately to changes in glucokinase (r1; 0.32) and oxidative phosphorylation (r41; -0.33). Apart from these, NADPH did not react significantly to changes in the levels of other enzymes. With respect to glycolysis and the pentose-phosphate pathway, the control distribution for ATP and NADH levels were similar. However, the values were proportionally lower for ATP, which was due to the stoichiometry, i.e. a P/O ratio of 2.5 was assumed for NADH (cf. sub-section model reconstruction). In both cases, the glycolytic enzymes (r1-r9, r17) had a positive, albeit low, control over the cofactors. As expected, glucose-phosphate dehydrogenase (r10) had a negative control over both intermediates, i.e. control coefficients of -0.06 for ATP and -0.27 for NADH, respectively. In contrast, the r12 (phosphogluconate dehydrogenase), r14 (ribulose-phosphate 3-epimerase), and r16 (transketolase: xylulose 5-phosphate + erythrose 4-phosphate = glyceraldehyde 3-phosphate + fructose-6-phosphate) reactions in the pentose-phosphate pathway had a positive control over the NADH and ATP levels.

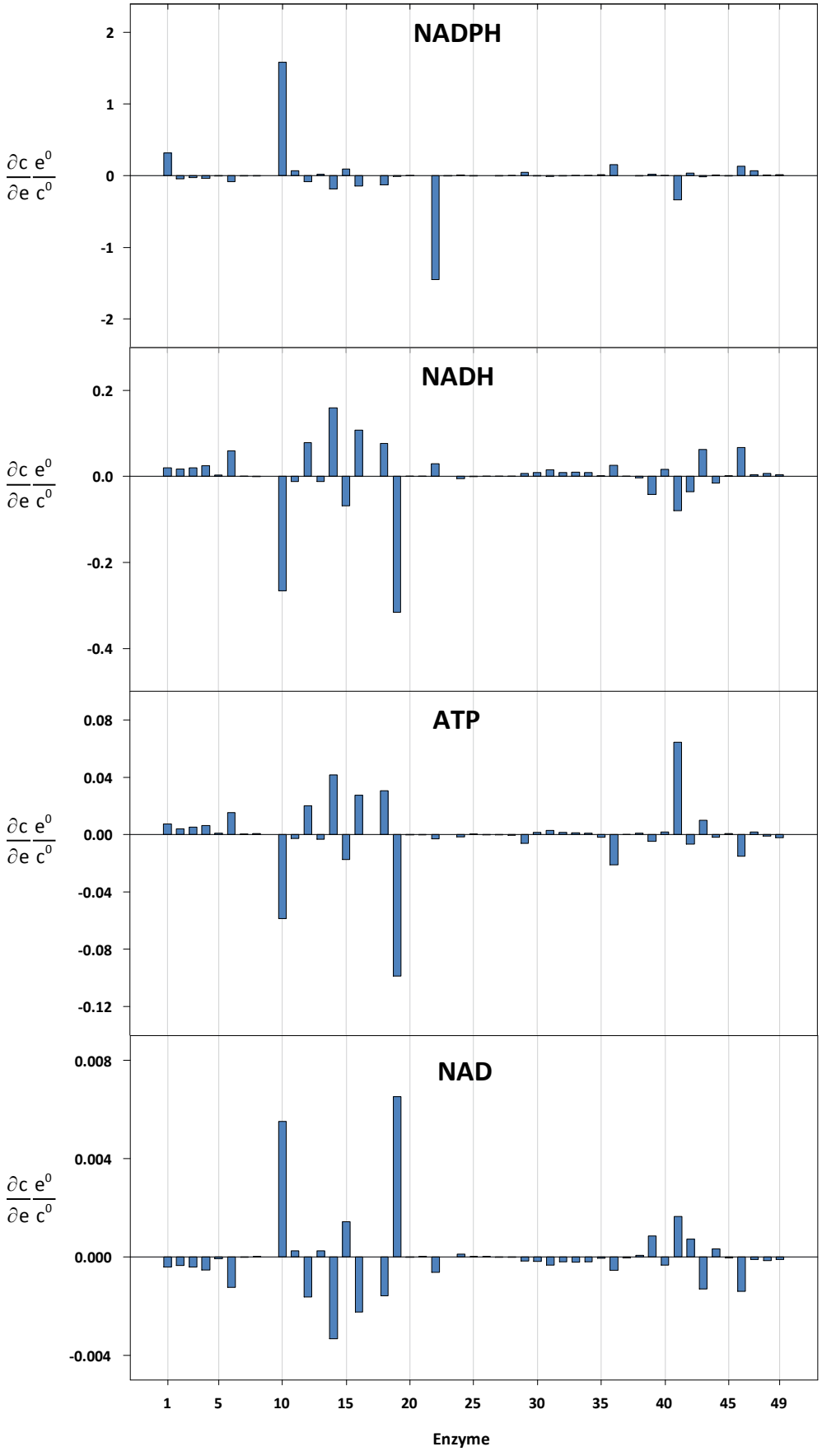

Figure 22. Concentration control coefficients over NADP, NADH, ATP, and NAD. The enzyme indices correspond to the reaction numbers shown in Table 11 and Figure 16.

A major characteristic of cancer cells, including the hepatoma cells analyzed in this study, is the secretion of lactate under aerobic conditions (Warburg et al. 1924). The aerobic production of lactate leads to an increase in the amount of ATP produced per time unit at the expense of a poorer yield coefficient. It was therefore assumed, and confirmed, that the lactate dehydrogenase had a positive control over the ATP level. The situation was different for NADH. On the one hand, increasing the flux through the lactate dehydrogenase enzyme decreases the NADH level by reducing pyruvate to lactate. On the other hand, it allows for an increased glycolytic flux, which leads to an increased level of NADH. Under the physiological conditions investigated in the present study, the latter effect was found to outweigh the former, which is the reason why a positive control coefficient was observed. ATP and NADH responded substantially and negatively to changes in the ATP-consuming reaction (r19; ATP: -0.1 and NADH: -0.31). It is not surprising that the control coefficients for the NAD level were complementary to those for NADH. However, the values were two orders of magnitude lower for NAD. The lower values for NAD compared to NADH are due to the normalization to the reference concentrations, which are higher for NAD.

5.3.7 Partial Internal Response Coefficients

Partial internal response coefficients quantify system responses to changes in the concentration of intermediates (Ainscow and Brand 1999a; Holzhütter et al. 1985; Sauro 1990). An asymptotically stable metabolic network operating at steady state will counteract an increase in one of its metabolites by either increasing the consumption of that metabolite, decreasing the production or by some combination thereof. In this context, partial internal response coefficients allow for the assessment of the relevance of individual reactions in counteracting a perturbation in order to restore the steady state. The internal response coefficients for the system under discussion are listed in Table 16. The cellular responses to elevated pyruvate level were in line with previous findings in rat hepatocytes, i.e. elevated pyruvate levels were mainly counteracted by an increased flux through the lactate dehydrogenase (r18) (Ainscow and Brand 1999a). However, the absolute value of the coefficient was lower in hepatoma cells, i.e. -0.63 compared to -0.84 as determined for rat hepatocytes. In HepG2 cells, a fraction of the additional pyruvate was secreted into the extracellular space (-0.23), another fraction was consumed by the pyruvate dehydrogenase complex (-0.1). In isolated rat hepatocytes, an increase in glucose-6-phosphate was counteracted by an increased release of glucose (-0.81) and by less glycogen being broken down (-0.17). The coefficient resulting from glycolytic degradation was negligible (Ainscow and Brand 1999a). In hepatoma cells, the control pattern was fundamentally different: An increase in glycogen synthesis played only a negligible role in counteracting elevated glucose-6-phosphate levels. The elevated glucose-6-phosphate levels were mainly counteracted by a reduced synthesis rate (-0.75) and an increased flux through glucose-6-phosphate isomerase (-0.61).

Furthermore, the internal response coefficient for the flux of glucose-6-phosphate through glucose-6-phosphate dehydrogenase was positive (0.36). It is interesting to note that in the cases of 1,3-bisphospho-glycerate, glycerate-3-phosphate, glycerate-2-phosphate, and phosphoenolpyruvate, an increase in intermediate was counteracted almost entirely by increased consumption. Ainscow and Brand attributed the high internal response coefficients for the flux of pyruvate through lactate dehydrogenase in rat hepatocytes to the fact that lactate dehydrogenase was working close to equilibrium (Ainscow and Brand 1999a). Similarly, in hepatoma cells the reactions in the lower part of glycolysis are possibly also close to equilibrium. Holzhütter et al. reported near equilibrium operation for the lower part of glycolysis in human erythrocytes (Holzhütter et al. 1985).

Table 16. Partial internal response coefficients. According to the connectivity theorem, the sum of the partial internal response coefficients for each intermediate is -1. Perturbations in moiety-conserved sets cannot be counteracted in order to reach the previous steady state, which is the reason why no partial response coefficients are listed for ATP, ADP, AMP, NADP, NADPH, NAD, and NADH.

	G6P	GLC	F6P	F16P	DHAP	GAP	13PG	3GP	2GP	PYR	PEP	GL6P	6PG	RIBU5P	RIBO5P	XYL5P	S7P	E4P	LAC	GLU	ALA	AKG	G1P	AMP	SER	CIT	OAC	ACOA	CISAC	ISOCIT	SUC	SUCOA	MAL	FUM
r1	-0.75	-0.03	-0.13	-	-	-	-	-	-	-	-	-	-	-	-	-	-	-	-	-	-	-	-	-	-	-	-	-	-	-	-	-	-	-
r2	-0.61	-	-0.52	-	-	-	-	-	-	-	-	-	0.24	-	-	-	-	-	-	-	-	-	-	-	-	-	-	-	-	-	-	-	-	-
r3	-	-	-0.42	-0.51	-	-	-	-	-	-	-	-	-	-	-	-	-	-	-	-	-	-	-	0.00	-	-0.08	-	-	-	-	-	-	-	-
r4	0.00	-	0.10	-0.49	-0.17	-0.31	-	-	-	-	-	-	-	-	0.00	-	-	-0.39	-	-	-	-	0.00	-	-	-	-	-	-	-	-	-	-	-
r5	-	-	-	-	-0.82	-0.16	-	-	-	-	-	-	-	-	-	-	-	-	-	-	-	-	-	-	-	-	-	-	-	-	-	-	-	-
r6	-	-	-	-	-	-0.04	-0.02	-	-	-	-	-	-	-	-	-	-	-	-	-	-	-	-	-	-	-	-	-	-	-	-	-	-	-
r7	-	-	-	-	-	-	-0.98	0.00	-	-	-	-	-	-	-	-	-	-	-	-	-	-	-	0.00	-	-	-	-	-	-	-	-	-	-
r8	-	-	-	-	-	-	-	-0.99	0.00	-	-	-	-	-	-	-	-	-	-	-	-	-	-	-	-	-	-	-	-	-	-	-	-	-
r9	0.00	-	0.00	0.00	-	-	-	-	-	0.00	-1.00	-	-	-	-	-	-	-	-	-	0.00	-	0.00	-	-	-	-	-	-	-	-	-	-	-
r10	0.36	-	-	-	-	-	-	-	-	-	-	-0.25	-	-	-	-	-	-	-	-	-	-	-	-	-	-	-	-	-	-	-	-	-	-
r11	-	-	-	-	-	-	-	-	-	-	-	-0.75	-0.23	-	-	-	-	-	-	-	-	-	-	-	-	-	-	-	-	-	-	-	-	-
r12	-	-	-	-	-	-	-	-	-	-	-	-	-1.01	-0.08	-	-	-	-	-	-	-	-	-	-	-	-	-	-	-	-	-	-	-	-
r13	-	-	-	-	-	-	-	-	-	-	-	-	-	-0.03	-0.97	-	-	-	-	-	-	-	-	-	-	-	-	-	-	-	-	-	-	-
r14	-	-	-	-	-	-	-	-	-	-	-	-	-	-0.90	-	-0.14	-	-	-	-	-	-	-	-	-	-	-	-	-	-	-	-	-	-
r15	-	-	-	-	-	1.57	-	-	-	-	-	-	-	-	-0.02	-1.60	-0.93	-	-	-	-	-	-	-	-	-	-	-	-	-	-	-	-	-
r16	-	-	0.32	-	-	-1.88	-	-	-	-	-	-	-	-	-	0.74	-	-0.22	-	-	-	-	-	-	-	-	-	-	-	-	-	-	-	-
r17	-	-	-	-	-	-	-	-	-1.00	-	0.00	-	-	-	-	-	-	-	-	-	-	-	-	-	-	-	-	-	-	-	-	-	-	-
r18	-	-	-	-	-	-	-	-	-	-0.63	-	-	-	-	-	-	-	-	-0.01	-	-	-	-	-	-	-	-	-	-	-	-	-	-	-
r19	-	-	-	-	-	-	-	-	-	-	-	-	-	-	-	-	-	-	-	-	-	-	-	-	-	-	-	-	-	-	-	-	-	-
r20	-	-	-	-	-	-	-	-	-	0.00	-	-	-	-	-	-	-	-	-	-0.41	-0.47	-0.04	-	-	-	-	-	-	-	-	-	-	-	-
r21	0.00	-	-	0.00	-	-	-	-	-	-	-	-	-	-	-	-	-	-	-	-	-	-	-0.83	-	-	-	-	-	-	-	-	-	-	-
r22	-	-	-	-	-	-	-	-	-	-	-	-	-	-	-	-	-	-	-	-	-	-	-	-	-	-	-	-	-	-	-	-	-	-
r23	-	-	-	-	-	-	-	-	-	-	-	-	-	-	-	-	-	-	-	-	-	-	-0.17	0.00	-	-	-	-	-	-	-	-	-	-
r24	-	-	-0.34	-	-	-0.19	-	-	-	-	-	-	-	-	-	-	-0.07	-0.40	-	-	-	-	-	-	-	-	-	-	-	-	-	-	-	-
r25	-	-	-	-	-	-	-	-	-	-	-	-	-	-	-	-	-	-	-	-	-	-	-	-0.49	-	-	-	-	-	-	-	-	-	-
r26	-	-	-	-	0.00	-	-	-	-	-	-	-	-	-	-	-	-	-	-	-	-	-	-	-	-	-	-	-	-	-	-	-	-	-
r27	-	-	-	-	-	-	-	-	-	-	-	-	-	-	-0.01	-	-	-	-	-	-	-	-	-0.51	-	-	-	-	-	-	-	-	-	-
r28	-	-	-	-	-	-	-	-0.01	-	-	-	-	-	-	-	-	-	-	-	-0.06	-	0.00	-	-	-0.76	-	-	-	-	-	-	-	-	-
r29	-	-	-	-	-	-	-	-	-	-	-	-	-	-	-	-	-	-	-	-	-	-	-	-	-	0.04	-0.10	-0.76	-	-	-	-	-	-
r30	-	-	-	-	-	-	-	-	-	-	-	-	-	-	-	-	-	-	-	-	-	-	-	-	-	-0.96	-	-	-0.03	-	-	-	-	-

Table 16 (continued)

	G6P	GLC	F6P	F16P	DHAP	GAP	13PG	3GP	2GP	PYR	PEP	GL6P	6PG	RIBU5P	RIBO5P	XYL5P	S7P	E4P	LAC	GLU	ALA	AKG	G1P	AMP	SER	CIT	OAC	ACOA	CISAC	ISOCIT	SUC	SUCOA	MAL	FUM
r31	-	-	-	-	-	-	-	-	-	-	-	-	-	-	-	-	-	-	-	-	-	-	-	-	-	-	-	-	-0.97	-0.01	-	-	-	-
r32	-	-	-	-	-	-	-	-	-	-	-	-	-	-	-	-	-	-	-	-	-	0.07	-	-	-	-	-	-	-	-0.99	-	-	-	-
r33	-	-	-	-	-	-	-	-	-	-	-	-	-	-	-	-	-	-	-	-	-	-	-	-	-	-	-	-	-	-	-0.92	-0.01	-	-
r34	-	-	-	-	-	-	-	-	-	-	-	-	-	-	-	-	-	-	-	-	-	-	-	-	-	-	-	-	-	-	-	-	-0.70	-0.23
r35	-	-	-	-	-	-	-	-	-	-	-	-	-	-	-	-	-	-	-	-	-	-	-	-	-	-	-0.90	-	-	-	-	-	-0.04	-
r36	-	-	-	-	-	-	-	-	-	-0.10	-	-	-	-	-	-	-	-	-	-	-	-	-	0.00	-	-	-	-0.24	-	-	-	-	-	-
r37	-	-	-	-	-	-	-	-	-	-	-	-	-	-	-	-	-	-	-	-	-	-0.05	-	-	-	-	-	-	-	-	-	-0.94	-	-
r38	-	-	-	-	-	-	-	-	-	-0.01	-	-	-	-	-	-	-	-	-	-	-	-	-	-	-	-	-	-	-	-	-	-	-	-
r39	-	-	-	-	-	-	-	-	-	-	-	-	-	-	-	-	-	-	-	-0.28	-	0.27	-	-	-	-	-	-	-	-	-	-0.05	-	-
r40	-	-	-	-	-	-	-	-	-	-	-	-	-	-	-	-	-	-	-	-	-	-	-	-	-	-	-	-	-	-	-0.08	-	-	-0.77
r41	-	-	-	-	-	-	-	-	-	-	-	-	-	-	-	-	-	-	-	-	-	-	-	-	-	-	-	-	-	-	-	-	-	-
r42	-	-	-	-	-	-	-	-	-	-	-	-	-	-	-	-	-	-	-	-	-	-0.86	-	-	-	-	-	-	-	-	-	-	-	-
r43	-	-	-	-	-	-	-	-	-	-0.03	-	-	-	-	-	-	-	-	-	-	-	-	-	-	-	-	-	-	-	-	-	-	-0.25	-
r44	-	-	-	-	-	-	-	-	-	-	-	-	-	-	-	-	-	-	-	-0.24	-	-0.40	-	-	-	-	-	-	-	-	-	-	-	-
r45	-	-	-	-	-	-	-	-	-	-	-	-	-	-	-	-	-	-	-0.99	-	-	-	-	-	-	-	-	-	-	-	-	-	-	-
r46	-	-	-	-	-	-	-	-	-	-0.23	-	-	-	-	-	-	-	-	-	-	-	-	-	-	-	-	-	-	-	-	-	-	-	-
r47	-	-0.97	-	-	-	-	-	-	-	-	-	-	-	-	-	-	-	-	-	-	-	-	-	-	-	-	-	-	-	-	-	-	-	-
r48	-	-	-	-	-	-	-	-	-	-	-	-	-	-	-	-	-	-	-	-	-0.53	-	-	-	-	-	-	-	-	-	-	-	-	-
r49	-	-	-	-	-	-	-	-	-	-	-	-	-	-	-	-	-	-	-	-	-	-	-	-	-0.24	-	-	-	-	-	-	-	-	-

5.4 Conclusions

This section dealt with the quantitative assessment of the dynamics and control of the central carbon metabolism in hepatoma cells. Metabolite time-series data analyzed in a stimulus response experiment revealed substantial changes in the concentrations of intermediates, and were used for identifying network dynamics. Control analysis was applied in order to break down the internal control structure of the central carbon metabolism in hepatoma cells. In comparison to previous top-down approaches, this study enabled the more detailed analysis of the underlying control patterns. Rather than describing how sub-systems interact with each other, the control distribution approach used quantifies the influences the individual enzymes have on each other. It was possible to unravel many different interactions: Glucose-6-phosphate dehydrogenase had a substantial negative control over the glycolytic flux. Partial flux control coefficients were determined in order to assess the importance of the individual interactions in mediating changes in the flux through the glucose-6-phosphate isomerase enzyme (Ainscow and Brand 1999a; Holzhütter et al. 1985; Sauro 1990). It was shown that the negative control of the glucose-6-phosphate dehydrogenase on the steady state flux through the glucose-6-phosphate isomerase was mediated by an elevated level of its inhibitor 6-phosphogluconate, which was partly compensated by increased substrate and decreased product levels. Another finding was that in HepG2 cells, oxidative phosphorylation had a significant positive control over the metabolic fluxes in glycolysis. This means that in contrast to primary rat hepatocytes (Ainscow and Brand 1999c), hepatoma cells are not affected by the Pasteur effect. This finding is in line with previous studies that found an increased glycolytic activity in the presence of adequate oxygen levels in liver cancer cells (Warburg effect) (Lopez-Lazaro 2008; Warburg et al. 1924). The positive control can possibly be ascribed to fewer mitochondria in hepatoma cells (Lo et al. 1968) or to mitochondrial dysfunction due to mitochondrial DNA mutations (Chen et al. 2007). This finding supports approaches that aim at exploiting the Warburg effect for the treatment of tumors (Lopez-Lazaro 2008; Pelicano et al. 2006). It is important to note that the NADPH-demand does not have exclusive control over the rate of NADPH consumption (0.65). Instead, the control is shared with the NADPH supply (0.38). In accordance with previous studies dealing with the control of the consumption of the cofactor ATP in isolated rat hepatocytes (Ainscow and Brand 1999c), it is increasingly becoming clear that also with regard to NADPH the production and the consumption share the control of the NADPH-consuming reactions. The pyruvate dehydrogenase complex was found to have a substantial positive control over the complete TCA cycle. In addition, different control patterns were observed for the first and the last fluxes in the TCA cycle. The metabolic influx into the TCA cycle could be enhanced by increasing the cellular NAD and pyruvate levels. However, an increase in pyruvate led to a decreased flux through the reaction mediated by the malic enzyme. This is the reason

why ATP consumption has both a positive and negative control over the first and last TCA cycle fluxes. Similarly, glucose-6-phosphate dehydrogenase negatively controls the end of the TCA cycle. The negative control is mainly mediated by an increased NADPH/NADP ratio. The subsequent reaction steps in the TCA cycle are negatively controlled by elevated product levels. The concept of partial flux control proved to be essential for unraveling these control structures. It should be noted that the detailed control structures unraveled in this work had been mainly compared with hepatic control principles obtained from applying top-down approaches in rat hepatocytes (Ainscow and Brand 1999a; Ainscow and Brand 1999c). To further compare our results with a healthy reference state, it would be interesting to see whether these previously reported control distributions based on finite perturbations can be reproduced using dynamic modeling and *in vivo* metabolite time-series measurements from primary human cells.

Partial internal response coefficients were determined in order to investigate the reaction steps that are most relevant in counteracting an increase in intermediates in order to return to the steady state (Ainscow and Brand 1999a; Kahn and Westerhoff 1993). Interestingly, in the case of the metabolites in the downstream part of the glycolysis (1,3-bisphospho-glycerate, glycerate-3-phosphate, glycerate-2-phosphate, and phosphoenolpyruvate), an increase in the concentration was almost exclusively counteracted by additional consumption. This possibly suggests that the corresponding enzymes were close to equilibrium (Ainscow and Brand 1999a).

It is envisaged that in the near future, it will be possible to predict the effects of nutrients in the liver at the inter-individual level by coupling metabolic network models to gene regulation and by integrating individual transcriptome and proteome data. Moreover, systems-oriented analyses of hepatic responses to xenobiotics might enable the personalized prognosis of drug actions and/or their persistency.

6

Conclusions and Outlook

Chapter Outline

6.1 Conclusions 105
6.2 Outlook 109

6.1 Conclusions

The present thesis dealt with data-driven model-based analyses of the hepatic metabolism. The main focus was on the model-assisted interpretation of metabolome and fluxome data. To arrive at a quantitative systems-level understanding, particular emphasize was placed (i) on the experimental observation of stationary and non-stationary ^{13}C-labeling and metabolite data, as well as (ii) on the model-based identification of metabolic fluxes, metabolite dynamics, and metabolic control patterns.

One major goal of this study was to establish the estimation of metabolic fluxes from non-stationary ^{13}C-labeling data in mammalian cells. It is worth noting that ^{13}C-labeling experiments have great potential for obtaining reliable quantitative snapshots of the mammalian metabolism. However, only the experimental observation of the isotopic transient provides the temporal resolution needed for identifying metabolic fluxes in slow- and non-growing mammalian cell fed-batch and batch cultures, in which long observation times would potentially put at risk the assumption of the metabolic steady state and/or cellular integrity. At the onset of this thesis, though, transient ^{13}C-flux analysis had been only just applied to prokaryotic systems (Nöh et al. 2007; Schaub 2007; Schaub et al. 2008; Shastri and Morgan 2007). Therefore, to enable non-stationary ^{13}C-flux analysis in mammalian cells, first of all, an experimental set-up for acquiring transient labeling data was implemented. Reliable procedures were provided for simultaneous quenching of metabolism and extraction of intracellular metabolites. To make a long story short, combined treatment with hot air (150 °C for 5 s) and boiling water yielded the best results in HepG2 cells with respect to energy charge (0.88) and reproducibility. An even higher energy charge of 0.93 was observed when perchloric acid (PCA) was used for extraction. However, the LC-MS methods applied for determining the metabolite data precluded perchloric acid treatment during sample workup. The chemical analyses for the determination of metabolite levels and mass fractions were developed and coordinated by Ute Hofmann (Hofmann et al. 2008). A dynamic labeling experiment was performed using HepG2 cells and ^{13}C-labeled glucose. Non-stationary isotopic abundances and stationary intermediate levels were determined for metabolites of glycolysis, the PPP, and the TCA cycle. For all metabolites replacement of non-labeled intermediate by the ^{13}C-labeled analogue was observed during the labeling experiment. The glycolytic metabolite pools were found to reach isotopic steady state in less than 30 min, while intermediates of the TCA cycle did not attain isotopic steady state even after 120 min. This means that the experimental set-up was adequate for observing transient mass isotopomer data in mammalian cells.

In parallel to establishing the sampling procedures and chemical analyses, a computational framework was developed from previous work by Jochen Schaub for analyzing transient ^{13}C-labeling data (Schaub 2007). The framework was applied to estimate intracellular fluxes, reaction reversibilities, and non-measured intermediate levels from the metabolite and mass fraction data collected from HepG2 cells. In order to reduce the parameter search space, anabolic fluxes into the biomass

were estimated by means of a comprehensive network model of the human hepatic metabolism. It is worth noting that the large-scale network may be used for further structural analyses of the hepatic fed-state, like e.g. the calculation of elementary flux modes or linear programming. In addition, an isotopomer model was set up for simulating the labeling dynamics in glycolysis, the PPP, and the TCA cycle, which was a sub-model of the large-scale model. The isotopomer model comprised 860 balance equations, which was the reason why compiling the balance equation system had to be automated. Moreover, testing different model designs heavily relies on a fast, dependable, and user-friendly method to generate the corresponding isotopomer balances. The analysis of the experimental data was based on an efficient ODE solver (LSODA) capable of switching dynamically between stiff and non-stiff integration methods (Hindmarsh 1983), a sophisticated global optimization routine (CMA-ES) (Hansen and Ostermeier 2001; Streichert and Ulmer 2005), and the concept of free fluxes using the Insilico Discovery software (Insilico Biotechnology AG, Stuttgart, Germany). The *in silico* labeling data were in accordance with the *in vivo* labeling dynamics underlining the suitability of the developed computational framework for analyzing transient ^{13}C-labeling data.

The significance of the tracer-based flux estimates in HepG2 cells was evaluated using sensitivity analysis. Thereby it was shown that the experimentally observed ^{13}C-labeling dynamics allowed for accurately quantifying the split ratio between glycolysis and the PPP. This was also confirmed in a follow-up study in which confidence limits were approximated using the Fisher information matrix (Maier et al. 2007). The split ratio was determined to 57 % and 43 % (glycolysis and PPP). In contrast, using the large-scale model and stoichiometric flux analysis, the split ratio was determined to 94 % and 6 % (glycolysis and PPP). As is known, ^{13}C-labeling experiments are excellent means for elucidating intracellular flux distributions without requiring any assumptions to be made on cofactor balances and energy yields. This means that there must have been at least one additional NADPH-consuming process that was not accounted for in the large-scale network, e.g. elevated scavenging of ROS via glutathione. Considering the level of sophistication of the large-scale model and the substantial difference between the split ratios estimated by conventional stoichiometric and non-stationary ^{13}C-flux analysis, it can be hypothesized that appropriately accounting for the metabolism of cofactors might be even more challenging in the case of mammalian systems than it is in the case of prokaryotic systems. Similarly, Lee et al. emphasized the increased difficulties in setting-up stoichiometric mammalian metabolism models compared to models for bacterial and yeast metabolism (Lee et al. 1999). Summarizing, the identification of metabolic fluxes from non-stationary ^{13}C-labeling data is the most reliable means for elucidating intracellular flux maps in mammalian cells.

The implementation of isotopic non-stationary ^{13}C-flux analysis paved the way for estimating metabolic fluxes in primary hepatocytes, which are characterized by even smaller growth rates than HepG2 cells and are prone to be affected by dedifferentiation. It should be noted that the second

goal of this thesis was to determine systems-level effects of a therapeutic concentration of the hypolipidemic drug atorvastatin on cholesterol synthesis and the central carbon metabolism in primary rat hepatocytes. This became possible by using transient ^{13}C-flux analysis to quantify the cholesterol synthesis rates and the central carbon fluxes. In preliminary experiments, primary hepatocytes were found to release glucose and therefore carbon-labeled glutamine was used as tracer instead of carbon-labeled glucose. This contribution was the first to use experimental observations of stationary and non-stationary ^{13}C-labeling data to analyze statin effects on cholesterol biosynthesis and the central metabolism in primary rat hepatocytes.

For simulation of the intracellular labeling dynamics, a compartmented isotopomer model was set up comprising both positional isotopomer and mass isotopomer balance equations. Modeling the cholesterol pathway with mass isotopomers decreased the number of required balance equations significantly, e.g. cholesterol can be either modeled with 28 mass isotopomer or with 2^{27} positional isotopomer balance equations. Alternatively, one could have applied the recently developed EMU approach to reduce the number of balance equations (Antoniewicz et al. 2007a; Young et al. 2008). The performance and stability of the numerical calculations could be further improved by exploiting the conservation relations to reformulate the ordinary differential equations as differential algebraic equations and by using the linearly implicit algebraic solver LIMEX (Deuflard et al. 1987) to simulate the time behavior of the resulting DAE-system.

Isotopic steady state was attained in less than 4 h in the central carbon metabolism but not in the cholesterol pathway, regardless of whether the hypolipidemic agent was administered or not. In other words, accounting for the isotopic transient proved to be essential for assessing metabolic fluxes in the cholesterol synthesis pathway in primary rat hepatocytes. One important finding was that the flux through the cholesterol pathway decreased from 0.27 to 0.08 mmol/(l_{cv}·h) in response to the administration of atorvastatin, while the cellular concentration of the marker metabolite lathosterol decreased from 0.022 to 0.003 mmol/l_{cv}. Consequently, the time constant of the lathosterol pool dropped from 6.2 to 4.6 min after administration of the drug. In contrast to the substantially decreased cholesterol flux, only minor differences were determined in the central carbon metabolism between untreated cells and cells treated with 50 nM atorvastatin. The decreased flux into the cholesterol pathway was compensated by increased release of ketone bodies, which has been also observed previously in rats treated with the hypocholesterolemic agents cholestyramine and pravastatin (Sato et al. 2002). To summarize, using a therapeutic atorvastatin level no pleiotropic effects could be detected with respect to the central carbon metabolism. It should be noted that such quantitative systems-oriented analyses of the modes of action are promising means for supporting future risk assessments of adverse side effects of new drug candidates.

Flux identification from non-stationary ^{13}C-labeling data provides estimates for both metabolic fluxes and intermediate levels. Utilizing this information, this work exemplified for the first time how transient ^{13}C-flux analysis can be applied in the context of metabolic control theory. It was possible to further deduce systems-level effects of the administered drug by quantifying the flux control of the targeted 3-hydroxy-3-methylglutaryl-coenzyme A (HMG-CoA) reductase enzyme. The flux control coefficient of the HMG-CoA reductase over the cholesterol synthesis flux was determined to 0.46. This means that, on account of the summation theorem for flux control coefficients, evidence was provided that the HMG-CoA reductase does not completely control cholesterol biosynthesis. Other enzymes may be also potent targets for lowering blood cholesterol levels.

Another major goal of the present thesis was to develop the first dynamic hepatic central carbon metabolism model and use it to unravel the internal control structure in hepatoma cells. For the dynamic modeling of the hepatic metabolism, canonical linlog kinetics were used for describing the reaction kinetics. The linlog formalism has been demonstrated previously to yield a good approximation quality while only requiring comparatively few parameters to be identified (Heijnen 2005; Kresnowati et al. 2005; Reuss et al. 2007; Visser and Heijnen 2003). A two-step approach was applied for parameterizing the kinetic model. In the sections 2 and 3 of this thesis the steady state flux map was estimated from non-stationary ^{13}C-labeling data. Subsequently, steady state metabolite levels and scaled elasticities, that is, the kinetic parameters, were determined from stationary and non-stationary metabolite data. It is worth emphasizing that the experimental observation of extra- and intracellular metabolite time-series from stimulus-response experiments are considered adequate means for identifying *in vivo* metabolite dynamics (Chassagnole et al. 2002; Nikerel et al. 2006; Rizzi et al. 1997; Theobald et al. 1997). Therefore, a stimulus-response experiment was designed and dynamic metabolite data were collected after perturbing hepatoma cells by depriving them of extracellular glucose. The experimentally observed metabolite time-series offered substantial changes in intermediate levels for identifying the network dynamics. In short, metabolites from glycolysis and the PPP showed substantial decreases in response to the stimulus, in the TCA cycle damped oscillations were observed for citrate, isocitrate, and cis-aconitate, and the cofactors NAD, ATP, and NADP were found to deviate only slightly from their initial values. The *in silico* metabolite dynamics were in accordance with the measured data.

Concentration and flux control coefficients, partial flux control coefficients, and internal response coefficients were deduced in order to break down the control structure of the central carbon metabolism in hepatoma cells. The novelty of this work arises from using a dynamic model for investigating the metabolic control patterns, which enabled the so far most detailed dissection of the control principles underlying the hepatoma metabolism. The glucose-6-phosphate dehydrogenase was found to exert a substantial negative control over glycolysis. In addition, it positively controlled the

PPP and the cellular NADPH level. From these findings and the previously determined steady state split ratio between glycolysis and the PPP of 57 % to 43 % it can be concluded that the hepatoma growth is limited by the NADPH supply. It is interesting to note that this supports the hypothesis of the glucose-6-phosphate dehydrogenase reaction being a promising target for tumor treatment, which had been coined previously by Boren et al. (Boren et al. 2002). Another finding was that, unlike primary cells (Ainscow and Brand 1999c), the HepG2 cells showed no Pasteur effect. In contrast, oxidative phosphorylation had a substantial positive control over the metabolic fluxes in glycolysis. This result was in accordance with the common characteristic of liver cancer cells referred to as Warburg effect or aerobic glycolysis. That is, in contrast to normal liver tissue, liver cancer cells have an increased glycolytic flux in the presence of an adequate oxygen supply. Interestingly, the elevated glycolysis flux of most malignant cells is also increasingly recognized as a promising target for cancer therapy (Lopez-Lazaro 2008; Pelicano et al. 2006), which is in line with the findings in this work. In addition, complex control patterns were unraveled for the TCA cycle reactions. Increased NAD and pyruvate levels were found to enhance the influx into the TCA cycle, whereas elevated pyruvate levels and an increased NADPH/NADP ratio mediated negative control over the malic enzyme reaction. This is the reason why glucose-6-phosphate dehydrogenase and the ATP consuming reaction were found to exert positive and negative control over the first and last reactions in the TCA cycle, respectively. A negative (positive) control over the malic enzyme was shown to be mediated through the downstream reactions in the TCA cycle by elevated (decreased) product levels. The forwarding mechanisms of the negative and positive controls of the malic enzyme reaction could be traced back by means of analyzing the corresponding partial flux control coefficients.

6.2 Outlook

This work provided adequate means for time-resolved experimental observations and model-based analyses of ^{13}C-labeling dynamics in mammalian cells. The higher temporal resolution of the flux distributions obtained from non-stationary mass fraction data enables the identification of metabolic fluxes in batch and fed-batch operated mammalian cell culture systems. Therefore, it is expected that the application of transient ^{13}C-flux analysis will play a major role in future process development and process control of biopharmaceuticals with mammalian production strains, like e.g. Chinese hamster ovary (CHO) cells. Moreover, the practicability of the outlined flux estimation method has been successfully demonstrated with primary rat hepatocytes treated with a therapeutic concentration of 50 nM atorvastatin, which was an important step on the avenue towards the (i) monitoring of disease progression by chemical biopsy, (ii) assessing the effects of therapeutics on basic cellular metabolism, and (iii) novel disease state classification strategies based on metabolic criteria (Lee et al. 1999).

Within the last years, the field of constrained-based metabolic network modeling has witnessed the emergence of several genome-scale stoichiometric models (Forster et al. 2003; Mo et al. 2007; Schilling et al. 2002). In contrast, the isotopomer models reported in the literature were mostly substantially smaller. Until now, the main limiting factor in reconstructing a large-scale isotopomer model was the size of the resulting DAE-/ODE-system. This is because when using the positional isotopomer (Schmidt et al. 1997) or cumomer (Wiechert et al. 1999) approaches, 2^n balance equations need to be set up for a metabolite containing n C-atoms. Therefore, mass isotopomer balances were used in this thesis for simulating the labeling dynamics in the cholesterol pathway of primary rat hepatocytes. Similarly, the recently proposed EMU approach aims at reducing the necessary number of balance equations (Antoniewicz et al. 2007a). Young et al. further improved on this method by adding block decoupling to reduce the computational difficulty (Young et al. 2008). This means that the ground is prepared for the reconstruction of large-scale isotopomer models for ^{13}C-flux analysis. Alternatively, Blank et al. and Suthers et al. combined constrained-based modeling with ^{13}C-flux analysis to unravel intracellular flux distributions at the large-scale in *Saccharomyces cerevisiae* (Blank et al. 2005) and *Escherichia coli* (Suthers et al. 2007).

The formulation of an isotopomer model requires detailed knowledge of the atom transitions in the metabolic pathways of interest. However, to date no open-access database offers this kind of information, i.e. currently the assembling of the information about atom mappings is tediously retrieved from literature search and biochemistry textbooks. Therefore, it is expected that the availability of manually curated databases containing organism-specific information on atom transitions in metabolic pathways could speed up the process of setting-up large-scale isotopomer models significantly. The proprietary Biochemical Pathways database hosted by the privately owned company Molecular Networks GmbH (Erlangen, Germany) provides access to biological transformations as described on the Roche Applied Science "Biochemical Pathways" wall chart. Moreover, up to now no specific computer-readable format has been proposed for representing and exchanging existing isotopomer models. For the time being, the Systems Biology Markup Language (SBML) could be used for that purpose. Pitkänen et al. contributed ReMatch, which is a web-based tool that allows for semi-automated augmentation of stoichiometric network models with the corresponding carbon mappings and exporting the results in the SBML archival format (Pitkänen et al. 2008). The computational framework developed in this work for analyzing stationary and non-stationary ^{13}C-labeling data allows to automatically compile an isotopomer model from an user-defined spreadsheet containing the information about the atom transfer mechanisms. This user-friendly approach facilitates accelerated model set-up and thus paves the way for routine quantifications of intracellular metabolite fluxes by ^{13}C-tracer experiments. Very recently, Quek et al. developed OpenFlux, which is a modeling environment for steady-state ^{13}C-based metabolic flux analysis (Quek et al. 2009). OpenFlux uses the

EMU framework and compiles the balance equations from an Excel file containing metabolic reactions and carbon atom mappings. It is worth noting that a graphically oriented network setup would further ease the model reconstruction process.

To enable flux identification at the large scale, comprehensive (non-stationary) ^{13}C-labeling data sets have to be provided. This creates the need for (i) the efficient extraction of a plethora of different chemical families and (ii) sensitive methods for the quantification of intermediate levels and mass fractions at high throughput. The experimental set-up developed in this thesis and the chemical analyses contributed by Ute Hofmann (Hofmann et al. 2008) allowed the estimation of metabolic fluxes in the central carbon metabolism and cholesterol biosynthesis from stationary and non-stationary mass isotopomer data. Nevertheless, considering the recent advances in ^{13}C-based modeling techniques, at present, the chemical analyses remain as bottleneck in large-scale ^{13}C-flux analysis. In order to decrease the necessary effort of the chemical analyses, model-based experimental design will play an increasingly prominent role. An important aspect in the design of labeling experiments is the choice of tracer such that the informational content of measurable compounds becomes maximal. On the other hand, *a priori* identification of promising metabolite pools with an expected high amount of information can guide the development of adequate analytical methods. Moreover, automation of the chemical labeling experiment has great potential for improving both the accuracy of the sampling process and the reproducibility of the experiment, and for increasing the data throughput. It should be noted that the microtiter 6-well plates used in this thesis are especially suited for automation. It is expected that automation will eventually allow for parallel operation of several ^{13}C-labeling experiments rendering this technology interesting for high throughput quantitative analyses of drug and/or nutrient effects at the systems-level.

In order to establish the uncertainties associated with the metabolic fluxes estimated from non-stationary ^{13}C-labeling data, a local sensitivity analysis was performed (chapter 3) and confidence limits were approximated by calculating the inverse of the Fisher information matrix (chapter 4). Without such information it would have been impossible to interpret the physiological significance of the obtained flux estimates. The methods used in this thesis were based on linearization and determined local properties. Moreover, according to the Cramér-Rao inequality the Fisher information matrix can only deliver a lower-bound estimate of the parameter covariance matrix (Schmid 2007). Monte Carlo based methods for estimating the confidence of flux estimates account for the inherent non-linearity of isotopomer systems but were found to be computationally demanding for large networks (Antoniewicz et al. 2006). To enable fast and accurate approximation of the true flux uncertainty, Antoniewicz et al. devised a parameter continuation approach (Antoniewicz et al. 2006). It was shown to deliver confidence limits that closely resembled those from using Monte Carlo and grid search methods in an example network. In addition to the determination of statistical properties of

flux estimates, structural identifiability is increasingly recognized as an essential tool in the design of chemical labeling experiments. Structural identifiability deals with the question which parameters of a particular system can be uniquely determined. Identifiability analysis is expected to improve the design of both future tracer experiments and isotopomer models significantly. The fact that some approaches for analyzing the structural identifiability of non-linear models become mathematically intractable with increasing model complexity led Hengl et al. to propose a data-based method to address the identifiability of non-linear dynamic systems (Hengl et al. 2007). To summarize, eventually modeling environments for isotopomer studies should provide adequate means for both deducing the statistical significance of flux estimates and addressing identifiability. Similarly, in the context of dynamic modeling, the determination of statistically sound confidence intervals and identifiability will gain importance with the advent of large-scale dynamic network models.

In this work the dynamic modeling of the hepatic metabolism was based on the canonical linlog formalism. The linlog approach approximates the *in vivo* enzyme kinetic mechanisms by summation of elasticity-weighted logarithmic concentration terms, which is the reason why some important biological regulation principles cannot be described adequately. For example, the phosphofructokinase enzyme is known to be inhibited by high ATP levels, whereas ATP at low concentrations exerts an activating effect (Berg et al. 2002). In this particular case, the linlog approximation combines both effects into a single elasticity value. To circumvent such limitations, hybrid modeling has been proposed in which only the central regulatory enzymes are described by detailed mechanistic rate equations and the majority of enzymes are approximated by simplified rate equations (Bulik et al. 2009). However, in this contribution the linlog-based model simulations were in accordance with the substantial changes in intermediate experimentally observed from HepG2 cells in a stimulus response experiment (cf. chapter 5). Therefore, it is no wonder that in his exploratory bachelor thesis performed at the Institute of Biochemical Engineering at the University of Stuttgart, Philipp Grimmer observed only minor differences between hybrid modeling and the purely linlog-based approach used in this work (Grimmer 2009). Nevertheless, hybrid modeling has great potential for appropriately describing large perturbations and complex regulation phenomena. Moreover, to approximate the real *in vivo* enzyme kinetics, comprehensive knowledge on activator and inhibitor effects is essential. It should be noted that this applies equally to any other modeling approach for describing intracellular reaction rates. This means that such knowledge, which at present is only fragmentary documented in biochemistry textbooks, primary literature, and internet-based databases like for example BRENDA (Chang et al. 2009; Schomburg et al. 2002) and SABIO-RK (Wittig et al. 2006), will gain in importance for the construction of dynamic whole-cell metabolic network models. To fill gaps in existing knowledge, Grimbs et al. proposed using structural information to deduce some modulator effects (Grimbs et al. 2007).

An inherent challenge in experimentally observing eukaryotic ^{13}C-labeling and metabolite dynamics data lies in the compartmentation of eukaryotic cells. In this thesis, cell-averaged experimental data were determined and analyzed. On this account, averaged isotopomer and metabolite time-series were simulated using non-compartmented models (chapters 3 and 5), and cell-averaged mass fraction and intermediate levels were calculated using a compartmented isotopomer model (chapter 4). To implement an experimental and analytical set-up for the acquisition of quantitative stationary and non-stationary ^{13}C-labeling and metabolite data in different cell compartments, sampling procedures for the quenching of metabolism and the extraction of metabolites have to be developed that ensure the efficient isolation of intact sub-cellular reaction compartments. Theobald et al. devised a method based on differential extraction for determining cytosolic intermediate levels in *Saccaromyces cerevisia* and applied it to the quantification of adenine nucleotides (Theobald et al. 1994) and orthophosphate (Theobald et al. 1996). Due to the increase in the amount of information, the identification of metabolite fluxes and dynamics from quantitative isotopomer and metabolite data at a sub-cellular resolution is expected to give further insights into the cellular physiology. Another interesting approach for increasing the information content of stimulus response experiments was coined by Wahl et al., who advocate using ^{13}C-labeled substrates in combination with experimental observations of mass isotopomers under metabolic non-stationary conditions (Wahl et al. 2008).

The dynamic hepatoma central carbon metabolism model developed in this work from experimental observations of stimulus response time-series data may open up new possibilities for quantifying the systems-level effects of drug candidates for tumor treatment. It is worth emphasizing that the internal control structure unraveled using the dynamic model supported the hypotheses of the glucose-6-phosphate dehydrogenase reaction and the Warburg effect being interesting targets for tumor treatment (Boren et al. 2002; Lopez-Lazaro 2008; Pelicano et al. 2006). The development of novel drugs and combination therapies could be guided by the presented dynamic network model. The metabolic changes through administering drugs and combinations of drugs can be predicted *in silico* given an estimate of their inhibitory impact. In addition, as was demonstrated in chapter 4, flux estimates from non-stationary ^{13}C-labeling data collected from primary cells allow for a quantitative systems-oriented analysis of the effects of the administered drugs.

The purpose that drove the reconstruction of the dynamic network model developed in this thesis was to describe the dynamics of the central carbon metabolism in hepatic cells. To expand the validity of the dynamic model, integration of adjacent metabolic pathways is straightforward. One of the major goals of the network detoxification in the second project phase of the systems biology BMBF-funding initiative “HepatoSys” was to provide systems-oriented analysis of the effects and the detoxification of statins. Thus, with respect to the central metabolism, the cholesterol pathway should be included to integrate the site of action of the hypolipidemic agents. In addition, the detoxification

module needs to be accounted for to allow for accurate time-resolved description of the degradation of the administered drugs. An exploratory attempt has been made and presented on the 9th International Conference on Systems Biology (ICSB 2008, Gothenburg, Sweden) to build a dynamic model of the central metabolism, cholesterol synthesis, and the detoxification of xenobiotics using linlog kinetics and experimentally determined metabolite time-series data from primary rat hepatocytes (Maier et al. 2008b). At present Joachim Bucher (Institute of biochemical engineering at the University of Stuttgart, network detoxification, HepatoSys) is in charge of developing a more sophisticated dynamic detoxification module based on mechanistic rate equations and experimental observations of intracellular metabolite dynamics. That is, the next step would be to substitute the detoxification module build by Joachim Bucher for the basic linlog-based sub-model. Moreover, Prem Murugan (Institute of Biochemical Engineering at the University of Stuttgart, network detoxification, HepatoSys) is working on unraveling and deciphering the corresponding transcriptional regulatory network from large-scale gene expression data using the framework of probabilistic Boolean modeling, Markov chain analysis, and neural network theory. The interactions between the central metabolism, drug detoxification, and key transcription factors are manifold. For example liver X receptors (LXRs) and farnesoid X receptor (FXR) are nuclear factors that are needed for maintaining a balanced regulation of cholesterol and bile acid metabolism, whereas primary bile acids were found to induce the transcription of the cytochrome P450 3A4 (CYP3A4) enzyme, which is the predominant CYP450 detoxifying enzyme in humans (Kalaany and Mangelsdorf 2006), to name but a few. Consequently, the accuracy and validity of the dynamic model could be improved by including the detoxification module developed by Joachim Bucher and the regulatory interactions inferred by Prem Murugan.

It is envisaged that the model-based integration of metabolome, fluxome, genome, transcriptome, and proteome data will become an essential step on the avenue towards predicting the effects of xenobiotics and nutrients in the liver at the inter-individual level. In other words, systems-aware analyses of the hepatic physiology might eventually enable the personalized prognosis of drug actions and/or their persistency. Furthermore, it is expected that systems-oriented investigations at the cellular, organ, and whole body level will gain in importance for expanding our knowledge of the actions of drugs and designing effective novel treatment strategies.

Appendix

Chapter Outline

A. Stoichiometry of the Large-Scale Network Model of Human Hepatic Metabolism 116
Reactions 116
Transporter 123
Compounds 126
B. Atom Mappings for Identifying Metabolic Fluxes in the Cholesterol Synthesis Pathway and Central Carbon Metabolism 132
C. Simulated and Measured Mass Fractions of Phosphoenolpyruvate, Malate, Fumarate, Alpha-Ketoglutarate, Citrate, and Cholesterol in Response to 0 and 50 nM Atorvastatin 134
D. Estimated Metabolic Fluxes and Reversibilities in Primary Rat Hepatocytes in Response to 0 and 50 nM Atorvastatin 136
E. Matrix of scaled elasticities 138
F. Experimentally Determined Initial Metabolite Concentrations 140
G. Matrix of Flux Control Coefficients 141
H. Matrix of Concentration Control Coefficients 143

Appendix A. Stoichiometry of the Large-Scale Network Model of Human Hepatic Metabolism. The model accounts for 415 reactions (including 39 extracellular and 89 intracellular transportation steps) and 416 balanced compounds. Six reaction compartments are discriminated: cytosol, mitochondrion, peroxisome, nucleus, golgi-apparatus, and endoplasmic reticulum.

REACTIONS

succinate dehydrogenase (ubiquinone) (EC Number : 1.3.5.1; mitochondria): fadh2+ coq=> fad+ coqr
5-aminolevulinate synthase (EC Number : 2.3.1.37; mitochondria): sucoa + gly +h= 5alev + coa + co2
2-aminoadipate transaminase (EC Number : 2.6.1.39; cytosol): amadip + akg = oxadip + glu
saccharopine dehydrogenase (NAD+, L-glutamate-forming) (EC Number : 1.5.1.9; cytosol): sap + h2o + nad = amaps + glu + nadh + h
saccharopine dehydrogenase (NAD+, L-lysine-forming) (EC Number : 1.5.1.7; cytosol): lys + akg + nadh + h = sap + h2o + nad + h
acetyl-CoA C-acyltransferase (EC Number : 2.3.1.16; peroxisom): oxcoa + coa = cholocoa + propcoa
acetyl-CoA C-acyltransferase (EC Number : 2.3.1.16; peroxisom): diox + coa = chencoa + propcoa
acetyl-CoA C-acyltransferase (EC Number : 2.3.1.16; mitochondria): macaccoa + coa = propcoa + accoa
acetyl-CoA carboxylase (EC Number : 6.4.1.2; cytosol): accoa + cccp = malcoa + bccp + h
biotin carboxylase (EC Number : 6.3.4.14; cytosol): atp + bccp + hco3 = adp + p + cccp
acyl-Coenzyme A dehydrogenase family (EC Number : 1.3.99.-; peroxisom): cholcoa + nad = cholencoa + nadh + h
acyl-Coenzyme A dehydrogenase family (EC Number : 1.3.99.-; peroxisom): dihycholanoylcoa + nad = dihycholenoylcoa + nadh + h
3-hydroxyisobutyryl-CoA hydrolase (EC Number : 3.1.2.4; mitochondria): hibutcoa + h2o = hibut + coa + h
butyryl-CoA dehydrogenase (EC Number : 1.3.99.2; mitochondria): mprocoa + fad = macrylcoa + fadh2
butyryl-CoA dehydrogenase (EC Number : 1.3.99.2; mitochondria): mbutycoa + fad = mcrotycoa + fadh2
acetyl-CoA C-acetyltransferase (EC Number : 2.3.1.9; mitochondria): 2*accoa = acaccoa + coa
acetyl-CoA C-acetyltransferase (EC Number : 2.3.1.9; cytosol): 2*accoa = acaccoa + coa
aminocarboxymuconate-semialdehyde decarboxylase (EC Number : 4.1.1.45; cytosol): amcarbsem = ammucsem + co2
aconitate hydratase (EC Number : 4.2.1.3; mitochondria): cit = cisac + h2o
aconitate hydratase (EC Number : 4.2.1.3; mitochondria): cisac + h2o = isocit
long-chain-fatty-acid-CoA ligase (EC Number : 6.2.1.3; cytosol): pal + atp + coa = palcoa + amp + pp + h
long-chain-fatty-acid-CoA ligase (EC Number : 6.2.1.3; cytosol): linol + atp + coa = lincoa + amp + pp + h
alcohol dehydrogenase (EC Number : 1.1.1.1; endoplasmic-reticulum): trihydchol + nad = dihycholal + nadh + h
adenylosuccinate lyase (EC Number : 4.3.2.2; cytosol): apris = fum + aicar
adenylosuccinate lyase (EC Number : 4.3.2.2; cytosol): adesuc = fum + amp
adenylosuccinate synthase (EC Number : 6.3.4.4; cytosol): gtp + imp + asp = gdp + p + adesuc + 2*h
1-acylglycerol-3-phosphate O-acyltransferase (EC Number : 2.3.1.51; endoplasmic-reticulum): acglyc3p + lincoa = coa + diacglyc3p
5'-nucleotidase (EC Number : 3.5.4.5; cytosol): cyt + h2o + h = uri + nh4
alpha-ketobutyrate dehydrogenase (EC Number : 1.2.1.-; mitochondria): oxob + nad + coa = propcoa + co2 + nadh
adenylate kinase (EC Number : 2.7.4.3; cytosol): atp + amp = 2*adp
3alpha-hydroxysteroid dehydrogenase (B-specific) (EC Number : 1.1.1.50; endoplasmic-reticulum): dihycholestan + nadph + h = tripos + nadp
3alpha-hydroxysteroid dehydrogenase (B-specific) (EC Number : 1.1.1.50; endoplasmic-reticulum): hycholestan + nadph + h = dipos + nadp
3-oxo-5beta-steroid 4-dehydrogenase (EC Number : 1.3.99.6; endoplasmic-reticulum): dihychol + nadph + h = dihycholestan + nadp
3-oxo-5beta-steroid 4-dehydrogenase (EC Number : 1.3.99.6; endoplasmic-reticulum): hydchol + nadph + h = hycholestan + nadp
aldehyde dehydrogenase (NAD+) (EC Number : 1.2.1.3; endoplasmic-reticulum): dihycholal + nad + h2o = dihycholoate + nadh + h
formyltetrahydrofolate dehydrogenase (EC Number : 1.5.1.6; cytosol): fthf10 + nadp + h2o = thf + co2 + nadph + h

methylmalonate-semialdehyde dehydrogenase (acylating) (EC Number : 1.2.1.27; mitochondria): mmalsald + coa + nad = propcoa + nadh + co2
fructose-bisphosphate aldolase (EC Number : 4.1.2.13; cytosol): fdp = dhap + gap
L-aminoadipate-semialdehyde dehydrogenase (EC Number : 1.2.1.31; cytosol): amaps + nad + h2o = amadip + nadh + h
2-aminomuconate dehydrogenase (EC Number : 1.5.1.-; cytosol): ammuc + nadh + h2o = oxadip + nad + nh4
aminomuconate-semialdehyde dehydrogenase (EC Number : 1.2.1.32; cytosol): ammucsem + nad + h2o= ammuc + nadh + h
arginase (EC Number : 3.5.3.1; cytosol): arg + h2o = orn + urea + h
arylformamidase (EC Number : 3.5.1.9; cytosol): kyn + form + h = formkyn + h2o
argininosuccinate lyase (EC Number : 4.3.2.1; cytosol): argsuc + h = fum + arg
Asparagine synthase (glutamine-hydrolysing) (EC Number : 6.3.5.4; cytosol): atp + asp + gln + h2o = amp + pp + asn + glu + 2*h
argininosuccinate synthase (EC Number : 6.3.4.5; cytosol): citl + asp + atp = argsuc + amp + pp + 3*h
phosphoribosylaminoimidazolecarboxamide formyltransferase (EC Number : 2.1.2.3; cytosol): fthf10 + aicar= thf + fpic
methylglutaconyl-CoA hydratase (EC Number : 4.2.1.18; mitochondria): mglutcoa + h2o = hmgcoa
album Synthesis (cytosol): 62*ala+24*arg+17*asn +36*asp+35*cys+61*glu+20*gln+13*gly+16*his+8*ileu+61*leu+59*lys+6*met+31*phe+24*pro+24*ser+28 *thr+1*try+18*tyr+41*val+584*atp+584*h2o = albumin+584*adp+584*p+584*h
glycine N-choloyltransferase (EC Number : 2.3.1.65; peroxisom): cholocoa + gly = glychol + coa + 4*h
glycine N-choloyltransferase (EC Number : 2.3.1.65; peroxisom): cholocoa + tau = tauchol + coa + 4*h
glycine N-choloyltransferase (EC Number : 2.3.1.65; peroxisom): chencoa + gly = chenochol + coa + 4*h
branched-chain-amino-acid transaminase (EC Number : 2.6.1.42; cytosol): leu + akg = glu + akcap
branched-chain-amino-acid transaminase (EC Number : 2.6.1.42; cytosol): val + akg = glu + akval
branched-chain-amino-acid transaminase (EC Number : 2.6.1.42; cytosol): ileu + akg = glu + akmval
3-methyl-2-oxobutanoate dehydrogenase (lipoamide) (EC Number : 1.2.4.4; mitochondria): akcap + liam + h = mbutliam + co2
3-methyl-2-oxobutanoate dehydrogenase (lipoamide) (EC Number : 1.2.4.4; mitochondria): akval + liam + h = mproliam + co2
3-methyl-2-oxobutanoate dehydrogenase (lipoamide) (EC Number : 1.2.4.4; mitochondria): akmval + liam +h = mbutyliam + co2
3-hydroxybutyrate dehydrogenase (EC Number : 1.1.1.30; mitochondria): aceace + nadh + h = hbut + nad
biomass synthesis (cytosol): 3097.1*protein+7.71*glyg+140.9638554 *triacylglycerol+0.173654*rna= bio
phosphoglycerate mutase (EC Number : 5.4.2.1; cytosol): g3p = g2p
bile formation (cytosol): 22.34*glychol+11.17*tauchol+33.50*chenochol+0.0004622*lipid+0.0391542678 *protein=bile
carbamoyl-phosphate synthase (glutamine-hydrolysing) (EC Number : 6.3.5.5; mitochondria): gln + co2 + 2 * h2o + 2*atp = glu + carbp + 2*adp + p + 3*h
aspartate carbamoyltransferase (EC Number : 2.1.3.2; cytosol): asp + carbp = carbasp + p + h
dihydroorotase (EC Number : 3.5.2.3; cytosol): carbasp + h = dhoro + h2o
Carbamoyl-phosphate synthase (glutamine-hydrolysing) (EC Number : 6.3.5.5; cytosol): gln + co2 + 2*h2o + 2*atp = glu + carbp + 2*adp + p + 3*h
cystathionine beta-synthase (EC Number : 4.2.1.22; cytosol): ser + hcys = cysio + h2o
CDP-diacylglycerol-inositol 3-phosphatidyltransferase (EC Number : 2.7.8.11; endoplasmic-reticulum): cdpdiacglyc + mino = cmp + ptyl3ino + h
cysteine dioxygenase (EC Number : 1.13.11.20; cytosol): cys + o2 = sulfala
phosphatidate cytidylyltransferase (EC Number : 2.7.7.41; endoplasmic-reticulum): ctp + diacglyc3p = pp + cdpdiacglyc
choline kinase (EC Number : 2.7.1.32; endoplasmic-reticulum): atp + choli => adp + phoschol + h
cholenCoa hydratase (EC Number : 4.2.1.-; peroxisom): cholencoa + h2o = cholestcoa
cholenCoa hydratase (EC Number : 4.2.1.-; peroxisom): dihycholenoylcoa + h2o = tricholcoa
cholestanetetraol 26-dehydrogenase (EC Number : 1.1.1.161; endoplasmic-reticulum): choles + nad = trichol + nadh + h
cholate-CoA ligase (EC Number : 6.2.1.7; peroxisom): tricholes + atp + coa + 2*h = amp + pp + cholcoa
cholate-CoA ligase (EC Number : 6.2.1.7; peroxisom): dihycholoate + atp + coa + 2*h= amp + pp + dihycholanoylcoa

diacylglycerol cholinephosphotransferase (EC Number : 2.7.8.2; endoplasmic-reticulum): cdpchol + diacglyc = cmp + ptylchol + h
carnitine O-palmitoyltransferase (EC Number : 2.3.1.21; cytosol): propcar + coa + h = propcoa + car
carnitine O-palmitoyltransferase (EC Number : 2.3.1.21; mitochondria): propcar + coa + h = propcoa + car
citrate (Si)-synthase (EC Number : 2.3.3.1; cytosol): oac + accoa + h2o = cit + coa + h
citrate (Si)-synthase (EC Number : 2.3.3.1; mitochondria): oac + accoa + h2o = cit + coa + h
sulfinoalanine decarboxylase (EC Number : 4.1.1.29; cytosol): sulfala + h = hyptau + co2
cystathionine gamma-lyase (EC Number : 4.4.1.1; cytosol): cysio + h2o = cys + nh4 + oxob
cholestanetriol 26-monooxygenase (EC Number : 1.14.13.15; endoplasmic-reticulum): tripos + nadph + h + o2 = choles + nadp + h2o
cholestanetriol 26-monooxygenase (EC Number : 1.14.13.15; endoplasmic-reticulum): dipos + nadph + h + o2 = trihydchol + nadp + h2o
cholesterol 7alpha-monooxygenase (EC Number : 1.14.13.-; endoplasmic-reticulum): hydchol + nadph + h + o2 = dihychol + nadp + h2o
cholesterol 7alpha-monooxygenase (EC Number : 1.14.13.17; endoplasmic-reticulum): chol + nadph + h + o2 = hychol + nadp + h2o
dihydrolipoamide branched chain transacylase (EC Number : 2.3.1.-; mitochondria): mbutliam + coa = dhliam + mbutcoa
dihydrolipoamide branched chain transacylase (EC Number : 2.3.1.-; mitochondria): mproliam + coa = dhliam + mprocoa
dihydrolipoamide branched chain transacylase (EC Number : 2.3.1.-; mitochondria): mbutyliam + coa = dhliam + mbutycoa
serine C-palmitoyltransferase (EC Number : 1.14.-.-; endoplasmic-reticulum): dihycer + nad = cer + nadh + h
3-dehydrosphinganine reductase (EC Number : 1.1.1.102; endoplasmic-reticulum): dehysphing + nadph + h = sphinga + nadp
diacylglycerol O-acyltransferase (EC Number : 2.3.1.20; endoplasmic-reticulum): 2*palcoa + acglyc3p +h2o = 2*coa + triacylglycerol + p
dihydroorotate oxidase (EC Number : 1.3.3.1; cytosol): dhoro + o2 = h2o2 + orot
dihydrolipoamide S-acetyltransferase (EC Number : 2.3.1.12; mitochondria): acedhliam + coa + h= dhliam_pdh + accoa
dihydrolipoamide dehydrogenase (EC Number : 1.8.1.4; mitochondria): dhliam + nad = liam + nadh+h
dihydrolipoamide dehydrogenase (EC Number : 1.8.1.4; mitochondria): dhliam_kgdh + 0.99668*nad + 0.00332*o2 = liam_kgdh + 0.99668*nadh + 0.00332*h2o2 + 0.99668*h
dihydrolipoamide dehydrogenase (EC Number : 1.8.1.4; mitochondria): dhliam_pdh + 0.998008*nad + 0.001992*o2 = liam_pdh + 0.998008*nadh + 0.001992*h2o2 + 0.998008*h
dihydrolipoamide S-succinyltransferase (EC Number : 2.3.1.61; mitochondria): sucdhliam + coa + h= dhliam_kgdh + sucoa
dihydrolipoamide S-succinyltransferase (EC Number : 2.3.1.61; mitochondria): glutliam + coa = dhliam + glutcoa
cholestenol DELTA-isomerase (EC Number : 5.3.3.5; endoplasmic-reticulum): zymos = lat
enoyl-CoA hydratase (EC Number : 4.2.1.17; mitochondria): crotcoa + h2o = hbutcoa
enoyl-CoA hydratase (EC Number : 4.2.1.17; mitochondria): macrylcoa + h2o = hibutcoa
enoyl-CoA hydratase (EC Number : 4.2.1.17; mitochondria): mcrotycoa + h2o = hmbutcoa
3-hydroxyacyl-CoA dehydrogenase (EC Number : 1.1.1.35; mitochondria): hbutcoa + nad = acaccoa + nadh + h
3-hydroxyacyl-CoA dehydrogenase (EC Number : 1.1.1.35; mitochondria): hmbutcoa + nad = macaccoa + nadh + h
phosphopyruvate hydratase (EC Number : 4.2.1.11; cytosol): g2p = pep + h2o + h
adenosinetriphosphatase (EC Number : 3.6.1.3; cytosol): atp + h2o => adp + p + h
fumarylacetoacetase (EC Number : 3.7.1.2; cytosol): faceace + h2o = aceace + fum + h
[acyl-carrier-protein] S-acetyltransferase (EC Number : 2.3.1.38; cytosol): accoa + acp = coa + acacp
enoyl-[acyl-carrier-protein] reductase (NADPH, B-specific) (EC Number : 1.3.1.10; cytosol): hexacp + nadp = transhexacp + nadph + h
3-oxoacyl-[acyl-carrier-protein] synthase (EC Number : 2.3.1.41; cytosol): hexacp + malacp + h = co2 + acp + oxoctacp
3-oxoacyl-[acyl-carrier-protein] reductase (EC Number : 1.1.1.100; cytosol): hyoctacp + nadp = nadph + h + oxoctacp
3-Hydroxypalmitoyl-[acyl-carrier-protein] dehydratase (EC Number : 4.2.1.61; cytosol): hyoctacp = transoctacp + h2o

enoyl-[acyl-carrier-protein] reductase (NADPH, B-specific) (EC Number : 1.3.1.10; cytosol): octacp + nadp = transoctacp + nadph + h
3-oxoacyl-[acyl-carrier-protein] synthase (EC Number : 2.3.1.41; cytosol): octacp + malacp + h = co2 + acp + oxdecacp
3-oxoacyl-[acyl-carrier-protein] reductase (EC Number : 1.1.1.100; cytosol): hydecacp + nadp = nadph + h + oxdecacp
3-hydroxypalmitoyl-[acyl-carrier-protein] dehydratase (EC Number : 4.2.1.61; v): hydecacp = transdecacp + h2o
enoyl-[acyl-carrier-protein] reductase (NADPH, B-specific) (EC Number : 1.3.1.10; cytosol): decacp + nadp = transdecacp + nadph + h
3-oxoacyl-[acyl-carrier-protein] synthase (EC Number : 2.3.1.41; cytosol): decacp + malacp + h = co2 + acp + oxdodecacp
[acyl-carrier-protein] S-malonyltransferase (EC Number : 2.3.1.39; cytosol): malcoa + acp = coa + malacp
3-oxoacyl-[acyl-carrier-protein] reductase (EC Number : 1.1.1.100; cytosol): hydodecacp + nadp = nadph + h + oxdodecacp
3-hydroxypalmitoyl-[acyl-carrier-protein] dehydratase (EC Number : 4.2.1.61; cytosol): hydodecacp = transdodecacp + h2o
enoyl-[acyl-carrier-protein] reductase (NADPH, B-specific) (EC Number : 1.3.1.10; cytosol): dodecacp + nadp = transdodecacp + nadph + h
3-oxoacyl-[acyl-carrier-protein] synthase (EC Number : 2.3.1.41; cytosol): dodecacp + malacp + h = co2 + acp + oxtetradecacp
3-oxoacyl-[acyl-carrier-protein] reductase (EC Number : 1.1.1.100; cytosol): hytetradecacp + nadp = nadph + h + oxtetradecacp
3-hydroxypalmitoyl-[acyl-carrier-protein] dehydratase (EC Number : 4.2.1.61; cytosol): hytetradecacp = transtetradecacp + h2o
enoyl-[acyl-carrier-protein] reductase (NADPH, B-specific) (EC Number : 1.3.1.10; cytosol): tetradecacp + nadp = transtetradecacp + nadph + h
3-oxoacyl-[acyl-carrier-protein] synthase (EC Number : 2.3.1.41; cytosol): tetradecacp + malacp + h = co2 + acp + oxhexdecacp
3-oxoacyl-[acyl-carrier-protein] reductase (EC Number : 1.1.1.100; cytosol): hyhexdecacp + nadp = nadph + h + oxhexdecacp
3-hydroxypalmitoyl-[acyl-carrier-protein] dehydratase (EC Number : 4.2.1.61; cytosol): hyhexdecacp = transhexdecacp + h2o
3-oxoacyl-[acyl-carrier-protein] synthase (EC Number : 2.3.1.41; cytosol): acacp + malacp + h = co2 + acp + acacacp
enoyl-[acyl-carrier-protein] reductase (NADPH, B-specific) (EC Number : 1.3.1.10; cytosol): hexdecacp + nadp = transhexdecacp + nadph + h
oleoyl-[acyl-carrier-protein] hydrolase (EC Number : 3.1.2.14; cytosol): hexdecacp + h2o = acp + pal + h
3-oxoacyl-[acyl-carrier-protein] reductase (EC Number : 1.1.1.100; cytosol): hbacp + nadp = nadph + h + acacacp
3-hydroxypalmitoyl-[acyl-carrier-protein] dehydratase (EC Number : 4.2.1.61; cytosol): hbacp = benacp + h2o
enoyl-[acyl-carrier-protein] reductase (NADPH, B-specific) (EC Number : 1.3.1.10; cytosol): butacp + nadp = benacp + nadph + h
3-oxoacyl-[acyl-carrier-protein] synthase (EC Number : 2.3.1.41; cytosol): butacp + malacp + h = co2 + acp + oxhexacp
3-oxoacyl-[acyl-carrier-protein] reductase (EC Number : 1.1.1.100; cytosol): hyhexacp + nadp = nadph + h + oxhexacp
3-hydroxypalmitoyl-[acyl-carrier-protein] dehydratase (EC Number : 4.2.1.61; cytosol): hyhexacp = transhexacp + h2o
farnesyl-diphosphate farnesyltransferase (EC Number : 2.5.1.21; endoplasmic-reticulum): 2*fasyl = psqual + pp + h
farnesyl-diphosphate farnesyltransferase (EC Number : 2.5.1.21; endoplasmic-reticulum): psqual + nadph = pp + squal + nadp
geranyltranstransferase (EC Number : 2.5.1.10; endoplasmic-reticulum): isyl + dmetp = geran + pp + h
geranyltranstransferase (EC Number : 2.5.1.10; endoplasmic-reticulum): isyl + geran = fasyl + pp + h
fumarate hydratase (EC Number : 4.2.1.2; mitochondria): fum + h2o = mal
glutamate formimidoyltransferase (EC Number : 2.1.2.5; cytosol): formglut + thf + h = glu + formthf
formimidoyltetrahydrofolate cyclodeaminase (EC Number : 4.3.1.4; cytosol): melthf + nh4 = formthf
formate-dihydrofolate ligase (EC Number : 6.3.4.3; cytosol): atp + form + thf = adp + p + fthf10

glucose-6-phosphate 1-dehydrogenase (EC Number : 1.1.1.49; cytosol): g6p + nadp => glac6p + nadph + h
glyceraldehyde-3-phosphate dehydrogenase (phosphorylating) (EC Number : 1.2.1.12; cytosol): gap + p + nad = pg13 + nadh + h
phosphoribosylamine-glycine ligase (EC Number : 6.3.4.13; cytosol): atp + gly + prib = adp + p + gar + h
phosphoribosylglycinamide formyltransferase (EC Number : 2.1.2.2; cytosol): gar + fthf10 = thf + formgar
phosphoribosylformylglycinamidine cyclo-ligase (EC Number : 6.3.5.1; cytosol): atp + fgam = adp + p + air + h
glycine C-acetyltransferase (EC Number : 2.3.1.29; cytosol): accoa + gly = coa + co2 + amac
glutaryl-CoA dehydrogenase (EC Number : 1.3.99.7; mitochondria): glutcoa + fad + h = crotcoa + fadh2 + co2
glucokinase (EC Number : 2.7.1.1; cytosol): glc + atp => g6p + adp + h
glutamate dehydrogenase [NAD(P)+] (EC Number : 1.4.1.3; mitochondria): akg + nh4 + nadh + h = glu + h2o + nad
glutamate-ammonia ligase (EC Number : 6.3.1.2; cytosol): glu + atp + nh4 = gln + adp + p + h
glutamate-ammonia ligase (EC Number : 6.3.1.2; mitochondria): glu + atp + nh4 = gln + adp + p + h
spontaneous breakdown of the semialdehyd glusald (cytosol): pylcx + h2o = glusald
GMP synthase (glutamine-hydrolysing) (EC Number : 6.3.5.2; cytosol): atp + xmp + gln + h2o = amp + pp + gmp + glu + 3*h
aspartate transaminase (EC Number : 2.6.1.1; mitochondria): oac + glu = akg + asp
aspartate transaminase (EC Number : 2.6.1.1; cytosol): oac + glu = akg + asp
aspartate transaminase (EC Number : 2.6.1.1; cytosol): sulfala + akg + h = sulfpyr + glu
glycerol-3-phosphate O-acyltransferase (EC Number : 2.3.1.15; endoplasmic-reticulum): glyc3p + palcoa = coa + acglyc3p
glycerol-3-phosphate dehydrogenase (NAD+) (EC Number : 1.1.1.8; endoplasmic-reticulum): dhap + nadh + h = glyc3p + nad
glucose-6-phosphate isomerase (EC Number : 5.3.1.9; cytosol): g6p = f6p
alanine transaminase (EC Number : 2.6.1.2; cytosol): ala + akg = pyr + glu
glutathione peroxidase (EC Number : 1.11.1.9; cytosol): 2*glutr + h2o2 = gluto + 2*h2o
glutathione peroxidase (EC Number : 1.11.1.9; mitochondria): 2*glutr + h2o2 = gluto + 2*h2o
glutathione reductase (EC Number : 1.8.1.7; cytosol): gluto + nadph + h = 2*glutr + nadp
glutathione reductase (EC Number : 1.8.1.7; mitochondria): gluto + nadph + h = 2*glutr + nadp
maleylacetoacetate isomerase (EC Number : 5.2.1.2; cytosol): maceace = faceace
guanylate kinase (EC Number : 2.7.4.8; cytosol): atp + gmp = adp + gdp
glycogen (starch) synthase (EC Number : 2.4.1.11; cytosol): 20*udpglc = 20*udp + glyg + 20*h
3-hydroxyanthranilate 3,4-dioxygenase (EC Number : 1.13.11.6; cytosol): hydant + o2 = amcarbsem
histidine ammonia-lyase (EC Number : 4.3.1.3; cytosol): his = uroc + nh4
solving of co2 in h2o (cytosol): co2 + h2o = hco3 + h
3-hydroxyisobutyrate dehydrogenase (EC Number : 1.1.1.31; mitochondria): hibut + nad = mmalsald + nadh + h
hydroxymethylglutaryl-CoA lyase (EC Number : 4.1.3.4; mitochondria): hmgcoa = aceace + accoa
hydroxymethylglutaryl-CoA reductase (NADPH) (EC Number : 1.1.1.34; endoplasmic-reticulum): hmgcoa + 2*nadph + 2*h = 2*nadp + mev + coa
hydroxymethylglutaryl-CoA synthase (EC Number : 2.3.3.10; mitochondria): accoa + h2o + acaccoa = hmgcoa + coa + h
hydroxymethylglutaryl-CoA synthase (EC Number : 2.3.3.10; cytosol): accoa + h2o + acaccoa = hmgcoa + coa + h
homogentisate 1,2-dioxygenase (EC Number : 1.13.11.5; cytosol): hmgent + o2 = maceace +h
4-hydroxyphenylpyruvate dioxygenase (EC Number : 1.13.11.27; cytosol): hppyr + o2 = hmgent + co2
hydroxysteroid (17-beta) dehydrogenase 12 (EC Number : 1.1.1.-; peroxisom): cholestcoa + nadp = oxcoa + nadph + h
hydroxysteroid (17-beta) dehydrogenase 12 (EC Number : 1.1.1.-; peroxisom): tricholcoa + nadp = diox + nadph + h
cholest-5-ene-3beta,7alpha-diol 3beta-dehydrogenase (EC Number : 1.1.1.181; endoplasmic-reticulum): hychol + nad = hydchol + nadh + h
hypotaurine dehydrogenase (EC Number : 1.8.1.3; cytosol): hyptau + h2o + nad = tau + nadh + h
isocitrate dehydrogenase (NAD+) (EC Number : 1.1.1.41; mitochondria): isocit + nad = akg + co2 + nadh
isopentenyl-diphosphate DELTA-isomerase (EC Number : 5.3.3.2; endoplasmic-reticulum): isyl = dmetp
phosphoribosylaminoimidazolecarboxamide formyltransferase (EC Number : 3.5.4.10; cytosol): fpic = imp + h2o
inositol-1(or 4)-monophosphatase (EC Number : 3.1.3.25; endoplasmic-reticulum): mino1p + h2o = mino + p
IMP dehydrogenase (EC Number : 1.1.1.205; cytosol): imp + nad + h2o = xmp + nadh + h
Imidazolonepropionase (EC Number : 3.5.2.7; cytosol): imiprop + h2o = formglut
inositol-3-phosphate synthase (EC Number : 5.5.1.4; endoplasmic-reticulum): g6p = mino1p

isovaleryl-CoA dehydrogenase (EC Number : 1.3.99.10; mitochondria): mbutcoa + fad = mcrotcoa + fadh2
kynurenine 3-monooxygenase (EC Number : 1.14.13.9; cytosol): kyn + nadph + h + o2 = hydkyn + nadp + h2o
kynureninase (EC Number : 3.7.1.3; cytosol): hydkyn + h2o = hydant + ala
L-lactate dehydrogenase (EC Number : 1.1.1.27; cytosol): pyr + nadh + h = lact + nad
lanosterol synthase (EC Number : 5.4.99.7; endoplasmic-reticulum): squepo + 13*nadph + 13*h +2*nad + 10*o2 = zymos + 13*nadp + 2*nadh + 2*h + 3*co2 + 14*h2o
amine oxidase (flavin-containing) (EC Number : 1.4.3.4; cytosol): amac + h2o + o2 + h = metgly + nh4 + h2o2
methylcrotonoyl-CoA carboxylase (EC Number : 6.4.1.4; mitochondria): mcrotcoa + atp + co2 + h2o = adp + p + mglutcoa + 2*h
malate dehydrogenase (EC Number : 1.1.1.37; mitochondria): mal + nad = oac + nadh + h
malate dehydrogenase (EC Number : 1.1.1.37; cytosol): mal + nad = oac + nadh + h
ceramide cholinephosphotransferase (EC Number : 2.7.8.3; golgi-apparatus): cer + cdpchol => cmp + sphingo + h
methylenetetrahydrofolate dehydrogenase (NADP+) (EC Number : 1.5.1.5; cytosol): metthfo + nadp = melthf + nadph
methenyltetrahydrofolate cyclohydrolase (EC Number : 3.5.4.9; cytosol): melthf + h2o = fthf10 + h
methylenetetrahydrofolate reductase (NADPH) (EC Number : 1.5.1.20; cytosol): mthf + nadp = metthfo + nadph + h
methionine synthase (EC Number : 2.1.1.13; cytosol): hcys + mthf + h = thf + met
methylmalonyl-CoA mutase (EC Number : 5.4.99.2; mitochondria): metmalcoa = sucoa
diphosphomevalonate decarboxylase (EC Number : 4.1.1.33; endoplasmic-reticulum): mev5pp + atp = adp + p + isyl + co2
mevalonate kinase (EC Number : 2.7.1.36; endoplasmic-reticulum): mev + atp = adp + mev5p + h
nucleoside-diphosphate kinase (EC Number : 2.7.4.6; cytosol): ctp + adp = cdp + atp
nucleoside-diphosphate kinase (EC Number : 2.7.4.6; cytosol): gtp + adp = gdp + atp
nucleoside-diphosphate kinase (EC Number : 2.7.4.6; cytosol): utp + adp = udp + atp
uridine kinase (EC Number : 3.1.3.5; cytosol): ump + h2o => uri + p
ornithine-oxo-acid transaminase (EC Number : 2.6.1.13; cytosol): orn + akg = glu + glusald
oxoglutarate dehydrogenase (lipoamide) (EC Number : 1.2.4.2; mitochondria): akg + liam_kgdh => sucdhliam + co2
oxoglutarate dehydrogenase (lipoamide) (EC Number : 1.2.4.2; mitochondria): oxadip + liam + h = glutliam + co2
ornithine carbamoyltransferase (EC Number : 2.1.3.3; mitochondria): carbp + orn = citl + p
2-oxoaldehyde dehydrogenase (NAD+) (EC Number : 1.2.1.23; mitochondria): metgly + nad + h2o = pyr + nadh + 2*h
phenylalanine 4-monooxygenase (EC Number : 1.14.16.1; cytosol): phe + tehydro + o2 = tyr + dihydro + h2o
phosphoribosylaminoimidazole carboxylase (EC Number : 4.1.1.21; cytosol): air + co2 = prai + h
phosphoribosylaminoimidazolesuccinocarboxamide synthase (EC Number : 6.3.2.6; cytosol): atp + prai + asp = adp + p + apris + h
propionyl-CoA carboxylase (EC Number : 6.4.1.3; mitochondria): propcoa + atp + co2 + h2o => adp + p + met-malcoa + 2*h
choline-phosphate cytidylyltransferase (EC Number : 2.7.7.15; endoplasmic-reticulum): ctp + phoschol = pp + cdpchol
pyruvate dehydrogenase (lipoamide) (EC Number : 1.2.4.1; mitochondria): pyr + liam_pdh => acedhliam + co2
phosphoribosylformylglycinamidine synthase (EC Number : 6.3.5.3; cytosol): atp + formgar + gln + h2o = adp + p + glu + fgam + 2*h
6-phosphofructokinase (EC Number : 2.7.1.11; cytosol): f6p + atp => fdp + adp + h
phosphogluconate dehydrogenase (decarboxylating) (EC Number : 1.1.1.44; cytosol): glt6p + nadp => ribu5p + co2 + nadph
phosphoglycerate kinase (EC Number : 2.7.2.3; cytosol): pg13 + adp + h= g3p + atp
6-phosphogluconolactonase (EC Number : 3.1.1.31; cytosol): glac6p + h2o => glt6p + h
phosphoglucomutase (EC Number : 5.4.2.2; cytosol): g6p = g1p
phosphoglycerate dehydrogenase (EC Number : 1.1.1.95; cytosol): g3p + nad = phxpyr + nadh + 2*h
phosphatidylserine decarboxylase (EC Number : 4.1.1.65; endoplasmic-reticulum): ptylser = ptyletham + co2
pyruvate kinase (EC Number : 2.7.1.40; cytosol): pep + adp + h => pyr + atp
phosphomevalonate kinase (EC Number : 2.7.4.2; endoplasmic-reticulum): atp + mev5p = mev5pp + adp
inorganic diphosphatase (EC Number : 3.6.1.1; cytosol): 2*p <= pp + h2o
inorganic diphosphatase (EC Number : 3.6.1.1; endoplasmic-reticulum): 2*p <= pp + h2o

inorganic diphosphatase (EC Number : 3.6.1.1; peroxisom): 2*p <= pp + h2o
phosphatidate phosphatase (EC Number : 3.1.3.4; endoplasmic-reticulum): diacglyc3p + h2o => diacglyc + p
amidophosphoribosyltransferase (EC Number : 2.4.2.14; cytosol): prib + pp + glu + 2*h = prpp + gln + h2o
protein synthesis (cytosol): 0.077*ala + 0.024*cys + 0.045*asp + 0.064*glu + 0.033*phe + 0.071*gly + 0.026*his + 0.037*ileu + 0.05*lys + 0.099*leu + 0.021*met + 0.031*asn + 0.07*pro + 0.048*gln + 0.061*arg + 0.086*ser + 0.054*thr + 0.06*val + 0.015*try + 0.023*tyr +atp+h2o= protein+adp+p+h
ribose-phosphate diphosphokinase (EC Number : 2.7.6.1; cytosol): rib5p + atp = prpp + amp + h
phosphoserine transaminase (EC Number : 2.6.1.52; cytosol): pser + akg = phxpyr + glu
phosphoserine phosphatase (EC Number : 3.1.3.3; cytosol): pser + h2o = ser + p
CDP-diacylglycerol-serine O-phosphatidyltransferase (EC Number : 2.7.8.8; endoplasmic-reticulum): cdpdiacglyc + ser = cmp + ptylser + h
pyrroline-5-carboxylate reductase (EC Number : 1.5.1.2; cytosol): pylcx + nadph + 2*h = pro + nadp
6,7-dihydropteridine reductase (EC Number : 1.5.1.34; cytosol): tehydro + nadp = dihydro + nadph + h
ribulose-phosphate 3-epimerase (EC Number : 5.3.1.1; cytosol): ribu5p = xyl5p
ribose-5-phosphate isomerase (EC Number : 5.3.1.6; cytosol): ribu5p = rib5p
lathosterol oxidase (EC Number : 1.3.3.2; endoplasmic-reticulum): lat + o2 + nadph + h = prod3 + h2o2 + nadp
succinate dehydrogenase (ubiquinone) (EC Number : 1.3.5.1; mitochondria): suc + fad = fum + fadh2
7-dehydrocholesterol reductase (EC Number : 1.3.1.21; endoplasmic-reticulum): prod3 + nadph + h = chol + nadp
sphingosine N-acyltransferase (EC Number : 2.3.1.24; endoplasmic-reticulum): sphinga + palcoa => dihycer + coa
spontaneous cleavage resulting in pyruvate and sulfite (cytosol): sulfpyr + h2o = pyr + so3 + 2*h
serine C-palmitoyltransferase (EC Number : 2.3.1.50; endoplasmic-reticulum): palcoa + ser = coa + dehysphing + co2
squalene monooxygenase (EC Number : 1.14.99.7; endoplasmic-reticulum): squal + o2 + nadph + h = squepo + nadp + h2o
succinate-CoA ligase (ADP-forming) (EC Number : 6.2.1.5; mitochondria): sucoa + p + adp = suc + coa + atp
sulfite oxidase (EC Number : 1.8.3.1; cytosol): so3 + o2 + h2o = so4 + h2o2
transaldolase (EC Number : 2.2.1.2; cytosol): f6p + ery4p = sed7p + gap
tyrosine transaminase (EC Number : 2.6.1.5; cytosol): tyr + akg = glu + hppyr
tryptophan 2,3-dioxygenase (EC Number : 1.13.11.11; cytosol): try + o2 = formkyn
transketolase (EC Number : 2.2.1.1; cytosol): xyl5p + ery4p = gap + f6p
transketolase (EC Number : 2.2.1.1; cytosol): rib5p + xyl5p = gap + sed7p
threonine ammonia-lyase (EC Number : 4.3.1.19; cytosol): thr = oxob + nh4
triose-phosphate isomerase (EC Number : 5.3.1.1; cytosol): dhap = gap
3alpha,7alpha,12alpha-trihydroxycholestan-26-al 26-oxidoreductase (EC Number : 1.2.1.40; endoplasmic-reticulum): trichol + nad + h2o = tricholes + nadh + h
uridine kinase (EC Number : 2.7.1.48; cytosol): atp + cyt => adp + cmp + h
UTP-glucose-1-phosphate uridylyltransferase (EC Number : 2.7.7.9; cytosol): utp + g1p = udpglc + pp
cytidylate kinase (EC Number : 2.7.4.14; cytosol): atp + ump = adp + udp
cytidylate kinase (EC Number : 2.7.4.14; cytosol): atp + cmp = adp + cdp
orotate phosphoribosyltransferase (EC Number : 2.4.2.10; cytosol): orot + prpp = orotp + pp + h
orotidine-5'-phosphate decarboxylase (EC Number : 4.1.1.23; cytosol): orotp + h = ump + co2
urocanate hydratase (EC Number : 4.2.1.49; cytosol): imiprop = uroc + h2o
uroporphyrinogen decarboxylase (EC Number : 4.1.1.37; cytosol): uroporIII = coproIII + 4*co2
uroporphyrinogen-III synthase (EC Number : 4.2.1.75; cytosol): hmbil = uroporIII + h2o
coproporphyrinogen oxidase (EC Number : 1.3.3.3; mitochondria): coproIII + o2 = protoIX + 2*co2 + 2*h2o
ferrochelatase (EC Number : 4.99.1.1; mitochondria): prophyrIX = haem
hydroxymethylbilane synthase (EC Number : 2.5.1.61; cytosol): 4*porgen + h2o + 4*h= hmbil + 4*nh4
porphobilinogen synthase (EC Number : 4.2.1.24; cytosol): 2*5alev = porgen + 2*h2o
protoporphyrinogen oxidase (EC Number : 1.3.3.4; mitochondria): protoIX + 1.5*o2 = prophyrIX + 3*h2o
rna_pol (nucleus): 553*atp+424*gtp+363*ctp+490*utp=rna+1830*pp+1830*h
superoxide dismutase (EC Number : 1.15.1.1; mitochondria): 2*h + 2*o2- => h2o2 + o2
membrane synthesis (cytosol): 17*chol + 24*ptylchol + 7*ptyletham + 4*ptylser + 19*sphingo + diacglyc3p + ptyl3ino = lipid

TRANSPORTER

NADH dehydrogenase (ubiquinone) (EC Number : 1.6.5.3; mitochondria - cytosol): nadh_mitochondria + h_mitochondria + 4*h_mitochondria + coq_mitochondria => nad_mitochondria + coqr_mitochondria + 4*hm_cytosol

ubiquinol-cytochrome-c reductase (EC Number : 1.10.2.2; mitochondria - cytosol): coqr_mitochondria + 2*cytco_mitochondria + 2*h_mitochondria => coq_mitochondria + 2*cytcr_mitochondria +4*hm_cytosol

cytochrome-c oxidase (EC Number : 1.9.3.1; mitochondria - cytosol): 7.94*cytcr_mitochondria + 15.84*h_mitochondria + 2*o2_mitochondria => 7.94*cytco_mitochondria + 7.92*hm_cytosol + 3.96*h2o_mitochondria + 0.02*o2-_mitochondria

H+-transporting two-sector ATPase (EC Number : 3.6.3.14; mitochondria - cytosol): adp_mitochondria + p_mitochondria + 4*hm_cytosol = atp_mitochondria + h2o_mitochondria + 3*h_mitochondria

T.5alev (mitochondria - cytosol): 5alev_mitochondria=5alev_cytosol

T.aceace _diffusion (cytosol - external): aceace_cytosol=aceace_external

pyruvate/acetoacetate antiporter (mitochondria - cytosol): hm_cytosol + aceace_cytosol = h_mitochondria + aceace_mitochondria

Mitochondrial ATP/ADP antiporter (mitochondria - cytosol): adp_cytosol + atp_mitochondria= adp_mitochondria+ atp_cytosol

atp/amp-antiport (peroxisom - cytosol): atp_cytosol + amp_peroxisom= atp_peroxisom + amp_cytosol

alpha-ketoisocaproate:carnitine shuttle (mitochondria - cytosol): akcap_cytosol = akcap_mitochondria

oxoglutarate/malate antiporter (mitochondria - cytosol): akg_mitochondria + mal_cytosol = akg_cytosol + mal_mitochondria

alpha-ketoisocaproate:carnitine shuttle (mitochondria - cytosol): akmval_cytosol = akmval_mitochondria

alpha-ketovalerate:carnitine shuttle (mitochondria - cytosol): akval_cytosol = akval_mitochondria

Sodium dependent neutral amino acid transporter (cytosol - external): ala_cytosol + na_cytosol = ala_external + na_external

T.albumin (cytosol - external): albumin_cytosol+atp_cytosol+h2o_cytosol=albumin_external+adp_cytosol+p_cytosol+h_cytosol

neutral and cationic amino acid Na+:Cl- Symporter (cytosol - external): arg_cytosol + na_cytosol = arg_external + na_external

system N1 [glutamin/histidin/asparagine/alanine][Na+ H+]sym/antiporter (cytosol - external): asn_cytosol + 2*na_cytosol + h_external = asn_external + 2*na_external + h_cytosol

aspartate/glutamate antiporter (mitochondria - cytosol): asp_mitochondria + glu_cytosol = asp_cytosol + glu_mitochondria

glutamate/aspartate permease (cytosol - external): asp_cytosol + na_cytosol = asp_external + na_external

atp-adp-antiporter (endoplasmic-reticulum - cytosol): atp_cytosol + adp_endoplasmic-reticulum = adp_cytosol + atp_endoplasmic-reticulum

bile excretion (cytosol - external): bile_cytosol+atp_cytosol+h2o_cytosol=bile_external+adp_cytosol+p_cytosol+h_cytosol

T.bio (cytosol - external): bio_cytosol=bio_external

CDPCholine-transport (endoplasmic-reticulum - cytosol): cdpchol_cytosol = cdpchol_endoplasmic-reticulum

CDPCholine-transport (golgi-apparatus - cytosol): cdpchol_cytosol = cdpchol_golgi-apparatus

ceramide-transport (endoplasmic-reticulum - cytosol): cer_cytosol = cer_endoplasmic-reticulum

ceramide-transport (golgi-apparatus - cytosol): cer_cytosol = cer_golgi-apparatus

chenochol-transporter (peroxisom - cytosol): chenochol_cytosol = chenochol_peroxisom

cholesterol-transporter (endoplasmic-reticulum - cytosol): chol_cytosol = chol_endoplasmic-reticulum

assumed free diffusion of choline (endoplasmic-reticulum - cytosol): choli_endoplasmic-reticulum = choli_cytosol

assumed free diffusion of choline (cytosol - external): choli_cytosol = choli_external

assumed free diffusion of cmp (endoplasmic-reticulum - cytosol): cmp_endoplasmic-reticulum = cmp_cytosol

cmp-transport (golgi-apparatus - cytosol): cmp_cytosol = cmp_golgi-apparatus

diffusion of carbon dioxide (endoplasmic-reticulum - cytosol): co2_cytosol = co2_endoplasmic-reticulum

carbon dioxide exchange (cytosol - external): co2_cytosol = co2_external

carbon dioxide exchange (mitochondria - cytosol): co2_cytosol = co2_mitochondria

coa-transporter (endoplasmic-reticulum - cytosol): coa_cytosol = coa_endoplasmic-reticulum

coa-transporter (peroxisom - cytosol): coa_cytosol = coa_peroxisom

T.coproIII (mitochondria - cytosol): coproIII_cytosol=coproIII_mitochondria

assumed free diffusion of ctp (endoplasmic-reticulum - cytosol): ctp_endoplasmic-reticulum = ctp_cytosol

glutamate/aspartate permease (cytosol - external): cys_cytosol + na_cytosol = cys_external + na_external
citrate carrier (mitochondria - cytosol): cit_mitochondria + h_mitochondria + mal_cytosol = cit_cytosol + hm_cytosol + mal_mitochondria
dihydroxyacetone-phosphate_transport (endoplasmic-reticulum - cytosol): dhap_cytosol = dhap_endoplasmic-reticulum
phosphatidate-transport (endoplasmic-reticulum - cytosol): diacglyc3p_cytosol = diacglyc3p_endoplasmic-reticulum
dihycholoate-transporter (endoplasmic-reticulum - cytosol): dihycholoate_cytosol = dihycholoate_endoplasmic-reticulum
dihycholoate-transporter (peroxisom - cytosol): dihycholoate_cytosol = dihycholoate_peroxisom
glucose-6_transporter (endoplasmic-reticulum - cytosol): g6p_cytosol = g6p_endoplasmic-reticulum
glucose exchange (GLUT2) (cytosol - external): glc_cytosol = glc_external
system N1 [glutamin/histidin/asparagine/alanine][Na+ H+]sym/antiporter (cytosol - external): gln_cytosol + 2*na_cytosol + h_external = gln_external + 2*na_external + h_cytosol
T.glu (mitochondria - cytosol): glu_mitochondria+h_mitochondria=glu_cytosol+hm_cytosol
glutamate/aspartate permease (cytosol - external): glu_cytosol + na_cytosol = glu_external + na_external
T.gly (mitochondria - cytosol): gly_mitochondria=gly_cytosol
sodium dependent neutral amino acid transporter (cytosol - external): gly_cytosol + na_cytosol = gly_external + na_external
gly-transporter (peroxisom - cytosol): gly_cytosol = gly_peroxisom
glychol-transporter (peroxisom - cytosol): glychol_cytosol = glychol_peroxisom
T.h (mitochondria - cytosol): h_mitochondria=hm_cytosol
T.h (cytosol - external): na_external+h_cytosol=h_external+na_cytosol
diffusion of h2o2 (endoplasmic-reticulum - cytosol): h2o2_cytosol = h2o2_endoplasmic-reticulum
diffusion of water (endoplasmic-reticulum - cytosol): h2o_cytosol = h2o_endoplasmic-reticulum
diffusion of water (cytosol - external): h2o_cytosol = h2o_external
diffusion of water (mitochondria - cytosol): h2o_cytosol = h2o_mitochondria
diffusion of water (peroxisom - cytosol): h2o_cytosol = h2o_peroxisom
h-transport (endoplasmic-reticulum - cytosol): h_cytosol = h_endoplasmic-reticulum
h-transport (golgi-apparatus - cytosol) h_cytosol = h_golgi-apparatus
h-transport (peroxisom - cytosol): h_cytosol = h_peroxisom
T.hbut (cytosol - external): hbut_cytosol=hbut_external
pyruvate/hydroxybutyrate antiporter (mitochondria - cytosol): hm_cytosol + hbut_cytosol = h_mitochondria + hbut_mitochondria
system N1 [glutamin/histidin/asparagine/alanine][Na+ H+]sym/antiporter (cytosol - external): his_cytosol + 2*na_cytosol + h_external = his_external + 2*na_external + h_cytosol
hmgcoa-transporter (endoplasmic-reticulum - cytosol): hmgcoa_cytosol = hmgcoa_endoplasmic-reticulum
sodium dependent neutral amino acid transporter (cytosol - external): ileu_cytosol + na_cytosol = ileu_external + na_external
lactate exchange (cytosol - external): lact_cytosol + h_cytosol = lact_external + h_external
sodium dependent neutral amino acid transporter (cytosol - external): leu_cytosol + na_cytosol = leu_external + na_external
lincoa-transporter (endoplasmic-reticulum - cytosol): lincoa_cytosol = lincoa_endoplasmic-reticulum
assumed free diffusion of linoleat (cytosol - external): linol_cytosol = linol_external
neutral and cationic amino acid Na+:Cl- Symporter (cytosol - external): lys_cytosol + na_cytosol = lys_external + na_external
T.mal (mitochondria - cytosol): mal_mitochondria + p_cytosol=mal_cytosol + p_mitochondria
malate/fumarate antiporter (mitochondria - cytosol): mal_mitochondria + fum_cytosol = mal_cytosol + fum_mitochondria
glutamate/aspartate permease (cytosol - external): met_cytosol + na_cytosol = met_external + na_external
methylglyoxalexchange (mitochondria - cytosol): metgly_cytosol + hm_cytosol = metgly_mitochondria + h_mitochondria
na+-translocating V-type ATPase (cytosol - external): na_cytosol + atp_cytosol + h2o_cytosol => na_external + adp_cytosol + p_cytosol + h_cytosol
nadh-nad-antiporter (endoplasmic-reticulum - cytosol): nad_cytosol + nadh_endoplasmic-reticulum = nadh_cytosol + nad_endoplasmic-reticulum
nad/nadh-antiport (peroxisom - cytosol): nad_cytosol + nadh_peroxisom= nad_peroxisom + nadh_cytosol

nadph-nadp-antiporter (endoplasmic-reticulum - cytosol): nadp_cytosol + nadph_endoplasmic-reticulum = nadph_cytosol + nadp_endoplasmic-reticulum
nadp/nadph-antiport (peroxisom - cytosol): nadp_cytosol + nadph_peroxisom= nadp_peroxisom + nadph_cytosol
ammonia exchange (cytosol - external): nh4_cytosol=nh4_external
ammonia exchange (mitochondria - cytosol): nh4_cytosol = nh4_mitochondria
diffusion of o2 (endoplasmic-reticulum - cytosol): o2_cytosol = o2_endoplasmic-reticulum
diffusion of o2 (: cytosol - external): o2_cytosol = o2_external
diffusion of o2 (mitochondria - cytosol): o2_cytosol = o2_mitochondria
ornithine-citrulline shuttle (mitochondria - cytosol): orn_cytosol + citl_mitochondria = orn_mitochondria + citl_cytosol
oxoglutarate/oxoadipate antiporter (mitochondria - cytosol): akg_mitochondria + oxadip_cytosol = akg_cytosol + oxadip_mitochondria
oxobutyrate symport (mitochondria - cytosol): oxob_mitochondria + h_mitochondria = oxob_cytosol + hm_cytosol
phosphate exchange (endoplasmic-reticulum - cytosol): p_cytosol = p_endoplasmic-reticulum
phosphate exchange (cytosol - external): p_cytosol+3*na_cytosol=p_external+3*na_external
phosphate exchange (mitochondria - cytosol): p_cytosol + 1*hm_cytosol = p_mitochondria+ 1*h_mitochondria
phosphate exchange (peroxisom - cytosol): p_cytosol = p_peroxisom
palcoa-transporter (endoplasmic-reticulum - cytosol): palcoa_cytosol = palcoa_endoplasmic-reticulum
T.phaem (cytosol - external): haem_cytosol=haem_external
T.phaem (mitochondria - cytosol): haem_mitochondria=haem_cytosol
sodium dependent neutral amino acid transporter (cytosol - external): phe_cytosol + na_cytosol = phe_external + na_external
glutamate/aspartate permease (cytosol - external): pro_cytosol + na_cytosol = pro_external + na_external
carnitine/acyl carnitine translocase (mitochondria - cytosol): car_mitochondria + propcar_cytosol = car_cytosol + propcar_mitochondria
propcoa-transporter (peroxisom - cytosol): propcoa_cytosol = propcoa_peroxisom
1-phosphatidyl-D-myo-inositol-transport (endoplasmic-reticulum - cytosol): ptyl3ino_cytosol = ptyl3ino_endoplasmic-reticulum
phosphatidylcholine-transport (endoplasmic-reticulum - cytosol): ptylchol_cytosol = ptylchol_endoplasmic-reticulum
phosphatidylethanolamine-transport (endoplasmic-reticulum - cytosol): ptyletham_cytosol = ptyletham_endoplasmic-reticulum
phosphatidyl-L-serine-transport (endoplasmic-reticulum - cytosol): ptylser_cytosol = ptylser_endoplasmic-reticulum
pyruvate exchange (mitochondria - cytosol): pyr_cytosol + hm_cytosol = pyr_mitochondria + h_mitochondria
serine-transport (endoplasmic-reticulum - cytosol): ser_cytosol = ser_endoplasmic-reticulum
glutamate/aspartate permease (cytosol - external): ser_cytosol + na_cytosol = ser_external + na_external
sulfate/anion transporter (cytosol - external): so4_cytosol + na_cytosol = so4_external + na_external
sphingomyelin-transport (golgi-apparatus - cytosol): sphingo_cytosol = sphingo_golgi-apparatus
tau-transporter (peroxisom - cytosol): tau_cytosol = tau_peroxisom
tauchol-transporter (peroxisom - cytosol): tauchol_cytosol = tauchol_peroxisom
neutral amino acid (alanine, serine, cysteine, threonine):Na+ symporter (cytosol - external): thr_cytosol + na_cytosol = thr_external + na_external
T.triacylglycerol (endoplasmic-reticulum - cytosol): triacylglycerol_endoplasmic-reticulum=triacylglycerol_cytosol
tricholes-transporter (endoplasmic-reticulum - cytosol): tricholes_cytosol = tricholes_endoplasmic-reticulum
tricholes-transporter (peroxisom - cytosol): tricholes_cytosol = tricholes_peroxisom
sodium dependent neutral amino acid transporter (cytosol - external): try_cytosol + na_cytosol = try_external + na_external
sodium dependent neutral amino acid transporter (cytosol - external): tyr_cytosol + na_cytosol = tyr_external + na_external
urea exchange (AQP9) (cytosol - external): urea_cytosol = urea_external
sodium dependent neutral amino acid transporter (cytosol - external): val_cytosol + na_cytosol = val_external + na_external
T.atp (nucleus - cytosol): atp_nucleus=atp_cytosol
T.ctp (nucleus - cytosol): ctp_nucleus=ctp_cytosol

T.gtp (nucleus - cytosol): gtp_nucleus=gtp_cytosol
T.h (nucleus - cytosol): h_nucleus=h_cytosol
T.pp (nucleus - cytosol): pp_nucleus=pp_cytosol
T.rna (nucleus - cytosol): rna_nucleus=rna_cytosol
T.utp (nucleus - cytosol): utp_nucleus=utp_cytosol
nad(p) transhydrogenase (EC Number : 1.6.1.1; mitochondria - cytosol): hm_cytosol + nadh_mitochondria + nadp_mitochondria = h_mitochondria + nad_mitochondria + nadph_mitochondria

COMPOUNDS

5alev = 5-aminolevulinate (Kegg ID : C00430)
acacacp = acetoacetyl-CoA (Kegg ID : C05744)
acaccoa = acetoacetyl-CoA (Kegg ID : C00332)
acacp = acetyl-[acyl-carrier protein] (Kegg ID : C03939)
accoa = acetyl-CoA (Kegg ID : C00024)
aceace = acetoacetate (Kegg ID : C000164)
acedhliam = S-acetyldihydrolipoamide (Kegg ID : C01136)
acglyc3p = 1-acyl-sn-glycerol 3-phosphate (Kegg ID : C00681)
acp = acyl-carrier protein (Kegg ID : C00229)
adesuc = adenylosuccinate (Kegg ID : C03794)
adp = adenosindiphosphate (Kegg ID : C00008)
aicar = aicar (1-(5'-Phosphoribosyl)-5-amino-4-imidazolecarboxamide) (Kegg ID : C04677)
air = 5-amino-1-(5-phospho-D-ribosyl)imidazole (Kegg ID : C03373)
akcap = alpha-ketoisocaproate (2-Oxoisocaproate) (Kegg ID : C00233)
akg = alpha-ketoglutarate (Kegg ID : C00026)
akmval = alpha-ketomethylvalerate (2-Oxo-3-methylvalerate) (Kegg ID : C03465)
akval = alpha-ketovaline (2-Oxoisovalerate) (Kegg ID : C00141)
ala = Trivial Name : L-alanine (Kegg ID : C00041)
albumin = serum albumin
amac = Aminoacetone (Kegg ID : C01888)
amadip = L-2-aminoadipate (Kegg ID : C00956)
amaps = L-2-Aminoadipate 6-semialdehyde (Kegg ID : C04076)
amcarbsem = 2-Amino-3-carboxymuconate semialdehyde (Kegg ID : C04409)
ammuc = 2-Aminomuconate (Kegg ID : C02220)
ammucsem = 2-Aminomuconate semialdehyde (Kegg ID : C03824)
amp = adenosinmonophosphate (Kegg ID : C00020)
apris = (S)-2-[5-amino-1-(5-phospho-D-ribosyl)imidazole-4-carboxamido]succinate (Kegg ID : C04823)
arg = L-arginine (Kegg ID : C00062)
argsuc = (Nomega-L-arginino)succinate (Kegg ID : C03406)
asn = L-asparagine (Kegg ID : C00152)
asp = L-aspartate (Kegg ID : C00049)
atp = adenosintriphosphate (Kegg ID : C00002)
bccp = Biotin-carboxyl-carrier protein (Kegg ID : C06250)
benacp = But-2-enoyl-[acyl-carrier protein] (Kegg ID : C04246)
bile = ductular bile
bio = biomass
butacp = Butyryl-[acyl-carrier protein] (Kegg ID : C05745)
car = L-carnitine (Kegg ID : C00318)
carbasp = N-Carbamoyl-L-aspartate (Kegg ID : C00439)
carbp = carbamoyl phosphate (Kegg ID : C00169)
cccp = Carboxybiotin-carboxyl-carrier protein (Kegg ID : C04419)
cdp = cytidine diphosphate (Kegg ID : C00112)
cdpchol = CDPcholine (Kegg ID : C00307)
cdpdiacglyc = CDPdiacylglycerol (Kegg ID : C00269)
cer = Ceramide (Kegg ID : C00195)
chencoa = Chenodeoxyglycocholoyl-CoA (Kegg ID : C00187)
chenochol = Chenodeoxyglycocholate (Kegg ID : C05462)
chol = cholesterol (Kegg ID : C00187)

cholcoa = 3alpha,7alpha,12alpha-Trihydroxy-5beta-cholestanoyl-CoA (Kegg ID : C04760)
cholencoa = 3alpha,7alpha,12alpha-Trihydroxy-5beta-cholest-24-enoyl-CoA (Kegg ID : C05460)
choles = 3alpha,7alpha,12alpha,26-Tetrahydroxy-5beta-cholestane (Kegg ID : C05446)
cholestcoa = 3alpha,7alpha,12alpha,24zeta-Tetrahydroxy-5beta-cholestanoyl-CoA (Kegg ID : C05460)
choli = Choline (Kegg ID : C00114)
cholocoa = Choloyl-CoA (Kegg ID : C01794)
cisac = cis-aconitate (Kegg ID : C00417)
cit = citrate (Kegg ID : C00158)
citl = L-Citrulline (Kegg ID : C00327)
cmp = cytidine monophosphate (Kegg ID : C00112)
co2 = carbon dioxide (Kegg ID : C00011)
coa = coenzyme A (Kegg ID : C00010)
coproIII = Coproporphyrinogen III (Kegg ID : C03263)
coq = coenzyme Q (oxidized) (Kegg ID : C00399)
crotcoa = crotonyl-coA (Kegg ID : C00877)
ctp = cytidine triphosphate (Kegg ID : C00063)
cys = L-cysteine (Kegg ID : C00097)
cysio = L-Cystathionine (Kegg ID : C00542)
cyt = cytidine (Kegg ID : C00475)
cytco = Ferricytochrome c (oxidized) (Kegg ID : C00125)
cytcr = Ferrocytochrome c (reduced) (Kegg ID : C00125)
decacp = Decanoyl-[acyl-carrier protein] (Kegg ID : C05755)
dehysphing = 3-Dehydro-D-sphinganine (Kegg ID : C02934)
dhap = dihydroxyacetone phosphate (Kegg ID : C00111)
dhliam = Dihydrolipoamide (Kegg ID : C00579)
dhliam_kgdh = Dihydrolipoamide (Kegg ID : C00579)
dhliam_pdh = Dihydrolipoamide (Kegg ID : C00579)
dhoro = (S)-Dihydroorotate (Kegg ID : C00337)
diacglyc = 1,2-Diacyl-sn-glycerol (Kegg ID : C00641)
diacglyc3p = 1,2-Diacyl-sn-glycerol 3-phosphate (Phosphatidic acid) (Kegg ID : C00416)
dihycer = Dihydroceramide (Kegg ID : C12126)
dihychol = 7alpha,12alpha-Dihydroxycholest-4-en-3-one (Kegg ID : C05457)
dihycholal = 3alpha,7alpha-Dihydroxy-5beta-cholestan-26-al (Kegg ID : C05445)
dihycholanoylcoa = 3alpha,7alpha-Dihydroxy-5beta-cholestanoyl-CoA (Kegg ID : C04644)
dihycholenoylcoa = 3alpha,7alpha-Dihydroxy-5beta-cholest-24-enoyl-CoA (Kegg ID : C05447)
dihycholestan = 7alpha,12alpha-Dihydroxy-5beta-cholestan-3-one (Kegg ID : C05453)
dihycholoate = 3alpha,7alpha-Dihydroxy-5beta-cholestanoate (Kegg ID : C04554)
dihydro = Dihydrobiopterin (Kegg ID : C00268)
diox = 3alpha,7alpha-Dihydroxy-5beta-24-oxocholestanoyl-CoA (Kegg ID : C05449)
dipos = 5beta-Cholestane-3alpha,7alpha-diol (Kegg ID : C05452)
dmetp = Dimethylallyl diphosphate (Kegg ID : C00235)
dodecacp = Dodecanoyl-[acyl-carrier protein] (Kegg ID : C05223)
ery4p = D-Erythrose 4-phosphate (Kegg ID : C00279)
f6p = beta-D-fructose-6-phosphate (Kegg ID : C05345)
faceace = 4-Fumarylacetoacetate (Kegg ID : C01061)
fad = flavin adenine dinucleotide (oxidized) (Kegg ID : C00016)
fadh2 = flavin adenine dinucleotide (reduced) (Kegg ID : C01352)
fasyl = trans,trans-farnesyl diphosphate (Kegg ID : C00448)
fdp = beta-D-fructose-1,6-phosphate (Kegg ID : C05378)
fgam = 2-(Formamido)-N1-(5-phospho-D-ribosyl)acetamidine (Kegg ID : C04640)
form = formate (Kegg ID : C00058)
formgar = N2-Formyl-N1-(5-phospho-D-ribosyl)glycinamide (Kegg ID : C04376)
formglut = N-Formimino-L-glutamate (Kegg ID : C00439)
formkyn = formylkynurenine (Kegg ID : C02700)
formthf = 5-Formiminotetrahydrofolate (Kegg ID : C00664)
fpic = 5-Formamido-1-(5-phospho-D-ribosyl)imidazole-4-carboxamide (Kegg ID : C04734)
fthf10 = 10-Formyltetrahydrofolate (Kegg ID : C00234)
fum = fumarate (Kegg ID : C00122)

g1p = alpha-glucose-1-phosphate (Kegg ID : C00103)
g2p = glycerate 2-phosphate (Kegg ID : C00631)
g3p = glycerate 3-phosphate ((2R)-2-Hydroxy-3-(phosphonooxy)-propanal) (Kegg ID : C00197)
g6p = alpha-glucose-6-phosphate (Kegg ID : C00668)
gap = glyceraldehyde 3-phosphate (Kegg ID : C00118)
gar = 5'-Phosphoribosylglycinamide (Kegg ID : C03838)
gdp = guanosine diphosphate (Kegg ID : C00035)
geran = Geranyl diphosphate (Kegg ID : C00341)
glac6p = D-Glucono-1,5-lactone 6-phosphate (Kegg ID : C01236)
glc = alpha-D-Glucose (Kegg ID : C00267)
gln = L-Glutamine (Kegg ID : C00064)
glt6p = 6-phospho-D-gluconate (Kegg ID : C00345)
glu = L-glutamate (Kegg ID : C00025)
glusald = L-Glutamate 5-semialdehyde (Kegg ID : C01165)
glutcoa = glutaryl-coA (Kegg ID : C00527)
glutliam = S-glutaryldihydrolipoamide (Kegg ID : C06157)
gluto = oxidized glutathione (glutathione disulfide) (Kegg ID : C00127)
glutr = Reduced glutathione (Kegg ID : C00051)
gly = L-glycine (Kegg ID : C00037)
glyc3p = sn-Glycerol 3-phosphate (Kegg ID : C00093)
glychol = Glycocholate (Kegg ID : C01921)
glyg = glycogen (amylose) (Kegg ID : C00718)
gmp = guanosine monophosphate (Kegg ID : C00144)
gtp = guanosine triphosphate (Kegg ID : C00044)
h = Proton (Kegg ID : C00080)
h2o = water (Kegg ID : C00001)
h2o2 = hydrogen peroxide (Kegg ID : C00027)
haem = Protoheme (Kegg ID : C00032)
hbacp = (3R)-3-Hydroxybutanoyl-[acyl-carrier protein] (Kegg ID : C04618)
hbut = (R)-3-Hydroxybutyrate (Kegg ID : C01089)
hbutcoa = (S)-3-Hydroxybutanoyl-CoA (Kegg ID : C01144)
hco3 = carbonic acid (Kegg ID : C00288)
hcys = L-homocysteine (Kegg ID : C00155)
hexacp = Hexanoyl-[acyl-carrier protein] (Kegg ID : C05749)
hexdecacp = Hexadecanoyl-[acyl-carrier protein] (Kegg ID : C05764)
hibut = (S)-3-Hydroxyisobutyrate (Kegg ID : C06001)
hibutcoa = (S)-3-Hydroxyisobutyryl-CoA (Kegg ID : C06000)
his = L-Histidine (Kegg ID : C00135)
hm = mitochondrial proton (Kegg ID : C00080)
hmbil = hydroxymethylbilane (Kegg ID : C01024)
hmbutcoa = (S)-3-Hydroxy-2-methylbutyryl-CoA (Kegg ID : C04405)
hmgcoa = (S)-3-Hydroxy-3-methylglutaryl-CoA (Kegg ID : C00356)
hmgent = Homogentisate (Kegg ID : C00544)
hppyr = 3-(4-Hydroxyphenyl)pyruvate (Kegg ID : C01179)
hychol = Cholest-5-ene-3beta,7alpha-diol (Kegg ID : C03594)
hycholestan = 7alpha-Hydroxy-5beta-cholestan-3-one (Kegg ID : C05451)
hydant = 3-Hydroxyanthranilate (Kegg ID : C05125)
hydchol = 7alpha-Hydroxycholest-4-en-3-one (Kegg ID : C05455)
hydecacp = (R)-3-Hydroxydecanoyl-[acyl-carrier protein] (Kegg ID : C04619)
hydkyn = 3-Hydroxy-L-kynurenine (Kegg ID : C03227)
hydodecacp = (R)-3-Hydroxydodecanoyl-[acyl-carrier protein] (Kegg ID : C05757)
hyhexacp = (R)-3-Hydroxyhexanoyl-[acyl-carrier protein] (Kegg ID : C05747)
hyhexdecacp = (R)-3-Hydroxyhexadecanoyl-[acyl-carrier protein] (Kegg ID : C04633)
hyoctacp = (R)-3-Hydroxyoctanoyl-[acyl-carrier protein] (Kegg ID : C04620)
hyptau = Hypotaurine (Kegg ID : C00519)
hytetradecacp = (R)-3-Hydroxytetradecanoyl-[acyl-carrier protein] (Kegg ID : C04688)
ileu = L-Isoluecine (Kegg ID : C00407)
imiprop = 4-Imidazolone-5-propanoate (Kegg ID : C03680)

imp = Inosine monophosphate (Kegg ID : C00130)
isocit = isocitrate (Kegg ID : C00311)
isyl = isopentenyl diphosphate (Kegg ID : C00129)
kyn = L-Kynurenine (Kegg ID : C00328)
lact = L-lactate (Kegg ID : C00186)
lat = Lathosterol (Kegg ID : C01189)
leu = L-leucine (Kegg ID : C00123)
liam = Lipoamide (Kegg ID : C00248)
liam_kgdh = Lipoamide (Kegg ID : C00248)
liam_pdh = Lipoamide (Kegg ID : C00248)
lincoa = Linoleate-Coa
linol = linoleic acid (cis-9,12-octodecanoate)
lipid = lipid
lys = L-lysine (Kegg ID : C00047)
macaccoa = 2-Methylacetoacetyl-CoA (Kegg ID : C03344)
maceace = 4-Maleylacetoacetate (Kegg ID : C01036)
macrylcoa = Methylacrylyl-CoA (Kegg ID : C03460)
mal = (S)-L-malate (Kegg ID : C000149)
malacp = Malonyl-[acyl-carrier protein] (Kegg ID : C01209)
malcoa = Malonyl-CoA (Kegg ID : C00083)
mbutcoa = 3-Methylbutanoyl-CoA (isovaleryl-coA) (Kegg ID : C02939)
mbutliam = S-(3-Methylbutanoyl)-dihydrolipoamide (Kegg ID : C05119)
mbutycoa = 2-Methylbutanoyl-CoA (Kegg ID : C01033)
mbutyliam = S-(2-Methylbutanoyl)-dihydrolipoamide (Kegg ID : C05118)
mcrotcoa = 3-Methylcrotonyl-CoA (Kegg ID : C03069)
mcrotycoa = methylcrotonyl-CoA (Kegg ID : C03345)
melthf = 5,10-Methenyltetrahydrofolate (Kegg ID : C00445)
met = L-methionine (Kegg ID : C00073)
metgly = methylglyoxal (Kegg ID : C00546)
metmalcoa = (S)-methylmalonyl-coA (Kegg ID : C00683)
metthfo = 5,10-Methylenetetrahydrofolate (Kegg ID : C00143)
mev = (R)-Mevalonate (Kegg ID : C00418)
mev5p = (R)-5-Phosphomevalonate (Kegg ID : C01107)
mev5pp = (R)-5-Diphosphomevalonate (Kegg ID : C01143)
mglutcoa = 3-Methylglutaconyl-CoA (Kegg ID : C03231)
mino = myo-Inositol (Kegg ID : C00137)
mino1p = 1D-myo-Inositol 1-monophosphate (Kegg ID : C01177)
mmalsald = (S)-Methylmalonate semialdehyde (Kegg ID : C06002)
mprocoa = 2-Methylpropanoyl-CoA (Kegg ID : C00630)
mproliam = S-(2-Methylpropanoyl)-dihydrolipoamide (Kegg ID : C04424)
mthf = 5-Methyltetrahydrofolate (Kegg ID : C00440)
na = sodium ion (Kegg ID : C01330)
nad = nicotinamide adenine dinucleotide (oxidized) (Kegg ID : C00003)
nadh = nicotinamide adenine dinucleotide (reduced) (Kegg ID : C00004)
nadp = nicotinamide adenine dinucleotide phosphate (oxidized) (Kegg ID : C00006)
nadph = nicotinamide adenine dinucleotide phosphate (reduced) (Kegg ID : C00036)
nh4 = ammonia ion (Kegg ID : C00014)
o2 = oxygen (Kegg ID : c00007)
o2- = reactive oxygen species (ROS)
oac = oxaloacetate (Kegg ID : C00036)
octacp = Octanoyl-[acyl-carrier protein] (Kegg ID : C05752)
orn = L-ornithine (Kegg ID : C00077)
orot = orotate (Kegg ID : C00295)
orotp = orotidine 5'-phosphate (Kegg ID : C01003)
oxadip = 2-oxoadipate (Kegg ID : C00322)
oxcoa = 3alpha,7alpha,12alpha-Trihydroxy-5beta-24-oxocholestanoyl-CoA (Kegg ID : C05467)
oxdecacp = 3-Oxodecanoyl-[acyl-carrier protein] (Kegg ID : C05753)
oxdodecacp = 3-Oxododecanoyl-[acyl-carrier protein] (Kegg ID : C05756)

oxhexacp = 3-Oxohexanoyl-[acyl-carrier protein] (Kegg ID : C05746)
oxhexdecacp = 3-Oxohexadecanoyl-[acyl-carrier protein] (Kegg ID : C05759)
oxob = 2-oxobutanoate (Kegg ID : C00109)
oxoctacp = 3-Oxooctanoyl-[acyl-carrier protein] (Kegg ID : C05750)
oxtetradecacp = 3-Oxotetradecanoyl-[acyl-carrier protein] (Kegg ID : C05759)
p = phosphate (orthophosphate) (Kegg ID : C00009)
pal = palmitate (hexadecanoate) (Kegg ID : C00249)
palcoa = palmitoyl-coa (Kegg ID : C00154)
pep = phosphoenolpyruvate (Kegg ID : C00074)
pg13 = 1,3-bisphospho-D-glycerate (3-Phospho-D-glyceroyl phosphate) (Kegg ID : C05378)
phe = L-Phneylalanine (Kegg ID : C00079)
phoschol = O-Phosphocholine (Kegg ID : C00588)
phxpyr = phosphohydroxypyruvate (Kegg ID : C03232)
porgen = porphobilinogen (Kegg ID : C00931)
pp = diphosphate (pyrophosphate) (Kegg ID : C00013)
prai = 5-Amino-1-(5-phospho-D-ribosyl)imidazole-4-carboxylate (Kegg ID : C04751)
prib = 5-Phosphoribosylamine (Kegg ID : C03090)
pro = L-Proline (Kegg ID : C00148)
prod3 = Provitamin D3 (Kegg ID : C01164)
propcar = propionyl-carnitin
propcoa = propionyl-coA (Kegg ID : C00100)
prophyrIX = Protoporphyrin IX (Kegg ID : C02191)
protein = protein
protoIX = Protoporphyrinogen IX (Kegg ID : C01079)
prpp = 5-Phospho-alpha-D-ribose 1-diphosphate (Kegg ID : C00119)
pser = O-phospho-L-serine (Kegg ID : C01005)
psqual = Presqualene diphosphate (Kegg ID : C03428)
ptyl3ino = 1-Phosphatidyl-D-myo-inositol (Kegg ID : C01194)
ptylchol = Phosphatidylcholine (Lecithin) (Kegg ID : C00157)
ptyletham = Phosphatidylethanolamine (Kegg ID : C00350)
ptylser = Phosphatidyl-L-serine (Kegg ID : C02737)
pylcx = (S)-1-Pyrroline-5-carboxylate (Kegg ID : C03912)
pyr = pyruvate (Kegg ID : C00022)
rib5p = D-Ribose 5-phosphate (Kegg ID : C00117)
ribu5p = D-Ribulose 5-phosphate (Kegg ID : C00199)
rna = Ribonucleic acid
sap = Saccharopine (N6-(L-1,3-Dicarboxypropyl)-L-lysine) (Kegg ID : C00449)
sed7p = Sedoheptulose 7-phosphate (Kegg ID : C00281)
ser = L-serine (Kegg ID : C00065)
so3 = sulfite (Kegg ID : C00094)
so4 = sulfate (Kegg ID : C00059)
sphinga = Sphinganine (Kegg ID : C00836)
sphingo = Sphingomyelin (Kegg ID : C00550)
squal = squalene (Kegg ID : C00751)
squepo = Squalene 2,3-epoxide (Kegg ID : C01054)
suc = succinate (Kegg ID : C00042)
sucoa = succinyl-coA (Kegg ID : C00091)
sucdhliam = S-succinyldihydrolipoamide (Kegg ID : C01169)
sulfala = 3-sulfino-L-alanine (Kegg ID : C00606)
sulfpyr = 3-sulfinylpyruvate (Kegg ID : C05527)
tau = Taurine (Kegg ID : C00245)
tauchol = Taurocholate (Kegg ID : C05122)
tehydro = Tetrahydrobiopterin (Kegg ID : C00272)
tetradecacp = Tetradecanoyl-[acyl-carrier protein] (Kegg ID : C05761)
thf = Tetrahydrofolate (Kegg ID : C00101)
thr = L-threonine (Kegg ID : C00188)
transdecacp = trans-Dec-2-enoyl-[acyl-carrier protein] (Kegg ID : C05754)
transdodecacp = trans-Dodec-2-enoyl-[acyl-carrier protein] (Kegg ID : C05758)

transhexacp = trans-Hex-2-enoyl-[acyl-carrier protein] (Kegg ID : C05748)
transhexdecacp = trans-Hexadec-2-enoyl-[acyl-carrier protein] (Kegg ID : C05763)
transoctacp = trans-Oct-2-enoyl-[acyl-carrier protein] (Kegg ID : C05751)
transtetradecacp = trans-Tetradec-2-enoyl-[acyl-carrier protein] (Kegg ID : C05760)
triacylglycerol = Triglyceride
trichol = 3alpha,7alpha,12alpha-Trihydroxy-5beta-cholestan-26-al (Kegg ID : C01301)
tricholcoa = 3alpha,7alpha,24-Trihydroxy-5beta-cholestanoyl-CoA (Kegg ID : C05448)
tricholes = 3alpha,7alpha,12alpha-Trihydroxy-5beta-cholestan-26-oate (Kegg ID : C04722)
trihydchol = 5beta-Cholestane-3alpha,7alpha,26-triol (Kegg ID : C05446)
tripos = 3alpha,7alpha,12alpha-Trihydroxycoprostane (Kegg ID : C05454)
try = L-tryptophan (Kegg ID : C00078)
tyr = L-tyrosine (Kegg ID : C00082)
udp = uridine diphosphate (Kegg ID : C00105)
udpglc = udpglucose (Kegg ID : C00029)
ump = uridine monophosphate (Kegg ID : C00105)
urea = urea (carbamide) (Kegg ID : C00086)
uri = uridine (Kegg ID : C00299)
uroc = Urocanate (Kegg ID : C00785)
uroporIII = Uroporphyrinogen III (Kegg ID : C01051)
utp = uridine triphosphate (Kegg ID : C00075)
val = L-valine (Kegg ID : C00183)
xmp = xanthosine 5'-phosphate (Kegg ID : C00655)
xyl5p = D-Xylulose 5-phosphate (Kegg ID : C00231)
zymos = zymosterol (delta8,24-Cholestadien-3beta-ol) (Kegg ID : C05437)

Appendix B. Atom Mappings for Identifying Metabolic Fluxes in the Cholesterol Synthesis Pathway and Central Carbon Metabolism. Bidireactional reaction steps and irreversible reactions are indicated by "$\rightleftharpoons$" and "$\longrightarrow$". Subscripts c, m, e and ex denote the compartmental localization, i.e. cytosol, mitochondrion, endoplasmic reticulum, and extracellular space, respectively.

Reaction	Substrates	Reversibility	Products
Glycolysis/ Gluconeogenesis/ Lactate			
r1	$3PG_{ex}(1,2,3)$	$\rightleftharpoons$	$3PG_{c}(1,2,3)$
r2	$3PG_{c}(1,2,3)$	$\rightleftharpoons$	$2PG_{c}(1,2,3)$
r3	$2PG_{c}(1,2,3)$	$\rightleftharpoons$	$PEP_{c}(1,2,3)$
r4	$PEP_{c}(1,2,3)$	$\longrightarrow$	$PYR_{c}(1,2,3)$
r5	$PYR_{c}(1,2,3)$	$\rightleftharpoons$	$LAC_{c}(1,2,3)$
TCA			
r6	$PYR_{m}(1,2,3)$	$\longrightarrow$	$CO2_{m}(1)+ACOA_{m}(2,3)$
r7	$ACOA_{m}(1,2)+OAC_{m}(3,4,5,6)$	$\longrightarrow$	$CIT_{m}(6,5,4,2,1,3)$
r8	$CIT_{m}(1,2,3,4,5,6)$	$\rightleftharpoons$	$ISOCIT_{m}(1,2,3,4,5,6)$
r9	$ISOCIT_{m}(1,2,3,4,5,6)$	$\rightleftharpoons$	$AKG_{m}(1,2,3,4,5)+CO2_{m}(6)$
r10	$AKG_{m}(1,2,3,4,5)$	$\rightleftharpoons$	$SUCOA_{m}(2,3,4,5)+CO2_{m}(1)$
r11	$SUCOA_{m}(1,2,3,4)$	$\rightleftharpoons$	$SUC_{m}(1,2,3,4)$
r12,a	$SUC_{m}(1,2,3,4)$	$\rightleftharpoons$	$FUM_{m}(1,2,3,4)$
r12,b	$SUC_{m}(1,2,3,4)$	$\rightleftharpoons$	$FUM_{m}(4,3,2,1)$
r13,a	$FUM_{m}(1,2,3,4)$	$\rightleftharpoons$	$MAL_{m}(1,2,3,4)$
r13,b	$FUM_{m}(1,2,3,4)$	$\rightleftharpoons$	$MAL_{m}(4,3,2,1)$
r14	$MAL_{m}(1,2,3,4)$	$\rightleftharpoons$	$OAC_{m}(1,2,3,4)$
Amino acid metabolism			
r15	$ALA_{c}(1,2,3)+AKG_{c}(4,5,6,7,8)$	$\rightleftharpoons$	$PYR_{c}(1,2,3)+GLU_{c}((4,5,6,7,8)$
r16	$GLN_{C}(1,2,3,4,5)$	$\rightleftharpoons$	$GLU_{c}(1,2,3,4,5)$
r17	$GLU_{m}(1,2,3,4,5)$	$\rightleftharpoons$	$AKG_{m}(1,2,3,4,5)$
r18	$GLU_{c}(1,2,3,4,5)$	$\rightleftharpoons$	$AKG_{c}(1,2,3,4,5)$
Ketone Bodies			
r19	$HMGCOA_{m}(1,2,3,4,5,6)$	$\rightleftharpoons$	$ACOA_{m}(1,2)+ACEACE_{m}(3,4,5,6)$
r20	$ACEACE_{m}(1,2,3,4)$	$\rightleftharpoons$	$HBUT_{m}(1,2,3,4)$
r21	$ACEACE_{m}(1,2,3,4)$	$\rightleftharpoons$	$ACEACE_{ex}(1,2,3,4)$
r22	$HBUT_{m}(1,2,3,4)$	$\rightleftharpoons$	$HBUT_{ex}(1,2,3,4)$
r23	$ACOA_{m}(1,2)(3,4)$	$\rightleftharpoons$	$ACACCOA_{m}(1,2,3,4)$
r24	$ACACCOA_{m}(1,2,3,4)+ACOA_{m}(5,6)$	$\rightleftharpoons$	$HMGCOA_{m}(1,2,3,4,5,6)$
Anaplerosis/ Cataplerosis			
r25	$OAC_{c}(1,2,3,4)$	$\longrightarrow$	$PEP_{c}(1,2,3)+CO2_{c}(4)$
r26	$CIT_{c}(1,2,3,4,5,6)$	$\longrightarrow$	$ACOA_{c}(5,4)+OAC_{c}(6,3,2,1)$
r27	$PYR_{c}(1,2,3)+CO2_{c}(4)$	$\rightleftharpoons$	$MAL_{c}(1,2,3,4)$
r28	$PYR_{m}(1,2,3)+CO2_{m}(4)$	$\rightleftharpoons$	$MAL_{m}(1,2,3,4)$
r29	$PYR_{m}(1,2,3)+CO2_{m}(4)$	$\longrightarrow$	$OAC_{m}(1,2,3,4)$
Cholesterol Biosynthesis			
r30	$HMGCOA_{e}(1,2,3,4,5,6)$	$\rightleftharpoons$	$MEV_{e}(1,2,3,4,5,6)$
r31	$MEV_{e}(1,2,3,4,5,6)$	$\rightleftharpoons$	$ISOPENT_{e}(1,2,3,4,6)+CO2_{e}(5)$
r32,a	$ISOPENT_{e}(1,2,3,4,5)(6,7,8,9,10)(11,12,13,14,15)$	$\longrightarrow$	$FARNESYLA_{e}(1,2,3,4,5,6,7,8,9,10,11,12,13,14,15)$
r32,b	$ISOPENT_{e}(1,2,3,4,5)(6,7,8,9,10)(11,12,13,14,15)$	$\longrightarrow$	$FARNESYLB_{e}(1,2,3,5,6,7,8,9,10,11,12,13) + CO2_{e}(4)(14)(15)$
r33	$FARNESYLA_{e}(1,2,3,4,5,6,7,8,9,10,11,12,13,14,15) +FARNESYLB_{e}(16,17,18,19,20,21,22,23,24,25,26,27)$	$\longrightarrow$	$ZYMO_{e}(1,2,3,4,5,6,7,8,9,10,11,12,13,14,15,16,17,18,19,20,21,22,23,24,25,26,27)$
r34	$ZYMO_{e}(1,2,3,4,5,6,7,8,9,10,11,12,13,14,15,16,17,18,19,20,21,22,23,24,25,26,27)$	$\longrightarrow$	$CHOL8_{e}(1,2,3,4,5,6,7,8,9,10,11,12,13,14,15,16,17,18,19,20,21,22,23,24,25,26,27)$

Appendix B (continued)

Reaction	Substrates	Reversibility	Products
r35	$CHOL8_e$(1,2,3,4,5,6,7,8,9,10,11,12,13,14,15,16,17,18,19,20,21,22,23,24,25,26,27)	⇌	$LATHO_e$(1,2,3,4,5,6,7,8,9,10,11,12,13,14,15,16,17,18,19,20,21,22,23,24,25,26,27)
r36	$LATHO_e$(1,2,3,4,5,6,7,8,9,10,11,12,13,14,15,16,17,18,19,20,21,22,23,24,25,26,27)	⇌	$DEHYDCHOL_e$(1,2,3,4,5,6,7,8,9,10,11,12,13,14,15,16,17,18,19,20,21,22,23,24,25,26,27)
r37	$ZYMO_e$(1,2,3,4,5,6,7,8,9,10,11,12,13,14,15,16,17,18,19,20,21,22,23,24,25,26,27)	⇌	$CHOL7_e$(1,2,3,4,5,6,7,8,9,10,11,12,13,14,15,16,17,18,19,20,21,22,23,24,25,26,27)
r38	$CHOL7_e$(1,2,3,4,5,6,7,8,9,10,11,12,13,14,15,16,17,18,19,20,21,22,23,24,25,26,27)	⇌	$DEHYDDESMO_e$(1,2,3,4,5,6,7,8,9,10,11,12,13,14,15,16,17,18,19,20,21,22,23,24,25,26,27)
r39	$DEHYDDESMO_e$(1,2,3,4,5,6,7,8,9,10,11,12,13,14,15,16,17,18,19,20,21,22,23,24,25,26,27)	⇌	$DESMO_e$(1,2,3,4,5,6,7,8,9,10,11,12,13,14,15,16,17,18,19,20,21,22,23,24,25,26,27)
r40	$DEHYDCHOL_e$(1,2,3,4,5,6,7,8,9,10,11,12,13,14,15,16,17,18,19,20,21,22,23,24,25,26,27)	⇌	$CHOL_e$(1,2,3,4,5,6,7,8,9,10,11,12,13,14,15,16,17,18,19,20,21,22,23,24,25,26,27)
r41	$DESMO_e$(1,2,3,4,5,6,7,8,9,10,11,12,13,14,15,16,17,18,19,20,21,22,23,24,25,26,27)	⇌	$CHOL_e$(1,2,3,4,5,6,7,8,9,10,11,12,13,14,15,16,17,18,19,20,21,22,23,24,25,26,27)
r42	$CHOL_e$(1,2,3,4,5,6,7,8,9,10,11,12,13,14,15,16,17,18,19,20,21,22,23,24,25,26,27)	⇌	$CHOL_{ex}$(1,2,3,4,5,6,7,8,9,10,11,12,13,14,15,16,17,18,19,20,21,22,23,24,25,26,27)
Inter-Compartmental Transport			
r43	LAC_c(1,2,3)	⇌	LAC_{ex}(1,2,3)
r44	ALA_c(1,2,3)	⇌	ALA_{ex}(1,2,3)
r45	PYR_c(1,2,3)	⇌	PYR_{ex}(1,2,3)
r46	AKG_c(1,2,3,4,5)	⇌	AKG_{ex}(1,2,3,4,5)
r47	GLN_c(1,2,3,4,5)	⇌	GLN_{ex}(1,2,3,4,5)
r48	GLU_c(1,2,3,4,5)	⇌	GLU_{ex}(1,2,3,4,5)
r49	$CO2_c$(1)	⇌	$CO2_{ex}$(1)
r50	MAL_c(1,2,3,4)	⇌	MAL_{ex}(1,2,3,4)
r51	$ISOCIT_c$(1,2,3,4,5,6)	⇌	$ISOCIT_{ex}$(1,2,3,4,5,6)
r52	CIT_c(1,2,3,4,5,6)	⇌	CIT_{ex}(1,2,3,4,5,6)
r53	FUM_c(1,2,3,4)	⇌	FUM_{ex}(1,2,3,4)
r54	$ACOA_c$(1,2)	⇌	$ACOA_{ex}$(1,2)
r55	PYR_c(1,2,3)	⇌	PYR_m(1,2,3)
r56	$CO2_c$(1)	⇌	$CO2_m$(1)
r57	$ACOA_c$(1,2)	⇌	$ACOA_m$(1,2)
r58	OAC_c(1,2,3,4)	⇌	OAC_m(1,2,3,4)
r59	CIT_c(1,2,3,4,5,6)	⇌	CIT_m(1,2,3,4,5,6)
r60	$ISOCIT_c$(1,2,3,4,5,6)	⇌	$ISOCIT_m$(1,2,3,4,5,6)
r61	AKG_c(1,2,3,4,5)	⇌	AKG_m(1,2,3,4,5)
r62	FUM_c(1,2,3,4)	⇌	FUM_m(1,2,3,4)
r63	MAL_c(1,2,3,4)	⇌	MAL_m(1,2,3,4)
r64	GLU_c(1,2,3,4,5)	⇌	GLU_m(1,2,3,4,5)
r65	$HMGCOA_c$(1,2,3,4,5,6)	⇌	$HMGCOA_m$(1,2,3,4,5,6)
r66	$HMGCOA_c$(1,2,3,4,5,6)	⇌	$HMGCOA_e$(1,2,3,4,5,6)
r67	$CO2_c$(1)	⇌	$CO2_e$(1)
r68	$Phenylalanine/Tyrosine_{ex}$(1,2,3,4)	⇌	FUM_c(1,2,3,4)
r69	$Valine/Isleucine/Methionine_{ex}$(1,2,3,4)	⇌	$SUCOA_m$(1,2,3,4)
r70	$Aspartate/Asparagine_{ex}$(1,2,3,4)	⇌	OAC_c(1,2,3,4)

Appendix C. Simulated and Measured Mass Fractions of Phosphoenolpyruvate (PEP), Malate (MAL), Fumarate (FUM), Alpha-Ketoglutarate (AKG), Citrate (CIT), and Cholesterol (CHOL) in Response to 0 and 50 nM Atorvastatin. The error bars indicate the standard deviations of the experimental data.

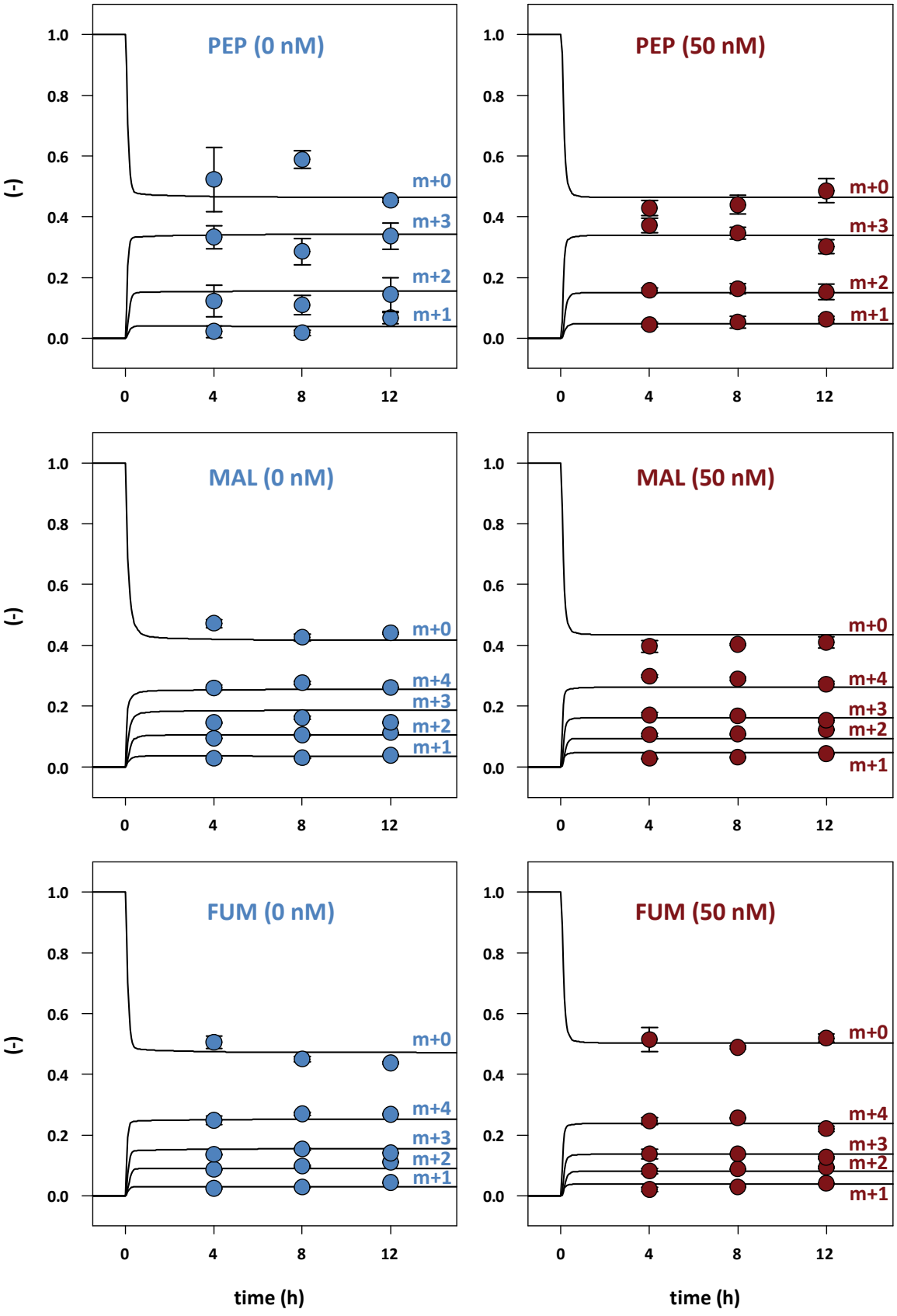

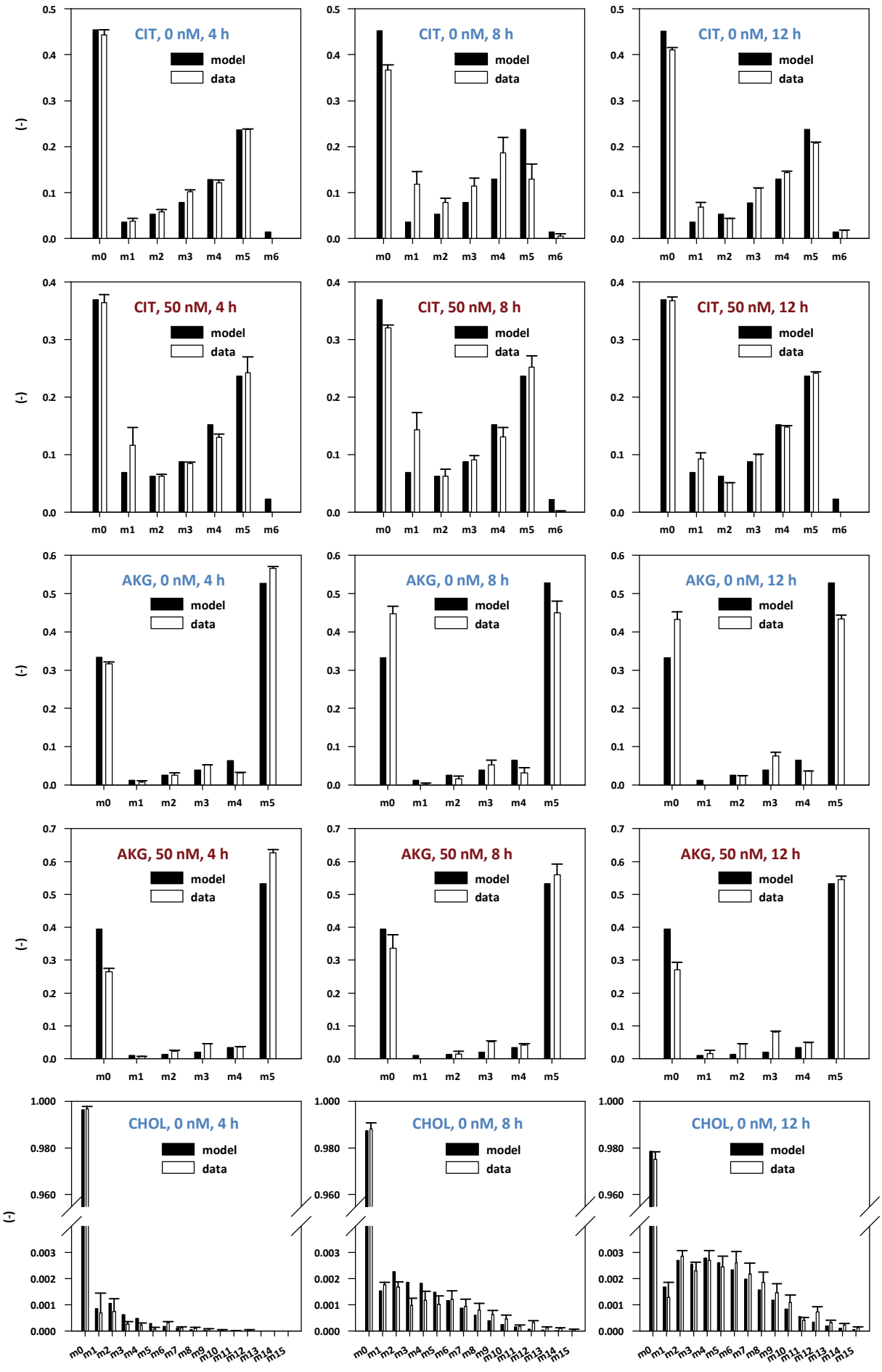
CIT, 0 nM, 4 h
CIT, 0 nM, 8 h
CIT, 0 nM, 12 h
CIT, 50 nM, 4 h
CIT, 50 nM, 8 h
CIT, 50 nM, 12 h
AKG, 0 nM, 4 h
AKG, 0 nM, 8 h
AKG, 0 nM, 12 h
AKG, 50 nM, 4 h
AKG, 50 nM, 8 h
AKG, 50 nM, 12 h
CHOL, 0 nM, 4 h
CHOL, 0 nM, 8 h
CHOL, 0 nM, 12 h
model
data
(-)

Appendix D. Estimated Metabolic Fluxes and Reversibilities in Primary Rat Hepatocytes in Response to 0 and 50 nM Atorvastatin. Metabolic fluxes are given in mmol/(lcv·h). The reversibility values denote the ratio of forward flux to net flux.

	0 nM Atorvastatin		50 nM Atorvastatin	
Reaction	Metabolic Flux	Reversibility	Metabolic Flux	Reversibility
r1	-18.9 ± 1.32	1.9 ± 1.0	-18.9 ± 7.9	1.1 ± 0.8
r2	-18.9 ± 1.32	5.0 ± 1.3	-18.9 ± 7.9	11.1 ± 2.9
r3	-18.9 ± 1.32	9.0 ± 1.7	-18.9 ± 7.9	11.2 ± 2.9
r4	62.3 ± 1.32		60.4 ± 7.83	
r5	45.5 ± 0.003	2.8 ± 1.2	46.6 ± 0.03	2.3 ± 1.0
r6	31.6 ± 1.31		29.8 ± 7.24	
r7	14.9 ± 0.02		14.1 ± 0.06	
r8	12.1 ± 0.09	78.1 ± 11.9	10.8 ± 0.1	148.5 ± 27.8
r9	12.1 ± 0.09	69.3 ± 10.6	10.8 ± 0.1	81.6 ± 4.8
r10	99.2 ± 0.14	2.2 ± 1.0	97.6 ± 0.56	2.5 ± 1.0
r11	99.8 ± 0.11	25.0 ± 4.8	98.0 ± 0.51	25.9 ± 2.4
r12,a	95.8 ± 0.11	26.5 ± 1.8	94.0 ± 0.52	33.0 ± 1.2
r12,b	4.0 ± 0.01	26.5 ± 7.4	3.9 ± 0.01	33.0 ± 4.2
r13,a	92.3 ± 0.09	72.2 ± 2.0	84.1 ± 0.46	42.2 ± 4.5
r13,b	8.0 ± 0.00	72.2 ± 13.6	14.5 ± 0.01	42.2 ± 2.4
r14	92.2 ± 0.05	13.5 ± 3.8	88.2 ± 0.26	5.8 ± 1.0
r15	12.0 ± 0.01	1.3 ± 1.0	11.6 ± 0.23	1.5 ± 1.0
r16	11.9 ± 0.004	34.5 ± 9.5	12.1 ± 0.19	17.1 ± 2.6
r17	89.1 ± 0.17	2.9 ± 1.0	82.1 ± 0.77	7.9 ± 1.1
r18	11.3 ± 0.001	8.2 ± 1.6	17.5 ± 0.004	8.1 ± 1.1
r19	7.1 ± 0.04	3.6 ± 1.3	8.6 ± 0.26	13.2 ± 1.2
r20	4.1 ± 0.04	10.1 ± 2.1	4.9 ± 0.15	20.0 ± 1.4
r21	3.1 ± 0.01	10.5 ± 1.9	3.7 ± 0.11	8.5 ± 1.1
r22	4.1 ± 0.04	17.1 ± 4.8	4.9 ± 0.15	6.5 ± 1.1
r23	8.7 ± 0.44	7.8 ± 1.5	9.0 ± 0.94	43.8 ± 6.0
r24	8.7 ± 0.44	7.5 ± 1.7	9.0 ± 0.94	1.8 ± 1.0
r25	81.2 ± 0.001		79.3 ± 0.07	
r26	2.3 ± 0.01		2.8 ± 0.02	
r27	0.3 ± 0.06	1.9 ± 1.1	0.6 ± 0.02	1.5 ± 1.0
r28	-8.2 ± 0.02	16.4 ± 3.2	-10.9 ± 0.15	11.9 ± 1.2
r29	1.3 ± 0.02		1.9 ± 0.03	
r30	1.6 ± 0.44	58.8 ± 9.0	0.5 ± 0.68	70.1 ± 13.3
r31	1.6 ± 0.44	51.7 ± 7.9	0.5 ± 0.68	162.7 ± 26.7
r32,a	0.27 ± 0.07		0.08 ± 0.02	
r32,b	0.27 ± 0.07		0.08 ± 0.02	
r33	0.27 ± 0.07		0.08 ± 0.02	
r34	0.21 ± 0.07		0.03 ± 0.03	
r35	0.21 ± 0.07	16.9 ± 2.8	0.03 ± 0.03	11.2 ± 2.5
r36	0.21 ± 0.07	30.4 ± 8.4	0.03 ± 0.03	9.7 ± 1.6
r37	0.06 ± 0.02		0.04 ± 0.01	
r38	0.06 ± 0.02	1.5 ± 1.0	0.04 ± 0.01	2.5 ± 1.1
r39	0.06 ± 0.02	1.1 ± 1.0	0.04 ± 0.01	2.7 ± 1.0
r40	0.21 ± 0.07	2.7 ± 2.7	0.03 ± 0.03	2.7 ± 1.2
r41	0.06 ± 0.02	1.3 ± 1.0	0.04 ± 0.01	2.6 ± 1.1
r42	0.27 ± 0.07	15.0 ± 2.5	0.08 ± 0.02	43.1 ± 2.5
r43	45.5 ± 0.003	1.8 ± 1.1	46.6 ± 0.03	1.8 ± 1.0
r44	-12.0 ± 0.01	2.8 ± 1.1	-11.6 ± 0.23	2.3 ± 1.0
r45	3.8 ± 0.04	1.2 ± 1.0	3.9 ± 0.13	2.2 ± 1.0
r46	1.2 ± 0.04	1.8 ± 1.0	1.2 ± 0.05	1.2 ± 1.0

Appendix D (continued)

	0 nM Atorvastatin		50 nM Atorvastatin	
Reaction	Metabolic Flux	Reversibility	Metabolic Flux	Reversibility
r47	-11.9 ± 0.00	29.2 ± 8.1	-12.1 ± 0.19	32.4 ± 4.9
r48	-76.4 ± 0.17	1.2 ± 0.9	-75.9 ± 0.73	1.2 ± 0.8
r49	233.1 ± 1.98	60.6 ± 16.7	226.6 ± 16.86	24.5 ± 1.6
r50	0.1 ± 0.04	1.5 ± 1.0	0.1 ± 0.03	1.3 ± 1.0
r51	0.02 ± 0.006	4.3 ± 1.6	0.02 ± 0.004	5.5 ± 1.7
r52	0.5 ± 0.09	3.9 ± 1.4	0.5 ± 0.01	3.1 ± 1.0
r53	0.05 ± 0.01	4.0 ± 1.5	0.05 ± 0.01	2.2 ± 1.0
r54	0.002 ± 0.001	2.9 ± 1.1	0.003 ± 0.001	1.4 ± 1.0
r55	24.7 ± 1.31	2.7 ± 1.2	20.9 ± 7.42	3.5 ± 1.2
r56	-149.9 ± 1.33	22.8 ± 3.6	-147.2 ± 8.96	13.7 ± 1.2
r57	2.3 ± 0.01	3.2 ± 1.3	2.8 ± 0.02	5.3 ± 1.2
r58	-78.6 ± 0.04	6.0 ± 1.4	-76.0 ± 0.17	4.3 ± 1.1
r59	-2.8 ± 0.09	1.1 ± 1.0	-3.3 ± 0.03	1.3 ± 1.0
r60	-0.02 ± 0.01	2.6 ± 1.1	-0.02 ± 0.004	2.0 ± 1.1
r61	-2.0 ± 0.04	2.2 ± 1.0	4.7 ± 0.28	2.5 ± 1.0
r62	0.5 ± 0.07	5.2 ± 1.2	0.7 ± 0.05	6.2 ± 1.1
r63	0.2 ± 0.07	5.8 ± 1.9	0.5 ± 0.04	4.6 ± 1.4
r64	89.1 ± 0.17	1.5 ± 1.0	82.1 ± 0.77	1.3 ± 1.0
r65	-1.6 ± 0.44	12.0 ± 2.1	-0.5 ± 0.68	39.4 ± 4.3
r66	1.6 ± 0.44	5.2 ± 1.3	0.5 ± 0.68	9.6 ± 1.1
r67	-2.4 ± 0.66	4.6 ± 1.2	-0.7 ± 1.53	4.0 ± 1.2
r68	0.5 ± 0.07	1.3 ± 1.0	0.7 ± 0.04	2.1 ± 1.1
r69	0.6 ± 0.09	1.7 ± 0.9	0.4 ± 0.05	1.3 ± 1.0
r70	0.3 ± 0.04	1.2 ± 1.0	0.4 ± 0.07	2.6 ± 1.0

Appendix E. Matrix of scaled elasticities. The elasticities were identified from metabolite time-series data. Only non-zero entries are shown. Extracellular metabolites are denoted with the subscript 'ex'.

	G6P	ADP	GLC	ATP	F6P	F16P	DHAP	GAP	13PG	NADH	NAD	3GP	2GP	PYR	PEP	GLAC6P	NADPH	NADP	GL6P	RIBU5P	RIBO5P	XYL5P	S7P	E4P	LAC	GLU	ALA	AKG	G1P	AMP	SER	CIT	OAC	ACOA	CISAC	ISOCIT	SUC	SUCOA	MAL	FUM	IAC_{ex}	PYR_{ex}	GLC_{ex}	ALA_{ex}	SER_{ex}
r1	-2.2	-0.2	0.6	2.8	-0.1	-	-	-	-	-	-	-	-	-	-	-	-	-	-	-	-	-	-	-	-	-	-	-	-	-	-	-	-	-	-	-	-	-	-	-	-	-	-	-	-
r2	16.6	-	-	-	-0.9	-	-	-	-	-	-	-	-	-	-	-	-	-	-3.9	-	-	-	-	-	-	-	-	-	-	-	-	-	-	-	-	-	-	-	-	-	-	-	-	-	-	-
r3	-	-1.3	-	8.4	1.2	-2.4	-	-	-	-	-	-	-	-	-	-	-	-	-	-	-	-	-	-	-	-	-	-	-	0.7	-	-2.4	-	-	-	-	-	-	-	-	-	-	-	-	-	-
r4	-0.1	-7.5	-	-0.9	-0.2	1.9	-0.9	-0.5	-	-	-	-	-	-	-	-	-	-	-	-	-0.2	-	-	-0.4	-	-	-	-	-0.04	-	-	-	-	-	-	-	-	-	-	-	-	-	-	-	-	-
r5	-	-	-	-0.7	-	-	6.8	-2.0	-	-	-	-	-	-	-	-	-	-	-	-	-	-	-	-	-	-	-	-	-	-	-	-	-	-	-	-	-	-	-	-	-	-	-	-	-	-
r6	-	-2.3	-	-1.1	-	-	-	0.7	-0.1	-16.2	2.3	-	-	-	-	-	-	-	-	-	-	-	-	-	-	-	-	-	-	-	-	-	-	-	-	-	-	-	-	-	-	-	-	-	-	-
r7	-	5.1	-	-3.4	-	-	-	-	9.5	-	-	-0.4	-	-	-	-	-	-	-	-	-	-	-	-	-	-	-	-	-	-0.3	-	-	-	-	-	-	-	-	-	-	-	-	-	-	-	-
r8	-	-	-	-	-	-	-	-	-	-	-	0.7	-0.3	-	-	-	-	-	-	-	-	-	-	-	-	-	-	-	-	-	-	-	-	-	-	-	-	-	-	-	-	-	-	-	-	-
r9	0.2	1.3	-	-3.1	0.1	0.05	-	-	-	-	-	-	-	-1.1	1.6	-	-	-	-	-	-	-	-	-	-	-	-0.2	-	1.1	-	-	-	-	-	-	-	-	-	-	-	-	-	-	-	-
r10	0.9	-	-	-0.7	-	-	-	-	-	-	-	-	-	-	-	-0.2	-0.4	0.9	-	-	-	-	-	-	-	-	-	-	-	-	-	-	-	-	-	-	-	-	-	-	-	-	-	-	-	-
r11	-	-	-	-	-	-	-	-	-	-	-	-	-	-	-	3.3	-	-	-1.6	-	-	-	-	-	-	-	-	-	-	-	-	-	-	-	-	-	-	-	-	-	-	-	-	-	-	-
r12	-	-	-	-	-	-	-	-	-	-	-	-	-	-	-	-	-0.4	3.9	0.6	-0.6	-	-	-	-	-	-	-	-	-	-	-	-	-	-	-	-	-	-	-	-	-	-	-	-	-	-
r13	-	-	-	-	-	-	-	-	-	-	-	-	-	-	-	-	-	-	-	2.2	-2.1	-	-	-	-	-	-	-	-	-	-	-	-	-	-	-	-	-	-	-	-	-	-	-	-	-
r14	-	-	-	-	-	-	-	-	-	-	-	-	-	-	-	-	-	-	-	0.5	-	-0.1	-	-	-	-	-	-	-	-	-	-	-	-	-	-	-	-	-	-	-	-	-	-	-	-
r15	-	-	-	-	-	-	-	-1.0	-	-	-	-	-	-	-	-	-	-	-	-	0.3	2.6	-1.5	-	-	-	-	-	-	-	-	-	-	-	-	-	-	-	-	-	-	-	-	-	-	-
r16	-	-	-	-	-0.2	-	-	-0.8	-	-	-	-	-	-	-	-	-	-	-	-	-	1.8	-	0.04	-	-	-	-	-	-	-	-	-	-	-	-	-	-	-	-	-	-	-	-	-	-
r17	-	-	-	-	-	-	-	-	-	-	-	-	9.5	-	-0.3	-	-	-	-	-	-	-	-	-	-	-	-	-	-	-	-	-	-	-	-	-	-	-	-	-	-	-	-	-	-	-
r18	-	-	-	-	-	-	-	-	-	2.2	-25.8	-	-	4.3	-	-	-	-	-	-	-	-	-	-	-0.1	-	-	-	-	-	-	-	-	-	-	-	-	-	-	-	-	-	-	-	-	-
r19	-	-0.9	-	4.2	-	-	-	-	-	-	-	-	-	-	-	-	-	-	-	-	-	-	-	-	-	-	-	-	-	-	-	-	-	-	-	-	-	-	-	-	-	-	-	-	-	-
r20	-	-	-	-	-	-	-	-	-	-	-	-	-	-0.7	-	-	-	-	-	-	-	-	-	-	-	-4.3	2.0	0.8	-	-	-	-	-	-	-	-	-	-	-	-	-	-	-	-	-	-
r21	8.0	-	-	-	-	-0.8	-	-	-	-	-	-	-	-	-	-	-	-	-	-	-	-	-	-	-	-	-	-	-2.8	-	-	-	-	-	-	-	-	-	-	-	-	-	-	-	-	-
r22	-	-	-	-	-	-	-	-	-	-	-	-	-	-	-	-	0.1	-0.9	-	-	-	-	-	-	-	-	-	-	-	-	-	-	-	-	-	-	-	-	-	-	-	-	-	-	-	-
r23	-	-	-	-	-	-	-	-	-	-	-	-	-	-	-	-	-	-	-	-	-	-	-	-	-	-	-	-	0.6	-0.8	-	-	-	-	-	-	-	-	-	-	-	-	-	-	-	-
r24	-	-	-	-	-3.2	-	-	1.4	-	-	-	-	-	-	-	-	-	-	-	-	-	-	17.7	-1.1	-	-	-	-	-	-	-	-	-	-	-	-	-	-	-	-	-	-	-	-	-	-	-
r25	-	-2.6	-	0.4	-	-	-	-	-	-	-	-	-	-	-	-	-	-	-	-	-	-	-	-	-	-	-	-	-	14.8	-	-	-	-	-	-	-	-	-	-	-	-	-	-	-	-
r26	-	-	-	-	-	-	2.0	-	-	-	-	-	-	-	-	-	-	-	-	-	-	-	-	-	-	-	-	-	-	-	-	-	-	-	-	-	-	-	-	-	-	-	-	-	-	-
r27	-	-	-	0.4	-	-	-	-	-	-	-	-	-	-	-	-	-	-	-	-	0.8	-	-	-	-	-	-	-	-	-15.8	-	-	-	-	-	-	-	-	-	-	-	-	-	-	-	-
r28	-	-	-	-	-	-	-	-	-	-0.4	2.7	0.9	-	-	-	-	-	-	-	-	-	-	-	-	-	2.4	-	-0.1	-	-	-3.9	-	-	-	-	-	-	-	-	-	-	-	-	-	-	-	-
r29	-	-	-	-	-	-	-	-	-	-	-	-	-	-	-	-	-	-	-	-	-	-	-	-	-	-	-	-	-	-	-	-0.6	0.8	4.1	-	-	-	-	-	-	-	-	-	-	-	-
r30	-	-	-	-	-	-	-	-	-	-	-	-	-	-	-	-	-	-	-	-	-	-	-	-	-	-	-	-	-	-	-	6.2	-	-	-6.0	-	-	-	-	-	-	-	-	-	-	-
r31	-	-	-	-	-	-	-	-	-	-	-	-	-	-	-	-	-	-	-	-	-	-	-	-	-	-	-	-	-	-	-	-	-	-	3.3	-1.8	-	-	-	-	-	-	-	-	-	-

Appendix E (continued)

	G6P	ADP	GLC	ATP	F6P	F16P	DHAP	GAP	13PG	NADH	NAD	3GP	2GP	PYR	PEP	GLAC6P	NADPH	NADP	GL6P	RIBU5P	RIBO5P	XYL5P	S7P	E4P	LAC	GLU	ALA	AKG	G1P	AMP	SER	CIT	OAC	ACOA	CISAC	ISOCIT	SUC	SUCOA	MAL	FUM	IAC_{ex}	PYR_{ex}	GLC_{ex}	ALA_{ex}	SER_{ex}
r32	-	4.8	-	-	-	-	-	-	-	-0.7	0.8	-	-	-	-	-	-	-	-	-	-	-	-	-	-	-	-	-2.4	-	-	-	-	-	-	-	3.0	-	-	-	-	-	-	-	-	-
r33	-	0.04	-	-0.6	-	-	-	-	-	-	-	-	-	-	-	-	-	-	-	-	-	-	-	-	-	-	-	-	-	-	-	-	-	-	-	-	-0.4	0.3	-	-	-	-	-	-	-
r34	-	-	-	-	-	-	-	-	-	-	-	-	-	-	-	-	-	-	-	-	-	-	-	-	-	-	-	-	-	-	-	-	-	-	-	-	-	-	-4.3	4.1	-	-	-	-	-
r35	-	-	-	-	-	-	-	-	-	-1.2	31.7	-	-	-	-	-	-	-	-	-	-	-	-	-	-	-	-	-	-	-	-	-	-2.8	-	-	-	-	-	1.1	-	-	-	-	-	-
r36	-	-	-	-	-	-	-	-	-	-0.2	29.9	-	-	1.0	-	-	-	-	-	-	-	-	-	-	-	-	-	-	0.1	-	-	-	-1.2	-	-	-	-	-	-	-	-	-	-	-	-
r37	-	0.004	-	-0.3	-	-	-	-	-	-1.2	1.2	-	-	-	-	-	-	-	-	-	-	-	-	-	-	-	-	0.8	-	-	-	-	-	-	-	-	-	-19.6	-	-	-	-	-	-	-
r38	-	-	-	-	-	-	-	-	-	-	-	-	-	-1.8	-	-	-	-	-	-	-	-	-	-	-	-	-	-	-	-	-	-	-	-	-	-	-	-	-	-	-	-	-	-	-
r39	-	-	-	-	-	-	-	-	-	-0.3	1.0	-	-	-	-	-	-	-	-	-	-	-	-	-	-	-0.3	-	0.1	-	-	-	-	-	-	-	-	-	-0.6	-	-	-	-	-	-	-
r40	-	-	-	-	-	-	-	-	-	-3.2	0.6	-	-	-	-	-	-	-	-	-	-	-	-	-	-	-	-	-	-	-	-	-	-	-	-	0.3	-	-	-	-2.5	-	-	-	-	-
r41	-	1.1	-	-1.6	-	-	-	-	-	2.2	-3.6	-	-	-	-	-	-	-	-	-	-	-	-	-	-	-	-	-	-	-	-	-	-	-	-	-	-	-	-	-	-	-	-	-	-
r42	-	-	-	-	-	-	-	-	-	-	-	-	-	-	-	-	-	-	-	-	-	-	-	-	-	-	-	-0.5	-	-	-	-	-	-	-	-	-	-	-	-	-	-	-	-	-
r43	-	-	-	-	-	-	-	-	-	-	-	-	-	-8.0	-	-	-0.7	3.8	-	-	-	-	-	-	-	-	-	-	-	-	-	-	-	-	-	-	-	-	0.6	-	-	-	-	-	-
r44	-	-	-	-	-	-	-	-	-	-1.2	0.1	-	-	-	-	-	-	-	-	-	-	-	-	-	-	0.6	-	-0.6	-	-	-	-	-	-	-	-	-	-	-	-	-	-	-	-	-
r45	-	-	-	-	-	-	-	-	-	-	-	-	-	-	-	-	-	-	-	-	-	-	-	-	4.0	-	-	-	-	-	-	-	-	-	-	-	-	-	-	-	-0.8	-	-	-	-
r46	-	-	-	-	-	-	-	-	-	-	-	-	-	2.0	-	-	-	-	-	-	-	-	-	-	-	-	-	-	-	-	-	-	-	-	-	-	-	-	-	-	-	-3.3	-	-	-
r47	-	-	-2.6	-	-	-	-	-	-	-	-	-	-	-	-	-	-	-	-	-	-	-	-	-	-	-	-	-	-	-	-	-	-	-	-	-	-	-	-	-	-	-	1.8	-	-
r48	-	-	-	-	-	-	-	-	-	-	-	-	-	-	-	-	-	-	-	-	-	-	-	-	-	-	-0.4	-	-	-	-	-	-	-	-	-	-	-	-	-	-	-	-	5.3	-
r49	-	-	-	-	-	-	-	-	-	-	-	-	-	-	-	-	-	-	-	-	-	-	-	-	-	-	-	-	-	-	0.8	-	-	-	-	-	-	-	-	-	-	-	-	-	-2.0

Appendix F. Experimentally Determined Reference Metabolite Concentrations. Extracellular metabolites are denoted with the subscript 'ex'. Intracellular and extracellular values are given in mmol/l_{cv} and mmol/l_{well}.

Metabolite	Measurement
ALA	5.1 ± 1.1
6PG	0.20 ± 0.07
S7P	0.10 ± 0.02
PEP	0.04 ± 0.0002
F16P	0.09 ± 0.03
3PG	0.18 ± 0.008
DHAP	0.07 ± 0.007
G6P	0.06 ± 0.02
RIBO5P	0.05 ± 0.004
RIBU5P	0.06 ± 0.004
ADP	0.08 ± 0.04
ATP	0.98 ± 0.019
AMP	0.02 ± 0.004
NADP	0.03 ± 0.001
NADPH	0.003 ± 0.0006
NAD	0.18 ± 0.007
NADH	0.004 ± 0.0001
FUM	0.11 ± 0.01
MAL	0.37 ± 0.06
CISAC	0.005 ± 0.0004
ISOCIT	0.005 ± 0.0005
CIT	0.28 ± 0.03
GLC	9.7 ± 1.4
PYR	0.74 ± 0.20
LAC	11.4 ± 2.1
ALA_{ex}	0.82 ± 0.02
GLC_{ex}	9.45 ± 0.4
PYR_{ex}	0.52 ± 0.05
LAC_{ex}	2.15 ± 0.08
SER_{ex}	0.11 ± 0.002

Appendix G. Matrix of Flux Control Coefficients. Only values ≥ 0.05 are reported. The value in row i and column j indicates the control that enzyme j exerts over the steady state flux i, i.e. $C^{J^\circ}_{ij} = \frac{\partial J_i}{\partial e_j}\frac{e^\circ_j}{J^\circ_i}$. The indices i and j correspond to the reaction numbers shown in Table 11 and Figure 16.

	e1	e2	e3	e4	r5	e6	e7	e8	e9	e10	e11	e12	e13	e14	e15	e16	e17	e18	e19	e20	e21	e22	e23	e24	e25	e26	e27	e28	e29	e30	e31	e32	e33	e34	e35	e36	e37	e38	e39	e40	e41	e42	e43	e44	e45	e46	e47	e48	e49
J1	0.12	0.06	0.07	0.09	0.01	0.21	-	0.01	-	-0.74	-0.03	0.28	-0.04	0.56	-0.24	0.38	-	0.43	-0.18	-	-	-0.03	-	-0.02	-	-	0.01	-0.01	-0.11	0.02	0.03	0.02	0.01	0.01	-0.03	-0.37	-	0.02	-0.05	0.01	0.82	-0.08	0.11	-0.02	0.01	-0.29	0.03	-0.02	-0.03
J2	0.15	0.11	0.13	0.16	0.02	0.38	0.01	0.02	-	-1.63	-0.07	0.50	-0.07	1.02	-0.44	0.69	-	0.81	-0.33	-0.01	-	-0.54	-	-0.04	0.01	-	0.01	-0.01	-0.20	0.03	0.06	0.04	0.02	0.02	-0.06	-0.67	-	0.03	-0.09	0.03	1.48	-0.15	0.21	-0.04	0.02	-0.53	0.03	-0.03	-0.06
J3	0.13	0.07	0.08	0.11	0.01	0.25	-	0.01	-	-0.94	-0.04	0.33	-0.05	0.67	-0.29	0.45	-	0.52	-0.21	-	-	-0.14	-	-0.02	-	-	0.01	-0.01	-0.13	0.02	0.04	0.02	0.01	0.01	-0.04	-0.44	-	0.02	-0.06	0.02	0.97	-0.10	0.13	-0.03	0.01	-0.35	0.03	-0.02	-0.04
J4	0.13	0.07	0.08	0.11	0.01	0.25	-	0.01	-	-0.94	-0.04	0.33	-0.05	0.67	-0.29	0.45	-	0.52	-0.21	-	-	-0.14	-	-0.02	-	-	0.01	-0.01	-0.13	0.02	0.04	0.02	0.01	0.01	-0.04	-0.44	-	0.02	-0.06	0.02	0.97	-0.10	0.13	-0.03	0.01	-0.35	0.03	-0.02	-0.04
J5	0.13	0.07	0.08	0.11	0.01	0.25	-	0.01	-	-0.93	-0.04	0.33	-0.05	0.66	-0.29	0.44	-	0.52	-0.21	-	-	-0.15	-	-0.02	-	-	0.01	-0.01	-0.13	0.02	0.04	0.02	0.01	0.01	-0.04	-0.44	-	0.02	-0.06	0.02	0.97	-0.10	0.13	-0.03	0.01	-0.35	0.03	-0.02	-0.04
J6	0.12	0.06	0.08	0.10	0.01	0.23	-	0.01	-	-0.83	-0.04	0.30	-0.04	0.61	-0.26	0.41	-	0.47	-0.19	-	-	-0.08	-	-0.02	-	-	-	-0.01	-0.12	0.02	0.04	0.02	0.01	0.01	-0.03	-0.40	-	0.02	-0.05	0.01	0.89	-0.09	0.12	-0.02	0.01	-0.32	0.03	-0.02	-0.03
J7	0.12	0.06	0.08	0.10	0.01	0.23	-	0.01	-	-0.83	-0.04	0.30	-0.04	0.61	-0.26	0.41	-	0.47	-0.19	-	-	-0.08	-	-0.02	-	-	-	-0.01	-0.12	0.02	0.04	0.02	0.01	0.01	-0.03	-0.40	-	0.02	-0.05	0.01	0.89	-0.09	0.12	-0.02	0.01	-0.32	0.03	-0.02	-0.03
J8	0.12	0.06	0.08	0.10	0.01	0.23	-	0.01	-	-0.84	-0.04	0.30	-0.05	0.61	-0.26	0.41	-	0.48	-0.20	-	-	-0.08	-	-0.02	-	-	-	-0.01	-0.12	0.02	0.04	0.02	0.01	0.01	-0.03	-0.40	-	0.02	-0.06	0.01	0.89	-0.09	0.12	-0.02	0.01	-0.32	0.03	-0.02	-0.04
J9	0.12	0.06	0.08	0.10	0.01	0.23	-	0.01	-	-0.84	-0.04	0.30	-0.05	0.61	-0.26	0.41	-	0.48	-0.20	-	-	-0.08	-	-0.02	-	-	-	-0.01	-0.12	0.02	0.04	0.02	0.01	0.01	-0.03	-0.40	-	0.02	-0.06	0.01	0.89	-0.09	0.12	-0.02	0.01	-0.32	0.03	-0.02	-0.04
J10	0.09	-0.01	-0.01	-0.01	-	-0.02	-	-	-	0.42	0.02	-0.02	-	-0.04	0.02	-0.03	-	-0.06	0.01	-	-	0.63	-	-	-	-	-	-	0.01	-	-	-	-	-	-	0.03	-	-	-	-	-0.06	0.01	-0.02	-	-	0.02	0.02	-	-
J11	0.09	-0.01	-0.01	-0.01	-	-0.02	-	-	-	0.42	0.02	-0.02	-	-0.04	0.02	-0.03	-	-0.06	0.01	-	-	0.63	-	-	-	-	-	-	0.01	-	-	-	-	-	-	0.03	-	-	-	-	-0.06	0.01	-0.02	-	-	0.02	0.02	-	-
J12	0.09	-0.01	-0.01	-0.01	-	-0.02	-	-	-	0.42	0.02	-0.02	-	-0.04	0.02	-0.03	-	-0.06	0.01	-	-	0.63	-	-	-	-	-	-	0.01	-	-	-	-	-	-	0.03	-	-	-	-	-0.06	0.01	-0.02	-	-	0.02	0.02	-	-
J13	0.09	-0.01	-0.01	-0.01	-	-0.02	-	-	-	0.40	0.02	-0.01	0.01	-0.05	0.02	-0.03	-	-0.05	-0.01	-	-	0.63	-	-	0.01	-	0.01	-	0.01	-	-	-	-	-	-	0.03	-	-	-	-	-0.05	0.01	-0.02	-	-	0.02	0.02	-	-
J14	0.09	-0.01	-0.01	-0.01	-	-0.02	-	-	-	0.43	0.02	-0.02	-	-0.04	0.02	-0.04	-	-0.06	0.03	-	-	0.63	-	-	-0.01	-	-0.01	-	0.01	-	-	-	-	-	-	0.03	-	-	0.01	-	-0.06	0.01	-0.02	-	-	0.02	0.02	-	-
J15	0.09	-0.01	-0.01	-0.01	-	-0.02	-	-	-	0.43	0.02	-0.02	-	-0.04	0.02	-0.04	-	-0.06	0.03	-	-	0.63	-	-	-0.01	-	-0.01	-	0.01	-	-	-	-	-	-	0.03	-	-	0.01	-	-0.06	0.01	-0.02	-	-	0.02	0.02	-	-
J16	0.09	-0.01	-0.01	-0.01	-	-0.02	-	-	-	0.43	0.02	-0.02	-	-0.04	0.02	-0.04	-	-0.06	0.03	-	-	0.63	-	-	-0.01	-	-0.01	-	0.01	-	-	-	-	-	-	0.03	-	-	0.01	-	-0.06	0.01	-0.02	-	-	0.02	0.02	-	-
J17	0.12	0.06	0.08	0.10	0.01	0.23	-	0.01	-	-0.84	-0.04	0.30	-0.05	0.61	-0.26	0.41	-	0.48	-0.20	-	-	-0.08	-	-0.02	-	-	-	-0.01	-0.12	0.02	0.04	0.02	0.01	0.01	-0.03	-0.40	-	0.02	-0.06	0.01	0.89	-0.09	0.12	-0.02	0.01	-0.32	0.03	-0.02	-0.04
J18	0.08	0.06	0.07	0.09	0.01	0.21	-	0.01	-	-0.88	-0.04	0.28	-0.04	0.56	-0.24	0.38	-	0.56	-0.26	-	-	0.04	-	-0.02	-	-	-	-0.01	-0.10	0.02	0.03	0.02	0.02	0.02	-0.03	-0.35	-	0.02	-0.09	0.03	0.72	-0.12	0.18	0.01	0.01	-0.29	0.02	0.03	-0.03
J19	0.08	0.05	0.06	0.07	0.01	0.17	-	0.01	-	-0.64	-0.03	0.22	-0.03	0.45	-0.19	0.30	-	0.34	-0.08	-	-	-0.03	-	-0.02	-	-	-	-	-0.07	0.02	0.03	0.02	0.01	0.01	-0.02	-0.23	-	0.01	-0.05	0.02	0.70	-0.07	0.11	-0.02	0.01	-0.16	0.02	-0.01	-0.02
J20	-0.28	-	-0.02	-0.02	-	-0.05	-	-0.02	-	-0.72	-0.03	-0.08	0.01	-0.15	0.05	-0.09	-	0.80	-0.49	0.08	-	1.04	-	-	-	-	-	0.01	0.08	-	-	-	0.09	0.09	0.02	0.27	0.01	-0.02	-0.40	0.15	-0.85	-0.36	0.58	0.34	0.02	0.44	-0.06	0.47	0.06
J21	0.36	-0.08	-0.05	-	-	-0.02	-	-	-	0.98	0.04	-0.43	-0.01	-0.52	-0.01	-0.01	-	-0.23	0.04	-	0.17	-0.13	0.83	-	0.02	-	-0.02	-	0.01	-0.02	-0.04	-0.02	-0.02	-0.02	-	0.03	-	-	0.09	-0.03	0.13	0.08	-0.14	0.03	-0.01	-0.07	0.08	-0.01	-0.01
J22	0.08	-0.01	-0.01	-0.01	-	-0.02	-	-	-	0.38	0.02	-0.02	-	-0.04	0.02	-0.03	-	-0.03	-	-	-	0.65	-	-	-	-	-	-	0.01	-	-	-	-	-	-	0.04	-	-	-	-	-0.08	0.01	-	-	-	0.03	0.02	-	-
J23	0.36	-0.08	-0.05	-	-	-0.02	-	-	-	0.98	0.04	-0.43	-0.01	-0.52	-0.01	-0.01	-	-0.23	0.04	-	0.17	-0.13	0.83	-	0.02	-	-0.02	-	0.01	-0.02	-0.04	-0.02	-0.02	-0.02	-	0.03	-	-	0.09	-0.03	0.13	0.08	-0.14	0.03	-0.01	-0.07	0.08	-0.01	-0.01
J24	0.09	-0.01	-0.01	-0.01	-	-0.02	-	-	-	0.43	0.02	-0.02	-	-0.04	0.02	-0.04	-	-0.06	0.03	-	-	0.63	-	-	-0.01	-	-0.01	-	0.01	-	-	-	-	-	-	0.03	-	-	0.01	-	-0.06	0.01	-0.02	-	-	0.02	0.02	-	-
J25	0.17	0.05	0.06	0.07	0.01	0.14	-	0.01	-	-0.50	-0.02	0.26	0.15	-0.34	-0.21	0.29	-	0.31	-1.15	-	-	0.43	-	-0.02	0.51	-	0.48	-	-0.05	0.02	0.03	0.02	0.01	0.01	-0.01	-0.17	-	0.01	-0.07	0.02	0.55	-0.08	0.12	-0.03	0.01	-0.10	0.04	-	-0.02
J26	0.30	0.24	0.29	0.37	-0.24	0.05	-	-0.01	-	-3.72	-0.17	1.12	-0.17	2.29	-0.99	1.54	-	1.16	-3.11	0.01	-	0.31	-	-0.08	-	1.00	0.02	0.01	0.04	0.12	0.21	0.13	0.13	0.12	0.01	0.15	0.02	-0.04	-0.55	0.21	-0.85	-0.48	0.83	-0.21	0.03	0.71	0.07	0.08	0.05

Appendix G (continued)

	e1	e2	e3	e4	r5	e6	e7	e8	e9	e10	e11	e12	e13	e14	e15	e16	e17	e18	e19	e20	e21	e22	e23	e24	e25	e26	e27	e28	e29	e30	e31	e32	e33	e34	e35	e36	e37	e38	e39	e40	e41	e42	e43	e44	e45	e46	e47	e48	e49
J27	0.17	0.05	0.06	0.07	0.01	0.14	-	0.01	-	-0.50	-0.02	0.26	0.15	-0.34	-0.21	0.29	-	0.31	-1.15	-	-	0.43	-	-0.02	0.51	-	0.48	-	-0.05	0.02	0.03	0.02	0.01	0.01	-0.01	-0.17	-	0.01	-0.07	0.02	0.55	-0.08	0.12	-0.03	0.01	-0.10	0.04	-	-0.02
J28	0.26	0.01	0.03	0.03	-	0.08	-	-0.20	-	0.51	0.02	0.12	-0.02	0.23	-0.09	0.14	-0.01	-0.61	0.45	0.04	-	-0.94	-	-0.01	-	-	-	0.17	-0.09	-	-	-	-0.08	-0.08	-0.03	-0.32	-0.01	0.03	0.35	-0.13	0.95	0.30	-0.50	-0.19	-0.01	-0.46	0.06	0.22	0.76
J29	-0.06	-0.01	-0.02	-0.02	-	-0.05	-	-	-	0.07	-	-0.07	0.01	-0.14	0.06	-0.09	-	-0.03	0.29	-	-	0.16	-	-	-	-	-	-	0.18	0.01	0.02	0.01	0.02	0.02	0.05	0.63	-	-	-0.05	0.04	-	-0.05	0.05	-0.01	-	-0.03	-0.01	0.01	-
J30	-0.06	-0.01	-0.02	-0.02	-	-0.05	-	-	-	0.07	-	-0.07	0.01	-0.14	0.06	-0.09	-	-0.03	0.29	-	-	0.16	-	-	-	-	-	-	0.18	0.01	0.02	0.01	0.02	0.02	0.05	0.63	-	-	-0.05	0.04	-	-0.05	0.05	-0.01	-	-0.03	-0.01	0.01	-
J31	-0.06	-0.01	-0.02	-0.02	-	-0.05	-	-	-	0.07	-	-0.07	0.01	-0.14	0.06	-0.09	-	-0.03	0.29	-	-	0.16	-	-	-	-	-	-	0.18	0.01	0.02	0.01	0.02	0.02	0.05	0.63	-	-	-0.05	0.04	-	-0.05	0.05	-0.01	-	-0.03	-0.01	0.01	-
J32	-0.06	-0.01	-0.02	-0.02	-	-0.05	-	-	-	0.07	-	-0.07	0.01	-0.14	0.06	-0.09	-	-0.03	0.29	-	-	0.16	-	-	-	-	-	-	0.18	0.01	0.02	0.01	0.02	0.02	0.05	0.63	-	-	-0.05	0.04	-	-0.05	0.05	-0.01	-	-0.03	-0.01	0.01	-
J33	-0.18	-	-0.01	-0.02	-	-0.04	-	-0.01	-	-0.43	-0.02	-0.06	0.01	-0.13	0.05	-0.08	-	0.45	-0.18	-	-	0.68	-	-	-	-	-	-	0.14	0.01	0.01	0.01	0.07	0.06	0.04	0.50	-	-0.01	-0.03	0.11	-0.49	-	0.37	-0.04	0.01	0.24	-0.04	-0.01	0.02
J34	-0.18	-	-0.01	-0.02	-	-0.04	-	-0.01	-	-0.43	-0.02	-0.06	0.01	-0.13	0.05	-0.08	-	0.45	-0.18	-	-	0.68	-	-	-	-	-	-	0.14	0.01	0.01	0.01	0.07	0.06	0.04	0.50	-	-0.01	-0.03	0.11	-0.49	-	0.37	-0.04	0.01	0.24	-0.04	-0.01	0.02
J35	-0.06	-0.01	-0.02	-0.02	-	-0.05	-	-	-	0.07	-	-0.07	0.01	-0.14	0.06	-0.09	-	-0.03	0.29	-	-	0.16	-	-	-	-	-	-	0.18	0.01	0.02	0.01	0.02	0.02	0.05	0.63	-	-	-0.05	0.04	-	-0.05	0.05	-0.01	-	-0.03	-0.01	0.01	-
J36	-0.06	-0.01	-0.02	-0.02	-	-0.05	-	-	-	0.07	-	-0.07	0.01	-0.14	0.06	-0.09	-	-0.03	0.29	-	-	0.16	-	-	-	-	-	-	0.18	0.01	0.02	0.01	0.02	0.02	0.05	0.63	-	-	-0.05	0.04	-	-0.05	0.05	-0.01	-	-0.03	-0.01	0.01	-
J37	-0.22	-	-0.01	-0.02	-	-0.05	-	-0.01	-	-0.55	-0.02	-0.07	0.01	-0.14	0.05	-0.08	-	0.55	-0.25	0.01	-	0.83	-	-	-	-	-	0.01	0.18	0.01	0.02	0.01	0.08	0.08	0.05	0.63	0.01	-0.02	-0.32	0.13	-0.61	0.01	0.46	-0.11	0.01	0.30	-0.05	0.05	0.02
J38	-0.01	-0.01	-0.01	-0.01	-	-0.02	-	-	-	0.07	-	-0.03	-	-0.06	0.02	-0.04	-	0.26	-0.25	-	-	0.02	-	-	-	-	-	-	0.05	-	-	-	-	-	0.01	0.18	-	0.99	-0.01	-	-0.40	0.01	-0.01	-0.02	0.01	0.20	-	-	0.02
J39	-0.06	-0.01	-0.01	-0.01	-	-0.03	-	-	-	-0.02	-	-0.05	0.01	-0.09	0.04	-0.06	-	0.11	0.05	-0.04	-	0.17	-	-	-	-	-	-	0.01	-	-0.01	-	0.01	0.01	-	0.04	-0.03	-	0.95	0.02	-0.11	-0.04	0.08	0.20	-	0.04	-0.01	-0.19	0.02
J40	-0.18	-	-0.01	-0.02	-	-0.04	-	-0.01	-	-0.43	-0.02	-0.06	0.01	-0.13	0.05	-0.08	-	0.45	-0.18	-	-	0.68	-	-	-	-	-	-	0.14	0.01	0.01	0.01	0.07	0.06	0.04	0.50	-	-0.01	-0.03	0.11	-0.49	-	0.37	-0.04	0.01	0.24	-0.04	-0.01	0.02
J41	-0.03	-	-	-0.01	-	-0.01	-	-0.01	-	-0.02	-	-0.02	-	-0.04	0.02	-0.03	-	-0.13	0.26	-	-	0.09	-	-	-	-	-	0.01	0.08	0.01	0.01	0.01	0.01	0.01	0.02	0.26	-	-0.02	-0.05	0.02	0.19	-0.01	0.04	-0.02	-	0.30	-0.01	0.03	0.03
J42	-0.60	0.03	-0.01	-0.01	-	-0.03	-	-0.02	-	-1.98	-0.09	-0.07	0.01	-0.13	0.03	-0.05	-	1.91	-1.52	0.03	-	2.41	-	-	-0.01	-	-	0.02	0.18	0.01	0.02	0.01	0.23	0.21	0.05	0.63	0.03	-0.06	-0.96	0.36	-2.04	0.14	1.40	-0.35	0.05	1.08	-0.13	0.15	0.08
J43	-0.33	0.01	-0.01	-0.01	-	-0.03	-	-0.01	-	-1.00	-0.05	-0.06	0.01	-0.11	0.04	-0.06	-	1.00	-0.73	-	-	1.29	-	-	-	-	-	0.01	0.10	-	0.01	0.01	0.12	0.11	0.03	0.34	-	-0.03	-	0.19	-1.07	0.05	0.73	-0.07	0.02	0.56	-0.07	-0.02	0.05
J44	-0.31	-	-0.02	-0.02	-	-0.06	-	-	-	-0.80	-0.04	-0.09	0.01	-0.17	0.06	-0.10	-	0.89	-0.55	0.09	-	1.17	-	0.01	-	-	-	-	0.09	-	-	-	0.11	0.10	0.03	0.30	0.01	-0.03	-0.44	0.17	-0.97	-0.40	0.65	0.38	0.02	0.49	-0.07	0.48	0.02
J45	0.08	0.06	0.07	0.09	0.01	0.21	-	0.01	-	-0.88	-0.04	0.28	-0.04	0.56	-0.24	0.38	-	0.56	-0.26	-	-	0.04	-	-0.02	-	-	-	-0.01	-0.10	0.02	0.03	0.02	0.02	0.02	-0.03	-0.35	-	0.02	-0.09	0.03	0.72	-0.12	0.18	0.01	0.01	-0.29	0.02	0.03	-0.03
J46	0.02	0.01	0.01	0.01	-	0.02	-	0.01	-	-0.08	-	0.03	-	0.06	-0.03	0.04	-	-0.30	0.28	-	-	-0.02	-	-	-	-	-	-	-0.06	-	-	-	-	-	-0.02	-0.20	-	0.01	0.01	-0.01	0.45	-0.01	0.01	0.03	-0.01	0.77	-	-	-0.02
J47	0.12	0.06	0.07	0.09	0.01	0.21	-	0.01	-	-0.74	-0.03	0.28	-0.04	0.56	-0.24	0.38	-	0.43	-0.18	-	-	-0.03	-	-0.02	-	-	0.01	-0.01	-0.11	0.02	0.03	0.02	0.01	0.01	-0.03	-0.37	-	0.02	-0.05	0.01	0.82	-0.08	0.11	-0.02	0.01	-0.29	0.03	-0.02	-0.03
J48	-0.28	-	-0.02	-0.02	-	-0.05	-	-0.02	-	-0.72	-0.03	-0.08	0.01	-0.15	0.05	-0.09	-	0.80	-0.49	0.08	-	1.04	-	-	-	-	-	0.01	0.08	-	-	-	0.09	0.09	0.02	0.27	0.01	-0.02	-0.40	0.15	-0.85	-0.36	0.58	0.34	0.02	0.44	-0.06	0.47	0.06
J49	0.26	0.01	0.03	0.03	-	0.08	-	-0.20	-	0.51	0.02	0.12	-0.02	0.23	-0.09	0.14	-0.01	-0.61	0.45	0.04	-	-0.94	-	-0.01	-	-	-	0.17	-0.09	-	-	-	-0.08	-0.08	-0.03	-0.32	-0.01	0.03	0.35	-0.13	0.95	0.30	-0.50	-0.19	-0.01	-0.46	0.06	0.22	0.76

Appendix H. Matrix of Concentration Control Coefficients. Only values ≥ 0.005 are reported. The value in row i and column j indicates the control that enzyme j exerts over the steady state concentration i, i.e. $C^{c^\circ}_{ij} = \frac{\partial C_i}{\partial e_j}\frac{e^\circ_j}{C^\circ_i}$. The indices i and j correspond to the reaction numbers shown in Table 11 and Figure 16.

	e1	e2	e3	e4	e5	e6	e7	e8	e9	e10	e11	e12	e13	e14	e15	e16	e17	e18	e19	e20	e21	e22	e23	e24	e25	e26	e27	e28	e29	e30	e31	e32	e33	e34	e35	e36	e37	e38	e39	e40	e41	e42	e43	e44	e45	e46	e47	e48	e49
G6P	-0.02	-0.03	-	-0.07	-	-	-	0.40	0.02	-0.19	0.01	-0.31	0.07	-0.12	-	-0.14	-0.09	-	-	0.05	-	0.01	-	-	-	-	0.04	-	-0.01	-0.01	-	-	0.01	0.13	-	-0.01	0.01	-	-0.26	0.02	-0.03	0.01	-	0.11	0.08	0.01	0.01	-	-
GLC	-0.03	-0.03	-	-0.08	-	-	-	0.29	0.01	-0.11	0.02	-0.22	0.09	-0.15	-	-0.17	0.07	-	-	0.01	-	0.01	-	-	-	-	0.04	-0.01	-0.01	-0.01	-	-	0.01	0.14	-	-0.01	0.02	-	-0.32	0.03	-0.04	0.01	-	0.11	0.38	0.01	0.01	-	-
ATP	0.01	0.01	-	0.02	-	-	-	-0.06	-	0.02	-	0.04	-0.02	0.03	-	0.03	-0.10	-	-	-	-	-	-	-	-	-	-0.01	-	-	-	-	-	-	-0.02	-	-	-	-	0.06	-0.01	0.01	-	-	-0.02	-	-	-	-	-
F6P	-0.35	-0.45	-0.06	-0.79	-0.01	-0.03	-	-4.37	-0.20	3.06	0.22	3.10	1.28	-1.73	-	-1.97	0.03	0.01	-	-1.46	-0.01	0.11	0.02	-	-0.01	0.02	0.42	-0.10	-0.18	-0.11	-0.06	-0.06	0.12	1.45	-0.01	-0.06	0.34	-0.09	-2.72	0.45	-0.61	0.14	-0.05	1.01	0.54	0.05	0.11	-	-
F16P	0.21	-0.26	-0.03	-0.48	-0.01	-0.04	-	-3.50	-0.16	1.37	0.13	1.24	0.74	-1.02	-	0.45	-1.40	0.03	-	1.27	-0.01	0.06	-0.01	-	-	0.03	0.29	0.11	0.20	0.12	0.14	0.13	0.08	1.01	0.02	-0.09	-0.59	0.23	-3.42	-0.43	0.79	-0.21	0.01	1.56	0.15	0.15	0.14	-	-
DHAP	0.15	0.19	-0.12	0.02	-	-0.01	-	-1.90	-0.09	0.57	-0.09	1.17	-0.51	0.79	-	0.59	-1.59	0.01	-	0.16	-	-0.04	-	-	0.01	0.01	0.02	0.06	0.11	0.06	0.07	0.06	0.01	0.08	0.01	-0.02	-0.28	0.10	-0.43	-0.25	0.43	-0.11	0.01	0.36	0.03	0.04	0.02	-	-
GAP	0.46	0.58	0.08	-0.05	-	-0.03	-	-5.94	-0.27	1.77	-0.27	3.61	-1.56	2.43	-	1.73	-5.24	0.03	-0.01	0.61	-	-0.13	-0.01	-0.01	0.02	0.02	0.14	0.19	0.35	0.21	0.22	0.21	0.04	0.49	0.03	-0.08	-0.92	0.35	-1.98	-0.78	1.37	-0.34	0.04	1.41	0.10	0.15	0.10	-	-
13PG	0.04	0.04	0.01	0.10	-0.10	-0.05	-	-0.40	-0.02	0.14	-0.02	0.28	-0.12	0.19	-	0.21	-0.47	-	-	-0.02	-	-0.01	-	-	-	-	-0.05	0.01	0.02	0.01	0.01	0.01	-0.01	-0.16	-	0.01	-0.03	0.01	0.43	-0.04	0.06	-0.01	0.01	-0.12	0.01	-0.01	-0.01	-	-
NAD	-	-	-	-	-	-	-	0.01	-	-	-	-	-	-	-	-	0.01	-	-	-	-	-	-	-	-	-	-	-	-	-	-	-	-	-	-	-	-	-	-	-	-	-	-	-	-	-	-	-	-
3GP	0.11	0.14	0.02	0.33	0.01	-1.37	-0.01	-1.21	-0.06	0.44	-0.06	0.88	-0.38	0.59	-0.04	0.69	-0.29	-0.01	-	-0.12	-	-0.03	-	-	0.01	-0.01	-0.17	0.03	0.05	0.03	0.01	0.01	-0.05	-0.58	-	0.03	-0.08	0.02	1.28	-0.13	0.18	-0.03	0.02	-0.46	0.04	-0.03	-0.06	-	-
2GP	0.01	0.01	-	0.03	-	-	-0.02	-0.14	-0.01	0.05	-0.01	0.10	-0.04	0.06	-0.11	0.07	-0.04	-	-0.01	-0.02	0.01	-	-	-	-	-	-0.02	-	0.01	-	-	-	-0.01	-0.06	-	-	-0.01	-	0.14	-0.01	0.02	-0.01	-	-0.05	-	-	-0.01	-	-
PYR	-	-	-	0.01	-	-	-	-0.04	-	0.02	-	0.03	-0.01	0.02	-	-0.15	0.14	-	-	-0.01	-	-	-	-	-	-	-0.03	-	-	-	-	-	-0.01	-0.10	-	0.01	-	-	0.22	-0.01	-	0.01	-	-0.11	-	-	-0.01	-	-
PEP	0.18	0.15	0.02	0.37	0.01	0.02	-0.62	-1.77	-0.08	0.78	-0.07	1.37	-0.41	0.65	-	0.54	-0.68	-0.03	-0.21	-0.30	0.21	-0.03	0.01	-	0.01	-0.02	-0.21	0.05	0.09	0.05	-	-	-0.06	-0.73	-	0.03	-0.04	0.01	1.64	-0.10	0.13	-0.19	0.01	-0.57	-0.08	0.18	-0.07	-	-
GL6P	-0.02	-0.02	-	-0.10	-	-0.01	-	1.66	-0.22	-0.81	0.01	-1.12	0.06	-0.13	-	-0.16	-0.13	-	-	0.52	-	-	-0.01	-	-0.01	-	0.06	-	-	-	-	-	0.02	0.19	-	-0.01	-0.01	-	-0.43	0.01	-0.02	-	-	0.18	0.09	0.01	0.02	-	-
NADP	-	-	-	0.01	-	-	-	-0.17	-0.01	0.01	-	0.02	-0.01	0.01	-	0.01	-	-	-	0.15	-	-	-	-	-	-	-	-	-	-	-	-	-	-0.02	-	-	-	-	0.03	-	-	-	-	-0.01	-0.01	-	-	-	-
6PG	-0.04	-0.05	-0.01	-0.19	-	-0.01	-	3.14	0.14	-1.64	0.01	-2.27	0.10	-0.25	-	-0.30	-0.28	-	-	0.68	-	0.01	-0.02	-	-0.01	0.01	0.11	-	-0.01	-	0.01	-	0.03	0.37	-	-0.02	-0.01	0.01	-0.84	0.02	-0.02	-	-0.01	0.36	0.18	0.03	0.03	-	-
RIBU5P	0.01	0.01	-	-0.06	-	-	-	0.46	0.02	0.12	-0.01	-1.88	-0.05	-0.01	-	-0.05	-0.28	-	-	1.39	-	-	-0.01	-	-0.01	-	0.04	0.01	0.01	0.01	0.01	0.01	0.01	0.13	-	-0.01	-0.04	0.01	-0.31	-0.03	0.03	-0.01	-	0.15	0.06	0.02	0.01	-	-
RIBO5P	0.01	0.01	-	-0.06	-	-	-	0.30	0.01	0.13	0.47	-1.96	-0.06	-	-	-0.03	-0.29	-	-	1.16	-	-0.01	-0.02	-	-0.02	-	0.03	0.01	0.01	0.01	0.01	0.01	0.01	0.12	-	-0.01	-0.05	0.01	-0.31	-0.03	0.04	-0.01	-	0.15	0.05	0.02	0.01	-	-
XYL5P	0.14	0.18	0.03	-0.11	-	-0.01	-	-2.63	-0.12	1.01	-0.10	1.83	-0.62	0.42	-	0.46	-2.07	0.01	-	0.37	-	-0.05	-	-	0.01	0.01	0.10	0.07	0.12	0.07	0.08	0.08	0.03	0.36	0.01	-0.04	-0.33	0.13	-1.10	-0.26	0.47	-0.12	0.01	0.67	0.10	0.07	0.05	-	-
S7P	-0.05	-0.07	-0.01	-0.15	-	-0.01	-	-0.79	-0.04	0.60	0.09	0.39	0.62	-0.89	-	-0.33	-0.15	-	-	0.03	-	-	-	-	-	0.01	0.09	-0.01	-0.02	-0.01	-0.01	-	0.02	0.29	-	-0.01	0.03	-0.01	-0.59	0.06	-0.08	0.02	-0.01	0.24	0.11	0.02	0.02	-	-
E4P	0.75	0.95	0.13	-0.24	-	-0.05	-	-8.08	-0.37	3.11	0.49	1.95	4.22	-6.07	-	2.64	-9.12	0.05	-0.01	4.93	-	0.36	-0.06	-0.01	-	0.04	0.33	0.32	0.60	0.35	0.38	0.35	0.09	1.13	0.05	-0.15	-1.59	0.59	-4.02	-1.33	2.28	-0.58	0.06	2.67	0.31	0.29	0.20	-	-
LAC	0.02	0.02	-	0.05	-	-	-	-0.22	-0.01	0.07	-0.01	0.14	-0.06	0.09	-	0.14	-0.06	-	-	0.01	-	-0.01	-	-	-	-	-0.03	-	0.01	-	-	-	-0.01	-0.09	-	-	-0.02	0.01	0.18	-0.03	0.05	-	-0.24	-0.07	-	0.01	-0.01	-	-
GLU	0.03	0.03	-	0.08	-	0.03	-	1.80	0.08	0.14	-0.02	0.26	-0.09	0.14	-	-1.87	1.26	0.09	-	-2.43	-	-0.01	0.01	-	-	-0.03	-0.18	-0.01	-0.01	-0.01	-0.22	-0.21	-0.05	-0.61	-0.03	0.06	0.94	-0.35	1.98	0.85	-1.37	-0.40	-0.05	-1.03	0.14	0.52	-0.12	-	-
ALA	0.04	0.06	0.01	0.13	-	0.04	-	2.00	0.09	0.22	-0.03	0.41	-0.15	0.24	-	-2.24	1.36	-0.23	-	-2.90	-	-0.01	0.01	-	-	-0.04	-0.21	-	-	-	-0.26	-0.25	-0.06	-0.74	-0.04	0.07	1.10	-0.41	2.38	0.99	-1.61	-0.96	-0.05	-1.22	0.17	1.49	-0.17	-	-
AKG	0.02	0.02	-	0.06	-	0.04	-	3.86	0.18	0.14	-0.01	0.24	-0.06	0.10	-	-3.71	2.95	-0.05	-	-4.69	-	-0.01	0.01	-	-	-0.04	-0.36	-0.03	-0.05	-0.03	-0.45	-0.41	-0.10	-1.23	-0.06	0.11	1.86	-0.69	3.96	1.67	-2.72	0.69	-0.09	-2.09	0.26	-0.29	-0.16	-	-
G1P	-0.10	-	-	-0.05	-	-	-	1.81	0.08	-0.78	-	-1.04	-0.01	-0.03	-	-0.44	0.14	-	0.30	-0.18	-0.30	-	-0.01	-	-	-	0.02	-0.04	-0.07	-0.04	-0.04	-0.03	0.01	0.07	-0.01	0.01	0.17	-0.06	0.18	0.16	-0.25	0.06	-0.01	-0.11	0.14	-0.02	-0.01	-	-
AMP	-	-	-	-0.01	-	-	-	0.05	-	-0.01	0.01	-0.08	0.01	-0.02	-	-0.02	0.06	-	-	0.03	-	-	-0.03	-	0.03	-	-	-	-	-	-	-	-	0.02	-	-	-	-	-0.05	-	-0.01	-	-	0.01	-	-	-	-	-

Appendix H (continued)

	e1	e2	e3	e4	e5	e6	e7	e8	e9	e10	e11	e12	e13	e14	e15	e16	e17	e18	e19	e20	e21	e22	e23	e24	e25	e26	e27	e28	e29	e30	e31	e32	e33	e34	e35	e36	e37	e38	e39	e40	e41	e42	e43	e44	e45	e46	e47	e48	e49
SER	0.03	0.04	0.01	0.09	-	-0.23	-	0.60	0.03	0.14	-0.02	0.27	-0.11	0.17	-0.01	-0.72	0.53	0.05	-	-1.11	-	-0.01	-	-	-	0.20	-0.11	-	-	-	-0.10	-0.09	-0.03	-0.38	-0.01	0.03	0.41	-0.15	1.12	0.36	-0.59	-0.22	-0.02	-0.55	0.07	0.26	-0.28	-	-
CIT	0.03	0.04	0.01	0.10	-	0.02	-	1.29	0.06	0.16	-0.02	0.30	-0.11	0.18	-	-1.41	0.77	-0.02	-	-1.94	-	-0.01	-	-	-	-0.02	-0.08	-0.16	-0.29	-0.17	-0.17	-0.16	-0.02	-0.26	-0.02	0.06	0.74	-0.26	2.13	0.64	-1.07	0.28	-0.03	-1.02	0.11	-0.12	-0.09	-	-
OAC	-0.01	-0.02	-	-0.04	-	-	-	0.45	0.02	-0.05	0.01	-0.10	0.05	-0.07	-	-0.25	0.35	-	-	-0.34	-	-	-	-	-	-	-0.13	-0.02	-0.03	-0.02	0.06	0.05	0.32	-0.44	-	0.01	0.08	0.09	0.27	0.06	-0.23	0.04	-0.01	-0.16	0.01	-0.01	-0.01	-	-
ACOA	-	-	-	0.01	-	-	-	0.10	-	0.01	-	0.03	-0.01	0.02	-	-0.15	0.11	-	-	-0.16	-	-	-	-	-	-	-0.18	-0.02	-0.03	-0.02	-0.03	-0.03	-0.05	0.20	-	0.01	0.07	-0.04	0.24	0.06	-0.09	0.03	-	-0.12	0.01	-0.01	-0.01	-	-
CISAC	0.04	0.05	0.01	0.11	-	0.02	-	1.32	0.06	0.18	-0.02	0.34	-0.13	0.20	-	-1.45	0.74	-0.02	-	-2.02	-	-0.01	-	-	-	-0.02	-0.11	-	-0.30	-0.18	-0.18	-0.17	-0.03	-0.38	-0.02	0.06	0.77	-0.28	2.19	0.67	-1.11	0.29	-0.04	-1.04	0.12	-0.13	-0.09	-	-
ISOCIT	0.08	0.10	0.01	0.23	-	0.04	-	2.36	0.11	0.36	-0.05	0.69	-0.26	0.41	-	-2.61	1.19	-0.04	-	-3.75	-	-0.02	0.01	-	-	-0.03	-0.30	-	0.01	-0.33	-0.34	-0.31	-0.09	-1.04	-0.05	0.10	1.42	-0.52	3.97	1.24	-2.04	0.52	-0.06	-1.87	0.23	-0.24	-0.16	-	-
SUC	0.02	0.03	-	0.07	-	0.01	-	1.32	0.06	0.12	-0.01	0.22	-0.08	0.12	-	-1.29	0.79	-	-	-1.82	-	-0.01	0.01	-	-	-0.01	-0.35	-0.02	-0.04	-0.03	2.24	-0.17	-0.10	-1.22	0.03	0.03	0.15	-0.29	1.20	0.08	-1.02	0.12	-0.03	-0.63	0.10	-	-0.05	-	-
SUCOA	-	-	-	-	-	-	-	0.20	0.01	-	-	0.01	-	-	-	-0.18	0.15	-	-	-0.23	-	-	-	-	-	-	-0.02	-	-	-	-0.02	-0.02	-0.01	-0.08	0.05	0.01	0.09	-0.04	0.20	0.07	-0.14	0.03	-	-0.10	0.01	-0.01	-0.01	-	-
MAL	-0.01	-0.02	-	-0.04	-	0.01	-	0.72	0.03	-0.05	0.01	-0.10	0.05	-0.07	-	-0.50	0.58	-	-	-0.64	-	-	-	-	-	-0.01	-0.13	-0.02	-0.03	-0.02	0.17	0.16	-0.04	-0.46	-	0.02	0.08	0.27	0.52	0.05	-0.41	0.05	-0.01	-0.30	0.03	-0.01	-0.02	-	-
FUM	-0.02	-0.02	-	-0.05	-	-	-	0.66	0.03	-0.06	0.01	-0.13	0.06	-0.10	-	-0.42	0.56	-	-	-0.51	-	0.01	-	-	-	-	-0.11	-0.02	-0.03	-0.02	0.20	-0.06	-0.03	-0.37	-	0.01	0.08	0.31	0.43	0.06	-0.34	0.05	-0.01	-0.25	0.02	-0.01	-0.02	-	-
ADP	-0.04	-0.05	-0.01	-0.12	-	-	-	0.45	0.02	-0.15	0.02	-0.31	0.13	-0.21	-	-0.24	0.76	-	-	0.02	-	0.01	-	-	-	-	0.05	-0.01	-0.02	-0.01	-0.01	-0.01	0.01	0.16	-	-0.01	0.04	-0.01	-0.49	0.05	-0.08	0.01	-0.01	0.12	-0.01	0.01	0.02	-	-
NADH	0.02	0.03	-	0.06	-	-	-	-0.27	-0.01	0.08	-0.01	0.16	-0.07	0.11	-	0.08	-0.31	-	-	0.03	-	-0.01	-	-	-	-	0.01	0.01	0.02	0.01	0.01	0.01	-	0.03	-	-	-0.04	0.02	-0.08	-0.04	0.06	-0.02	-	0.07	-	0.01	-	-	-
NADPH	-0.03	-0.03	-	-0.08	-	-	-	1.58	0.07	-0.08	0.02	-0.18	0.09	-0.14	-	-0.13	-0.01	-	-	-1.45	-	0.01	-	-	-	-	0.04	-0.01	-0.01	-0.01	-	-	0.01	0.15	-	-0.01	0.02	-	-0.33	0.03	-0.02	0.01	-	0.13	0.07	0.01	0.01	-	-

References

Ainscow EK, Brand MD. 1999a. Internal regulation of ATP turnover, glycolysis and oxidative phosphorylation in rat hepatocytes. Eur J Biochem 266(3):737-49.

Ainscow EK, Brand MD. 1999b. The responses of rat hepatocytes to glucagon and adrenaline. Application of quantified elasticity analysis. Eur J Biochem 265(3):1043-55.

Ainscow EK, Brand MD. 1999c. Top-down control analysis of ATP turnover, glycolysis and oxidative phosphorylation in rat hepatocytes. Eur J Biochem 263(3):671-85.

Aiston S, Hampson L, Gomez-Foix AM, Guinovart JJ, Agius L. 2001. Hepatic glycogen synthesis is highly sensitive to phosphorylase activity - Evidence from metabolic control analysis. Journal of Biological Chemistry 276(26):23858-23866.

Altamirano C, Illanes A, Casablancas A, Gamez X, Cairo JJ, Godia C. 2001. Analysis of CHO cells metabolic redistribution in a glutamate-based defined medium in continuous culture. Biotechnol Prog 17(6):1032-41.

Andersen KB, von Meyenburg K. 1980. Are growth rates of Escherichia coli in batch cultures limited by respiration? J Bacteriol 144(1):114-23.

Antoniewicz MR, Kelleher JK, Stephanopoulos G. 2006. Determination of confidence intervals of metabolic fluxes estimated from stable isotope measurements. Metab Eng 8(4):324-37.

Antoniewicz MR, Kelleher JK, Stephanopoulos G. 2007a. Elementary metabolite units (EMU): a novel framework for modeling isotopic distributions. Metab Eng 9(1):68-86.

Antoniewicz MR, Kraynie DF, Laffend LA, Gonzalez-Lergier J, Kelleher JK, Stephanopoulos G. 2007b. Metabolic flux analysis in a nonstationary system: fed-batch fermentation of a high yielding strain of E. coli producing 1,3-propanediol. Metab Eng 9(3):277-92.

Axelson M, Mork B, Everson GT. 1991. Bile acid synthesis in cultured human hepatoblastoma cells. J Biol Chem 266(27):17770-7.

Bailey JE. 1998. Mathematical modeling and analysis in biochemical engineering: Past accomplishments and future opportunities. Biotechnology Progress 14(1):8-20.

Bais R, James HM, Rofe AM, Conyers RA. 1985. The purification and properties of human liver ketohexokinase. A role for ketohexokinase and fructose-bisphosphate aldolase in the metabolic production of oxalate from xylitol. Biochem J 230(1):53-60.

Balcarcel RR, Clark LM. 2003. Metabolic screening of mammalian cell cultures using well-plates. Biotechnol Prog 19(1):98-108.

Ballet F, Bouma ME, Wang SR, Amit N, Marais J, Infante R. 1984. Isolation, culture and characterization of adult human hepatocytes from surgical liver biopsies. Hepatology 4(5):849-54.

Bandsma RH, Stellaard F, Vonk RJ, Nagel GT, Neese RA, Hellerstein MK, Kuipers F. 1998. Contribution of newly synthesized cholesterol to rat plasma and bile determined by mass isotopomer distribution analysis: bile-salt flux promotes secretion of newly synthesized cholesterol into bile. Biochem J 329 (Pt 3):699-703.

Bederman IR, Kasumov T, Reszko AE, David F, Brunengraber H, Kelleher JK. 2004a. In vitro modeling of fatty acid synthesis under conditions simulating the zonation of lipogenic [13C]acetyl-CoA enrichment in the liver. J Biol Chem 279(41):43217-26.

Bederman IR, Reszko AE, Kasumov T, David F, Wasserman DH, Kelleher JK, Brunengraber H. 2004b. Zonation of labeling of lipogenic acetyl-CoA across the liver: implications for studies of lipogenesis by mass isotopomer analysis. J Biol Chem 279(41):43207-16.

Berg J, Tymoczko J, Stryer L. 2002. Biochemistry, Fifth Edition: International Version: New York: W.H. Freeman & Co.

Bhattacharya M, Fuhrman L, Ingram A, Nickerson KW, Conway T. 1995. Single-run separation and detection of multiple metabolic intermediates by anion-exchange high-performance liquid chromatography and application to cell pool extracts prepared from Escherichia coli. Anal Biochem 232(1):98-106.

Blank LM, Kuepfer L, Sauer U. 2005. Large-scale 13C-flux analysis reveals mechanistic principles of metabolic network robustness to null mutations in yeast. Genome Biol 6(6):R49.

Bloxham DP, Lardy HA. 1973. Phosphofructokinase. The Enzymes, (Boyer, P.D., ed.) 3rd Ed. 8:239-278.

Bonarius HP, Hatzimanikatis V, Meesters KPH, de Gooijer CD, Schmid G, Tramper J. 1996. Metabolic flux analysis of hybridoma cells in different culture media using mass balances. Biotechnol Bioeng 50:299-318.

Bonarius HP, Ozemre A, Timmerarends B, Skrabal P, Tramper J, Schmid G, Heinzle E. 2001. Metabolic-flux analysis of continuously cultured hybridoma cells using (13)CO(2) mass spectrometry in combination with

(13)C-lactate nuclear magnetic resonance spectroscopy and metabolite balancing. Biotechnol Bioeng 74(6):528-38.

Bonarius HP, Schmid G, Tramper J. 1997. Flux analysis of underdetermined metabolic networks: The quest for the missing constraints. Trends Biotech 15:308–314.

Bonarius HP, Timmerarends B, de Gooijer CD, Tramper J. 1998. Metabolite-balancing techniques vs. 13C tracer experiments to determine metabolic fluxes in hybridoma cells. Biotechnol Bioeng 58(2-3):258-62.

Boren J, Montoya AR, de Atauri P, Comin-Anduix B, Cortes A, Centelles JJ, Frederiks WM, Van Noorden CJ, Cascante M. 2002. Metabolic control analysis aimed at the ribose synthesis pathways of tumor cells: a new strategy for antitumor drug development. Mol Biol Rep 29(1-2):7-12.

Brand A, Engelmann J, Leibfritz D. 1992. A 13C NMR study on fluxes into the TCA cycle of neuronal and glial tumor cell lines and primary cells. Biochimie 74(9-10):941-8.

Brown GC, Lakinthomas PL, Brand MD. 1990. Control of Respiration and Oxidative-Phosphorylation in Isolated Rat-Liver Cells. European Journal of Biochemistry 192(2):355-362.

Buchholz A, Takors R, Wandrey C. 2001. Quantification of intracellular metabolites in Escherichia coli K12 using liquid chromatographic-electrospray ionization tandem mass spectrometric techniques. Anal Biochem 295(2):129-37.

Bulik S, Grimbs S, Huthmacher C, Selbig J, Holzhutter HG. 2009. Kinetic hybrid models composed of mechanistic and simplified enzymatic rate laws - a promising method for speeding up the kinetic modelling of complex metabolic networks. Febs Journal 276(2):410-424.

Carew JS, Zhou Y, Albitar M, Carew JD, Keating MJ, Huang P. 2003. Mitochondrial DNA mutations in primary leukemia cells after chemotherapy: clinical significance and therapeutic implications. Leukemia 17(8):1437-47.

Cascante M, Boros LG, Comin-Anduix B, de Atauri P, Centelles JJ, Lee PWN. 2002. Metabolic control analysis in drug discovery and disease. Nature Biotechnology 20(3):243-249.

Chalasani N. 2005. Statins and hepatotoxicity: focus on patients with fatty liver. Hepatology 41(4):690-5.

Chan C, Berthiaume F, Lee K, Yarmush ML. 2003a. Metabolic flux analysis of cultured hepatocytes exposed to plasma. Biotechnol Bioeng 81(1):33-49.

Chan C, Berthiaume F, Lee K, Yarmush ML. 2003b. Metabolic flux analysis of hepatocyte function in hormone- and amino acid-supplemented plasma. Metab Eng 5(1):1-15.

Chance EM, Seeholzer SH, Kobayashi K, Williamson JR. 1983. Mathematical analysis of isotope labeling in the citric acid cycle with applications to 13C NMR studies in perfused rat hearts. J Biol Chem 258(22):13785-94.

Chandel NS, McClintock DS, Feliciano CE, Wood TM, Melendez JA, Rodriguez AM, Schumacker PT. 2000. Reactive oxygen species generated at mitochondrial complex III stabilize hypoxia-inducible factor-1alpha during hypoxia: a mechanism of O2 sensing. J Biol Chem 275(33):25130-8.

Chang A, Scheer M, Grote A, Schomburg I, Schomburg D. 2009. BRENDA, AMENDA and FRENDA the enzyme information system: new content and tools in 2009. Nucleic Acids Research 37:D588-D592.

Chassagnole C, Noisommit-Rizzi N, Schmid JW, Mauch K, Reuss M. 2002. Dynamic Modeling of the Central Carbon Metabolism of *Escherichia Coli*. Biotechnol Bioeng 79(1):53-73.

Chen JP, Yu SC, Hsu BR, Fu SH, Liu HS. 2003. Loofa sponge as a scaffold for the culture of human hepatocyte cell line. Biotechnol Prog 19(2):522-7.

Chen Z, Lu W, Garcia-Prieto C, Huang P. 2007. The Warburg effect and its cancer therapeutic implications. J Bioenerg Biomembr 39(3):267-74.

Cho SW, Joshi JG. 1990. Characterization of glucose-6-phosphate dehydrogenase isozymes from human and pig brain. Neuroscience 38(3):819-28.

Christensen B, Gombert AK, Nielsen J. 2002. Analysis of flux estimates based on (13)C-labelling experiments. Eur J Biochem 269(11):2795-800.

Christensen B, Nielsen J. 1999. Isotopomer analysis using GC-MS. Metab Eng 1(4):282-90.

Clarenbach JJ, Lindenthal B, Dotti MT, Federico A, Kelleher JK, von Bergmann K. 2005. Isotopomer spectral analysis of intermediates of cholesterol synthesis in patients with cerebrotendinous xanthomatosis. Metabolism 54(3):335-44.

Clarke PR, Hardie DG. 1990. Regulation of HMG-CoA reductase: identification of the site phosphorylated by the AMP-activated protein kinase in vitro and in intact rat liver. EMBO J 9(8):2439-46.

Clausen J. 1969. Lactate dehydrogenase isoenzymes of sperm cells and tests. Biochem J 111(2):207-18.

Cohen DE, Anania FA, Chalasani N. 2006. An assessment of statin safety by hepatologists. Am J Cardiol 97(8A):77C-81C.

Connor WE, Witiak DT, Stone DB, Armstrong ML. 1969. Cholesterol balance and fecal neutral steroid and bile acid excretion in normal men fed dietary fats of different fatty acid composition. J Clin Invest 48(8):1363-75.

Crow KE, Braggins TJ, Batt RD, Hardman MJ. 1982. Rat liver cytosolic malate dehydrogenase: purification, kinetic properties, role in control of free cytosolic NADH concentration. Analysis of control of ethanol metabolism using computer simulation. J Biol Chem 257(23):14217-25.

Dauner M, Bailey JE, Sauer U. 2001. Metabolic flux analysis with a comprehensive isotopomer model in Bacillus subtilis. Biotechnol Bioeng 76(2):144-56.

Dauner M, Sauer U. 2000. GC-MS analysis of amino acids rapidly provides rich information for isotopomer balancing. Biotechnol Prog 16(4):642-9.

de Koning W, van Dam K. 1992 A method for the determination of changes of glycolytic metabolites in yeast on a subsecond time scale using extraction at neutral pH. Anal Biochem 204(1):118-23.

Des Rosiers C, Di Donato L, Comte B, Laplante A, Marcoux C, David F, Fernandez CA, Brunengraber H. 1995. Isotopomer analysis of citric acid cycle and gluconeogenesis in rat liver. Reversibility of isocitrate dehydrogenase and involvement of ATP-citrate lyase in gluconeogenesis. J Biol Chem 270(17):10027-36.

Deuflard P, Hairer E, Zugck J. 1987. One Step and Extrapolation Methods for Differential- Algebraic Systems. Numer. Math. 51:501-516.

Di Buono M, Jones PJ, Beaumier L, Wykes LJ. 2000. Comparison of deuterium incorporation and mass isotopomer distribution analysis for measurement of human cholesterol biosynthesis. J Lipid Res 41(9):1516-23.

Dombrauckas JD, Santarsiero BD, Mesecar AD. 2005. Structural basis for tumor pyruvate kinase M2 allosteric regulation and catalysis. Biochemistry 44(27):9417-29.

Doverskog M, Ljunggren J, Ohman L, Haggstrom L. 1997. Physiology of cultured animal cells. J Biotechnol 59(1-2):103-15.

Dräger A, Kronfeld M, Ziller MJ, Supper J, Planatscher H, Magnus JB, Oldiges M, Kohlbacher O, Zell A. 2009. Modeling metabolic networks in C. glutamicum: a comparison of rate laws in combination with various parameter optimization strategies. Bmc Systems Biology 3:-.

Echols N, Harrison P, Balasubramanian S, Luscombe NM, Bertone P, Zhang Z, Gerstein M. 2002. Comprehensive analysis of amino acid and nucleotide composition in eukaryotic genomes, comparing genes and pseudogenes. Nucleic Acids Res 30(11):2515-23.

Emmison N, Agius L. 1988. Fatty acid uptake and metabolism to ketone bodies and triacyglycerol in rat and human hepatocyte cultures is dependent on chain-length and degree of saturation. Effects of carnitine and glucagon. FEBS Lett 236(1):83-8.

Enosawa S, Suzuki S, Kakefuda T, Amemiya H. 1996. Examination of 7-ethoxycoumarin deethylation and ammonia removal activities in 31 hepatocyte cell lines. Cell Transplant 5(5 Suppl 1):S39-40.

Espenshade PJ. 2006. SREBPs: sterol-regulated transcription factors. J Cell Sci 119(Pt 6):973-6.

Fazi A, Piacentini MP, Piatti E, Accorsi A. 1990. Purification and partial characterization of the phosphoglucomutase isozymes from human placenta. Prep Biochem 20(3-4):219-40.

Fell DA. 1992. Metabolic Control Analysis - a Survey of Its Theoretical and Experimental Development. Biochemical Journal 286:313-330.

Fischer E, Zamboni N, Sauer U. 2004. High-throughput metabolic flux analysis based on gas chromatography-mass spectrometry derived 13C constraints. Anal Biochem 325(2):308-16.

Fletcher R, Powell MJD. 1963. A Rapidly Convergent Descent Method for Minimization. Computer Journal 6(2):163-&.

Forster J, Famili I, Fu P, Palsson BO, Nielsen J. 2003. Genome-scale reconstruction of the Saccharomyces cerevisiae metabolic network. Genome Res 13(2):244-53.

Fulgencio JP, Kohl C, Girard J, Pegorier JP. 2001. Effect of metformin on fatty acid and glucose metabolism in freshly isolated hepatocytes and on specific gene expression in cultured hepatocytes. Biochem Pharmacol 62(4):439-46.

Gaitonde MK, Murray E, Cunningham VJ. 1989. Effect of 6-phosphogluconate on phosphoglucose isomerase in rat brain in vitro and in vivo. J Neurochem 52(5):1348-52.

Gibbons GF. 2003. Regulation of fatty acid and cholesterol synthesis: co-operation or competition? Progress in Lipid Research 42(6):479-497.

Gibson GE, Park LC, Sheu KF, Blass JP, Calingasan NY. 2000. The alpha-ketoglutarate dehydrogenase complex in neurodegeneration. Neurochem Int 36(2):97-112.

Goel A, Ferrance J, Jeong J, Ataai MM. 1993. Analysis of metabolic fluxes in batch and continous cultures of Bacillus subtilis. Biotechnol Bioeng 42:686-696.

Gonzalez B, Francois J, Renaud M. 1997. A rapid and reliable method for metabolite extraction in yeast using boiling buffered ethanol. Yeast 13(14):1347-1355.

Gracy RW. 1975. Triosephosphate isomerase from human erythrocytes. Methods Enzymol 41:442-7.

Gregus Z, Nemeti B. 2005. The glycolytic enzyme glyceraldehyde-3-phosphate dehydrogenase works as an arsenate reductase in human red blood cells and rat liver cytosol. Toxicol Sci 85(2):859-69.

Grimbs S, Selbig J, Bulik S, Holzhutter HG, Steuer R. 2007. The stability and robustness of metabolic states: identifying stabilizing sites in metabolic networks. Molecular Systems Biology 3:-.

Grimmer P. 2009. Vergleich von mechanistischer Modellierung und linlog-Approximation am Beispiel der Glykolyse in Hepatozyten. Bachelor Thesis, University of Stuttgart, Institute of Biochemical Engineering.

Groen AK, Vanroermund CWT, Vervoorn RC, Tager JM. 1986. Control of Gluconeogenesis in Rat-Liver Cells - Flux Control Coefficients of the Enzymes in the Gluconeogenic Pathway in the Absence and Presence of Glucagon. Biochemical Journal 237(2):379-389.

Groen AK, Wanders RJA, Westerhoff HV, Vandermeer R, Tager JM. 1982. Quantification of the Contribution of Various Steps to the Control of Mitochondrial Respiration. Journal of Biological Chemistry 257(6):2754-2757.

Guo W, Huang N, Cai J, Xie WS, Hamilton JA. 2006. Fatty acid transport and metabolism in HepG2 cells. American Journal of Physiology-Gastrointestinal and Liver Physiology 290(3):G528-G534.

Hadlich F, Noack S, Wiechert W. 2008. Translating biochemical network models between different kinetic formats. Metab Eng.

Hansen N, Ostermeier A. 2001. Completely derandomized self-adaption in evolutionary strategies. Proceedings of the 1996 IEEE Int. Conf. on Evolutionary Computation:312-317.

Harrison MF. 1953. Composition of the liver cell. Proc R Soc Lond B Biol Sci 141(903):203-16.

Heijnen JJ. 2005. Approximative kinetic formats used in metabolic network modeling. Biotechnol Bioeng 91(5):534-45.

Heinrich R, Rapoport TA. 1974. A linear steady-state treatment of enzymatic chains. General properties, control and effector strength. Eur J Biochem 42(1):89-95.

Heller RA, Gould RG. 1974. Reversible cold inactivation of microsomal 3-hydroxy-3-methylglutaryl coenzyme A reductase from rat liver. J Biol Chem 249(16):5254-60.

Hengl S, Kreutz C, Timmer J, Maiwald T. 2007. Data-based identifiability analysis of non-linear dynamical models. Bioinformatics 23(19):2612-2618.

Hermes M, von Hippel S, Osswald H, Kloor D. 2005. S-adenosylhomocysteine metabolism in different cell lines: effect of hypoxia and cell density. Cell Physiol Biochem 15(5):233-44.

Hindmarsh AC. 1983. Odepack, a systemized collection of ode solvers. In Stepleman, R.S.e.a. (Ed.). IMACS Transactions on Scientific Computation, , North-Holland, Amsterdam, The Netherlands Scientific Computing 1:55-64.

Hinkle PC. 2005. P/O ratios of mitochondrial oxidative phosphorylation. Biochim Biophys Acta 1706(1-2):1-11.

Hoek JB, Rydstrom J. 1988. Physiological roles of nicotinamide nucleotide transhydrogenase. Biochem J 254(1):1-10.

Hofmann U, Maier K, Niebel A, Vacun G, Reuss M, Mauch K. 2008. Identification of metabolic fluxes in hepatic cells from transient 13C-labeling experiments: Part I. Experimental observations. Biotechnol Bioeng 100(2):344-54.

Hofmeyr J-HS. 2001. Metabolic control analysis in a nutshell. ICSB2001, Caltech:291-300.

Hold C, Panke S. 2009. Towards the engineering of in vitro systems. J R Soc Interface.

Holzhütter HG, Jacobasch G, Bisdorff A. 1985. Mathematical modelling of metabolic pathways affected by an enzyme deficiency. A mathematical model of glycolysis in normal and pyruvate-kinase-deficient red blood cells. Eur J Biochem 149(1):101-11.

Hua Q, Yang C, Baba T, Mori H, Shimizu K. 2003. Responses of the central metabolism in Escherichia coli to phosphoglucose isomerase and glucose-6-phosphate dehydrogenase knockouts. J Bacteriol 185(24):7053-67.

Ingledew WJ, Poole RK. 1984. The respiratory chains of Escherichia coli. Microbiol Rev 48(3):222-71.

Jamshidi N, Palsson BO. 2008. Formulating genome-scale kinetic models in the post-genome era. Mol Syst Biol 4:171.

Javitt NB. 1990. Hep-G2 Cells as a Resource for Metabolic Studies - Lipoprotein, Cholesterol, and Bile-Acids. Faseb Journal 4(2):161-168.

Jeske DJ, Dietschy JM. 1980. Regulation of rates of cholesterol synthesis in vivo in the liver and carcass of the rat measured using [3H]water. J Lipid Res 21(3):364-76.

Jones JG, Garcia P, Barosa C, Delgado TC, Diogo L. 2009. Hepatic anaplerotic outflow fluxes are redirected from gluconeogenesis to lactate synthesis in patients with Type 1a glycogen storage disease. Metabolic Engineering 11(3):155-162.

Joshi M, Seidel-Morgenstern A, Kremling A. 2006. Exploiting the bootstrap method for quantifying parameter confidence intervals in dynamical systems. Metab Eng 8(5):447-55.

Jucker BM, Lee JY, Shulman RG. 1998. In vivo 13C NMR measurements of hepatocellular tricarboxylic acid cycle flux. J Biol Chem 273(20):12187-94.

Kacser H, Burns JA. 1973. The control of flux. Symp Soc Exp Biol 27:65-104.

Kacser H, Burns JA. 1979. Molecular democracy: who shares the controls? Biochem Soc Trans 7(5):1149-60.

Kahn A, Marie J. 1982. Pyruvate kinases from human erythrocytes and liver. Methods Enzymol 90 Pt E:131-40.

Kahn D, Westerhoff HV. 1993. The Regulatory Strength - How to Be Precise About Regulation and Homeostasis. Acta Biotheoretica 41(1-2):85-96.

Kalaany NY, Mangelsdorf DJ. 2006. LXRs AND FXR: The Yin and Yang of cholesterol and fat metabolism. Annual Review of Physiology 68:159-191.

Kallien G, Lange K, Stange EF, Scheibner J. 1999. The pravastatin-induced decrease of biliary cholesterol secretion is not directly related to an inhibition of cholesterol synthesis in humans. Hepatology 30(1):14-20.

Kanehisa M, Goto S. 2000. KEGG: kyoto encyclopedia of genes and genomes. Nucleic Acids Res 28(1):27-30.

Kather H, Rivera M, Brand K. 1972. Interrelationship and Control of Glucose-Metabolism and Lipogenesis in Isolated Fat-Cells - Control of Pentose Phosphate Cycle Activity by Cellular Requirement for Reduced Nicotinamide Adenine-Dinucleotide Phosphate. Biochemical Journal 128(5):1097-&.

Kauffman KJ, Prakash P, Edwards JS. 2003. Advances in flux balance analysis. Curr Opin Biotechnol 14(5):491-6.

Kelleher JK, Kharroubi AT, Aldaghlas TA, Shambat IB, Kennedy KA, Holleran AL, Masterson TM. 1994. Isotopomer spectral analysis of cholesterol synthesis: applications in human hepatoma cells. Am J Physiol 266(3 Pt 1):E384-95.

Keller GA, Pazirandeh M, Krisans S. 1986. 3-Hydroxy-3-methylglutaryl coenzyme A reductase localization in rat liver peroxisomes and microsomes of control and cholestyramine-treated animals: quantitative biochemical and immunoelectron microscopical analyses. J Cell Biol 103(3):875-86.

Kempen HJ, Glatz JF, Gevers Leuven JA, van der Voort HA, Katan MB. 1988. Serum lathosterol concentration is an indicator of whole-body cholesterol synthesis in humans. J Lipid Res 29(9):1149-55.

Klamt S, Schuster S. 2002. Calculating as many fluxes as possible in underdetermined metabolic networks. Mol Biol Rep 29(1-2):243-8.

Klamt S, Schuster S, Gilles ED. 2002. Calculability analysis in underdetermined metabolic networks illustrated by a model of the central metabolism in purple nonsulfur bacteria. Biotechnol Bioeng 77(7):734-51.

Knowles BB, Howe CC, Aden DP. 1980. Human hepatocellular carcinoma cell lines secrete the major plasma proteins and hepatitis B surface antigen. Science 209(4455):497-9.

Kresnowati MT, van Winden WA, Heijnen JJ. 2005. Determination of elasticities, concentration and flux control coefficients from transient metabolite data using linlog kinetics. Metab Eng 7(2):142-53.

Kuntz E, Kuntz H-D. 2001. Hepatology Principles and Practice. Springer-Verlag Berlin.

Lange Y, Ye J, Steck TL. 2004. How cholesterol homeostasis is regulated by plasma membrane cholesterol in excess of phospholipids. Proceedings of the National Academy of Sciences of the United States of America 101(32):11664-11667.

Large V, Brunengraber H, Odeon M, Beylot M. 1997. Use of labeling pattern of liver glutamate to calculate rates of citric acid cycle and gluconeogenesis. Am J Physiol 272(1 Pt 1):E51-8.

Lazo PA, Sols A. 1980. Pyruvate dehydrogenase complex of ascites tumour. Activation by AMP and other properties of potential significance in metabolic regulation. Biochem J 190(3):705-10.

Lee K, Berthiaume F, Stephanopoulos GN, Yarmush DM, Yarmush ML. 2000. Metabolic flux analysis of postburn hepatic hypermetabolism. Metab Eng 2(4):312-27.

Lee K, Berthiaume F, Stephanopoulos GN, Yarmush ML. 1999. Metabolic flux analysis: a powerful tool for monitoring tissue function. Tissue Eng 5(4):347-68.

Lee K, Berthiaume F, Stephanopoulos GN, Yarmush ML. 2003. Profiling of dynamic changes in hypermetabolic livers. Biotechnol Bioeng 83(4):400-15.

Lee WN, Boros LG, Puigjaner J, Bassilian S, Lim S, Cascante M. 1998. Mass isotopomer study of the nonoxidative pathways of the pentose cycle with [1,2-13C2]glucose. Am J Physiol 274(5 Pt 1):E843-51.

Lee WN, Byerley LO, Bassilian S, Ajie HO, Clark I, Edmond J, Bergner EA. 1995. Isotopomer study of lipogenesis in human hepatoma cells in culture: contribution of carbon and hydrogen atoms from glucose. Anal Biochem 226(1):100-12.

Lindenthal B, Aldaghlas TA, Holleran AL, Sudhop T, Berthold HK, Von Bergmann K, Kelleher JK. 2002. Isotopomer spectral analysis of intermediates of cholesterol synthesis in human subjects and hepatic cells. Am J Physiol Endocrinol Metab 282(6):E1222-30.

Link H, Weuster-Botz D. 2007. Steady-state analysis of metabolic pathways: Comparing the double modulation method and the lin-log approach. Metabolic Engineering 9(5-6):433-441.

Lo C, Cristofalo VJ, Morris HP, Weinhouse S. 1968. Studies on respiration and glycolysis in transplanted hepatic tumors of the rat. Cancer Res 28(1):1-10.

Lopez-Lazaro M. 2008. The Warburg effect: Why and how do cancer cells activate glycolysis in the presence of oxygen? Anti-Cancer Agents in Medicinal Chemistry 8(3):305-312.

Luo B, Groenke K, Takors R, Wandrey C, Oldiges M. 2007. Simultaneous determination of multiple intracellular metabolites in glycolysis, pentose phosphate pathway and tricarboxylic acid cycle by liquid chromatography-mass spectrometry. Journal of Chromatography A 1147(2):153-164.

Magnus JB. 2008. Metabolic egineering of the valine pathway in corynebacterium glutamicum : analysis and modelling. Dissertation, University of Stuttgart, Institute of Biochemical Engineering.

Magnus JB, Hollwedel D, Oldiges M, Takors R. 2006. Monitoring and modeling of the reaction dynamics in the valine/leucine synthesis pathway in Corynebacterium glutamicum. Biotechnology Progress 22(4):1071-1083.

Maharjan RP, Ferenci T. 2003. Global metabolite analysis: the influence of extraction methodology on metabolome profiles of Escherichia coli. Anal Biochem 313(1):145-54.

Maier K, Hofmann U, Bauer A, Niebel A, Vacun G, Reuss M, Mauch K. 2009. Quantification of statin effects on hepatic cholesterol synthesis by transient (13)C-flux analysis. Metab Eng 11(4-5):292-309.

Maier K, Hofmann U, Reuss M, Mauch K. 2008a. Identification of metabolic fluxes in hepatic cells from transient 13C-labeling experiments: Part II. Flux estimation. Biotechnol Bioeng 100(2):355-70.

Maier K, Mauch K, Hofmann U, Niebel A, Vacun G, Reuss M. 2008b. Parameterization of a large-scale, autonomous network model of the hepatic metabolism from transient metabolite data. 9th International Conference on Systems Biology (ICSB).

Maier K, Mauch K, Reuss M. 2007. A systems oriented analysis of flux estimates from transient 13C labeling experiments. Proceedings of the FOSBE conference.

Malaisse WJ, Zhang TM, Verbruggen I, Willem R. 1996. Enzyme-to-enzyme channelling of Krebs cycle metabolic intermediates in Caco-2 cells exposed to [2-13c]propionate. Biochem J 317 (Pt 3):861-3.

Malloy CR, Sherry AD, Jeffrey FM. 1988. Evaluation of carbon flux and substrate selection through alternate pathways involving the citric acid cycle of the heart by 13C NMR spectroscopy. J Biol Chem 263(15):6964-71.

Malloy CR, Sherry AD, Jeffrey FM. 1990. Analysis of tricarboxylic acid cycle of the heart using 13C isotope isomers. Am J Physiol 259(3 Pt 2):H987-95.

Maron DJ, Fazio S, Linton MF. 2000. Current perspectives on statins. Circulation 101(2):207-13.

Mauch K, Schmid JW, Reuss M, Ulmer H. 2004. In silico identification of whole cell metabolite dynamics through evolutionary algorithms and parallel computing. 5th International Conference on Systems Biology (ICSB).

McGee TP, Cheng HH, Kumagai H, Omura S, Simoni RD. 1996. Degradation of 3-hydroxy-3-methylglutaryl-CoA reductase in endoplasmic reticulum membranes is accelerated as a result of increased susceptibility to proteolysis. J Biol Chem 271(41):25630-8.

Melendezhevia E, Mateo F, Torres NV. 1992. Control Analysis of Rat-Liver Glycolysis under Different Glucose-Concentrations - the Substrate Approach and the Role of Glucokinase. Molecular and Cellular Biochemistry 115(1):1-9.

Mitropoulos KA, Venkatesan S, Balasubramaniam S, Peters TJ. 1978. The submicrosomal localization of 3-hydroxy-3-methylglutaryl-coenzyme-A reductase, cholesterol 7alpha-hydroxylase and cholesterol in rat liver. Eur J Biochem 82(2):419-29.

Mo ML, Jamshidi N, Palsson BO. 2007. A genome-scale, constraint-based approach to systems biology of human metabolism. Mol Biosyst 3(9):598-603.

Moreno-Sanchez R, Saavedra E, Rodriguez-Enriquez S, Olin-Sandoval V. 2008. Metabolic control analysis: a tool for designing strategies to manipulate metabolic pathways. J Biomed Biotechnol 2008:597913.

Naoumova RP, Dunn S, Rallidis L, AbuMuhana O, Neuwirth C, Rendell NB, Taylor GW, Thompson GR. 1997. Prolonged inhibition of cholesterol synthesis explains the efficacy of atorvastatin. Journal of Lipid Research 38(7):1496-1500.

Neese RA, Faix D, Kletke C, Wu K, Wang AC, Shackleton CH, Hellerstein MK. 1993. Measurement of endogenous synthesis of plasma cholesterol in rats and humans using MIDA. Am J Physiol 264(1 Pt 1):E136-47.

Newsholme EA, Crabtree B, Ardawi MS. 1985. Glutamine metabolism in lymphocytes: its biochemical, physiological and clinical importance. Q J Exp Physiol 70(4):473-89.

Nielsen J. 2003. It is all about metabolic fluxes. Journal of Bacteriology 185(24):7031-7035.

Nikerel IE, van Winden WA, van Gulik WM, Heijnen JJ. 2006. A method for estimation of elasticities in metabolic networks using steady state and dynamic metabolomics data and linlog kinetics. BMC Bioinformatics 7:540.

Niklas J, Noor F, Heinzle E. 2009. Effects of drugs in subtoxic concentrations on the metabolic fluxes in human hepatoma cell line Hep G2. Toxicol Appl Pharmacol.

Nöh K, Gronke K, Luo B, Takors R, Oldiges M, Wiechert W. 2006a. Metabolic flux analysis at ultra short time scale: Isotopically non-stationary (13)C labeling experiments. J Biotechnol.

Nöh K, Gronke K, Luo B, Takors R, Oldiges M, Wiechert W. 2007. Metabolic flux analysis at ultra short time scale: isotopically non-stationary 13C labeling experiments. J Biotechnol 129(2):249-67.

Nöh K, Wahl A, Wiechert W. 2006b. Computational tools for isotopically instationary (13)C labeling experiments under metabolic steady state conditions. Metab Eng.

Nöh K, Wiechert W. 2006. Experimental design principles for isotopically instationary 13C labeling experiments. Biotechnol Bioeng 94(2):234-51.

Nyberg GB, Balcarcel RR, Follstad BD, Stephanopoulos G, Wang DI. 1999. Metabolism of peptide amino acids by Chinese hamster ovary cells grown in a complex medium. Biotechnol Bioeng 62(3):324-35.

Ogata H, Goto S, Sato K, Fujibuchi W, Bono H, Kanehisa M. 1999. KEGG: Kyoto Encyclopedia of Genes and Genomes. Nucleic Acids Res 27(1):29-34.

Owen OE, Kalhan SC, Hanson RW. 2002. The key role of anaplerosis and cataplerosis for citric acid cycle function. J Biol Chem 277(34):30409-12.

Parr CW. 1956. Inhibition of phosphoglucose isomerase. Nature 178(4547):1401.

Pelicano H, Martin DS, Xu RH, Huang P. 2006. Glycolysis inhibition for anticancer treatment. Oncogene 25(34):4633-46.

Pitkänen E, Åkerlund A, Rantanen A, Jouhten P, Ukkonen E. 2008. ReMatch: a web-based tool to construct, store and share stoichiometric metabolic models with carbon maps for metabolic flux analysis. Journal of Integrative Bioinformatics 5(2):102.

Press WH, Flannery BP, Teukolsky SA, Vetterling WT. 1992. Numerical Recipes in C: The art of Scientific Computing. Cambridge University Press, 2nd ed.

Previs SF, Des Rosiers C, Beylot M, David F, Brunengraber H. 1996. Assay of the 13C and 2H mass isotopomer distribution of phosphoenolpyruvate by gas chromatography/mass spectrometry. J Mass Spectrom 31(6):643-8.

Quek LE, Wittmann C, Nielsen LK, Kromer JO. 2009. OpenFLUX: efficient modelling software for C-13-based metabolic flux analysis. Microbial Cell Factories 8:-.

Ramadori G, Moriconi F, Malik I, Dudas J. 2008. Physiology and pathophysiology of liver inflammation, damage and repair. J Physiol Pharmacol 59 Suppl 1:107-17.

Reuss M, Aguilera-Vazquez L, Mauch K. 2007. Reconstruction of dynamic network models from metabolite measurements. Metabolomics A Powerful Tool in Systems Biology 18(Topics in Current Genetics. Springer Berlin / Heidelberg.):97-127.

Ridders CJF. 1982. Technical Note: Accurate Computation of F'(x) and F (x)F (x)". Advances in Engineering Software 4(2):75-76.

Rizzi M, Baltes M, Theobald U, Reuss M. 1997. In vivo analysis of metabolic dynamics in Saccharomyces cerevisiae .2. Mathematical model. Biotechnology and Bioengineering 55(4):592-608.

Robins SJ, Fasulo JM, Collins MA, Patton GM. 1985. Cholesterol exchange and synthesis in the live rat. J Lipid Res 26(10):1230-40.

Sabate L, Franco R, Canela EI, Centelles JJ, Cascante M. 1995. A model of the pentose phosphate pathway in rat liver cells. Mol Cell Biochem 142(1):9-17.

Sato H, Takahashi N, Nakamoto M, Ohgami M, Yamazaki M, Fukui T. 2002. Effects of streptozotocin-induced diabetes on acetoacetyl-CoA synthetase activity in rats. Biochem Pharmacol 63(10):1851-5.

Sauer U. 2006. Metabolic networks in motion: 13C-based flux analysis. Mol Syst Biol 2:62.

Sauer U, Zamboni N. 2008. From biomarkers to integrated network responses. Nature Biotechnology 26(10):1090-1092.

Sauro HM. 1990. Regulatory responses and control analysis: assessment of the relative importance of internal effectors. Control of Metabolic Processes (Cornish-Bowden, A. and Cárdenas, M.L.), Plenum Press, New York:225–230.

Schaub J. 2007. Isotopisch instationäre 13C-Stoffflussanalyse in Escherichia coli. Dissertation, University of Stuttgart, Institute of Biochemical Engineering.

Schaub J, Mauch A, Reuss M. 2008. Metabolic flux analysis in Escherichia coli by integrating isotopic dynamic and isotopic stationary C-13 labeling data. Biotechnology and Bioengineering 99(5):1170-1185.

Schaub J, Reuss M. 2008. In Vivo Dynamics of Glycolysis in Escherichia coli Shows Need for Growth-Rate Dependent Metabolome Analysis. Biotechnology Progress 24(6):1402-1407.

Schilling CH, Covert MW, Famili I, Church GM, Edwards JS, Palsson BO. 2002. Genome-scale metabolic model of Helicobacter pylori 26695. J Bacteriol 184(16):4582-93.

Schippers IJ, Moshage H, Roelofsen H, Muller M, Heymans HS, Ruiters M, Kuipers F. 1997. Immortalized human hepatocytes as a tool for the study of hepatocytic (de-)differentiation. Cell Biol Toxicol 13(4-5):375-86.

Schmid JW. 2007. Design metabolischer Stoffwechselsysteme am Beispiel der Tryptophansynthese in Escherichia coli. Dissertation, Universität Stuttgart, Fachbereich Bioverfahrenstechnik.

Schmidt K, Carlsen M, Nielsen J, Villadsen J. 1997. Modeling Isotopomer Distributions in Biochemical Networks Using Isotopomer Mapping Matrices. Biotechnol Bioeng 55(6):831-840.

Schmidt K, Marx A, de Graaf AA, Wiechert W, Sahm H, Nielsen J, Villadsen J. 1998. 13C tracer experiments and metabolite balancing for metabolic flux analysis: comparing two approaches. Biotechnol Bioeng 58(2-3):254-7.

Schomburg I, Chang A, Schomburg D. 2002. BRENDA, enzyme data and metabolic information. Nucleic Acids Res 30(1):47-9.

Schuster S, Schuster R. 1991. Detecting Strictly Detailed Balanced Subnetworks in Open Chemical-Reaction Networks. Journal of Mathematical Chemistry 6(1):17-40.

Scopes RK. 1973. 3-Phosphoglycerate kinase. The Enzymes, (Boyer, P.D., ed.) 3rd. Ed. 8:335-351.

Shastri AA, Morgan JA. 2007. A transient isotopic labeling methodology for C-13 metabolic flux analysis of photo auto trophic microorganisms. Phytochemistry 68(16-18):2302-2312.

Sherry AD, Sumegi B, Miller B, Cottam GL, Gavva S, Jones JG, Malloy CR. 1994. Orientation-conserved transfer of symmetric Krebs cycle intermediates in mammalian tissue. Biochemistry 33(20):6268-75.

Soboll S, Brown GC. 2000. The use of in situ haemoglobin-free perfused liver in metabolic-control analysis. Biochem Soc Trans 28(2):109-13.

Soboll S, Oh MH, Brown GC. 1998. Control of oxidative phosphorylation, gluconeogenesis, ureagenesis and ATP turnover in isolated perfused rat liver analyzed by top-down metabolic control analysis. Eur J Biochem 254(1):194-201.

Sonderegger M, Jeppsson M, Hahn-Hagerdal B, Sauer U. 2004. Molecular basis for anaerobic growth of Saccharomyces cerevisiae on xylose, investigated by global gene expression and metabolic flux analysis. Appl Environ Microbiol 70(4):2307-17.

Soundar S, Park JH, Huh TL, Colman RF. 2003. Evaluation by mutagenesis of the importance of 3 arginines in alpha, beta, and gamma subunits of human NAD-dependent isocitrate dehydrogenase. J Biol Chem 278(52):52146-53.

Staal GEJ, Koster JF, Veeger C. 1975. Human erythrocyte pyruvate kinase. Methods Enzymol. 42C:182-186.

Stephanopoulos G, Aristidou AA, Nielsen J. 1998. Metabolic Engineering Principles and Methodologies. Academic Press.

Streichert F, Ulmer H. 2005. JavaEvA : a Java based framework for Evolutionary Algorithms. Manual and Documentation. Wilhelm-Schickard-Institut für Informatik (WSI), Center for Bioinformatics Tübingen (ZBIT), Eberhard-Karls-University Tübingen, Germany. Tech Report WSI-2005-06.

Stryer L. 1995. Biochemistry. W. H. Freeman and Company (1995). 4.

Sumegi B, Sherry AD, Malloy CR. 1990. Channeling of TCA cycle intermediates in cultured Saccharomyces cerevisiae. Biochemistry 29(39):9106-10.

Sumegi B, Sherry AD, Malloy CR, Srere PA. 1993. Evidence for orientation-conserved transfer in the TCA cycle in Saccharomyces cerevisiae: 13C NMR studies. Biochemistry 32(47):12725-9.

Suthers PF, Burgard AP, Dasika MS, Nowroozi F, Van Dien S, Keasling JD, Maranas CD. 2007. Metabolic flux elucidation for large-scale models using C-13 labeled isotopes. Metabolic Engineering 9(5-6):387-405.

Teusink B, Diderich JA, Westerhoff HV, van Dam K, Walsh MC. 1998. Intracellular glucose concentration in derepressed yeast cells consuming glucose is high enough to reduce the glucose transport rate by 50%. J Bacteriol 180(3):556-62.

Teusink B, Passarge J, Reijenga CA, Esgalhado E, van der Weijden CC, Schepper M, Walsh MC, Bakker BM, van Dam K, Westerhoff HV and others. 2000. Can yeast glycolysis be understood in terms of in vitro kinetics of the constituent enzymes? Testing biochemistry. European Journal of Biochemistry 267(17):5313-5329.

Thannickal VJ. 2003. The paradox of reactive oxygen species: injury, signaling, or both? Am J Physiol Lung Cell Mol Physiol 284(1):L24-5.

Thannickal VJ, Fanburg BL. 2000. Reactive oxygen species in cell signaling. Am J Physiol Lung Cell Mol Physiol 279(6):L1005-28.

Theobald U, Mailinger W, Baltes M, Rizzi M, Reuss M. 1997. In vivo analysis of metabolic dynamics in Saccharomyces cerevisiae .1. Experimental observations. Biotechnology and Bioengineering 55(2):305-316.

Theobald U, Mailinger W, Rizzi M. 1994. Use of Hgcl2 to Investigate Dynamic Phenomena in Yeast Cytoplasm. Biotechnology Techniques 8(10):723-728.

Theobald U, Mohns J, Rizzi M. 1996. Dynamics of orthophosphate in yeast cytoplasm. Biotechnology Letters 18(4):461-466.

Thorens B. 1992. Molecular and cellular physiology of GLUT-2, a high-Km facilitated diffusion glucose transporter. Int Rev Cytol 137:209-38.

Thorens B. 1996. Glucose transporters in the regulation of intestinal, renal, and liver glucose fluxes. Am J Physiol 270(4 Pt 1):G541-53.

Torres NV, Mateo F, Melendezhevia E, Kacser H. 1986. Kinetics of Metabolic Pathways - a System Invitro to Study the Control of Flux. Biochemical Journal 234(1):169-174.

Tsuboi KK, Fukunaga K, Chervenka CH. 1971. Phosphoglucose isomerase from human erythrocyte. Preparation and properties. J Biol Chem 246(24):7586-94.

van Dam JC, Eman MR, Frank J, Lange HC, van Dedem GWK, Heijnen SJ. 2002. Analysis of glycolytic intermediates in Saccharomyces cerevisiae using anion exchange chromatography and electrospray ionization with tandem mass spectrometric detection. Analytica Chimica Acta 460(2):209-218.

van der Heijden RTJM, Romein B, Heijnen JJ, Hellinga C, Luyben KCAM. 1994. Linear constraint relations in biochemical reaction systems: II. Diagnosis and estimation of gross errors. Biotechnol Bioeng 43(1):11-20.

van Winden W, Verheijen P, Heijnen S. 2001. Possible pitfalls of flux calculations based on (13)C-labeling. Metab Eng 3(2):151-62.

van Winden WA, Heijnen JJ, Verheijen PJ. 2002. Cumulative bondomers: a new concept in flux analysis from 2D [13C,1H] COSY NMR data. Biotechnol Bioeng 80(7):731-45.

van Winden WA, van Dam JC, Ras C, Kleijn RJ, Vinke JL, van Gulik WM, Heijnen JJ. 2005. Metabolic-flux analysis of Saccharomyces cerevisiae CEN.PK113-7D based on mass isotopomer measurements of (13)C-labeled primary metabolites. FEMS Yeast Res 5(6-7):559-68.

Vaseghi S, Baumeister A, Rizzi M, Reuss M. 1999. In vivo dynamics of the pentose phosphate pathway in Saccharomyces cerevisiae. Metab Eng 1(2):128-40.

Veiga-da-Cunha M, Van Schaftingen E. 2002. Identification of fructose 6-phosphate- and fructose 1-phosphate-binding residues in the regulatory protein of glucokinase. J Biol Chem 277(10):8466-73.

Villas-Boas SG, Mas S, Akesson M, Smedsgaard J, Nielsen J. 2005. Mass spectrometry in metabolome analysis. Mass Spectrom Rev 24(5):613-46.

Visser D, Heijnen JJ. 2002. The mathematics of metabolic control analysis revisited. Metab Eng 4(2):114-23.

Visser D, Heijnen JJ. 2003. Dynamic simulation and metabolic re-design of a branched pathway using linlog kinetics. Metab Eng 5(3):164-76.

Visser D, Schmid JW, Mauch K, Reuss M, Heijnen JJ. 2004. Optimal re-design of primary metabolism in Escherichia coli using linlog kinetics. Metab Eng 6(4):378-90.

Vogt JA, Yarmush DM, Yu YM, Zupke C, Fischman AJ, Tompkins RG, Burke JF. 1997. TCA cycle flux estimates from NMR- and GC-MS-determined [13C]glutamate isotopomers in liver. Am J Physiol 272(6 Pt 1):C2049-62.

Wahl SA, Noh K, Wiechert W. 2008. C-13 labeling experiments at metabolic nonstationary conditions: An exploratory study. Bmc Bioinformatics 9:-.

Wang LQ, Hatzimanikatis V. 2006. Metabolic engineering under uncertainty. I: Framework development. Metabolic Engineering 8(2):133-141.

Wang NS, Stephanopoulos G. 1983. Application of macroscopic balances to the identification of gross measurement errors. Biotechnol Bioeng 25(9):2177-2208.

Warburg O, Posener K, Negelein E. 1924. Über den Stoffwechsel der Tumoren. Biochemische Zeitschrift 152:309-344.

Wehner F, Sauer H, Kinne RK. 1995. Hypertonic stress increases the Na+ conductance of rat hepatocytes in primary culture. J Gen Physiol 105(4):507-35.

Westerhoff HV, van Dam K. 1987. Thermodynamics and Control of Biological Free-Energy Transduction. Amsterdam: Elsevier.

Wiechert W. 2001. 13C metabolic flux analysis. Metab Eng 3(3):195-206.

Wiechert W, de Graaf AA. 1996. In vivo stationary flux analysis by 13C labeling experiments. Adv Biochem Eng Biotechnol 54:109-54.

Wiechert W, Möllney M, Isermann N, Wurzel M, de Graaf AA. 1999. Bidirectional reaction steps in metabolic networks: III. Explicit solution and analysis of isotopomer labeling systems. Biotechnol Bioeng 66(2):69-85.

Wiechert W, Möllney M, Petersen S, de Graaf AA. 2001. A universal framework for 13C metabolic flux analysis. Metab Eng 3(3):265-83.

Wiechert W, Nöh K. 2005. From stationary to instationary metabolic flux analysis. Adv Biochem Eng Biotechnol 92:145-72.

Wiseman MS, McKay D, Crow KE, Hardman MJ. 1991. Rat liver mitochondrial malate dehydrogenase: purification, kinetic properties, and role in ethanol metabolism. Arch Biochem Biophys 290(1):191-6.

Wittig U, Golebiewski M, Kania R, Krebs O, Mir S, Weidemann A, Anstein S, Saric J, Rojas I. 2006. SABIO-RK: Integration and curation of reaction kinetics data. Data Integration in the Life Sciences, Proceedings 4075:94-103.

Wu CH, Ho YS, Tsai CY, Wang YJ, Tseng H, Wei PL, Lee CH, Liu RS, Lin SY. 2009. In vitro and in vivo study of phloretin-induced apoptosis in human liver cancer cells involving inhibition of type II glucose transporter. Int J Cancer 124(9):2210-9.

Wu L, Wang W, van Winden WA, van Gulik WM, Heijnen JJ. 2004. A new framework for the estimation of control parameters in metabolic pathways using lin-log kinetics. Eur J Biochem 271(16):3348-59.

Xie L, Wang DI. 1994. Applications of improved stoichiometric model in medium design and fed-batch cultivation of animal cells in bioreactor. Cytotechnology 15(1-3):17-29.

Yang MS, Yu LC, Gupta RC. 2004a. Analysis of changes in energy and redox states in HepG2 hepatoma and C6 glioma cells upon exposure to cadmium. Toxicology 201(1-3):105-13.

Yang TH, Wittmann C, Heinzle EE. 2004b. Metabolic network simulation using logical loop algorithm and Jacobian matrix. Metab Eng 6(4):256-67.

Yarmush DM, MacDonald AD, Foy BD, Berthiaume F, Tompkins RG, Yarmush ML. 1999. Cutaneous burn injury alters relative tricarboxylic acid cycle fluxes in rat liver. J Burn Care Rehabil 20(4):292-302.

Yarmush ML, Banta S. 2003. Metabolic engineering: advances in modeling and intervention in health and disease. Annu Rev Biomed Eng 5:349-81.

Yarmush ML, Berthiaume F. 1997. Metabolic engineering and human disease. Nat Biotechnol 15(6):525-8.

Yoo H, Antoniewicz MR, Stephanopoulos G, Kelleher JK. 2008. Quantifying reductive carboxylation flux of glutamine to lipid in a brown adipocyte cell line. J Biol Chem 283(30):20621-7.

Young JD, Walther JL, Antoniewicz MR, Yoo H, Stephanopoulos G. 2008. An elementary metabolite unit (EMU) based method of isotopically nonstationary flux analysis. Biotechnol Bioeng 99(3):686-99.

Zhao Z, Kuijvenhoven K, Ras C, van Gulik WM, Heijnen JJ, Verheijen PJ, van Winden WA. 2008. Isotopic nonstationary 13C gluconate tracer method for accurate determination of the pentose phosphate pathway split-ratio in Penicillium chrysogenum. Metab Eng 10(3-4):178-86.

Zhou L, Salem JE, Saidel GM, Stanley WC, Cabrera ME. 2005. Mechanistic model of cardiac energy metabolism predicts localization of glycolysis to cytosolic subdomain during ischemia. Am J Physiol Heart Circ Physiol 288(5):H2400-11.

Zilversmit DB, Entenman C, Fishler MC. 1943. On the calculation of "turnover time" and "turnover rate" from experiments involving the use of labeling agents. Journal of General Physiology 26(3):325-331.

Zupke C, Sinskey AJ, Stephanopoulos G. 1995. Intracellular flux analysis applied to the effect of dissolved oxygen on hybridomas. Appl Microbiol Biotechnol 44(1-2):27-36.

Zupke C, Stephanopoulos G. 1994. Modeling of Isotope Distributions and Intracellular Fluxes in Metabolic Networks Using Atom Mapping Matrices. Biotechnol Prog 10(489-498).

Erklärung

Hiermit erkläre ich, dass ich die Dissertation, abgesehen von den ausdrücklich bezeichneten Hilfsmitteln und den Ratschlägen der jeweils namentlich aufgeführten Personen, selbständig verfasst habe.

Datum _____ Unterschrift _____